VORTEX-INDUCED VIBRATION OF CYLINDRICAL STRUCTURES

Enhao Wang

A thesis submitted in fulfilment of the requirements for the degree of Doctor of Philosophy

Department of Naval Architecture, Ocean and Marine Engineering
University of Strathclyde
Glasgow

October 2017

To my grandfather

"Water is fluid, soft and yielding. But water will wear away rock, which is rigid and cannot yield. As a rule, whatever is fluid, soft, and yielding will overcome whatever is rigid and hard. This is another paradox: what is soft is strong."

- Lao Tzu

Acknowledgements

"When I walk along with two others, from at least one I will be able to learn."

- Confucius

Studying in the Department of Naval Architecture, Ocean and Marine Engineering is one of the most memorable experiences in my life. When I turn to contemplate the years that it took to achieve my PhD degree, I realise that without all of those encouraging words, helping hands, and material assistance, I would never have made it up this hill.

I am deeply indebted to my PhD supervisors Dr Qing Xiao and Prof Atilla Incecik for their invaluable guidance, encouragement and inspiration.

Dr Xiao has always been very understanding both at a professional and personal level. With her hands-on approach, friendly personality and extensive knowledge of fluid mechanics, she creates an inspiring atmosphere for academic thriving.

Prof Incecik with his inexhaustible energy and excitement and his ingenuity, has been a constant source of inspiration for me. His approaches to research raised my thinking at higher levels.

I am grateful for the insightful discussions and suggestions from Dr Narakorn Srinil, Dr Hossein Zanganeh, Dr Mahdi Khorasanchi, Dr Laibing Jia and Dr Qiang Zhu about my PhD topic. I would also like to thank Prof Peilin Zhou for his supports and advice ever since I first came to Glasgow.

I must acknowledge as well the many friends and colleagues who provided advice, support and assistance for my research over these years. Especially, I would like to express my gratitude and deep appreciation to Dr Jianxin Hu, Dr Wendi Liu, Dr Yuanchuan Liu, Dr Ruoxin Li, Dr Zhenkai Zhao, Dr Zhiming Yuan, Dr Zhengqiang Xu, Dr Aijun Wang, Dr Wei Jin, Dr Xue Wang, and Dr Pengfei Zhang etc. whose

friendship, knowledge and wisdom have supported and enlightened me over the many years.

I would like to thank all the staff of the Department of Naval Architecture, Ocean and Marine Engineering, especially Mrs Thelma Will and Mrs Susan Pawson for being so helpful and caring.

I also want to thank all the staff of the ARCHIE-WeSt supercomputer centre at the University of Strathclyde for providing access to the high performance computing facilities. All the results in this thesis were obtained using the EPSRC funded ARCHIE-WeSt High Performance Computer (www.archie-west.ac.uk). EPSRC grant no. EP/K000586/1.

I would like to express my special feeling of gratitude to my loving grandparents, parents and parents-in-law. They always have faith in me and support me by all means possible. I thank my wife Zeyi for her support, encouragement, quiet patience and unwavering love.

Finally, I would like to acknowledge the financial support provided by the Faculty of Engineering and the Department of Naval Architecture, Ocean and Marine Engineering via the ‘Faculty Engineering Technology Studentship’.

Enhao Wang

October 2017

Abstract

Vortex-induced vibration (VIV) of cylindrical structures is a classical topic within fluid-structure interaction (FSI). In offshore engineering, it often causes the fatigue of slender structures, such as risers, mooring lines and pipelines. Detailed understanding of this FSI phenomenon and an efficient prediction of such self-excited and self-sustained oscillations are required for the reliable estimation of the fatigue damage and the development of VIV suppression techniques.

Over the past few decades, VIV has been extensively studied and the majority of the existing publications in the literature are experiments or semi-empirical modelling. In contrast, FSI simulations by combining high-fidelity computational fluid dynamics (CFD) and computational structural dynamics (CSD) solvers have received less attention. The main objective of this thesis is to investigate VIV of elastically mounted rigid cylinders and flexible cylinders using fully three-dimensional (3D) FSI simulations. Apart from important VIV aspects, such as response amplitude, response frequency and fatigue damage etc., the present research is also focussed on the aspects which have not been fully addressed by previous studies such as correlation lengths and time-dependent 3D flow structures.

Two-degree-of-freedom (2DOF) VIV of an elastically mounted circular cylinder with varying in-line (IL) to cross-flow (CF) natural frequency ratios ($f^* = f_{nx}/f_{ny}$) is first studied using a 3D CFD approach. Numerical simulation is carried out for a constant mass ratio $m^* = 2$ at a fixed Reynolds number Re = 500. The reduced velocity V_r ranges from 2 to 12. Three natural frequency ratios are considered, i.e., $f^* = 1$, 1.5 and 2. The structural damping is set to zero to maximise the response of the cylinder. The main objective of the first study is to investigate the effect of f^* on the 2DOF VIV responses and the 3D characteristics of the flow. It is discovered that there is a significant increase in the vibration amplitude and the peak amplitude shifts to a higher reduced velocity when f^* increases from 1 to 2. A single-peak cross-flow response is observed for the identical in-line and cross-flow mass ratios when $f^* = 2$. Dual resonance is found to exist over the range of f^* studied. The preferable

trajectories of the cylinder in the lock-in range are counterclockwise figure-eight orbits, whereas clockwise orbits primarily occur in the initial branch. The number of clockwise orbits decreases as f^* increases from 1 to 2. Oblique figure-eight trajectories appear at V_r = 6, 7 and 8 when f^* = 1. The third harmonic component which is observed in the lift fluctuation increases with f^*. The correlation decreases in the lock-in range and reaches its minimum value around the transition region between the lock-in and post-lock-in ranges. Three vortex shedding modes (2S, P + S and 2P) appear in the present simulation. A dominant P + S mode is associated with the oblique figure-eight trajectories. Variation of vortex shedding flows along the cylinder is observed leading to the poor correlation of the sectional lift forces.

Then, a numerical investigation of VIV of a vertical riser subject to uniform and linearly sheared currents is presented. The model vertical riser tested at the MARINTEK by ExxonMobil is considered. The predicted numerical results are in good agreement with the experimental data. It is found that the dominant mode numbers, the maximum root mean square amplitudes, the dominant frequencies and the fatigue damage indices increase with the flow velocity. Dual resonance is found to occur at most of the locations along the riser. At some locations along the riser, a third harmonic frequency component is observed in the CF response and a frequency component at the CF response frequency is found in the IL response apart from the frequency component at twice the CF response frequency. The majority of the vortex shedding shows a clear 2S pattern, whereas a 2P mode is observed near the position where the maximum vibration amplitude appears. The higher IL fatigue damage in the second study emphasises the importance of the IL fatigue damage analysis especially in the design of low flow velocity or low mode number applications.

The third study is on VIV of two tandem flexible cylinders at different spacing ratios (S_x/D) at a fixed Reynolds number Re = 500 using a two-way FSI method. The main objective is to investigate the effect of spacing on the hydrodynamic interactions and the VIV responses of these cylinders. It is found that the responses of the two tandem flexible cylinders are similar to the classical VIV responses when S_x/D is small. Once S_x/D is large enough for the vortices to be completely detached from the upstream

cylinder, the response of the upstream cylinder is similar to the typical VIV response whereas the downstream cylinder undergoes wake-induced vibration (WIV). The characteristics of the response of the downstream cylinder in the present study are similar to those of the first two response regimes. The third response regime is not observed for the flexible downstream cylinder with both ends fixed. The two changes in the phase relation between the cross-flow displacements of the two tandem flexible cylinders are discovered to be linked with the initial-upper branch transition and the upper-lower branch transition, respectively. The correlation lengths of the two tandem flexible cylinders decrease significantly in the transition range between the upper and lower branches. Three vortex shedding modes (2S, P + S and 2P) have been identified in the present study. It is found that the upper-branch 2P mode is associated with large-amplitude vibration of the upstream cylinder and the P + S mode is related to large-amplitude vibration of the downstream cylinder for S_x/D = 3.5 and 5. On the other hand, the lower-branch 2P mode leads to small-amplitude vibration of the downstream cylinder in the post-lock-in range at S_x/D = 2.5. The relative phase shifts of the sectional lift coefficients on different spanwise cross sections can be attributed to the variation of the vortex shedding flow along the flexible cylinders and these phase shifts result in poor phasing between the forces and the displacements which is related to the decrease of the correlation lengths.

Table of Contents

Nomenclature

Roman Symbols

A_x/D, A_y/D	Nondimensional in-line and cross-flow amplitudes
A_{xm}/D, A_{ym}/D	Maximum in-line and cross-flow amplitudes
A_{xrm}/D, A_{yrm}/D	Maximum root mean square in-line and cross-flow amplitudes
A_{xrms}/D, A_{yrms}/D	Root mean square in-line and cross-flow amplitudes
$\mathbf{B}$	Strain-displacement matrix
$\mathbf{C}$	Global damping matrix
c	Damping coefficient
C_a	Potential added mass coefficient
c_{cr}	Critical damping coefficient
C_{Dmean}	Mean drag coefficient
C_{D2}	Magnitude of the second harmonic component of the fluctuating drag coefficient
$\mathbf{C}^e$	Elements' damping matrix
c_i	Damping coefficient in the x_i-direction
C_{L1}	Magnitude of the first harmonic component of the fluctuating lift coefficient
Co	Courant number
$Co_{\max}$	Maximum Courant number
C_w	WALE model constant
c_x, c_y	In-line and cross-flow damping coefficients
C_D, C_L	Drag and lift coefficients
C'_D, C'_L	Oscillating drag and lift coefficients
C_{Drms}, C_{Lrms}	Root mean square drag and lift coefficients
C_{mx}, C_{my}	In-line and cross-flow effective added mass coefficients
D	Cylinder diameter
D_o	Outer diameter of the cylinder
$\mathbf{E}$	Elasticity matrix
E	Young's modulus

$\mathbf{F}$	Hydrodynamic force matrix
F_{Dmean}	Mean drag force
F_i	Hydrodynamic force in the x_i-direction
F_D, F_L	Drag and lift forces
F'_D, F'_L	Oscillating drag and lift forces
F_x, F_y	Hydrodynamic forces in the in-line and cross-flow directions
f_n	Natural frequency
$f_{n,\,beam}$	n^{th} eigenfrequency for a nontensioned beam
$f_{n,\,string}$	n^{th} eigenfrequency for a tensioned string
$f_{n,\,t\text{-}beam}$	n^{th} eigenfrequency for a tensioned beam
f_v	Vortex shedding frequency
f_w	Equivalent natural frequency of the wake stiffness
$f_{\varepsilon,z}$	Zero-crossing frequency of the bending strain
f_1	Fundamental natural frequency of a flexible cylinder
f^*	In-line to cross-flow natural frequency ratio
f_{nx}, f_{ny}	In-line and cross-flow natural frequencies
f_{ox}, f_{oy}	In-line and cross-flow oscillation frequencies
I	Moment of inertia
$\mathbf{K}$	Global stiffness matrix
K	Stiffness
$\mathbf{K}^e$	Elements' stiffness matrix
K_i	Stiffness in the x_i-direction
L	Length of the cylinder
L_C	Correlation length
L_C/D	Nondimensional correlation length
L/D	Length-to-diameter ratio
$\mathbf{M}$	Global mass matrix
m	Mass of the cylinder
$\mathbf{M}^e$	Elements' mass matrix
m_{ea}	Effective added mass
m_i	Mass in the x_i-direction
m^*	Mass ratio of the cylinder

m_{cr}^*	Critical mass ratio
m_x^*, m_y^*	In-line and cross-flow mass ratios
N	Matrix of shape functions
p	Pressure
q	Nodal displacement vector
Re	Reynolds number
S	Symmetric part of the velocity gradient tensor
Sc	Scruton number
S_i	Displacement of nodal points in the x_i-direction
$\overline{S}_{ij}$	Rate of strain tensor
S_{ij}^d	Traceless symmetric part of the square of the velocity gradient tensor
St	Strouhal number
S_x	Centre-to-centre spacing between two tandem cylinders
S_x/D	Centre-to-centre spacing ratio
$(S_x/D)_{cr}$	Critical spacing ratio
T	Top tension
T_{oy}	Period of cross-flow vibration
t	Time
t_w	Wall thickness
$\bar{u}$	Mean flow velocity
u_f	Friction velocity
u_i	Fluid velocity component in the x_i-direction
$\hat{u}_i$	Grid velocity component in the x_i-direction
u^+	Nondimensional velocity
V	Freestream velocity
V_{max}	Maximum velocity
V_{min}	Minimum velocity
V_r	Reduced velocity
x	Dimensional in-line displacement
x_i	Cartesian coordinate
y	Dimensional cross-flow displacement

y^+	Nondimensional mesh size

Greek Symbols

Γ	Mesh stiffness
Δ	Filter width
δ_{ij}	Kronecker symbol
ε	Root mean square strain
ζ	Damping ratio
θ	Phase difference between the in-line and cross-flow displacements
θ_x, θ_y	Phase angles of the in-line and cross-flow displacements
λ	Wave length of cylinder trajectory
λ_2	Second eigenvalue of the symmetric tensor $\mathbf{S}^2 + \mathbf{\Omega}^2$
λ_z/D	Wavelength of spanwise flow structures
μ	Dynamic viscosity of the fluid
ν	Kinematic viscosity of the fluid
ν_{sgs}	Subgrid-scale eddy-viscosity
ρ	Fluid density
ρ_L	Mass per unit length of the cylinder
ρ_s	Structural density
τ_{ij}	Subgrid-scale stress
τ_w	Wall shear stress
ϕ	Phase difference between the cross-flow displacements of two tandem cylinders
ϕ_x	Phase angle between fluctuating drag and in-line displacement
ϕ_y	Phase angle between fluctuating lift and cross-flow displacement
$\mathbf{\Omega}$	Antisymmetric part of the velocity gradient tensor
Ω_{ij}	Vorticity tensor
ω_z	Spanwise vorticity

Other Symbols

$\forall$	Control volume size
∇	Nabla operator

Abbreviations

ALE	Arbitrary Lagrangian-Eulerian
C	Clockwise
CC	Counterclockwise
CCS	Carbon capture and storage
CF	Cross-flow
CFD	Computational fluid dynamics
CFL	Courant-Friedrichs-Lewy
CO_2	Carbon dioxide
DES	Detached eddy simulation
DI	Damage index
DNS	Direct numerical simulation
DVM	Discrete vortex method
FEA	Finite element analysis
FEM	Finite element method
FSI	Fluid-structure interaction
FVM	Finite volume method
HHT	Hilber-Hughes-Taylor
IL	In-line
IP	Independence principle
P + S	A pair and a single vortices formed in each cycle
LSB	Laminar separation bubble
LES	Large eddy simulation
Q3D	Quasi-three-dimensional
RANS	Reynolds-averaged Navier-Stokes
VIV	Vortex-induced vibration
WIV	Wake-induced vibration

1D	One-dimensional
1DOF	One-degree-of-freedom
2D	Two-dimensional
2DOF	Two-degree-of-freedom
2P	Two pairs of vortices formed in each cycle
2S	Two single vortices formed in each cycle
2T	Two triplets of vortices formed in each cycle
3D	Three-dimensional

List of Tables

List of Figures

Chapter 1 Introduction

"A journey of a thousand miles begins with a single step."

- Lao Tzu

1.1 Background

1.1.1 Deep-Sea Carbon Dioxide Sequestration

One of the most pressing technical and economic challenges of our time is how to supply the world with sufficient energy for its economic growth without affecting the Earth's climate. If fossil fuels remain the dominant energy source of the 21st century, then stabilising the concentration of atmospheric carbon dioxide (CO_2) will require developing the capability to capture CO_2 from the combustion of fossil fuels and store it safely away from the atmosphere (Lackner, 2002).

It has been shown that deep-sea sediments might be able to provide a virtually unlimited and permanent reservoir for CO_2 captured from fossil fuel combustion (House *et al.*, 2006). When CO_2 is injected below the ocean floor at an ocean depth larger than 3000 m, the high pressure and low temperature will keep it below a layer of more buoyant pore fluid. Hydrate formation will also impede the upward flow of CO_2 as it cools along the geothermal gradient. The unique environmental conditions make the deep-sea sediments perfect for CO_2 sequestration.

Two solutions have been proposed for deep-sea CO_2 sequestration. Ozaki *et al.* (2013) proposed shuttle-type shipping and operation for CO_2 injection from the ship to the well (Fig. 1.1(a)). Another solution was proposed by Shell UK Limited and SSE Generation Limited (Spence *et al.*, 2014). As shown in Fig. 1.1(b), they are going to deliver the world's first full-scale carbon capture and storage (CCS) project in Scotland. The CO_2 emissions from Peterhead Power station will be transported by existing and newly-built pipelines to the depleted Goldeneye platform and the CO_2 will be injected through the existing production riser into the depleted gas reservoir.

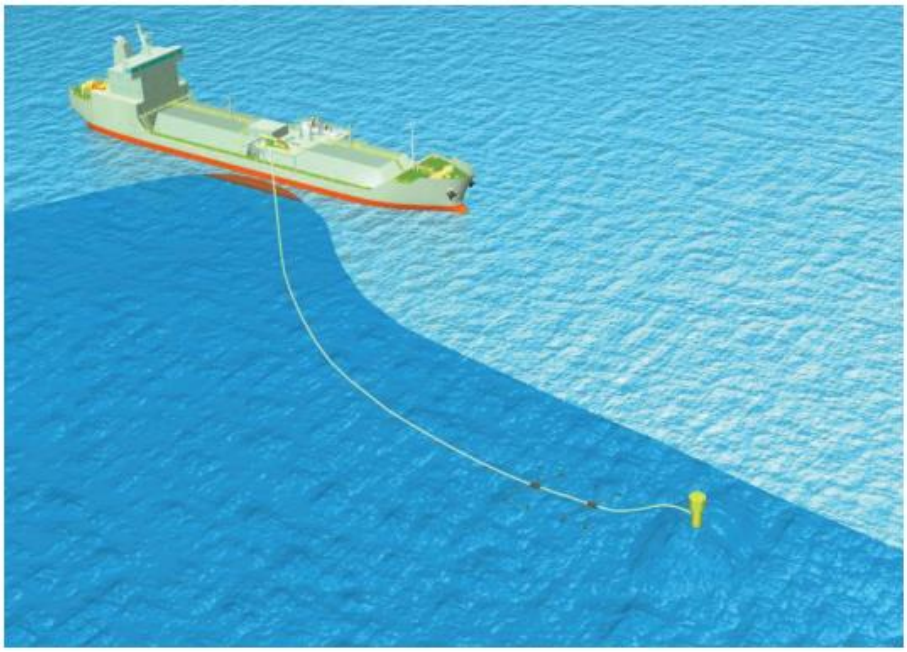

(a)

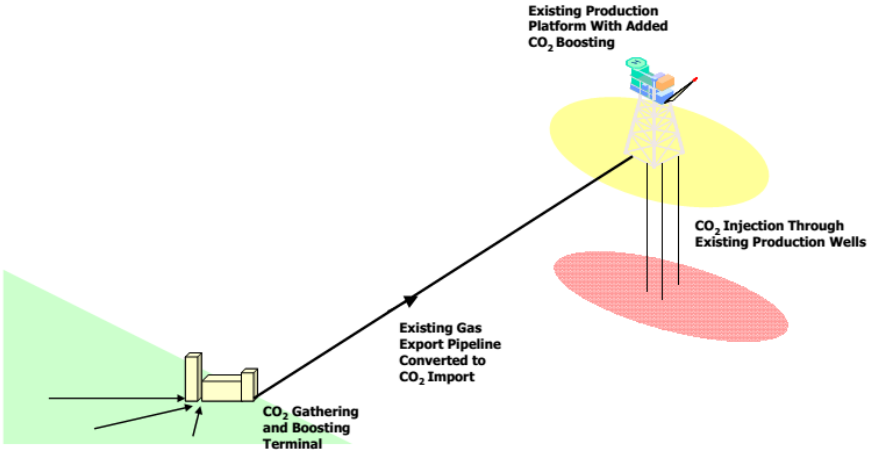

(b)

Fig. 1.1 Solutions to deep-sea CO_2 sequestration: (a) conceptual view of proposed ship-based CCS featuring shuttle ship equipped with injection facilities (Ozaki *et al.*, 2013) and (b) CO_2 injection in depleted gas field (Pershad and Slater, 2007).

In either method, CO_2 needs to be transported through flexible riser pipes. These riser pipes usually have lengths ranging from several hundred metres to several thousand metres. One of their key features is the large length-to-diameter ratio (L/D). Furthermore, the pipes used for CO_2 transport are often made of lightweight, high-

elasticity composite materials. From fluid-structure interaction (FSI) point of view, they suffer from larger lock-in ranges, which makes these pipes more vulnerable to vortex-induced vibration (VIV).

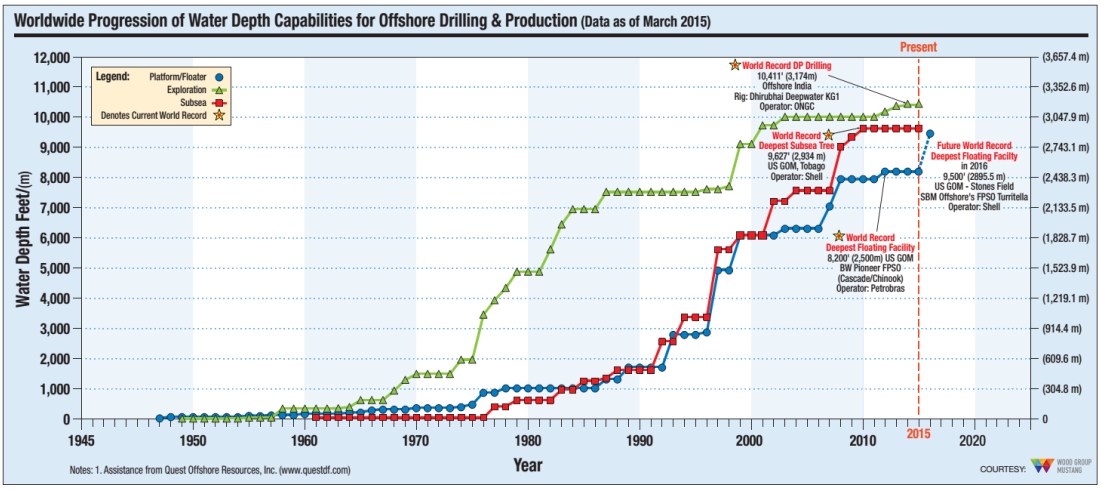

Fig. 1.2 Worldwide progression of water depth capabilities for offshore drilling and production (Barton *et al.*, 2015).

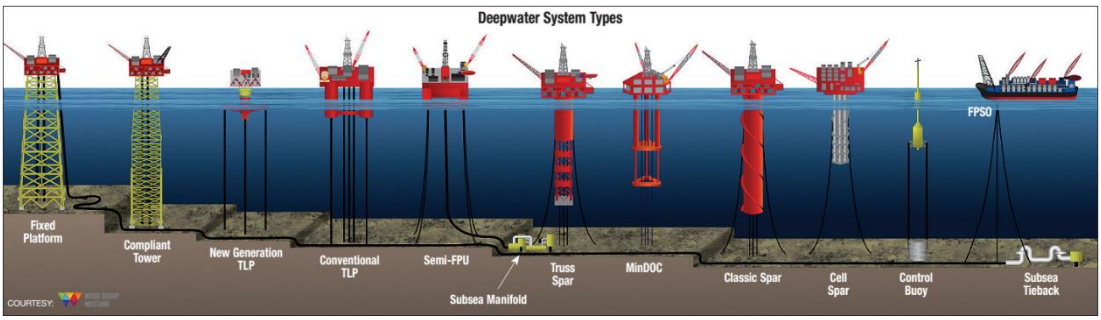

Fig. 1.3 Deepwater system types (Barton *et al.*, 2015).

1.1.2 Deepwater Oil/Gas Exploitation

The last decades have been marked by a considerable development of offshore oil and gas activities. Because of an increasing energy demand and technological innovations, drilling activities extended and moved into deep and ultra-deep water areas. In convention, deepwater is defined as water depths greater than or equal to 1000 feet (305 m) and ultra-deep water is defined as water depths greater than or equal to 5000 feet (1524 m). Fig. 1.2 shows the progression of water depth capabilities for offshore drilling and production (Barton *et al.*, 2015). It can be seen

that during the past few decades, the water depth has increased dramatically from several hundred metres in the 1970s to more than 3000 m in 2015. There are seven different types of drilling rigs currently in use offshore around the world.

1. Fixed platforms: Fixed platforms consist a tall, steel structure that supports a deck with space for drilling rigs, production facilities and crew quarters. They are anchored to the seabed. The maximum water depth they can drill to is about 520 m.

2. Jack-up rigs: Jack-up rigs can be moved around, and the legs are then lowered to the seabed and locked into place. They can only be placed in relatively shallow waters with water depths less than 200 m.

3. Compliant-tower rigs: Compliant-tower rigs are very similar to fixed platforms. Both types are anchored to the seabed with work places above the water surface. However, the compliant-tower rigs are taller and narrower, and can operate up to 1000 m below the water surface.

4. Floating production systems: Floating production systems are the most common rigs used in the Gulf of Mexico. These rigs are buoyant with the bulks of them floating above the water surface. They can operate anywhere from 200 to 2000 m below the water surface.

5. Tension-leg platforms: Tension-leg platforms consist of a floating structure, held in place by tendons that run down to the seabed. These rigs can drill anywhere from 200 to 1200 m below the water surface.

6. Subsea systems: Subsea systems are actually wellheads, which sit on the seabed and extract oil straight from the ground.

7. Spar platforms: Spar platforms use a large cylinder to support the deck. Most spar platforms are used up to water depths of 1000 m, but new technology can extend them to function up to 3500 m.

Schematics of different types of deepwater systems are given in Fig. 1.3 with jack-up rigs being excluded due to the fact that they are usually operated in relatively shallow waters.

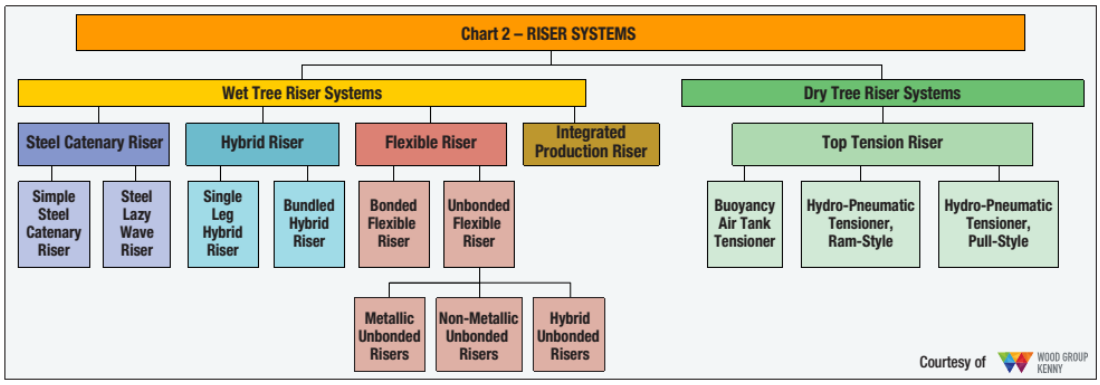

Fig. 1.4 Different categories of riser systems (Brany *et al.*, 2015).

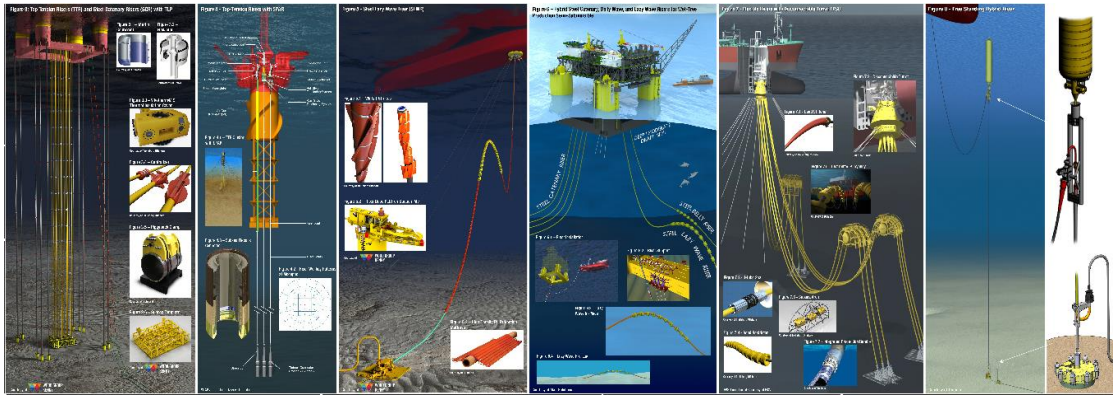

(a) (b) (c) (d) (e) (f)

Fig. 1.5 Commonly used riser configurations: (a) top tension risers and steel catenary risers, (b) top tension risers, (c) steel lazy wave riser, (d) hybrid steel catenary, belly wave, and lazy wave risers, (e) flexible risers with disconnectable turret, and (f) free standing hybrid riser (Brany *et al.*, 2015).

One of the key components of deepwater oil and gas exploitation is the riser system. A riser system is essentially conductor pipes connecting floaters on the surface and the wellheads at the seabed. Two kinds of subsea production systems are used in

deepwater fields, i.e., dry tree systems and wet tree systems. In dry tree systems, trees are located on or close to the platform, whereas wet trees can be anywhere in a field in terms of cluster, template, or tie-back methods. Different categories of the riser systems are summarised in Fig. 1.4. Fig. 1.5 shows some commonly used riser configurations in offshore drilling and production. Similar to the flexible riser pipes used in CO_2 sequestration, the drilling/production risers often possess large *L/D* although metallic pipes with larger diameters are tended to be used in deepwater oil/gas exploitation operations. Nevertheless, VIV is one of the major design issues for all deepwater riser systems.

1.2 Objectives of the Thesis

VIV of cylindrical structures has been extensively studied by various researchers over the past few decades. Comprehensive reviews can be found in Blevins (1977), Williamson and Govardhan (2004), Gabbai and Benaroya (2005), Sumer and Fredsøe (2006), Bearman (2011), Wu *et al.* (2012), Païdoussis *et al.* (2014) and Triantafyllou *et al.* (2016). The majority of the existing publications on VIV are experiments or semi-empirical modelling. Previous computational fluid dynamics (CFD) studies on VIV are mainly two-dimensional (2D). Three-dimensional (3D) FSI simulations of VIV of cylindrical structures are still quite limited. Therefore, the main objectives of this thesis are to develop 3D numerical models for FSI simulation of rigid and flexible structures and use the developed models to investigate VIV of cylindrical structures. Apart from the important aspects of the VIV phenomenon, the present research is focussed on the aspects which have not been fully addressed by previous studies such as the correlations and the 3D wake structures. 3D FSI simulations can provide more comprehensive force measurements than experiments and semi-empirical modelling. Furthermore, the flow visualisation techniques make it possible to analyse the time dependent 3D wake structures which are difficult to obtain and so far to date, have not been measured in experiments. Therefore, it is expected that the 3D modelling in this thesis could provide more detailed insights into the mechanism of VIV of rigid and flexible cylinders.

Owing to the complexity of the vortex hydrodynamics, the intrinsic mechanism of the structure, the overall elasto-hydro nonlinearities and the influence of several mechanical/physical parameters, modelling VIV remains a challenging theme and there are many topics worth investigating. Of course, it is impossible for one single thesis to cover every aspect within the scope of the VIV phenomenon, but efforts have been made to select the topics with both theoretical and practical significance. Among the various different topics, the following three are selected for research in the present thesis.

- In the first study, 3D numerical simulation of two-degree-of freedom (2DOF) VIV of an elastically mounted circular cylinder is conducted with the purpose of investigating the effect of the natural frequency ratio on the 2DOF VIV response and the 3D flow structures of a rigid cylinder.

- The 3D numerical simulation of VIV of a vertical riser in the second study is mainly focussed on the effect of incoming flow conditions on the VIV response of the riser and addressing the importance of in-line fatigue damage in low flow velocity or low mode number applications.

- The third study is a 3D numerical investigation of VIV of two flexible circular cylinders in tandem arrangement at different spacing ratios. The main objective is to numerically study the effect of spacing on the hydrodynamic interactions and VIV responses of the two flexible cylinders arranged in tandem.

1.3 An Outline of the Thesis

This thesis can be seen as seven chapters assembled logically to meet the objectives defined in Section 1.2 and the outline of the thesis is as follows. The background of the research on VIV of cylindrical structures and the objectives of the thesis are provided in Chapter 1. The intrinsic nature of flow past stationary cylinders and the fundamental mechanisms of the VIV phenomenon together with previous studies on

topics relevant to this thesis are reviewed in Chapter 2. Chapter 3 outlines the detailed numerical methods for FSI simulation of VIV of rigid and flexible cylindrical structures. Chapter 4 to Chapter 6 form the core of the thesis. A three-dimensional numerical simulation of 2DOF VIV of a circular cylinder with varying natural frequency ratios is given in Chapter 4. In Chapter 5, a large eddy simulation of VIV of a vertical riser in uniform and linearly sheared currents is presented. The effect of spacing on the VIV of two tandem flexible cylinders is investigated in Chapter 6 and this thesis is concluded in Chapter 7.

Chapter 2 Critical Review

"Study the past, if you would divine the future."

-Confucius

2.1 Flow around Stationary Cylinders

2.1.1 Flow around a Stationary Cylinder

2.1.1.1 Flow Separation and Mechanism of Vortex Shedding

When fluid flow approaches a bluff cylinder, due to the high stagnation pressure at its leading edge, the developing boundary layer is impelled about both sides of the cylinder. Depending on the Reynolds number, which is defined as

$$\mathrm{Re} = \frac{VD}{\nu} \tag{2.1}$$

where D is the diameter of the cylinder, V is the freestream velocity and ν is the kinematic viscosity of the fluid, the flow around the cylinder can be classified into different regimes. Fig. 2.1 summarises different flow regimes around a smooth circular cylinder (Sumer and Fredsøe, 2006). When Re < 5, the flow attaches to the cylinder surface and no separation occurs. With the increase of Re, due to the adverse pressure gradients imposed by the divergent geometry of the flow environment, the pressure forces gradually become insufficient to force the boundary layers around the back side of the cylinder. Then, the boundary layers separate from each side of the cylinder surface and form two free shear layers in the wake. The separation first appears when Re becomes 5. A sketch of flow separation is shown in Fig. 2.2.

For the range of 5 < Re < 40, a pair of symmetric vortices forms in the wake of the cylinder. With a further increase of Re, the two symmetric vortices become unstable as the result of the small disturbances. Consequently, one vortex will grow larger than the other if Re > 40. As shown in Fig. 2.3, when the larger vortex (Vortex A)

becomes strong enough, it will draw the opposing vortex (Vortex B) across the wake. The approach of vorticity of the opposite sign will cut off the supply of vorticity of Vortex A from its boundary layer and this is the instant where Vortex A is shed. Upon shedding of Vortex A, it becomes a free vortex and is then convected downstream by the flow.

(a)	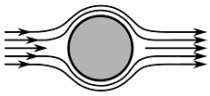	No separation. Creeping flow	$Re < 5$
(b)	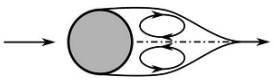	A fixed pair of symmetric vortices	$5 < Re < 40$
(c)	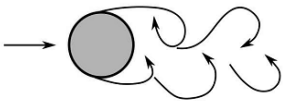	Laminar vortex street	$40 < Re < 200$
(d)	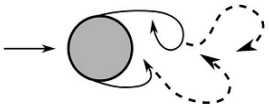	Transition to turbulence in the wake	$200 < Re < 300$
(e)	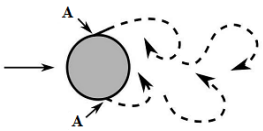	Wake completely turbulent. A: Laminar boundary layer separation	$300 < Re < 3 \times 10^5$ Subcritical
(f)	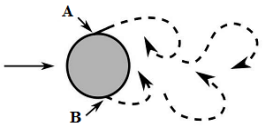	A: Laminar boundary layer separation B: Turbulent boundary layer separation; but boundary layer laminar	$3 \times 10^5 < Re < 3.5 \times 10^5$ Critical (Lower Transition)
(g)	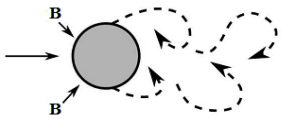	B: Turbulent boundary layer separation; the boundary layer partly laminar partly turbulent	$3.5 \times 10^5 < Re < 1.5 \times 10^6$ Supercritical
(h)	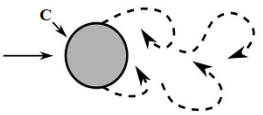	C: Boundary layer completely turbulent at one side	$1.5 \times 10^6 < Re < 4 \times 10^6$ Upper transition
(i)	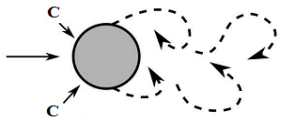	C: Boundary layer completely turbulent at two sides	$Re > 4 \times 10^6$ Transcritical

Fig. 2.1 Regimes of flow around a smooth circular cylinder (Sumer and Fredsøe, 2006).

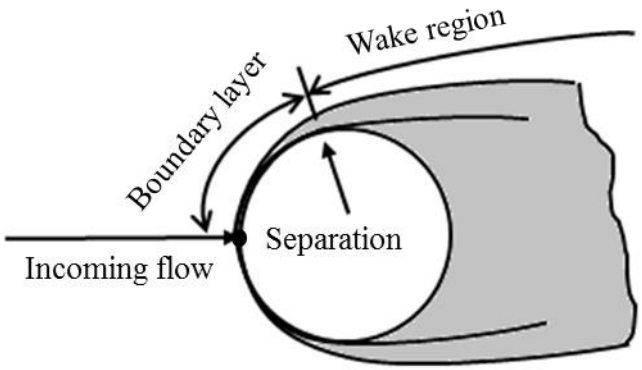

Fig. 2.2 A sketch of flow separation (Sumer and Fredsøe, 2006).

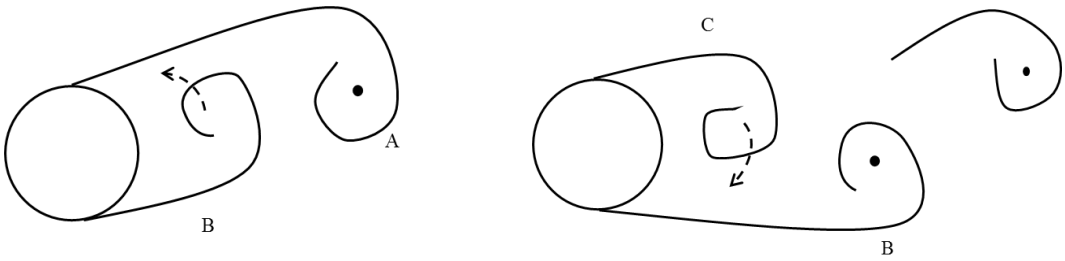

(a) (b)

Fig. 2.3 Mechanism of vortex shedding (Sumer and Fredsøe, 2006).

Following the shedding of Vortex A, a new vortex will be formed on the same side of the cylinder, namely Vortex C as shown in Fig. 2.3(b). Vortex B will now play the same role as Vortex A, resulting in the detachment and the shedding of Vortex B. In this continuous manner, the vortices are shed alternatively from either side of the cylinder at a certain frequency. Consequently, the wake has an appearance of a vortex street as shown in Fig. 2.4. The frequency at which the alternative vortices are shed, f_v can be normalised with the flow velocity V and the cylinder diameter D to form the so-called Strouhal number.

$$\mathrm{St} = \frac{f_v D}{V} \tag{2.2}$$

2.1.1.2 Flow Regimes and the Strouhal Number

Since the flow around a smooth cylinder is governed by Re, St can on dimensional grounds be seen to be a function of Re. Fig. 2.5 presents the variation of St with Re.

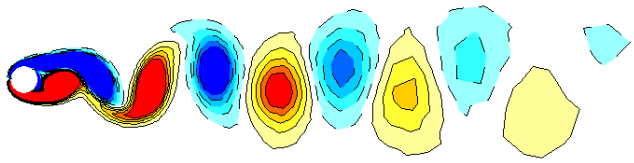

Fig. 2.4 Vortex street behind a circular cylinder at Re = 150.

The report of St starts from Re = 40. As it is illustrated in Fig. 2.1(a) and (b), for Re < 40, the vortices are attached to the cylinder and there is no vortex shedding. For 40 < Re < 200, the vortex street is laminar and the vortex shedding is essentially 2D. In this range, St increases linearly with Re. The transition in the wake region occurs when 200 < Re < 300. Two discontinuities are observed in St in the experimental data by Williamson (1992). The dislocation of the vortices leads to the first discontinuity as the flow changes from 2D to Mode A (see Fig. 2.6(a)). The second discontinuity occurs as the flow transits from Mode A to Mode B as illustrated in Fig. 2.6(b). For 300 < Re < 3×10^5, the wake is completely turbulent whereas the boundary layer over the cylinder surface remains laminar. This regime is known as the subcritical flow regime where St is almost constant at St ≈ 0.2. With a further increase of Re, the flow enters the critical regime (3×10^5 < Re < 3.5×10^5). In the critical regime, the boundary layer separation is turbulent on one side of the cylinder and laminar on the other side. The next flow regime is the so-called supercritical flow regime where 3.5×10^5 < Re < 1.5×10^6. In this regime, the boundary layer on both sides of the cylinder is turbulent at the separation points. This results in a delay in the boundary-layer separation where the separation points move downstream. This means the vortices would interact at a faster rate. Therefore, a dramatic increase of St from 0.2 to 0.45 is seen in this regime. The Strouhal number experiences another discontinuity when Re reaches the value of 1.5×10^6. At this Re, transition to turbulence in one of the boundary layers has been completed (Fig. 2.1(h)). The boundary layer on one side of the cylinder is completely turbulent and that on the other side is partly laminar and partly turbulent. The asymmetric situation causes the formation of the lee-wake vortices and it prevails over the whole upper transition

regime ($1.5 \times 10^6 < Re < 4 \times 10^6$). The regular vortex shedding is re-established in the transcritical flow regime where St takes the value of 0.25 – 0.3.

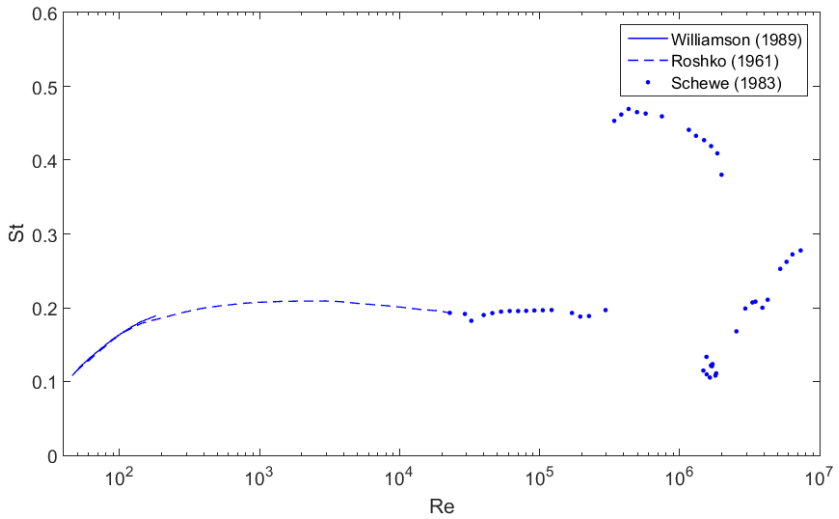

Fig. 2.5 Strouhal number for a smooth cylinder: —: (Williamson, 1989), ---: (Roshko, 1961), and ●: (Schewe, 1983).

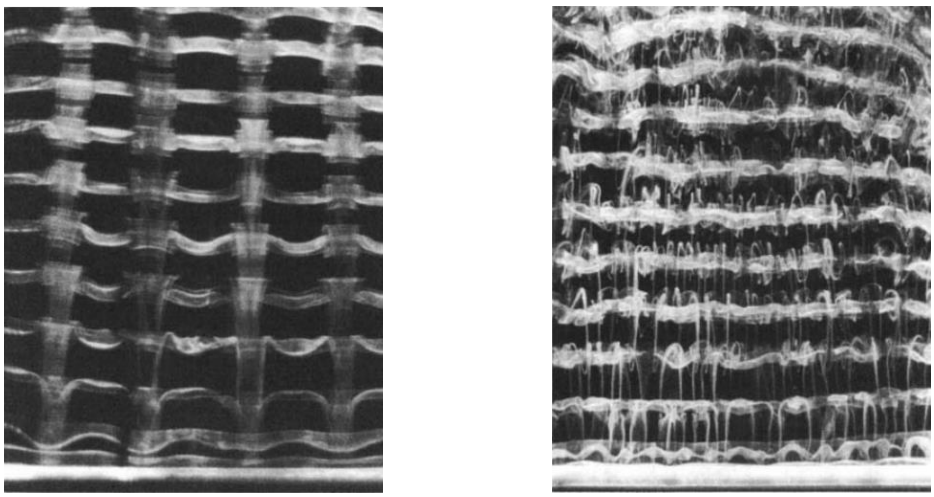

(a) (b)

Fig. 2.6 Mode A and B three-dimensional vortex shedding. (a) Mode A represents the inception of streamwise vortex loops and (b) Mode B represents the formation of finer-scale streamwise vortex pairs (Williamson, 1992).

2.1.1.3 Hydrodynamic Forces

Fig. 2.7 shows the pressure distributions in one vortex shedding cycle at Re = 150 obtained from CFD simulation. Fig. 2.8 depicts the time histories of the hydrodynamic force coefficients corresponding to the same simulation.

The uneven and asymmetric pressure distributions between the front and back sides of the cylinder along with the friction effects of viscosity result in a mean drag force (F_{Dmean}). On the other hand, the alternatively shed vortices lead to a periodically changing pressure field and cause the oscillating drag and lift forces (F'_D and F'_L). The mean drag coefficient (C_{Dmean}) and the oscillating drag and lift coefficients (C'_D and C'_L) are defined as follows.

$$C_{Dmean} = \frac{F_{Dmean}}{\frac{1}{2}\rho V^2 DL} \tag{2.3}$$

$$C'_D = \frac{F'_D}{\frac{1}{2}\rho V^2 DL} \tag{2.4}$$

$$C'_L = \frac{F'_L}{\frac{1}{2}\rho V^2 DL} \tag{2.5}$$

where ρ is the fluid density and L is the length of the cylinder.

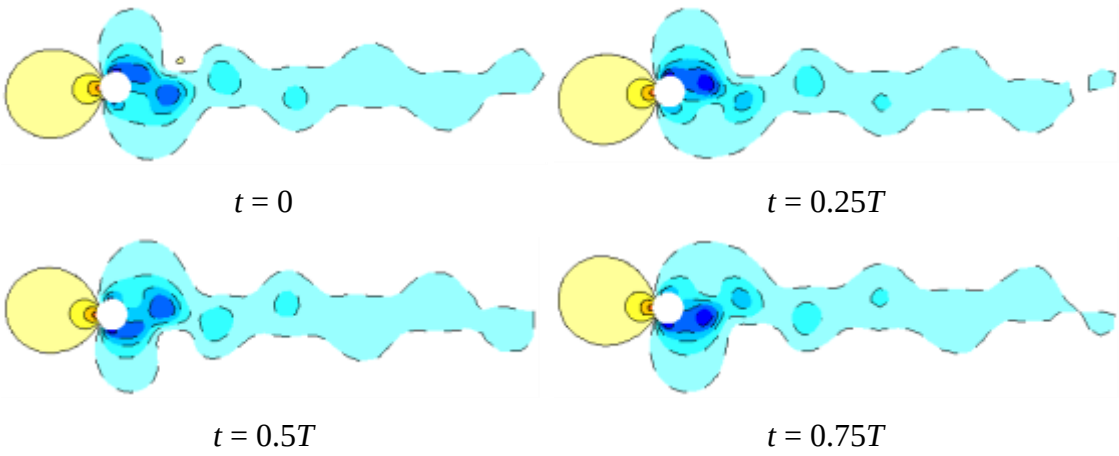

Fig. 2.7 Pressure distributions in one vortex shedding cycle at Re = 150.

Fig. 2.9 shows the variation of C_{Dmean} and the root mean square (rms) values of oscillating drag and lift coefficients (C_{Drms} and C_{Lrms}) with Re. It can be seen that

C_{Dmean} decreases monotonously with Re until Re reaches the value of about 300. However, from this Re onwards, C_{Dmean} reaches a constant value of approximately 1.2 and it nearly remains constant in the subcritical range. When Re increases to the value 3×10^5, a dramatic change occurs in C_{Dmean} with its value decreasing abruptly. This phenomenon is called the drag crisis. In this regime, the laminar boundary layer separates near the shoulder of the cylinder. The separated shear layer undergoes transition to a turbulent state and reattaches to the surface of the cylinder, leading to the formation of a laminar separation bubble (LSB). The reattached turbulent boundary layer separates further downstream. As a result, the wake is narrower and base suction pressure higher, leading to the drag crisis. C_{Dmean} increases as the flow regime is changed from the supercritical to upper-transition and then attains a constant value of about 0.5 as Re is further increased to transcritical values (namely $Re > 4.5 \times 10^6$). The fluctuating drag and lift coefficients are very low in the supercritical range due to the large separation angles.

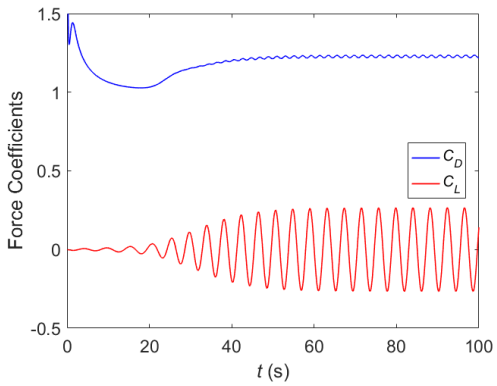

Fig. 2.8 Time histories of the drag and lift coefficients at Re = 150.

2.1.2 Flow around Two Stationary Cylinders in Tandem Arrangement

2.1.2.1 Flow Patterns

Compared to the flow around a single circular cylinder, the flow around multiple-cylinder configurations is less well studied and understood due to the fact that it involves complex interactions between the shear layers, vortices, wakes and Kármán vortex streets. One of the idealised arrangements of the cylinders which have

received the most study is the tandem configuration as shown in Fig. 2.10. An additional geometric parameter, the centre-to-centre spacing between the two tandem cylinders S_x is introduced to describe the system. The spacing is usually expressed in nondimensional form as the spacing ratio S_x/D.

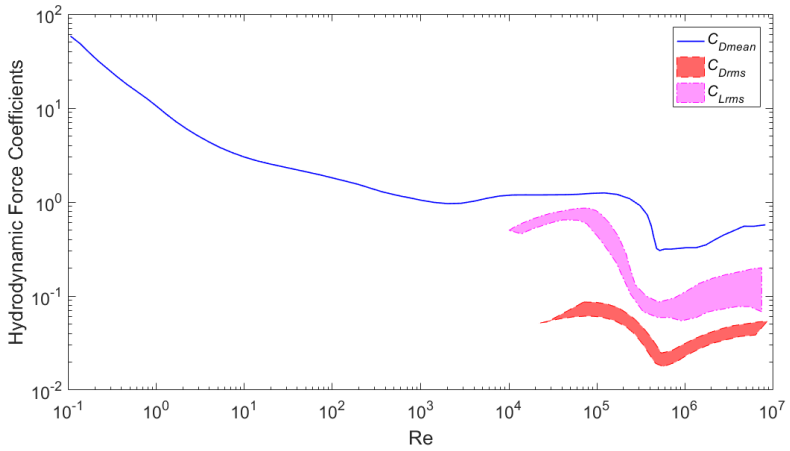

Fig. 2.9 Variation of the mean drag coefficient and rms values of fluctuating drag and lift coefficients (Sumer and Fredsøe, 2006).

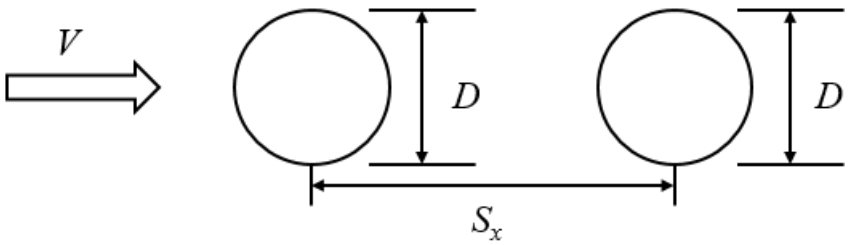

Fig. 2.10 A sketch of two stationary cylinders in tandem arrangement.

The pioneering studies on the classification of the flow patterns around two tandem stationary cylinders by Igarashi (1981, 1984) identified eight different flow patterns as shown in Fig. 2.11(a). Igarashi's map of the flow patterns in Re – S_x/D space is shown in Fig. 2.11(b). Following the approach of Zdravkovich (1987), the flow patterns in Fig. 2.11 can be subdivided into three basic types of wake interference behaviours. When the two cylinders are placed in very close proximity, the two cylinders behave as a single body. The separated shear layers from the upstream cylinder wrap around the downstream cylinder without reattaching onto its surface and form a single Kármán vortex street in the wake. This regime is referred to as the

"extended-body regime" by Xu and Zhou (2004) and Zhou and Yiu (2006). At intermediate S_x/D, the separated shear layers from the upstream cylinder reattach onto the surface of the downstream cylinder. When the spacing between the cylinders increases beyond a critical spacing $(S_x/D)_{cr}$, vortex shedding occurs in the gap region between the two cylinders so that the wake behind the cylinders is a combination of the wakes of the two cylinders. This regime is termed as the "binary vortex regime" by Papaioannou (2004) or "co-shedding regime" by Xu and Zhou (2004) and Zhou and Yiu (2006).

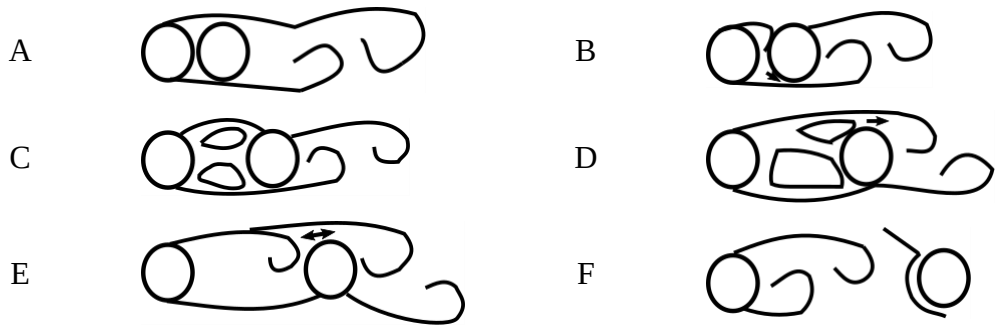

(a)

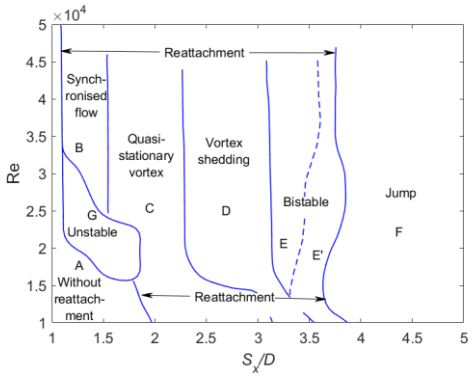

(b)

Fig. 2.11 (a) Classification of flow patterns for two tandem circular cylinders and (b) map of flow patterns in the Re – S_x/D space (Igarashi, 1981).

2.1.2.2 Reynolds number effects

The critical spacing is particularly sensitive to Re, and from the various studies in the literature, its value varies from 3 to 5. It is noted that the critical spacing ratio behaviour closely follows the Reynolds number sensitivity of the vortex formation length (Fig. 2.12) (Ljungkrona and Sundén, 1993). Also contributing to the Reynolds

number effects is the behaviour of the shear layers from the upstream cylinder and the development of shear layer instability (Kelvin – Helmholtz) vortices (Lin *et al.*, 2002). Within the reattachment regime, the small-scale shear-layer instability vortices buffet the surface of the downstream cylinder. From Fig. 2.11 and Fig. 2.12, the trend in the experimental data is towards a larger critical spacing ratio at low Re.

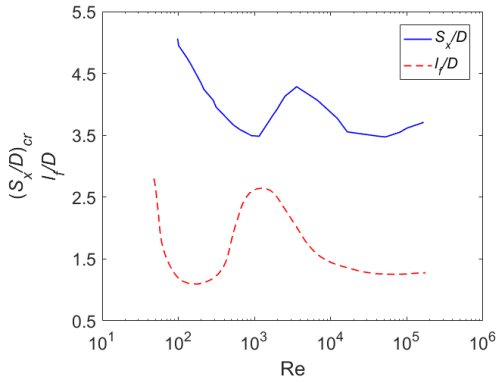

Fig. 2.12 Reynolds number sensitivity of the vortex formation length l_f/D for a single circular cylinder and the critical spacing ratio (Ljungkrona and Sundén, 1993).

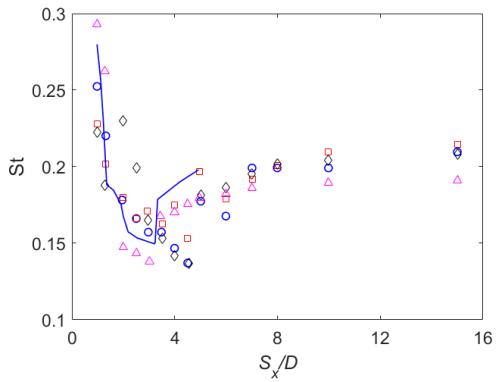

Fig. 2.13 Strouhal number data for two tandem stationary cylinders as a function of spacing ratio: ○, Re = 1.2×10^3; □, Re = 2.9×10^3; ◊, Re = 7×10^3; Δ, Re = 4.2×10^4; solid line, Re = 2.2×10^4 (Xu and Zhou, 2004).

2.1.2.3 Strouhal Number

The most extensive set of Strouhal number data for two tandem stationary cylinders is that of Xu and Zhou (2004), for a wide range of Re (Re = 800 – 4.2×10^4) and

spacing ratios (S_x/D = 1 – 15). The relationship between St and spacing ratio is shown in Fig. 2.13.

When the cylinders behave as a single bluff body at small S_x/D, St is initially higher than the single-cylinder value but decreases rapidly with increasing S_x/D. The higher shedding frequency for the extended-body regime is a reflection of the shorter vortex formation length when the cylinders are placed very close together (Zdravkovich, 1977). At the boundary between the extended-body and reattachment regimes (e.g., Pattern G shown in Fig. 2.11(b)), two dominant frequencies (Strouhal numbers) may be found (Igarashi, 1981, 1984; Ljungkrona *et al.*, 1991). A slower decrease of St occurs during the reattachment regime as S_x/D increases, and St becomes lower than the value for a single cylinder. The lower shedding frequency reflects a "stabilisation" of the flow field by the presence of the downstream cylinder.

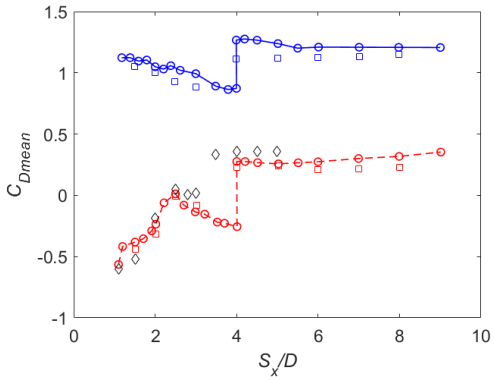

Fig. 2.14 Mean drag coefficient data for two tandem stationary cylinders in cross-flow as function of spacing ratio: ○, upstream cylinder, Re = 6.5×10^4 (Alam *et al.*, 2003); ○, downstream cylinder, Re = 6.5×10^4 (Alam *et al.*, 2003); □, upstream cylinder (Biermann and Herrnstein, 1934); □, downstream cylinder (Biermann and Herrnstein, 1934); ◊, downstream cylinder (Zdravkovich and Pridden, 1977).

A discontinuous jump in St occurs at critical spacing, as St suddenly increases from a low value to a high value. The existence of bistable flow patterns at the boundary between the reattachment and binary vortex regimes (e.g., Patterns E and E' shown in Fig. 2.11(b)) means that over a small range of spacing ratio two dominant frequencies are found. Within the binary vortex regime, the same St value is

measured behind both cylinders and the value of St slowly increases and approaches the single-cylinder value as S_x/D increases.

2.1.2.4 Hydrodynamic Forces

The complexity of C_{Dmean} for the upstream and downstream cylinders is shown in Fig. 2.14. For the upstream cylinder, C_{Dmean} is typically lower than the single-cylinder value in the extended-body and reattachment regimes due to the stabilisation effect of the downstream cylinder. There is a slow decrease in C_{Dmean} with increasing S_x/D until the end of the reattachment regime. After the critical spacing, where the flow suddenly transitions to the binary vortex regime, C_{Dmean} jumps to a higher value close to that of a single cylinder.

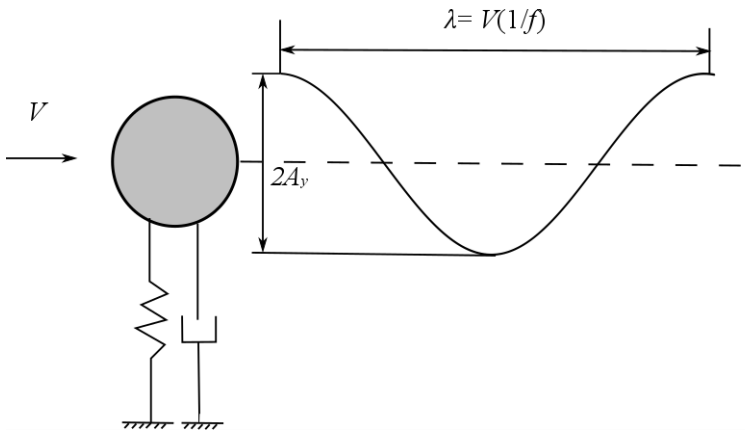

Fig. 2.15 Definition sketch for cross-flow vibrations.

In the extended-body and reattachment regimes, C_{Dmean} of the downstream cylinder is negative (and may reach zero drag at a given value of S_x/D, depending on Re) indicating this cylinder experiences a thrust force. A discontinuous jump from a small negative C_{Dmean} to a larger positive value occurs as the flow jumps from reattachment regime to the binary vortex regime. At increasingly large spacing ratios, C_{Dmean} values for the cylinder will eventually approach the single-cylinder value. Since C_{Dmean} of the downstream cylinder is for the most part negative when $S_x/D < (S_x/D)_{cr}$, and positive for $S_x/D > (S_x/D)_{cr}$, the critical spacing has also been termed the 'drag inversion' spacing (Carmo *et al.*, 2010a, b).

2.2 Vortex-Induced Vibration of Cylinders

As discussed in the previous section, the vortex shedding process gives rise to oscillatory drag and lift which, if the cylinder is elastically mounted or flexible, can result in VIV.

2.2.1 Nondimensional Variables Influencing One-Degree-of-Freedom VIV

2.2.1.1 Reduced Velocity

In VIV analysis, the freestream velocity V is commonly reported in nondimensional form using the natural frequency of the system f_n and it is called the reduced velocity (Gabbai and Benaroya, 2005).

$$V_r = \frac{V}{f_n D} \tag{2.6}$$

A simple interpretation of V_r would be viewing it as the ratio of the wave length of the cylinder trajectory λ to the diameter D if the cylinder is subject to a fluid flow with a constant velocity V as illustrated in Fig. 2.15. The wave length of the periodic motion of the cylinder will be

$$\lambda = V\left(1/f\right) \tag{2.7}$$

where f is the oscillation frequency. Therefore,

$$\frac{\lambda}{D} = \frac{V}{fD} = V_r \tag{2.8}$$

It is obvious that V_r plays an extremely important role with respect to the vortex motion around the cylinder which would apparently determine the excitation range of the vibration.

Fig. 2.16(b) shows the frequency response of an elastically mounted rigid cylinder subject to one-degree-of-freedom (1DOF) cross-flow (CF) VIV (Khalak and

Williamson, 1997b). When V_r is low, the oscillation frequency (f_{oy}) follows the stationary-cylinder Strouhal frequency (f_v) until it approaches the natural frequency of the cylinder. From this point on, with a further increase of V_r, f_{oy} deviates from f_v and the ratio of the oscillation frequency to the natural frequency of the cylinder (f_{oy}/f_{ny}) remains constant. The synchronisation between the oscillation frequency and the vortex shedding frequency is known as the lock-in phenomenon and this corresponding range of V_r in which the cylinder undergoes large-amplitude vibration is referred to as the lock-in range (Williamson and Govardhan, 2004). Beyond the lock-in range, f_{oy} returns to f_v.

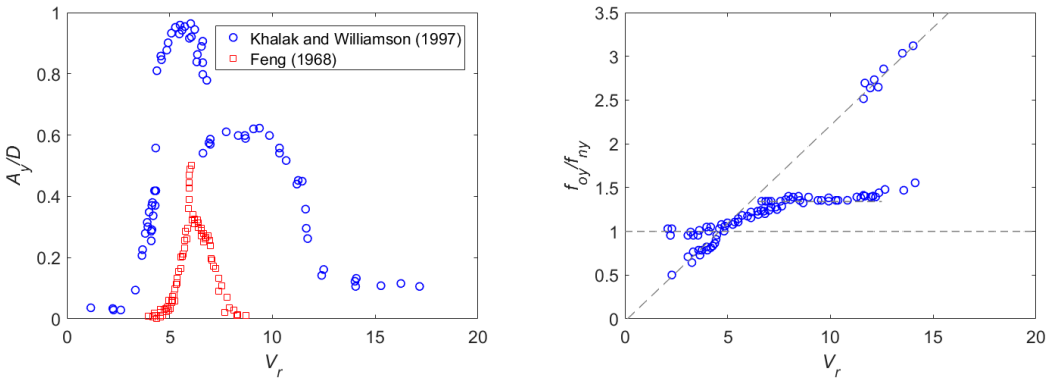

(a) (b)

Fig. 2.16 1DOF VIV responses of a cylinder: (a) amplitude response and (b) frequency response.

2.2.1.2 Mass Ratio

The mass ratio of a circular cylinder is given by

$$m^* = \frac{m}{\frac{1}{4}\rho\pi D^2 L} \tag{2.9}$$

where m is the mass of the cylinder. It influences both the amplitude and frequency responses. Fig. 2.16(a) shows the amplitude responses of cylinders with a low mass ratio $m^* = 2.4$ (Khalak and Williamson, 1997b) and a high mass ratio $m^* = 248$ (Feng, 1968). It can be seen that the amplitude response changes from two branches to three branches as a result of decreasing m^* and the additional branch with large-amplitude vibration is known as the upper branch. Regarding the frequency response, for high

m^*, f_{oy}/f_{ny} remains close to unity (Feng, 1968). However, when m^* is low, the cylinder oscillates at a distinctly high frequency. In the case of m^* = 2.4 in Fig. 2.16, f_{oy}/f_{ny} = 1.4. Experimentally, the departure of f_{oy}/f_{ny} from unity, through the lock-in range was shown by Moe and Wu (1990), Khalak and Williamson (1999) and Gharib *et al.* (1998).

Previous studies by Williamson and Govardhan (2004) and Blevins and Coughran (2009) revealed that as m^* decreases the range of V_r over which there are large-amplitude vibrations widens. The experimental results of Govardhan and Williamson (2002, 2004) showed that in each VIV system there existed a critical mass ratio below which the lock-in range would extend to infinity. Fig. 2.17 shows the effect of m^* on the lock-in range of CF VIV of an elastically mounted rigid cylinder presented by Govardhan and Williamson (2000) in which the end of synchronisation yielded a good collapse of data onto a single curve fit based on:

$$V_{r_{\text{end of synchronisation}}} = 9.25\sqrt{\frac{m^* + C_a}{m^* - 0.54}} \tag{2.10}$$

where C_a is the potential added mass coefficient assumed to be unity for a circular cylinder. Eq. (2.10) indicates the existence of a critical mass ratio m^*_{cr} = 0.54.

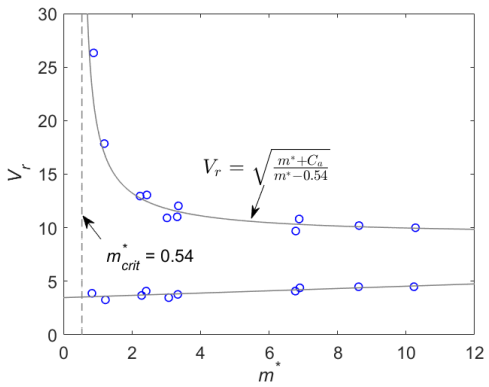

Fig. 2.17 Effect of m^* on the cross-flow VIV of an elastically mounted rigid cylinder (Govardhan and Williamson, 2000).

2.2.1.3 Damping Ratio

Damping can be interpreted as the energy dissipation from a vibrating system. In classic vibration analysis, it is considered to be a force proportional to velocity which opposes the motion of the structure. The structural damping coefficient is usually denoted by c. Depending on the relation between c and the critical damping $c_{cr} = 2\sqrt{km}$, a vibrating system can be classified as under damped, critically damped or over damped ($c < c_{cr}$, $c = c_{cr}$ and $c > c_{cr}$, respectively). Normalising the damping coefficient with $2\sqrt{km}$ results in the so-called damping ratio ζ given by

$$\zeta = \frac{c}{c_r} = \frac{c}{2\sqrt{km}} \tag{2.11}$$

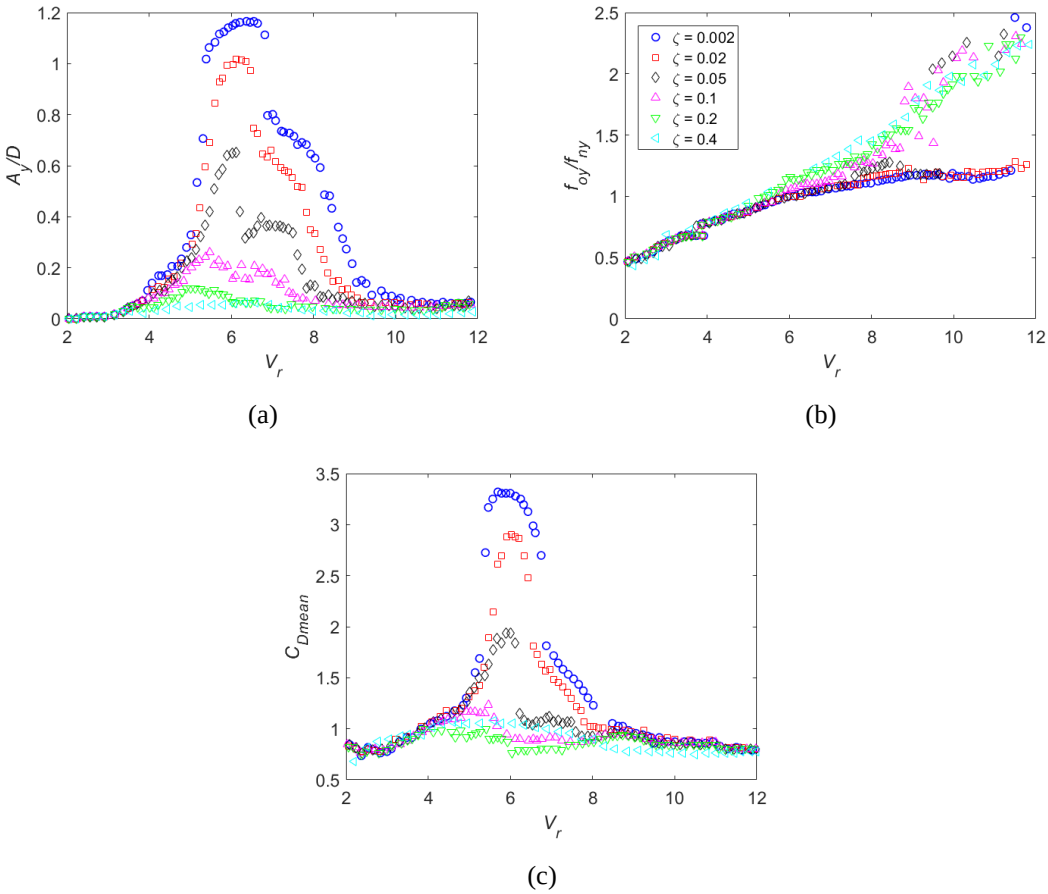

Fig. 2.18 Effect of damping ratio on the cross-flow VIV of a rigid cylinder with m^* = 5.4: (a) amplitude response, (b) frequency response and (c) mean drag coefficient (Blevins and Coughran, 2009).

The effect of the damping ratio on VIV has been reported by various researchers (Klamo *et al.*, 2006; Williamson and Govardhan, 2004). Blevins and Coughran

(2009) examined the effect of damping ratio on the amplitude response, frequency response and the mean drag coefficient of a rigid cylinder with $m^* = 5.4$ undergoing cross-flow (CF) VIV. As illustrated in Fig. 2.18(a), the increasing ζ leads to lower oscillation amplitudes and the variation of ζ can result in the alternation of the amplitude response from three branches to two branches. Fig. 2.18(c) shows that the mean drag coefficient follows the same trend as the amplitude response, i.e., the mean drag coefficient amplifies when the amplitude of VIV oscillation increases.

2.2.2 Nondimensional Variables Influencing Two-Degree-of-Freedom VIV

Since the fundamental mechanism of two-degree-of-freedom (2DOF) VIV is the same as that of CF VIV, the same parameters must also control 2DOF VIV. In addition to the parameters mentioned in Section 2.2.1, having different natural frequencies in the IL and CF directions results in a new parameter known as the natural frequency ratio f^* which is defined as $f^* = f_{nx}/f_{ny}$. The importance of f^* stems from the following reasons. First, the excitation frequencies in the IL and CF directions are not the same. The frequency of the lift force fluctuations is f_v and the drag force oscillates at a frequency of $2f_v$. Therefore, the different natural frequency ratios lead to simultaneous or non-simultaneous IL and CF resonance conditions. Moreover, the real engineering structures can possess multiple frequency ratios. In this section, the effects of m^*, ζ and f^* on 2DOF VIV of a circular cylinder are discussed. Based on the conventions in previous studies by Dahl *et al.* (2006), Dahl *et al.* (2010), Bao *et al.* (2012) and Srinil *et al.* (2013), V_r in 2DOF system is defined as $V_r = V/f_{ny}D$.

2.2.2.1 Mass Ratio

In one of the most influential and pioneering studies on 2DOF VIV, Jauvtis and Williamson (2004) found that the effect of the in-line (IL) degree of freedom on the CF vibration was surprisingly small when $m^* \geq 6$. In contrast, recent studies revealed dramatic changes in the fluid-structure interaction if $m^* < 6$ (Blevins and Coughran, 2009; Dahl *et al.*, 2006, 2007; Dahl *et al.*, 2010; Jauvtis and Williamson, 2004). The

changes include a new amplitude response branch (super-upper branch) characterised by a maximum IL vibration amplitude of $A_{xm}/D \approx 0.3$ and a maximum CF vibration amplitude as large as $A_{ym}/D \approx 1.5$ as shown in Fig. 2.19. Jauvtis and Williamson (2004) also examined the critical mass ratio for their 2DOF VIV experimental setup. Their results showed that for an elastically mounted rigid cylinder free to vibrate in both the IL and CF directions, the critical mass ratio is $m^*_{cr} = 0.52$, which is comparable to 0.54 of a 1DOF VIV system by Govardhan and Williamson (2000).

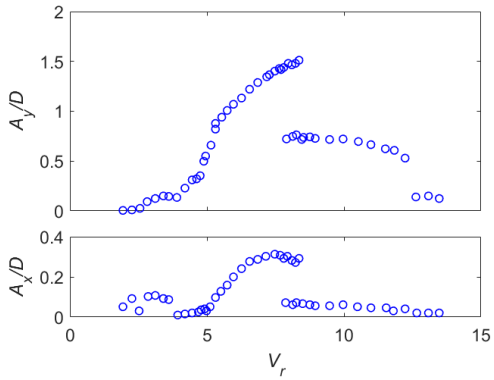

Fig. 2.19 Two-degree of freedom VIV response (Jauvtis and Williamson, 2004).

2.2.2.2 Damping Ratio

Apart from the effect of ζ on 1DOF VIV, Blevins and Coughran (2009) also investigated the effect of ζ on 2DOF VIV of an elastically mounted rigid cylinder with $m^* = 5.4$. The corresponding results are shown in Fig. 2.20. The comparison between Fig. 2.18 and Fig. 2.20 shows that higher CF vibration amplitudes are attained when the cylinder is free to oscillate in both the IL and CF directions. Similar to m^*, the effect of the IL degree of freedom becomes predominant as ζ decreases. The results also illustrate the excitation of the third IL lock-in range coinciding with the CF lock-in range when $\zeta < 0.02$. At very low damping $\zeta = 0.002$, the super-upper branch is observed.

2.2.2.3 Natural Frequency Ratio

For 2DOF VIV of an elastically mounted rigid cylinder, f^* is one of the influential physical parameters. The effect of f^* on 2DOF VIV was experimentally studied by Dahl *et al.* (2006), Dahl (2008) and Dahl *et al.* (2010). In their experimental setup, the mass ratios in the IL and CF directions were different (i.e., $m_x^* \neq m_y^*$).

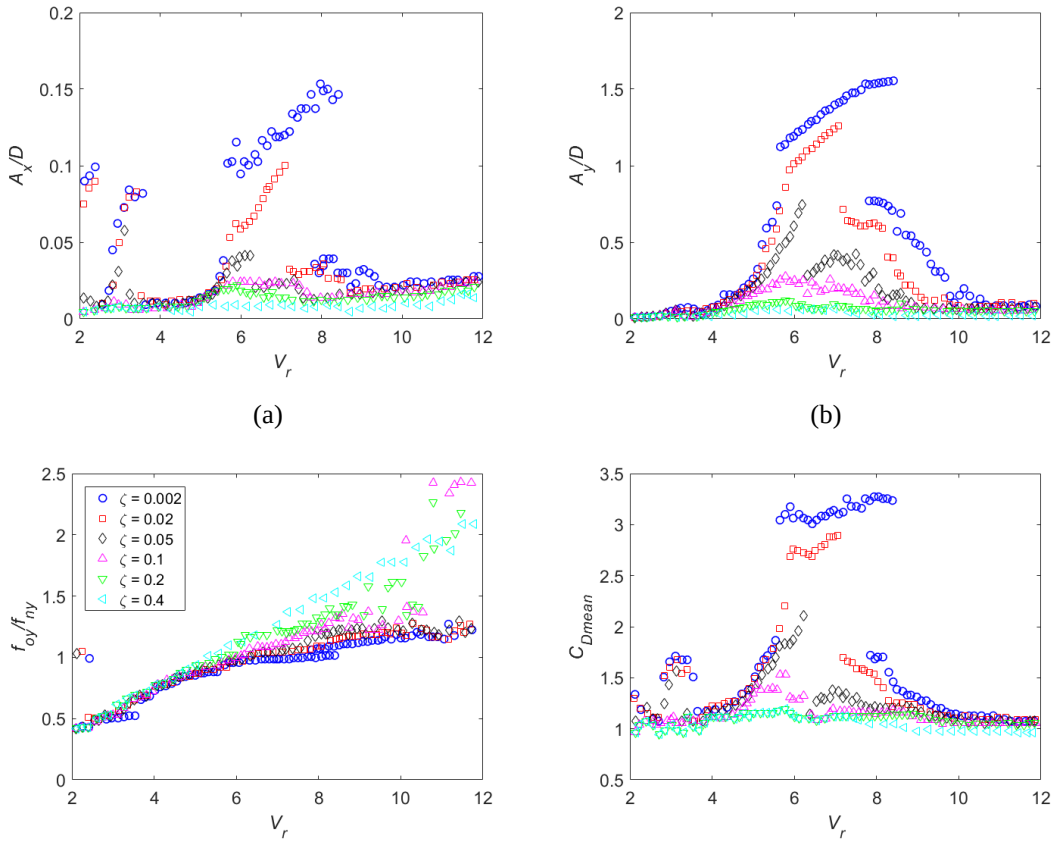

Fig. 2.20 Effect of the damping ratio on the 2DOF VIV of a rigid cylinder with m^* = 5.4: (a) IL amplitude response, (b) CF amplitude response, (c) CF frequency response and (d) mean drag coefficient (Blevins and Coughran, 2009).

Dahl (2008) observed multiple vortex shedding modes accompanied with large third harmonics in the lift force. A peak-to-peak IL vibration amplitude of 1.2D was reported in his thesis. Dahl *et al.* (2006) showed a two-peak CF amplitude response when f^* approached 2, which was also noticed by Sarpkaya (1995). Dahl *et al.* (2010) highlighted different orbital trajectories in the subcritical and supercritical Re ranges ($1.5 \times 10^4 < \mathrm{Re} < 6 \times 10^4$ and $3.2 \times 10^5 < \mathrm{Re} < 7.1 \times 10^5$) and described the occurrence of figure-eight trajectories as a representation of dual resonance. Under

dual resonance, the cylinder vibrates at frequencies near the f_v in the CF direction and $2f_v$ in IL direction, respectively. In addition, a large third harmonic component was observed in the lift force.

2.2.3 Modes of vortex formation

There has been some debate concerning the vortex formation modes that might be associated with the different response branches as outlined in Govardhan and Williamson (2000). For the high mass-damping case, there is some flow visualisation from Brika and Laneville (1993) to suggest that the initial branch is associated with the 2S mode (2 single vortices formed per cycle), while the lower branch comprises the 2P mode (2 pairs of vortices formed per cycle).

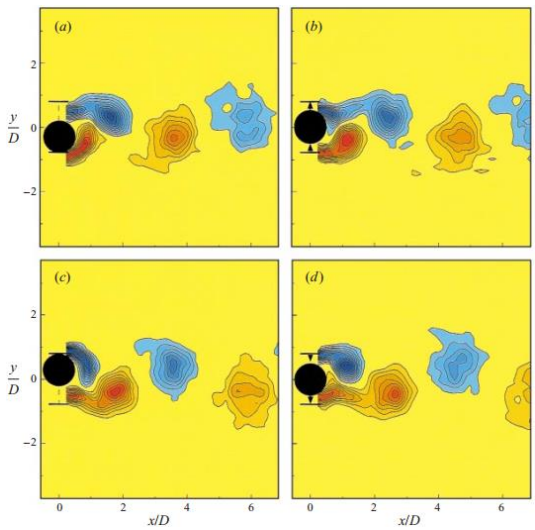

Fig. 2.21 Initial-branch vorticity plots, showing the 2S mode (Govardhan and Williamson, 2000).

The low mass-damping CF VIV study by Govardhan and Williamson (2000) shows that the initial branch clearly exhibits the classical 2S vortex formation mode as shown in Fig. 2.21. The dynamics of the concentrate regions of vorticity follow a pattern similar to what is found in a classical von Kármán vortex street. The upper-branch sequences in Fig. 2.22 demonstrate quite a different wake mode, which is, in essence, a 2P mode. As the body is moving downward, the lower counterclockwise vorticity concentration, which forms due to the roll-up of the lower shear layer, is deformed and split into two parts. The upper part forms a weak counterclockwise

vortex beside the much stronger clockwise vortex, thus forming a vortex pair. A similar process of deforming and splitting, for a clockwise vortex, is seen as the body moves upwards, forming a second vortex pair in the cycle of motion. However, the second vortex of each vortex pair is rapidly weakened by the relatively stronger first vortex. The 2P mode of wake formation for the lower branch is shown in Fig. 2.23. Again one finds deformation, stretching and splitting of the main vorticity concentrations, which lead to the formation of vortex pairs. However, the second vortex of each pair is now considerably stronger than the equivalent second vortex in the upper-branch 2P mode in Fig. 2.22 with almost equal vortex strength to the first vortex in the vortex pair.

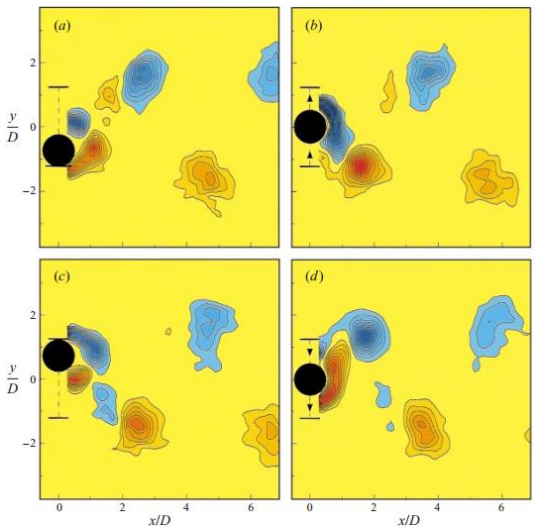

Fig. 2.22 Upper-branch vorticity plots, showing the 2P mode (Govardhan and Williamson, 2000).

The appearance of the super-upper branch in 2DOF VIV of low mass-damping structures in Jauvtis and Williamson (2004), would suggest that there is a corresponding vortex formation mode. The vorticity plots in Fig. 2.24 shows a 2T vortex shedding mode which comprises two triplets of vortices per cycle. In this mode, it can be observed that Vortices 1 and 2 in Fig. 2.24(a), comprising a counter-rotating vortex pair which can be compared directly to the vortex pair of the 2P mode in Fig. 2.22(a) at the same phase of the cyclic body motion. The major difference at this point in the cycle, for the 2T mode, appears to be the third principal vortex (labelled 3) which is generated in addition to the classical vortex pair.

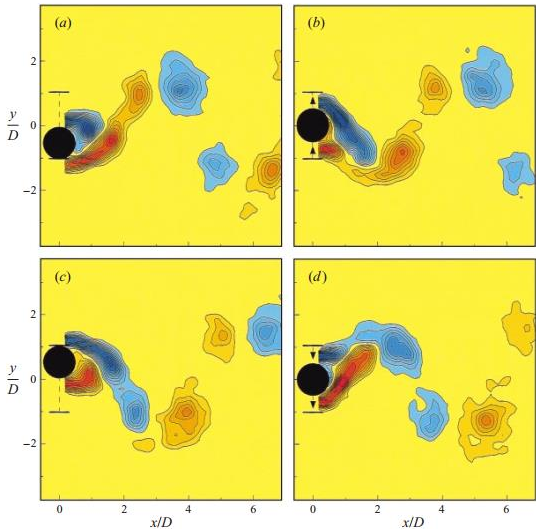

Fig. 2.23 Lower-branch vorticity plots, showing the 2P mode (Govardhan and Williamson, 2000).

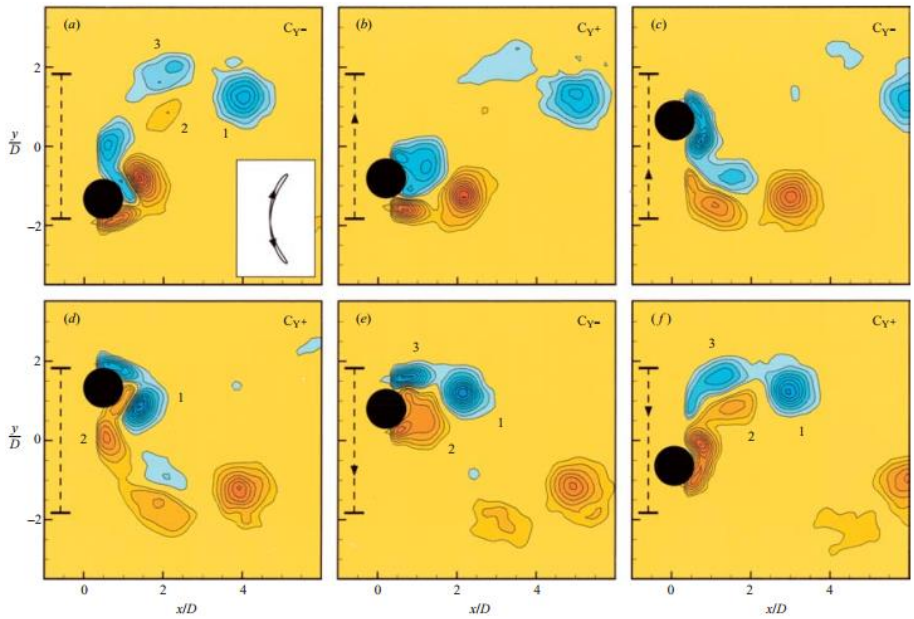

Fig. 2.24 Supper-upper branch vorticity plots, showing the 2T mode (Jauvtis and Williamson, 2004).

Apart from the aforementioned vortex shedding modes (2S, 2P and 2T), there are also other modes being observed in free vibrations of cylindrical structures, such as the P + S mode which is characterised by a single vortex and a vortex pair formed per cycle. As shown in Fig. 2.25, the counterclockwise vorticity concentration is deformed and split into two parts when the cylinder moves upward. The lower counterclockwise vortex forms a vortex pair with the clockwise vortex. In contrast to the 2P mode, the deforming and splitting process is not applicable to the clockwise

vortex, which results in the upper counterclockwise vortex being shed as a single vortex. The P + S mode was usually identified in forced vibration experiments (Griffin and Ramberg, 1974; Zdero *et al.*, 1995) and numerical simulations (Blackburn and Henderson, 1996; Meneghini and Bearman, 1995). It recently has also been detected in free vibration studies by Singh and Mittal (2005), Bao *et al.* (2012) and Gedikli and Dahl (2014).

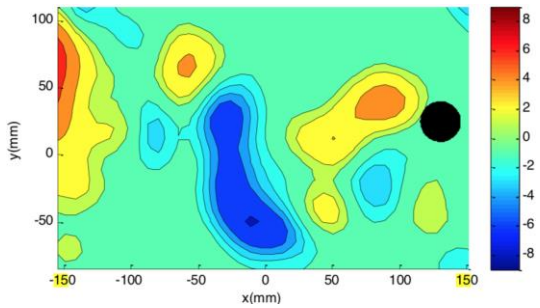

Fig. 2.25 Vorticity plots showing the P + S mode (Gedikli and Dahl, 2014).

2.2.4 Review of Previous Studies on VIV of Cylindrical Structures

In the following sections, some of the previous studies related to the scenarios which are going to be investigated in this thesis are summarised. The review is mainly focussed on CFD studies while some representative experimental as well as semi-empirical modelling investigations are also included.

2.2.4.1 VIV of an Elastically Mounted Rigid Circular Cylinder

The preponderance of existing publications have focussed on 1DOF CF motion of an elastically mounted rigid circular cylinder (Facchinetti *et al.*, 2004; Farshidianfar and Zanganeh, 2010; Govardhan and Williamson, 2000; Khalak and Williamson, 1999; Sarpkaya, 1995). Nevertheless, several recent experimental studies have revealed the significant effect of the IL degree of freedom on the VIV response especially when $m^* < 6$ (Blevins and Coughran, 2009; Dahl *et al.*, 2006, 2007; Dahl *et al.*, 2010; Jauvtis and Williamson, 2004). Furthermore, studies by Vandiver and Jong (1987), Tognarelli *et al.* (2004) and Wang and Xiao (2016) have proven that the IL VIV can contribute as much, or even higher, fatigue damage than the CF VIV to the structures

because of the doubled oscillation frequency. Therefore, the number of studies being conducted on 2DOF VIV continues to grow (Bai and Qin, 2014; Kang and Jia, 2013; Srinil and Zanganeh, 2012; Srinil *et al.*, 2013; Wu *et al.*, 2016; Zanganeh and Srinil, 2014).

The majority of the aforementioned studies are experiments or semi-empirical modelling. Apart from those studies, there have also been an increasing number of studies on VIV of an elastically mounted circular cylinder based on CFD tools. The greater part of previous CFD studies were conducted using 2D models. Guilmineau and Queutey (2004) presented their simulation results of 1DOF VIV of a circular cylinder, the response of which was well captured in the initial and lower branches. However, the response in the upper branch did not correspond with the experimental results. Singh and Mittal (2005) studied the hysteresis behaviour of 2DOF VIV at low Reynolds numbers. In their study, hysteresis was observed at both the low- and high-ends of the lock-in range and they also observed the P + S vortex shedding mode in free vibration for the first time. Leontini *et al.* (2006) investigated the branching behaviour of 1DOF VIV at Re = 200. Two response branches similar to the upper and lower branches at higher Re were discovered in their numerical study. The 2D and 3D flow behaviours were also ascertained to have similarities which suggested that the 3D flow branching behaviour has its genesis in the 2D flow. Lucor and Triantafyllou (2008) performed 2D simulation of 2DOF VIV of a circular cylinder in a wide range of in-line to cross-flow natural frequency ratios ($f^* = f_{nx}/f_{ny}$). They observed that the vibration amplitude increases and the peak amplitude shifts to a higher V_r as f^* increases. Zhao and Cheng (2011) simulated 2DOF VIV of a circular cylinder by solving the 2D Reynolds-averaged Navier-Stokes (RANS) equations and reproduced the 2T vortex shedding mode and the response in the super-upper branch.

It was found that the flow in the wake of a circular cylinder is 3D when the Reynolds number exceeds 200 (Williamson, 1988, 1989). Therefore, a series of 3D CFD studies on VIV of a circular cylinder have been conducted. Lucor *et al.* (2005) presented results of a direct numerical simulation (DNS) of 1DOF VIV and found

that there existed a sharp drop in the spanwise correlation of the wake and forces in the region of V_r around the mode transition between the upper and lower branches. Pontaza and Chen (2006) employed large eddy simulation (LES) and overset (Chimera) grids to study 2DOF VIV of a circular cylinder with low structural mass and damping at V_r = 6 and Re = 10^5. A response characterised by a figure-eight pattern was observed and the vortex shedding exhibited a 2S mode. Saltara *et al.* (2011) used detached eddy simulation (DES) to simulate 1DOF VIV of a circular cylinder with a low mass-damping parameter at Re = 10^4. In general, their simulation results agreed with the experimental results of Khalak and Williamson (1997a), however, the vibration amplitudes and force coefficients were overpredicted for V_r > 6. Kondo (2012), who examined the different excitation mechanisms in the IL and CF directions based on the numerical results from a 3D computation, captured the first and second excited vibrations of the IL direction in the V_r range of V_r = 1.7 – 3.5 with a low Scruton number (Sc = $4\pi m\zeta/(\rho D^2)$, where ζ is the structural damping ratio). Navrose and Mittal (2013) investigated the transition of responses of 2DOF VIV in the three branches and noted that the cylinder responses and force coefficients exhibited beats in the initial branch. The initial-upper branch transition was found to be hysteretic and intermittency was observed in the transition between the upper and lower branches. Zhao *et al.* (2014) studied the transition from 2D to 3D for 1DOF VIV of a circular cylinder. In their study, the three-dimensionality of the flow appeared to be strongest in the upper branch and weakest in the initial branch. Additionally, the 2S and 2P vortex shedding modes were acknowledged as coexisting in the upper branch which led to the strong variation of the lift coefficient along the span. Gsell *et al.* (2016) simulated 2DOF VIV of a circular cylinder at Re = 3900 with direct numerical simulation of the 3D Navier-Stokes equations. The predicted structural responses and forces were consistent with the experimental results reported by Jauvtis and Williamson (2004). The numerical results of their study confirmed the large-amplitude VIV and the shape of the responses. The IL to CF oscillation frequency ratio was equal to 2 and it was also found that the phase difference between the IL and CF motions varied across the lock-in range.

The most common scenario for 2DOF VIV is that the IL and CF natural frequencies are identical (i.e., $f_{nx} = f_{ny}$). However, it has been previously stressed that cylindrical offshore structures, such as risers, mooring lines and pipelines usually possess an infinite number of natural frequencies in different directions (Srinil *et al.*, 2007; Srinil and Rega, 2007). Therefore, it is of practical interest to study 2DOF VIV with varying f^*; particularly, when $f^* = 2$, where perfect 2DOF resonance may occur due to the fact that the fluctuating drag oscillates at a frequency twice that of the fluctuating lift. Sarpkaya (1995) and Dahl *et al.* (2006) observed two-peak CF responses with unequal mass ratios in the IL and CF directions ($m_x^* \neq m_y^*$) and f^* around 2. The orbital trajectories and dual resonance of 2DOF VIV of a circular cylinder with varying f^* were further investigated by Dahl *et al.* (2010) in subcritical and supercritical Reynolds number ranges. Under dual resonance, the IL to CF oscillation frequency ratio was found to be $f_{ox}/f_{oy} \approx 2$ and a third harmonic component was observed in the lift force. A more practical case with $m_x^* = m_y^*$ and varying f^* has also been investigated. Srinil *et al.* (2013) experimentally and numerically studied the 2DOF VIV of a circular cylinder with low mass-damping and varying f^*. In their study, figure-eight orbital motions were observed for a wide range of V_r values indicating the occurrence of dual resonance. A flattened single-peak upper branch similar to the experimental results of Assi *et al.* (2009) was observed when f^* approaches 2 in their study. Bao *et al.* (2012) performed a 2D CFD simulation of the 2DOF VIV of a circular cylinder with $m_x^* = m_y^*$ and varying f^* at Re = 150. They indicated that dual resonance existed over a wide range of f^*. A third harmonic frequency component was also observed in the lift fluctuation. Multiple small peaks occurred in the cross-flow response amplitudes of the cylinder when $f^* = 2$.

2.2.4.2 VIV of a Single Flexible Cylinder

As riser pipes often possess *L/D* of the order of 10^3 (Chaplin *et al.*, 2005), many experiments have been carried out on deepwater risers with large *L/D* (Chaplin *et al.*, 2005; Gao *et al.*, 2015; Gu *et al.*, 2013; Huang *et al.*, 2011b; Lie and Kaasen, 2006; Tognarelli *et al.*, 2004; Tognarelli *et al.*, 2008; Trim *et al.*, 2005; Vandiver *et al.*,

2009; Vandiver *et al.*, 2006). These experiments investigated flexible riser VIV responses under different flow conditions and some also assessed the effectiveness of VIV suppression techniques, such as using helical strakes, which weaken the intensity of vortices and reduce the fluid force by disrupting the spatial correlation of vortices by gradually changing the flow separation angle in the longitudinal direction. Better insights into some important VIV aspects (i.e., response amplitude, dominant mode, dominant frequency and fatigue damage etc.) were obtained from these experiments and thus provided some good benchmarks for verifying numerical prediction models.

Apart from the various experimental investigations, there have been a number of CFD studies on VIV of flexible cylinders.

Willden and Graham (2001) used a quasi-three-dimensional (Q3D) method to simulate the transverse vibration of an L/D = 100 cylinder subject to a sheared inflow at low Reynolds numbers. A high tension was applied to the cylinder so that the fundamental mode would be excited. A maximum amplitude of 0.36D was found at L/D = 44 which was slightly below the midpoint of the cylinder span. The results also showed that the majority of the shedding frequencies along the cylinder were modified towards the natural frequency and a significant spanwise correlation was observed.

Meneghini *et al.* (2004) and Yamamoto *et al.* (2004) presented the numerical simulations of long marine risers with L/D up to 4600 with Q3D discrete vortex method (DVM). In their simulations, the riser tended to select a vibration mode which could keep the reduced velocity in the range of $4 \leq V_r \leq 7$ where the energy was transferred from the fluid to the structure. Visualisations of the wake indicated a hybrid mode of vortex shedding along the span with a 2S mode being found in regions of small amplitudes, changing to a 2P mode in regions of larger amplitudes.

The simulations described above were based on Q3D method with several 2D strips over the length of the riser. However, Q3D simulations have many shortcomings,

e.g., 3D vortex structures cannot be treated correctly and straked risers and variations in the angle of attack cannot be studied directly. Therefore, a series of fully 3D numerical simulations emerged.

Newman and Karniadakis (1997) simulated VIV of an infinitely long flexible cable at Re = 100 and Re = 200 with a spectral/hp element method. Both the standing wave and travelling wave responses were realised. It was found that an interwoven pattern of vorticity was associated with a standing wave cable response while oblique vortex shedding was produced by a travelling wave cable response. A mixed standing wave/travelling wave response together with chevron-like vortex shedding was found to be related to a sheared inflow.

Evangelinos and Karniadakis (1999) studied VIV of an infinitely long flexible cylinder at Re = 1000. The structure's bending stiffness was varied to obtain different responses. The authors found that the modulated travelling wave motion of a free-free beam or cable led to a mixed response consisting of oblique and parallel shedding. In the case of structures with pinned endpoints, a standing wave response was obtained with lace-like flow structures.

Holmes *et al.* (2006) and Menter *et al.* (2006) investigated riser VIV with fully 3D finite element method (FEM) and finite volume method (FVM), respectively. Both of the simulations used relatively coarse meshes with high element aspect ratios and the results were in good agreement with the experimental data by Trim *et al.* (2005) and Chaplin *et al.* (2005), respectively.

Constantinides and Oakley (2008) compared their CFD results with the data obtained in the field experiments by Jhingran and Vandiver (2007). The results were able to match the experimental data. Both the first and third harmonic components were well captured. The authors emphasised the importance of the third harmonic component in fatigue damage analysis due to the fact that it produced strains of the same order of magnitude as the first harmonic component and had a frequency of three times the first harmonic component, which returned roughly three times more fatigue damage.

Huang *et al.* (2009, 2011a) performed finite-analytic Navier-Stokes (FANS) simulations on three different risers with *L/D* ranging from 482 to 3350. The simulation results showed good agreement with the experimental data by Lehn (2003) and Trim *et al.* (2005) and the numerical results using other commercial software by Holmes *et al.* (2006). It was observed in their simulations that the VIV of a long riser tended to have more than one dominant modes. The dominant modes could be sensitive to the incoming flow velocity profile and the riser tension. The CF VIV was influenced by the IL deflection. Vortex shedding showed a 2S pattern and the CF VIV demonstrated higher harmonic responses.

Bourguet *et al.* (2011a, b, c, 2012, 2013, 2015) did a series of fundamental studies on VIV of long flexible cylinders. Their research revealed some important flexible cylinder VIV mechanisms, such as the occurrence of lock-in, the orbital trajectories which dominate the wake-body resonance, the phasing mechanisms between the IL and CF VIV and the validity of the independence principle (IP) applied to VIV.

2.2.4.3 VIV of Two Elastically Mounted Circular Cylinders in Tandem Arrangement

Some experimental studies have been conducted to investigate the interference between two rigid circular cylinders undergoing VIV. Hover and Triantafyllou (2001), Assi *et al.* (2010) and Assi *et al.* (2013) considered the effect of the upstream cylinder wake on the response of the downstream cylinder. In their investigations, the upstream cylinder was stationary whilst the downstream cylinder was elastically mounted and free to vibrate in the CF direction only. In Hover and Triantafyllou (2001), the downstream cylinder was placed at 4.75*D* behind the upstream cylinder and the Reynolds number was $\mathrm{Re} = 3 \times 10^4$. Large-amplitude galloping response was observed for the downstream cylinder. The results also indicated that the frequency lock-in began at a low reduced velocity which was nearly the same as a single cylinder and its range extended to a V_r of at least 17. A phase change in the lift force, which was typically associated with the frequency lock-in, occurred at higher V_r. The force spectra suggested that the shedding from the upstream cylinder was not

affected by motions of the downstream cylinder. Assi *et al.* (2010) elaborated the excitation mechanism of wake-induced vibration (WIV) of the downstream cylinder. The Reynolds number in their study was up to 3×10^4. They suggested that the WIV of the downstream cylinder was excited by the unsteady vortex-structure interactions between the body and the upstream wake. In a recent research by Assi *et al.* (2013), the authors investigated how the cylinder responded to the vortex-structure interactions excitation. They introduced the concept of wake stiffness and concluded that it was the wake stiffness phenomenon that defined the character of the WIV response. Zdravkovich (1985) studied VIV of two elastically mounted rigid cylinders in tandem arrangement with different centre-to-centre spacing ratios (S_x/D) in the Re range of $10^4 - 10^5$. It was observed that for a very small S_x/D up to 1.1, the two cylinders acted as a single body. With a slight increase of S_x/D up to 1.6, the shear layers from the upstream cylinder reattached onto the downstream cylinder. A bistable regime was found when S_x/D varied from 2.5 to 4, which indicated the minimum spacing required for the upstream cylinder to have regular vortex shedding. In this regime, the oscillation amplitudes of the upstream cylinder were larger than those of the downstream cylinder. For S_x/D larger than 4, the response of the upstream cylinder was smaller and less regular than that of the downstream cylinder.

Apart from the experiments, there have also been a number of numerical studies on VIV of two tandem cylinders. The majority of existing numerical studies were 3D and focussed on 1DOF CF motions of rigid cylinders. Carmo *et al.* (2011) conducted 2D numerical simulations of the flow around two tandem circular cylinders at Re = 150. The upstream cylinder was fixed and the downstream cylinder was free to vibrate in the transverse direction. S_x/D was varied from 1.5 to 8. Compared to an isolated cylinder, the downstream cylinder was found to have higher maximum amplitudes and wider lock-in ranges. The vibration amplitudes for higher V_r beyond the lock-in range were very significant. Carmo *et al.* (2013) investigated VIV of a cylinder which was completely free to move in the cross-flow direction (i.e., with no spring or damper attached to it) subject to the wake of an identical stationary cylinder. A fixed spacing ratio $S_x/D = 4$ was considered and Re varied from 100 to 645. Three different regimes were identified in their 2D simulations. A monotonically

decreasing amplitude with increasing Re was observed in the first regime ($90 \leq Re \leq 165$). The second regime was characterised by significant scatter in the vibration amplitude and its range is from $Re \approx 180$ to $Re = 360$. Gradual transition between the second and third regimes took place for $360 \leq Re \leq 405$. The third regime extended up to the highest Re tested. The amplitude was found to grow monotonically with Re. Zhao (2013) presented the results of VIV of two rigidly coupled circular cylinders in tandem arrangement with four spacing ratios ranging from 1.5 to 6 at Re = 150. The results showed that the gap between the two cylinders had a significant effect on the response. When two rigidly coupled tandem cylinders were subject to VIV, the critical spacing for vortex shedding from the upstream cylinder was significantly smaller than that for two tandem stationary cylinders. The vortex shedding from the upstream cylinder took place at $S_x/D = 2$ in the lock-in range and the lock-in range was found to be narrower than that of a single cylinder for $S_x/D = 1.4$ and 2, and wider for $S_x/D = 4$ and 6. Ding *et al.* (2017) used 2D unsteady RANS equations with the Spalart-Allmaras turbulence model to study the effect of tandem spacing on VIV of two cylinders with passive turbulence control in the Re range of 30000 – 100000. The spacing between the cylinders varied from 2*D* to 6*D*. The numerical simulation successfully predicted all the ranges of responses including VIV and galloping. Furthermore, the results agreed well with the experimental measurements. The influence of the downstream cylinder on the amplitude and frequency responses of the upstream cylinder was found to be negligible when the spacing is larger than 2*D*. A rising trend of the vibration amplitude of the downstream cylinder was observed in all the cases when $2 \times 10^4 < Re < 3 \times 10^5$. The galloping branch merged with the VIV upper branch for spacing larger than 3*D*. Vortex structures showed significant variation in different flow regimes.

2DOF VIV of two tandem rigid cylinders has also been studied using 2D numerical simulations. Papaioannou *et al.* (2008) studied the effect of spacing on VIV of two rigid cylinders in tandem arrangement. The computations were carried out for S_x/D in the range of 2.5 – 5 at Re = 160. It was observed that the range of the response region of the upstream cylinder became wider with the decrease of S_x/D. The synchronisation curve shifted on the V_r axis depending on the spacing. There was an

increase in the maximum vibration amplitude of the downstream cylinder when the cylinders were brought to the spacing corresponding to the reattachment regime in the stationary system. Prasanth and Mittal (2009) investigated VIV of two circular cylinders in tandem arrangement with S_x/D = 5.5 at Re = 100 using a 2D stabilised FEM. V_r ranged from 2 to 15. The downstream cylinder was found to undergo large-amplitude vibrations in both the IL and CF directions. Lock-in and hysteresis were observed for both the upstream and downstream cylinders. The large-amplitude vibrations of the downstream cylinder were maintained even beyond the lock-in range. The phase difference between the cross-flow displacement and the lift force went through an 180° jump in the middle of the synchronisation regimes of both cylinders. The flow regime was divided into five sub-regimes based on the phase difference and the flow patterns. Bao *et al.* (2012) studied the 2DOF VIV of two tandem cylinders with varying natural frequency ratios at Re = 150 by solving the 2D incompressible Navier-Stokes equations using a characteristic-based-split FEM. The spacing between the two cylinders was 5*D*. They found that the in-line response of the downstream cylinder was more sensitive to the natural frequency ratio than that in the transverse direction. As dual resonance was excited, the vortex shedding of the upstream cylinder in the tandem arrangement might show a P + S pattern, which strongly suppressed the vortex shedding of the downstream cylinder.

Compared to the popularity of 2D numerical studies, 3D numerical simulations of VIV of two tandem cylinders have received less attention. Carmo *et al.* (2011) compared the 3D numerical simulation results of VIV of a rigid cylinder exposed to an upstream stationary cylinder wake at Re = 300 with their 2D simulation results at Re = 150. For all the configurations investigated, they observed that the 3D results follow the same trend as the 2D results. However, the flow field was strongly 3D for most of the configurations. Therefore, they concluded that 3D simulations were strictly necessary in order to obtain accurate values of forces or structural response. Carmo *et al.* (2013) carried out 3D numerical simulations with the same parameters as their 2D calculations in the same study. The results showed that the variation of amplitude within the Re range tested was very small. The oscillation frequency of the downstream cylinder and the shedding frequency of the upstream cylinder were

constant and had the same value throughout the entire Re range. The amplitudes observed in the 3D results are smaller than those observed in the 2D results for the same Re which, according to the authors, was caused by the weakening of the spanwise vortices.

2.2.4.4 VIV of Two Flexible Cylinders in Tandem Arrangement

The interference between two tandem flexible cylinders undergoing VIV has also been investigated. Brika and Laneville (1997, 1999) investigated VIV of a long flexible circular cylinder immersed in the wake of an identical stationary cylinder. S_x/D between the two cylinders ranged from 7 to 25 and Re ranged from 5000 to 27000. It was found that the response of the flexible cylinder was no longer hysteretic and showed a single branch with a wider synchronisation region which decreased with the increase of the spacing between the two cylinders. The onset of the synchronisation shifted to higher V_r compared to the case of an isolated cylinder. Brika and Laneville (1997) also considered the case in which both cylinders were allowed to vibrate. In that case, the response of the downstream cylinder became hysteretic. Huera-Huarte and Bearman (2011) and Huera-Huarte and Gharib (2011) experimentally studied the vortex- and wake-induced vibrations of two tandem flexible cylinders with near and far wake interferences in a Re range up to 12000. It was found that the responses of both cylinders showed classical VIV resonance when V_r was close to the typical lock-in reduced velocities. When S_x/D is small, the maximum vibration amplitude of the upstream cylinder is higher than that of the downstream cylinder and the maximum vibration amplitude of the upstream cylinder increased with the decrease in spacing. For a large S_x/D, the response of the downstream cylinder exhibited non-classical VIV resonance with large amplitudes at high reduced velocities.

Numerical studies on VIV of two tandem flexible cylinders have rarely been reported in the literature. Chen *et al.* (2013) simulated VIV and WIV for two vertical risers in tandem and side-by-side arrangements at Re = 8400 using an unsteady RANS numerical method in conjunction with a Chimera domain decomposition approach

with overset grids. The IL and CF responses of the risers were calculated using a tensioned beam motion equation. For two vertical risers in tandem arrangement, the vortex street was suppressed between the risers and there was a reattachment of the shear layers to the downstream riser when S_x/D = 3. When S_x/D increased to 4, a vortex street started to appear in the gap between the risers with intermittent reattachment of shear layers on the downstream riser surface. In general, the computed vortex patterns and dynamic responses of the risers were in good agreement with experimental data. González *et al.* (2015) presented the results of their numerical simulation attempts for the experimental campaigns on a tandem arrangement of flexible cylinders by Huera-Huarte *et al.* (2014) at Re = 16000. The numerical simulation qualitatively reproduced the physical phenomena. However, the numerical model oversimplified the mechanical complexity of the flexible cylinder and the application of the axial tensions caused the numerical instability of the computation. Therefore, the authors suggested that future research was required in order to make a quantitative comparison with the experimental data.

2.3 Concluding Remarks

In this chapter, a broad review has been made on the fundamentals of flow past stationary and vibrating cylinders and existing publications on topics relevant to this thesis. From the critical review of previous studies, the following gaps in the literature have been identified.

1. The majority of existing publications on VIV of cylindrical structures are experiments or semi-empirical modelling. Compared to the popularity of these two methods, FSI simulations by coupling computational structural dynamics (CSD) solvers to high-fidelity CFD solvers have received less attention.

2. Existing FSI simulations on VIV of cylindrical structures are mainly 2D. 3D numerical simulations are still quite limited.

3. Most of the previous studies on VIV of cylindrical structures are devoted to the response of the cylinder and the 2D flow behaviour. Detailed information about the correlation lengths and the transient 3D wake structures is rarely reported.

4. Previously, it was widely believed that increasing the amplitude of motion increases the spanwise correlation. However, the fact is that there exists a sharp drop in the spanwise correlation in the transition region between the upper and lower branches, which does not diminish the response of the cylinder. This fact has not been fully addressed.

5. 1DOF VIV of an elastically mounted rigid circular cylinder has been widely studied during the past few decades. There have been several studies on 2DOF VIV of a rigid cylinder; however, most of these studies focussed predominantly on the case of $f_{nx} = f_{ny}$ with fewer studies on the more practical case with varying f^*.

6. A large number of riser analysis tools are designed to account only for CF bending. However, when only a few lower modes are participating in the response, IL fatigue damage can be significant. The importance of the IL fatigue damage in low flow velocity or low mode number applications has not been properly emphasised.

7. There have been several numerical studies on the effect of spacing on VIV of two elastically mounted circular cylinders in tandem arrangement. However, there is no systematic numerical study on the effect of spacing on VIV of two tandem flexible cylinders.

Therefore, the main chapters of this thesis are aimed at filling the gaps listed above using 3D FSI simulations.

Chapter 3 Numerical Methods

"Be stubborn about your goals, and flexible about your methods."

-Anonymous

3.1 Flow Model

3.1.1 Navier-Stokes Equations

The governing equations for the flow in Chapter 4 and Chapter 6 are the unsteady incompressible Navier-Stokes equations. The Arbitrary Lagrangian-Eulerian (ALE) scheme is adopted to solve the governing equations in a moving mesh system. The Navier-Stokes equations in the ALE scheme are expressed as

$$\frac{\partial u_i}{\partial x_i} = 0 \tag{3.1}$$

$$\frac{\partial u_i}{\partial t} + \left(u_j - \hat{u}_j\right)\frac{\partial u_i}{\partial x_j} = -\frac{1}{\rho}\frac{\partial p}{\partial x_i} + \nu\frac{\partial^2 u_i}{\partial x_j^2} \tag{3.2}$$

where x_i ($x_1 = x$, $x_2 = y$, $x_3 = z$) represents the Cartesian coordinate, u_i is the fluid velocity component in the x_i-direction, t is the time, $\hat{u}_i$ is the grid velocity component in the x_i-direction, ρ is the fluid density, p is the pressure and ν is the kinematic viscosity of the fluid.

The governing equations are discretised using an element-based FVM (ANSYS Inc., 2013a). Rhie-Chow interpolation (Rhie and Chow, 1982) is used to obtain the pressure-velocity coupling on collocated grids. A second-order backward Euler scheme is adopted for the temporal discretisation and a high resolution scheme is used as the convection scheme. Detailed information about the numerical schemes can be found in Section 3.4.

3.1.2 Large Eddy Simulation Wall-Adapted Local Eddy-Viscosity (WALE) Model

The flow field around the riser in Chapter 5 is modelled by solving the unsteady, incompressible Navier-Stokes equations in conjunction with the large eddy simulation (LES) wall-adapted local eddy-viscosity (WALE) model (Nicoud and Ducros, 1999). The ALE scheme is also employed to deal with the moving boundary of the riser. The ALE form of the filtered Navier-Stokes equations in the Cartesian coordinate system is expressed as

$$\frac{\partial \overline{u}_i}{\partial x_i} = 0 \tag{3.3}$$

$$\frac{\partial \overline{u}_i}{\partial t} + (\overline{u}_j - \hat{u}_j)\frac{\partial \overline{u}_i}{\partial x_j} = -\frac{1}{\rho}\frac{\partial \overline{p}}{\partial x_i} + \frac{\partial}{\partial x_j}\left[\nu\left(\frac{\partial \overline{u}_i}{\partial x_j} + \frac{\partial \overline{u}_j}{\partial x_i}\right)\right] - \frac{\partial \tau_{ij}}{\partial x_j} \tag{3.4}$$

where $(x_1, x_2, x_3) = (x, y, z)$ are the Cartesian coordinates, an overbar denotes that the variable is a filtered variable, u_i is the velocity component in the x_i-direction, $\hat{u}_i$ is the grid velocity component in the x_i-direction, p is the pressure, t is the time, ρ is the fluid density, ν is the kinematic viscosity of the fluid and τ_{ij} is the subgrid-scale stress defined by

$$\tau_{ij} = \overline{u_i u_j} - \overline{u}_i \overline{u}_j \tag{3.5}$$

Based on the Boussinesq's approximation

$$-\left(\tau_{ij} - \frac{\delta_{ij}}{3}\tau_{kk}\right) = 2\nu_{sgs}\overline{S}_{ij} \tag{3.6}$$

where δ_{ij} is the Kronecker symbol. The isotropic part of the subgrid-scale stresses τ_{kk} is not modelled, but added to the filtered static pressure. $\overline{S}_{ij}$ is the rate-of-strain tensor for the resolved scale defined by

$$\overline{S}_{ij} = \frac{1}{2}\left(\frac{\partial \overline{u}_i}{\partial x_j} + \frac{\partial \overline{u}_j}{\partial x_i}\right) \tag{3.7}$$

The eddy-viscosity is computed by

$$\nu_{sgs} = \left(C_w \Delta\right)^2 \frac{\left(S_{ij}^d S_{ij}^d\right)^{3/2}}{\left(\overline{S}_{ij}\overline{S}_{ij}\right)^{5/2} + \left(S_{ij}^d S_{ij}^d\right)^{5/4}} \tag{3.8}$$

The model constant C_w is chosen as 0.325. The filter-width is taken as the local grid size, i.e., $\Delta = \left(\Delta x \Delta y \Delta z\right)^{1/3}$. S_{ij}^d denotes the traceless symmetric part of the square of the velocity gradient tensor:

$$S_{ij}^d = \frac{1}{2}\left(\bar{g}_{ij}^2 + \bar{g}_{ji}^2\right) - \frac{1}{3}\delta_{ij}\bar{g}_{kk}^2 \tag{3.9}$$

where $\bar{g}_{ij}^2 = \bar{g}_{ik}\bar{g}_{kj}$, $\bar{g}_{ij} = \partial\bar{u}_i / \partial x_j$. The tensor S_{ij}^d can be rewritten in terms of the strain-rate and vorticity tensors:

$$S_{ij}^d = \bar{S}_{ik}\bar{S}_{kj} + \bar{\Omega}_{ik}\bar{\Omega}_{kj} - \frac{1}{3}\delta_{ij}\left(\bar{S}_{mn}\bar{S}_{mn} - \bar{\Omega}_{mn}\bar{\Omega}_{mn}\right) \tag{3.10}$$

where the vorticity tensor is given by

$$\bar{\Omega}_{ij} = \frac{1}{2}\left(\frac{\partial\bar{u}_i}{\partial x_j} - \frac{\partial\bar{u}_j}{\partial x_i}\right) \tag{3.11}$$

The main advantages of the LES WALE model are the capability of reproducing the laminar to turbulent transition and the design of the model to return the correct wall-asymptotic y^{+3}-variation of the subgrid-scale viscosity (ANSYS Inc., 2013a).

Similar to the previous section, the governing equations are discretised using the element-based FVM (ANSYS Inc., 2013a), Rhie-Chow interpolation (Rhie and Chow, 1982) is used to obtain pressure-velocity coupling on collocated grids and the second-order backward Euler scheme is adopted for the temporal discretisation. A bounded central difference scheme is used as the convection scheme. One may refer to Section 3.4 for the detailed numerical schemes.

3.2 Near-Wall Treatment for Turbulent Flows past Cylinders

Turbulent flows could be significantly affected by the presence of walls where the viscosity-affected regions have large gradients in the solution variables. Hence, successful prediction of wall bounded turbulent flows is partly determined by the accurate presentation of the near-wall region. Similarly, for turbulent flows past circular cylinders, the accurate calculation of the separation point, which affect the

prediction of flow parameters such as drag coefficient and Strouhal number (Young and Ooi, 2004), also depends on the proper modelling of the near-wall region.

3.2.1 Law of the Wall

Central issues of wall bounded turbulent flows are the forms of the mean velocity profiles and the friction laws, which describe the shear stress exerted by the fluid on the wall. Close to the wall, the flow is affected by viscous effects and the mean flow velocity depends on several parameters as formulised below:

$$\bar{u} = f\left(y, \rho, \mu, \tau_w\right) \tag{3.12}$$

where y is the distance from the wall, ρ is the fluid density, μ is the dynamic viscosity of the fluid and τ_w is the wall shear stress.

Nondimensionalising $\bar{u}$ with the friction velocity $u_f = \sqrt{\tau_w / \rho}$ gives

$$u^+ = \frac{\bar{u}}{u_f} = f\left(\frac{y \rho u_f}{\mu}\right) = f\left(y^+\right) \tag{3.13}$$

Eq. (3.13) contains the definitions of two important dimensionless parameters, u^+ and y^+. The relationship between them is called 'Law of the Wall', which represents the different layers of the near-wall region as shown in Fig. 3.1.

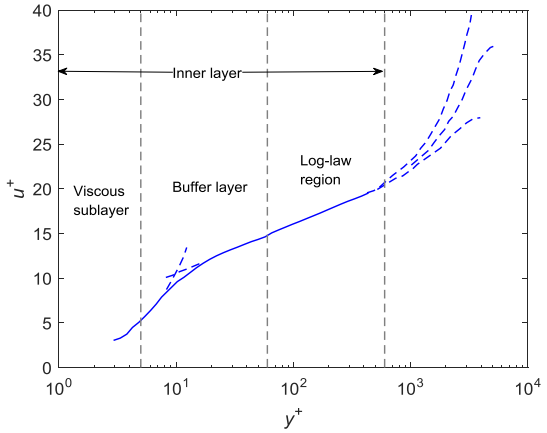

Fig. 3.1 Subdivisions of the near-wall region.

The near-wall region has larger gradients in the solution variables, and momentum and other scalar transports occur most vigorously. From Fig. 3.1, it can be observed that the inner layer is made up of three zones (with their corresponding wall y^+), namely the:

- Viscous sublayer ($y^+ < 5$): viscous stresses dominate the flow;
- Buffer layer ($5 < y^+ < 30$): viscous and turbulent stresses are of similar magnitude;
- Log-law region ($y^+ > 30$ to 60): turbulent stresses dominate.

The wall y^+ is a nondimensional distance similar to local Reynolds number, often used in CFD to describe how coarse or fine a mesh for a particular flow. The most desirable values of y^+ are close to the lower bound ($y^+ \approx 30$) for wall functions while $y^+ \approx 1$ for near-wall modelling.

3.2.2 Near-Wall Treatment

There are two approaches to modelling the near-wall region (i.e., wall functions and near-wall modelling). The first approach uses semi-empirical formulae (wall functions) to bridge the viscosity-affected region (viscous sublayer and buffer layer) between the wall and the fully-turbulent region, which means the viscous sublayer and buffer layer are not resolved. The use of wall functions obviates the need to modify the turbulence models to account for the presence of the wall, while in the second approach the turbulence models are modified to enable the viscosity-affected region to be directly resolved with a mesh all the way to the wall. The second approach is normally termed as the near-wall modelling approach.

The wall function approach substantially saves computational resources in most high Reynolds number wall-bounded flows and is popular because it is economical, robust and can be reasonably accurate. It can be a practical option for the near-wall treatment of industrial flow simulations. However, the wall function approach becomes less reliable when the flow conditions depart too much from the ideal

conditions underlying the wall functions. One example of limitations of the wall function approach is for flows with severe pressure gradients leading to boundary layer separations.

One needs to carefully consider the ramification of using wall functions for the flow with separations, although wall functions together with near wall coarse mesh can be employed, often with some success, to reduce the cost of LES for wall-bounded flows (Catalano *et al.*, 2003). Rodi (1997) questioned the validity of wall function approach for separated flows by comparing the effect of different near-wall treatments on the simulation results of flows around bluff bodies. The wall function approach or a two-layer approach in which the viscous layer is resolved was adopted for the RANS models. It was found that a considerable improvement can be obtained by the RANS models combined with two-layer approach resolving the near-wall region. In his studies, the LES with wall models were also used to simulate the flow around bluff bodies and simulation results were compared with the results obtained from RANS models as well as experimental data. Overall, significantly better predictions were obtained by LES methods, but the discrepancies from the experiments still existed, which could originate from insufficient resolution near the side walls of the bluff body.

The near-wall modelling approach is adopted in this thesis where the mesh in the boundary layer is fine enough to resolve the viscous sublayer. To guarantee fine enough mesh in the near-wall region, values of wall $y^+ \leq 1$ are much desirable.

3.3 Courant Number and Time-Step Size Selection

The Courant number is of fundamental importance for transient flows. For a one-dimensional (1D) grid, it is defined by:

$$Co = \frac{V \Delta t}{\Delta x} \tag{3.14}$$

where V is the flow velocity, Δt is the time-step size and Δx is the mesh size. The Courant number calculated in ANSYS CFX is a multidimensional generalisation of

this expression where the velocity and length scales are based on the mass flow into the control volume and the dimension of the control volume.

For explicit CFD methods, the time-step size should be chosen such that the Courant-Friedrichs-Lewy (CFL) condition is satisfied (i.e., $Co \leq Co_{\max}$). The detailed values of $Co_{\max}$ depend on the particular scheme, but it is usually of order unity. As an implicit code, ANSYS CFX does not require the Courant number to be small for stability. However, for some transient calculations (for example, LES), one may need the Courant number to be ≤ 1 in order to accurately resolve transient details. In order to ensure that the numerical results are independent of the time-step size, a time-step size dependency test is carried out before performing parametric simulations in each study.

3.4 Numerical Schemes

3.4.1 Transient Term

The general discrete approximation of the transient term for the n^{th} time step is:

$$\frac{\partial \phi}{\partial t} = \frac{\phi^{n+\frac{1}{2}} - \phi^{n-\frac{1}{2}}}{\Delta t} \tag{3.15}$$

With the second order backward Euler scheme, the start and end of time step values are respectively approximated as:

$$\phi^{n-\frac{1}{2}} = \phi^{o} + \frac{1}{2}\left(\phi^{o} - \phi^{oo}\right) \tag{3.16}$$

$$\phi^{n+\frac{1}{2}} = \phi + \frac{1}{2}\left(\phi - \phi^{o}\right) \tag{3.17}$$

When these values are substituted into Eq. (3.15), the resulting discretisation is:

$$\frac{\partial \phi}{\partial t} = \frac{1}{\Delta t}\left(\frac{3}{2}\phi - 2\phi^{o} + \frac{1}{2}\phi^{oo}\right) \tag{3.18}$$

3.4.2 Control Volume Gradients

The Gauss' divergence theorem is used to evaluate control volume gradients:

$$\nabla\phi = \frac{1}{V}\sum_{ip}\left(\phi\Delta\mathbf{n}\right)_{ip} \tag{3.19}$$

where $\Delta\mathbf{n}$ is the outward surface vector at the integration point *ip*. This requires that ϕ is evaluated at integration points using finite-element shape functions.

3.4.3 Convective Term

The convective term requires the integration point values of ϕ to be approximated in terms of the nodal values of ϕ. The convective schemes can be cast in the form:

$$\phi_{ip} = \phi_{up} + \beta\nabla\phi\cdot\Delta\mathbf{r} \tag{3.20}$$

where ϕ_{up} is the value at the upwind node, and $\Delta\mathbf{r}$ is the vector from the upwind node to the *ip*. Particular choices for β and $\nabla\phi$ yield different schemes as described below.

3.4.3.1 First Order Upwind Differencing Scheme

A value of $\beta = 0$ yields a first order upwind difference scheme. This scheme is very robust, but it will introduce diffusive discretisation errors that tend to smear steep spatial gradients.

3.4.3.2 High Resolution Scheme

The high resolution scheme uses a special nonlinear recipe for β at each node, computed to be as close to 1 as possible without introducing new extrema. The convective flux is then evaluated using the values of β and $\nabla\phi$ from the upwind node. The recipe for β is based on the boundedness principles used by Barth and Jespersen (1989). This methodology involves first comping a $\phi_{\min}$ and $\phi_{\max}$ at each node using a stencil involving adjacent nodes (including the node itself). Next, for each integration

point around the node, the following equation is solved for β to ensure that it does not undershoot $\phi_{\min}$ or overshoot $\phi_{\max}$:

$$\phi_{ip} = \phi_{up} + \beta \nabla \phi \cdot \Delta \mathbf{r} \tag{3.21}$$

The nodal value for β is taken to be the minimum value of all integration point values surrounding the node. The value of β is also not permitted to exceed 1.

3.4.3.3 Central Difference Scheme

With the central difference scheme, β is set to 1 and $\nabla \phi$ is set to the local element gradient. An alternative interpretation is that ϕ_{ip} is evaluated using the tri-linear shape functions:

$$\phi_{ip} = \sum_n N_n \left(s_{ip}, t_{ip}, u_{ip} \right) \phi_n \tag{3.22}$$

The resulting scheme is also second-order-accurate.

3.4.3.4 Bounded Central Difference Scheme

The central differencing scheme described above is an ideal choice in view of its low numerical diffusion. However, it often leads to unphysical oscillations in the solution fields. In order to avoid these oscillations, the bounded central difference scheme can be used as the convective scheme.

The bounded central difference scheme is essentially based on the normalised variable diagram approach (Leonard, 1991) together with the convection boundedness criterion (Jasak *et al.*, 1999). It uses the central difference scheme wherever possible, but blends to the first-order upwind scheme when the convection boundedness criterion is violated.

3.4.4 Diffusion Term

Following the standard finite-element approach, shape functions are used to evaluate spatial derivatives for all the diffusion terms. For example, for a derivative in the *x*-direction at the *ip*:

$$\frac{\partial \phi}{\partial x}\Big|_{ip} = \sum_n \frac{\partial N_n}{\partial x}\Big|_{ip} \phi_n \tag{3.23}$$

The summation is over all the shape functions for the element. The Cartesian derivatives of the shape functions can be expressed in terms of their local derivatives via the Jacobian transformation matrix:

$$\begin{bmatrix} \frac{\partial N}{\partial x} \\ \frac{\partial N}{\partial y} \\ \frac{\partial N}{\partial z} \end{bmatrix} = \begin{bmatrix} \frac{\partial x}{\partial s} & \frac{\partial y}{\partial s} & \frac{\partial z}{\partial s} \\ \frac{\partial x}{\partial t} & \frac{\partial y}{\partial t} & \frac{\partial z}{\partial t} \\ \frac{\partial x}{\partial u} & \frac{\partial y}{\partial u} & \frac{\partial z}{\partial u} \end{bmatrix}^{-1} \begin{bmatrix} \frac{\partial N}{\partial s} \\ \frac{\partial N}{\partial t} \\ \frac{\partial N}{\partial u} \end{bmatrix} \tag{3.24}$$

The shape function gradients can be evaluated at the actual location of each integration point (that is, true tri-linear interpolation), or at the location where each *ip* surface intersects the element edge (that is, linear-linear interpolation). The latter formulation improves solution robustness at the expense of locally reducing the spatial order-accuracy of the discrete approximation.

3.4.5 Pressure Gradient Term

The surface integration of the pressure gradient in the momentum equations involves evaluation of the expression:

$$\left(p\Delta n_{ip}\right)_{ip} \tag{3.25}$$

The value of p_{ip} is evaluated using the shape functions:

$$p_{ip} = \sum_n N_n\left(s_{ip}, t_{ip}, u_{ip}\right) p_n \tag{3.26}$$

As with the diffusion terms, the shape function used to interpolate *p* can be evaluated at the actual location of each integration point (that is, true tri-linear interpolation), or at the location where each *ip* surface intersects the element edge (that is, linear-linear interpolation).

3.5 Structural Dynamic Model

3.5.1 Rigid Structures

According to Zhao and Cheng (2011), the 2DOF motion of an elastically mounted circular cylinder in Chapter 4 can be described as

$$m_i\ddot{x}_i + c_i\dot{x}_i + K_i x_i = F_i \tag{3.27}$$

where $x_1 = x$ and $x_2 = y$ are the cylinder displacements in the *x*- and *y*-directions, respectively. m_i, c_i, K_i and F_i are the mass, damping coefficient, structural stiffness and hydrodynamic force in the x_i-direction, respectively. Eq. (3.27) is integrated by using a Newmark integration scheme with a second-order accuracy (Hughes, 1987). The method relates displacements, velocities and accelerations from time step *n* to *n*+1:

$$\dot{x}_i^{n+1} = \dot{x}_i^n + \Delta t\left[\left(1-\gamma\right)\ddot{x}_i^n + \gamma\ddot{x}_i^{n+1}\right] \tag{3.28}$$

$$x_i^{n+1} = x_i^n + \Delta t\dot{x}_i^n + \frac{\Delta t^2}{2}\left[\left(1-2\beta\right)\ddot{x}_i^n + 2\beta\ddot{x}_i^{n+1}\right] \tag{3.29}$$

where x_i is the displacement in the x_i-direction, a dot denotes differentiation with respect to time and the superscripts represent the corresponding time step. Δt is the time-step size. β and γ are two real parameters which are directly linked to the accuracy and stability of the scheme. In the present simulation, β = 1/4 and γ = 1/2 are chosen. The choice of the parameters corresponds to a trapezoidal rule with a second-order accuracy and unconditional stability.

Eq. (3.28) and Eq. (3.29) can be rewritten as

$$\ddot{x}_i^{n+1} = \frac{1}{\beta\Delta t^2}\left(x_i^{n+1} - x_i^n\right) - \frac{1}{\beta\Delta t}\dot{x}_i^n - \left(1-\frac{1}{2\beta}\right)\ddot{x}_i^n \tag{3.30}$$

$$\dot{x}_i^{n+1} = \frac{\gamma}{\beta\Delta t}\left(x_i^{n+1} - x_i^n\right) - \left(\frac{\gamma}{\beta} - 1\right)\dot{x}_i^n - \left(\frac{\gamma}{2\beta} - 1\right)\Delta t\ddot{x}_i^n \tag{3.31}$$

Then the displacement in the x_i-direction at time step n+1 can be expressed as

$$x_i^{n+1} = \frac{F_i + m_i\left[\frac{1}{\beta\Delta t^2}x_i^n + \frac{1}{\gamma\Delta t}\dot{x}_i^n + \left(1 - \frac{1}{2\beta}\right)\ddot{x}_i^n\right] + c_i\left[\frac{\gamma}{\beta\Delta t}x_i^n + \left(\frac{\gamma}{\beta} - 1\right)\dot{x}_i^n + \left(\frac{\gamma}{2\beta} - 1\right)\Delta t\ddot{x}_i^n\right]}{\left(\frac{1}{\beta\Delta t^2}m_i + \frac{\gamma}{\beta\Delta t}c_i + K_i\right)} \tag{3.32}$$

3.5.2 Flexible Structures

According to Huang *et al.* (2011a), a top tension riser (Chapter 5) can be simplified as a tensioned beam whose lateral motion is described as

$$\frac{\partial^2}{\partial z^2}\left[EI\frac{\partial^2 x_i}{\partial z^2}\right] - \frac{\partial}{\partial z}\left[T\frac{\partial x_i}{\partial z}\right] + \rho_L\frac{\partial^2 x_i}{\partial t^2} + c\frac{\partial x_i}{\partial t} = F_i \tag{3.33}$$

where E is the Young's modulus, I is the moment of inertia, T is the top tension, ρ_L is the mass per unit length, c is the structural damping coefficient, z is the undeflected riser axis, x_1 and x_2 denote the IL and CF displacements, respectively and F_1 and F_2 are the hydrodynamic forces in the IL and CF directions, respectively. For the above differential equation in the case of a pin-ended beam, the boundary conditions are:

$$x_i(0,t) = 0, \;\; x_i(L,t) = 0 \qquad \forall t \tag{3.34}$$

$$\frac{\partial^2 x_i(0,t)}{\partial z^2} = 0, \;\; \frac{\partial^2 x_i(L,t)}{\partial z^2} = 0 \qquad \forall t \tag{3.35}$$

The two tandem flexible cylinders in Chapter 6 are modelled as beams with two fixed ends and free to vibrate in the transverse direction. The vibrations of the cylinders satisfy the Euler-Bernoulli beam theory. The transverse motions of the two flexible cylinders can be described as

$$\frac{\partial^2}{\partial z^2}\left(EI\frac{\partial^2 y}{\partial z^2}\right) + \rho_L\frac{\partial^2 y}{\partial t^2} + c\frac{\partial y}{\partial t} = F_y \tag{3.36}$$

where E is the Young's modulus, I is the moment of inertia, ρ_L is the mass per unit length, c is the structural damping, z is the undeflected cylinder axis, y is the transverse displacement and F_y is the hydrodynamic force in the transverse direction. The boundary conditions for a beam fixed at the two ends are given by

$$y(0,t)=0,\ \ y(L,t)=0 \qquad \forall t \tag{3.37}$$

$$\frac{\partial y(0,t)}{\partial z}=0,\ \ \frac{\partial y(0,t)}{\partial z}=0 \qquad \forall t \tag{3.38}$$

A finite element method is used to discretise the finite element analysis (FEA) models and the corresponding global equation system is given by

$$\mathbf{M}\ddot{\mathbf{q}}+\mathbf{C}\dot{\mathbf{q}}+\mathbf{K}\mathbf{q}=\mathbf{F} \tag{3.39}$$

where **q** is the nodal displacement vector and a dot denotes differentiation with respect to time. The global mass, damping and stiffness matrices (**M**, **C** and **K)** are the collective effects of the individual elements' mass, damping and stiffness matrices ($\mathbf{M}^e = \iiint \mathbf{N}^T \rho_s \mathbf{N} dxdydz$, $\mathbf{C}^e = \iiint \mathbf{N}^T c \mathbf{N} dxdydz$ and $\mathbf{K}^e = \iiint \mathbf{B}^T \mathbf{E} \mathbf{B} dxdydz$, where **N** is the matrix of shape functions, ρ_s is the structural density, **B** is the strain-displacement matrix and **E** is the elasticity matrix) derived from the principle of virtual work. **F** is the hydrodynamic force vector. The governing equation is solved using the Hilber-Hughes-Taylor (HHT) method (Hilber *et al.*, 1977) with a second-order accuracy.

3.6 Mesh Deformation

To accommodate the motion of the cylinder, the displacement diffusion model (Wang and Xiao, 2016; Zhao and Cheng, 2011) for mesh motion is adopted. The displacements of the mesh points are calculated based on the following equation:

$$\nabla \cdot (\Gamma \nabla S_i) = 0 \tag{3.40}$$

where S_i represents the displacements of the nodal points in the x_i-direction, Γ is the mesh stiffness. Previous simulations by Wang and Xiao (2016) showed that $\Gamma = 1/\forall^2$ with $\forall$ being the control volume size could lead to satisfactory results.

3.7 Fluid-Structure Interaction

3.7.1 Rigid Structures

The 2DOF VIV of an elastically mounted circular cylinder can be solved using a staggered algorithm, i.e., the flow field and the dynamic response of the structure are solved successively at a given time step (Placzek *et al.*, 2009). The solution procedures of the FSI problem within one time step are displayed in Fig. 3.2.

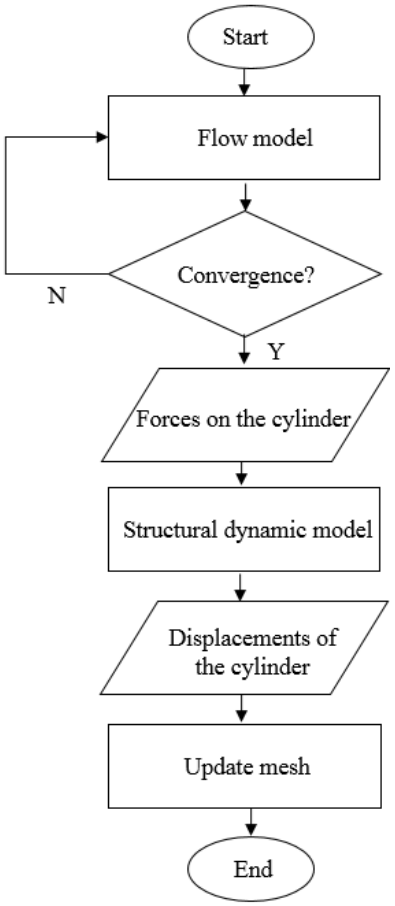

Fig. 3.2 Flow chart of the FSI solution procedures for rigid structures within one time step.

The Navier-Stokes equations are solved to obtain the forces on the cylinder. Then the forces are transferred to the structural dynamic model to obtain the displacements of the cylinder. The new mesh configuration is evaluated based on the displacements of the cylinder using Eq. (3.40) and the Navier-Stokes equations are solved on the new

mesh configuration. Such an FSI loop is repeated during each time step of the simulation.

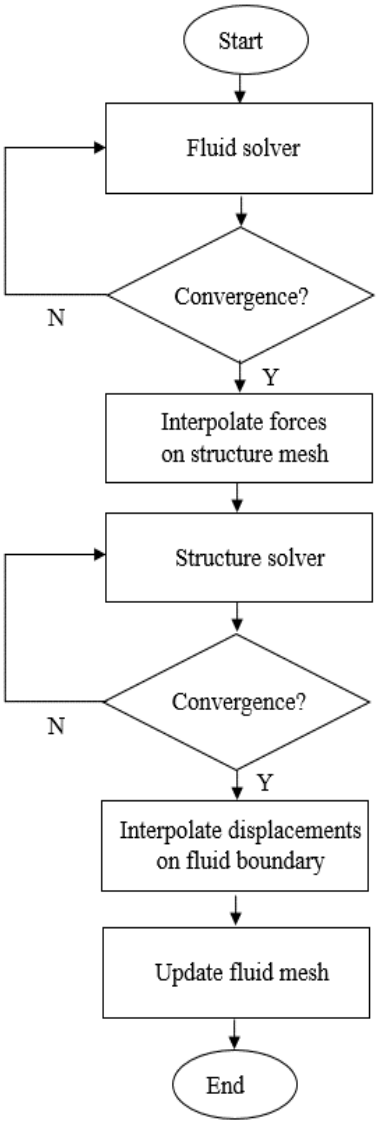

Fig. 3.3 Flow chart of two-way explicit FSI solution procedures for flexible structures within one time step.

3.7.2 Flexible Structures

A two-way explicit approach is utilised in the present FSI simulation, i.e., the fluid and solid equations are solved separately and there are no iterations between the fluid and solid fields within one time step. The flow chart of the two-way explicit FSI solution procedures for one time step is shown in Fig. 3.3. It can be seen that within

one time step, the flow equations are solved to obtain the forces on the flexible cylinders. Then the forces are interpolated to the structural mesh using the conservative interpolation and the structural dynamic equation is solved to obtain the quantities of motions of the flexible cylinders. After that, the displacements are interpolated to the fluid mesh with the profile preserving interpolation and the positions of the mesh points are calculated and updated using the displacement diffusion model in Eq. (3.40). The next time step begins with solving the flow equations on the updated mesh. The solvers follow the same FSI procedures until the last time step of the simulation.

Chapter 4 Three-Dimensional Numerical Simulation of Two-Degree-of-Freedom Vortex-Induced Vibration of a Circular Cylinder with Varying Natural Frequency Ratios

"It is possible to imagine a four-dimensional space. I personally find it hard enough to visualise a three-dimensional space."

-Stephen Hawking

2DOF VIV of an elastically mounted circular cylinder with varying IL to CF natural frequency ratios is studied using a 3D CFD approach. The numerical simulations are carried out for a constant mass ratio m^* = 2 at a fixed Reynolds number Re = 500. The reduced velocity V_r ranges from 2 to 12. Three natural frequency ratios are considered, i.e., f^* = 1, 1.5 and 2. The structural damping is set to zero to maximise the response of the cylinder. The main objective of this study is to investigate the effect of f^* on the 2DOF VIV responses and the 3D characteristics of the flow.

4.1 Problem Descriptions

4.1.1 Simulation Parameters

In the present study, 3D numerical simulation is conducted for an elastically mounted circular cylinder with diameter D and length L. The Reynolds number is defined as Re = VD/v and a constant Reynolds number Re = 500 is adopted in the simulation. The choice of Re stems from several important considerations. First, at Re = 500, the flow around the cylinder is 3D and it can be modelled by directly solving the 3D Navier-Stokes equations with affordable computational efforts which also avoids the potential uncertainties that might be introduced by the utilisation of turbulence models. Second, the flow structures at low Re are more regular than those at high Re which is good for analysing the detailed wake structures and the three-dimensionality of the flow. More importantly, previous studies by Bao *et al.* (2012) and Leontini *et al.* (2006) revealed that VIV of rigid structures at low Re shares comparable response

features to that at high Re. Studies on 2DOF VIV at low Re are also of fundamental research interest from a flow physics point of view.

Batcho and Karniadakis (1991) studied the flow past a circular cylinder at Re = 500 with length-to-diameter ratios (L/D) of π and 2π and obtained sufficiently accurate results of the force coefficients. The L/D = 8 and 12 were used in the 3D simulation of the flow around two circular cylinders in tandem at Re $\leq$ 500 by Carmo *et al.* (2010a); in the present study, the L/D is also set to 12. As the wavelength of spanwise flow structures at Re = 500 is $\lambda_z/D \approx 1$, the current spanwise length of 12D is believed to be sufficient for capturing the three-dimensionality of the flow at this Reynolds number. Furthermore, this L/D is also comparable to those used in some recent experimental studies on VIV of an elastically mounted circular cylinder (Jauvtis and Williamson, 2004; Kang and Jia, 2013; Sanchis *et al.*, 2008; Srinil *et al.*, 2013; Stappenbelt *et al.*, 2007).

The cylinder is free to vibrate in both the IL and CF directions. The mass ratios of the cylinder in the IL and CF directions are set to be identical and take the value of $m_x^* = m_y^* = m^* = 2$. Such a low mass ratio is chosen because a dramatic change in the fluid-structure interactions of 2DOF VIV was observed by Jauvtis and Williamson (2004) when the mass ratio m^* is less than 6. The mass ratios in the IL and CF directions are set to be identical, as the scenario in which $m_x^* = m_y^*$ is of more practical relevance to the real cylindrical offshore structures (Srinil *et al.*, 2013). As the vibration amplitudes reported in previous CFD simulations at low Re (Bao *et al.*, 2012; Gsell *et al.*, 2016; Lucor and Triantafyllou, 2008; Singh and Mittal, 2005) are relatively small compared to the amplitudes observed in experiments at higher Re (Blevins and Coughran, 2009; Dahl *et al.*, 2006; Jauvtis and Williamson, 2004; Srinil *et al.*, 2013), in order to maximise the vortex-induced response of the cylinder, the damping coefficients are set to zero by the various authors in their numerical simulations. Similarly, zero damping coefficients in the IL and CF directions are also adopted in the present study, i.e., $c_x = c_y = c = 0$. The reduced velocity is varied from 2 to 12 with an increment of 1 and for each reduced velocity, three natural frequency ratios are considered, i.e., f^* = 1, 1.5, and 2.

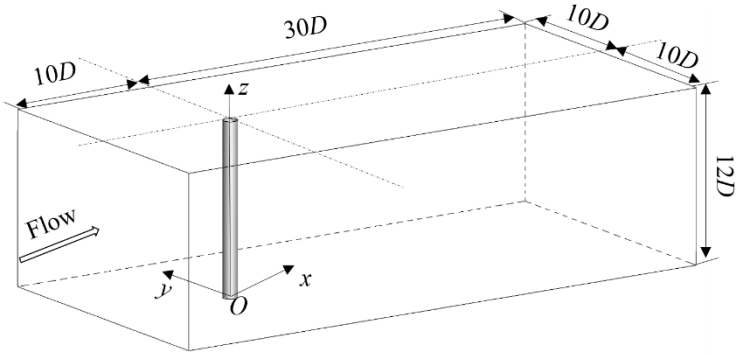

(a)

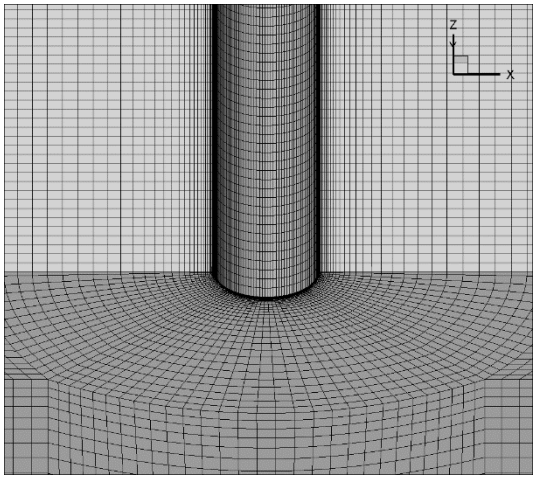

(b)

Fig. 4.1 (a) Computational domain and (b) computational mesh.

4.1.2 Computational Domain and Boundary Conditions

Fig. 4.1(a) shows the computational domain that is used in the present simulation. The size of the domain is $40D \times 20D \times 12D$ where D is the diameter of the cylinder. The cylinder is located at $10D$ downstream the inlet boundary and the origin of the Cartesian coordinate system is located at the centre of the bottom end of the cylinder. The computational mesh is displayed in Fig. 4.1(b). There are 120 nodes along the circumference of the cylinder and the minimum mesh size next to the cylinder surface in the radial direction is $0.001D$. The boundary conditions for the governing equations are as follows. The surface of the cylinder is assumed to be a no-slip wall. The velocity at the inlet boundary is set to be the same as the freestream velocity. At

the outflow boundary, the gradients of the fluid velocity in the streamwise direction are set to zero and the pressure at the outflow boundary is given a reference value of zero. The free-slip boundary condition with the velocity in the direction normal to the boundary being zero is used on the two transverse boundaries and a periodic boundary condition is imposed on the top and bottom boundaries. At t = 0, the velocities and displacements of the cylinder are zero ($x_1 = x_2 = 0$ and $\dot{x}_1 = \dot{x}_2 = 0$).

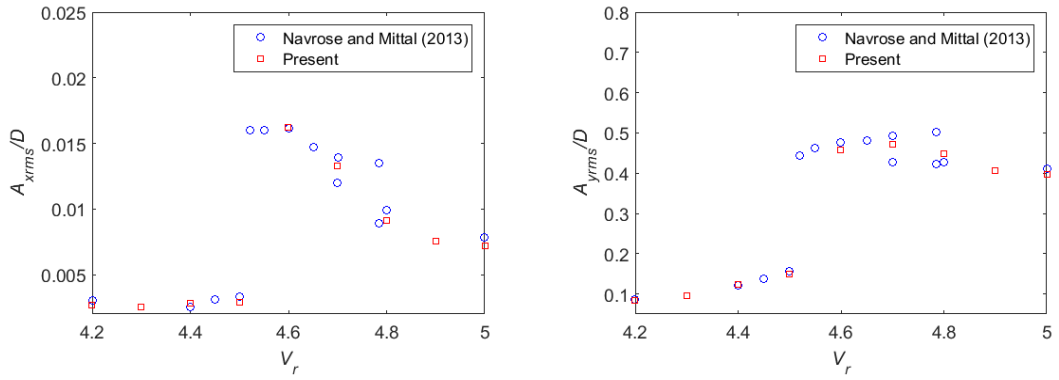

(a) (b)

Fig. 4.2 Comparison of the present numerical results with numerical results by Navrose and Mittal (2013) for increasing V_r: (a) rms of in-line vibration amplitudes and (b) rms of cross-flow vibration amplitudes.

4.1.3 Validation Test

As there are no experimental data on 2DOF VIV of a circular cylinder at early subcritical Reynolds numbers available, the numerical results from the 3D CFD simulation of 2DOF VIV of a circular cylinder with m^* = 10 and L/D = 4 at Re = 1000 by Navrose and Mittal (2013) are used to verify the present numerical methods. For the purpose of making a reasonable comparison with the results for increasing V_r in their simulation, the V_r in the present validation test is also increased in small steps. Fig. 4.2(a) and (b) are the comparisons of the root mean square (rms) of the vibration amplitudes against V_r in the IL and CF directions, respectively. It shows that good agreement is achieved between the present results and those of Navrose and Mittal (2013). The maximum rms IL and CF vibration amplitudes predicted in both studies are $A_{xrm}/D \approx 0.016$ and $A_{yrm} \approx 0.5$, respectively. This test case demonstrates that the

present numerical methods are capable of accurately predicting 2DOF VIV response of an elastically mounted circular cylinder at early subcritical Reynolds numbers.

4.1.4 Mesh Dependency Study

In order to quantify the dependency of the numerical results on the mesh density, numerical simulation of 2DOF VIV of a circular cylinder at $f^* = 2$ and $V_r = 6$ is performed using three different meshes as summarised in Table 4.1 in which N_{node}, $N_{element}$, Δz, Δr and N_c represent the number of nodes, the number of elements, the mesh size in the spanwise direction, the minimum mesh size next to the cylinder surface in radial direction and the number of nodes along the circumference of the cylinder, respectively. Quantitative comparisons of the oscillation amplitudes (A_x/D, A_y/D), oscillation frequencies (f_{ox}/f_{ny}, f_{oy}/f_{ny}) and phase differences (θ) between the IL and CF displacements calculated from the different meshes are provided in Table 4.1. As observed in Table 4.1, the IL and CF oscillation frequencies predicted by the three meshes are identical. The differences in A_y/D and θ between Mesh 2 and Mesh 3 are 1.4% and 0.2%, respectively. The maximum difference of 4.1% occurs in A_x/D between Mesh 2 and Mesh 3. The comparison among the results from the different meshes suggests that the mesh density of Mesh 2 is adequate for predicting accurate results of 2DOF VIV at Re = 500.

Table 4.1 Comparison of the results from three different meshes.

Mesh	N_{node} (M)	$N_{element}$ (M)	$\Delta z/D$	$\Delta r/D$	N_c	A_x/D	A_y/D	f_{ox}/f_{ny}	f_{oy}/f_{ny}	θ (deg)
1	0.37	0.39	0.2	0.002	96	0.408	0.818	1.875	0.937	341.140
2	0.89	0.93	0.1	0.001	120	0.355	0.797	1.875	0.937	343.540
3	2.27	2.34	0.05	0.001	160	0.341	0.786	1.875	0.937	344.300

4.1.5 Time-Step Size Dependency Test

A time-step size dependency test is conducted on Mesh 2 with three nondimensional time-step sizes ($V\Delta t/D$ = 0.005, 0.002 and 0.001) for the same case as used in the mesh dependency study. The corresponding results are tabulated in Table 4.2. It shows that the maximum difference between $V\Delta t/D$ = 0.005 and 0.002 is around 3.6%

and it decreases to approximately 1.5% between $V\Delta t/D$ = 0.002 and 0.001. Therefore, the numerical results are independent of the time-step size when $V\Delta t/D \leq 0.002$. In the consideration of computational efforts, $V\Delta t/D$ = 0.002 is adopted for the simulation in this study.

Table 4.2 Comparison of the results using different time-step sizes.

$V\Delta t/D$	A_x/D	A_y/D	f_{ox}/f_{ny}	f_{oy}/f_{ny}	θ (deg)
0.005	0.368	0.819	1.875	0.937	342.560
0.002	0.355	0.797	1.875	0.937	343.540
0.001	0.350	0.808	1.875	0.937	343.870

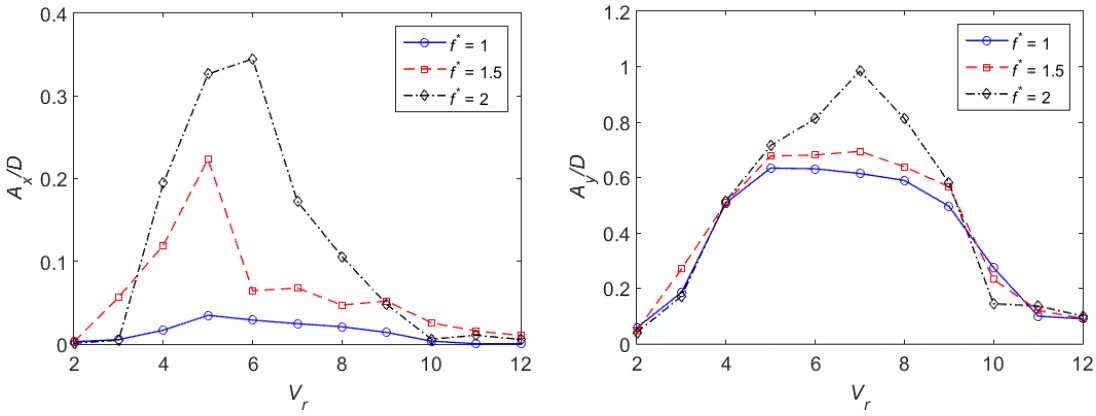

(a) (b)

Fig. 4.3 Variation of the response amplitudes with the reduced velocity at different natural frequency ratios: (a) in-line response amplitudes and (b) cross-flow response amplitudes.

4.2 Results and Discussions

2DOF VIV of a circular cylinder with varying IL to CF natural frequency ratios (f^* = 1, 1.5 and 2) at an early subcritical Reynolds number Re = 500 is simulated in a reduced velocity range of V_r = 2 – 12. The effect of the natural frequency ratio on the 2DOF VIV responses and the 3D flow features around the cylinder is examined.

4.2.1 Response Amplitudes

Previous studies have shown that f^* has a significant influence on the vibration amplitudes of the cylinder especially when f^* is close to 2 (Bao *et al.*, 2012; Dahl *et al.*, 2006; Lucor and Triantafyllou, 2008; Sarpkaya, 1995). In this section, the effect of f^* on the response amplitudes is explicated. Fig. 4.3 shows the variation of the dimensionless vibration amplitudes (A_x/D and A_y/D) with V_r at different f^*. As observed in Fig. 4.3(a), the maximum IL amplitude (A_{xm}/D) increases with the increase of f^*. The peak IL amplitudes of $f^* = 1$ and 1.5 appear at an identical reduced velocity $V_r = 5$ and take the values of $A_{xm}/D = 0.035$ and 0.224, respectively. When f^* increases to 2, A_{xm}/D increases to 0.345 and shifts to a higher reduced velocity $V_r = 6$. As for the CF amplitudes, the amplitude curves of $f^* = 1$ and 1.5 exhibit similar trends against V_r with a slight increase in the maximum cross-flow amplitude (A_{ym}/D) from 0.634 to 0.695 when f^* increases from 1 to 1.5. A dramatic increase in the CF amplitude is observed when f^* increases to 2. Similar to A_{xm}/D, A_{ym}/D also shifts to a higher reduced velocity $V_r = 7$ and its value increases to $A_{ym}/D \approx 1$. The increase of vibration amplitude and the shift of the peak amplitude to a higher reduced velocity when f^* varies from 1 to 2 were also observed in the 2D numerical simulation of Lucor and Triantafyllou (2008) at Re = 1000 and Bao *et al.* (2012) at Re = 150.

The shapes of the response curves in the present study are qualitatively similar to those obtained from the 2D CFD simulation at Re = 150 by Bao *et al.* (2012) (Fig. 4.4). The lock-in ranges of present results are wider than those in Bao *et al.* (2012) owing to the lower m^* used in the present simulation. When $f^* = 2$, multiple small peaks were observed by Bao *et al.* (2012) whereas the CF response at $f^* = 2$ in the present simulation shows a single peak. In order to investigate the possible explanations for this discrepancy, a 2D simulation of 2DOF VIV of a circular cylinder with the same parameters as in Bao *et al.* (2012) is conducted at $f^* = 2$ and the results are plotted in Fig. 4.4(c). As shown in Fig. 4.4(c), the CF response in the present 2D simulation also displays a single peak. It is thus speculated that the discrepancy can be attributed to the difference related to the stability of the numerical methods used for solving the structural dynamic equations. In fact, Bao *et al.* (2012)

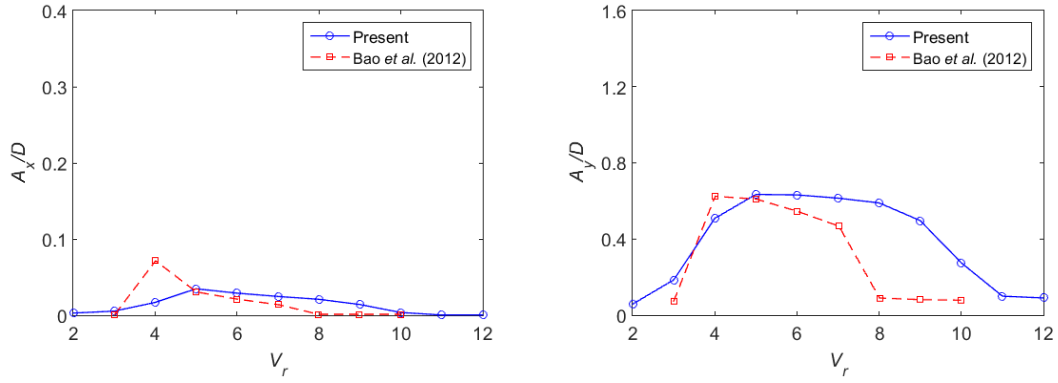

(a)

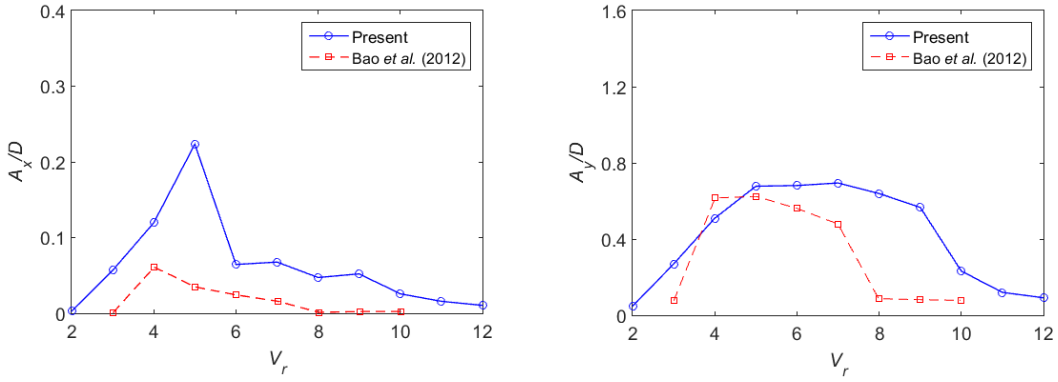

(b)

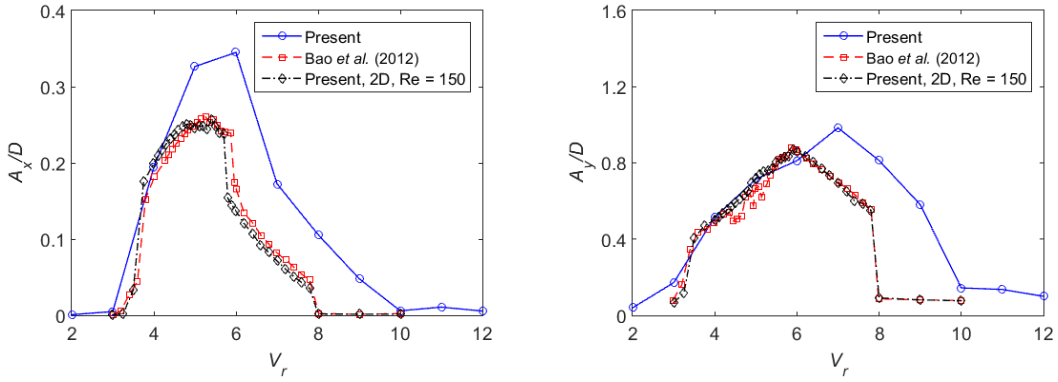

(c)

Fig. 4.4 Comparison of amplitude response curves between the present simulation and Bao *et al.* (2012): (a) $f^* = 1$, (b) $f^* = 1.5$ and (c) $f^* = 2$.

used an explicit time integration method which is conditionally stable while the Newmark integration scheme used in the present study is unconditionally stable.

With $m_x^* \neq m_y^*$, Sarpkaya (1995) and Dahl *et al.* (2006) reported the observation of a two-peak CF response when f^* approaches 2. However, the studies by Lucor and Triantafyllou (2008) and Srinil *et al.* (2013) with $m_x^* = m_y^*$ revealed a single-peak CF response. Srinil *et al.* (2013) attributed the single-peak CF response at $f^* \approx 2$ to the identical mass ratios in the IL and CF directions. The observation of the single-peak CF responses in the present 2D and 3D simulations when $f^* = 2$ for identical IL and CF mass ratios is consistent with the conclusion by Srinil *et al.* (2013).

As noted above, in the present 3D simulation, the vibration amplitude increases and the peak amplitude shifts to a higher reduced velocity when f^* increases from 1 to 2, which is consistent with the numerical simulation results by Lucor and Triantafyllou (2008) at Re = 1000 and Bao *et al.* (2012) at Re = 150. Conversely, the change in the vibration amplitude as well as the shift of the peak amplitude when f^* varies from 1 to 2 in the experimental studies by Dahl *et al.* (2006) (Re = 11000 – 60000) and Srinil *et al.* (2013) (Re = 2000 – 50000) at higher Re are not obvious. Furthermore, compared to the maximum CF amplitudes around 1.5D in the experimental studies, the present maximum CF amplitudes are relatively small. The aforementioned differences in the amplitude responses indicate the possible influence of the Reynolds number on 2DOF VIV as suggested by Swithenbank *et al.* (2008).

4.2.2 Response Frequencies

The occurrence of dual resonance has been widely reported for 2DOF VIV by Dahl *et al.* (2010), Bao *et al.* (2012), Srinil and Zanganeh (2012), Srinil *et al.* (2013), Zanganeh and Srinil (2014) and Wang and Xiao (2016). Fig. 4.5 shows the variation of the normalised oscillation frequencies in the IL and CF directions (f_{ox}/f_{ny} and f_{oy}/f_{ny}) with the reduced velocity at different natural frequency ratios. According to the synchronisation between the response frequency and the natural frequency in Fig. 4.5, the lock-in ranges of the three different natural frequency ratios are identical, i.e., V_r = 5 – 10. The normalised oscillation frequencies in the IL and CF directions are almost constant within the lock-in range and are linear functions of the reduced velocity in the pre-lock-in ($2 \leq V_r < 5$) and post-lock-in ($10 < V_r \leq 12$) ranges. It can

be seen from Fig. 4.5 that the ratio of the IL oscillation frequency to the CF oscillation frequency is around 2 regardless of the natural frequency ratio. As explained by Dahl *et al.* (2010), under dual resonance, the cylinder vibrates at frequencies near the Strouhal frequency f_v in the CF direction and $2f_v$ in IL direction, respectively. The 2:1 IL to CF oscillation frequency ratio in the present study indicates that dual resonance exists over a wide range of the natural frequency ratios.

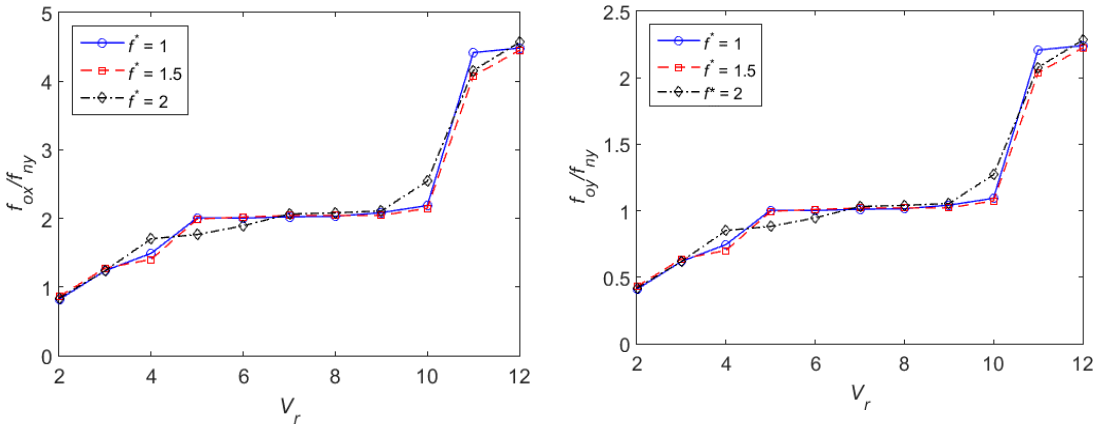

(a) (b)

Fig. 4.5 Variation of the response frequencies with the reduced velocity at different natural frequency ratios: (a) in-line response frequencies and (b) cross-flow response frequencies.

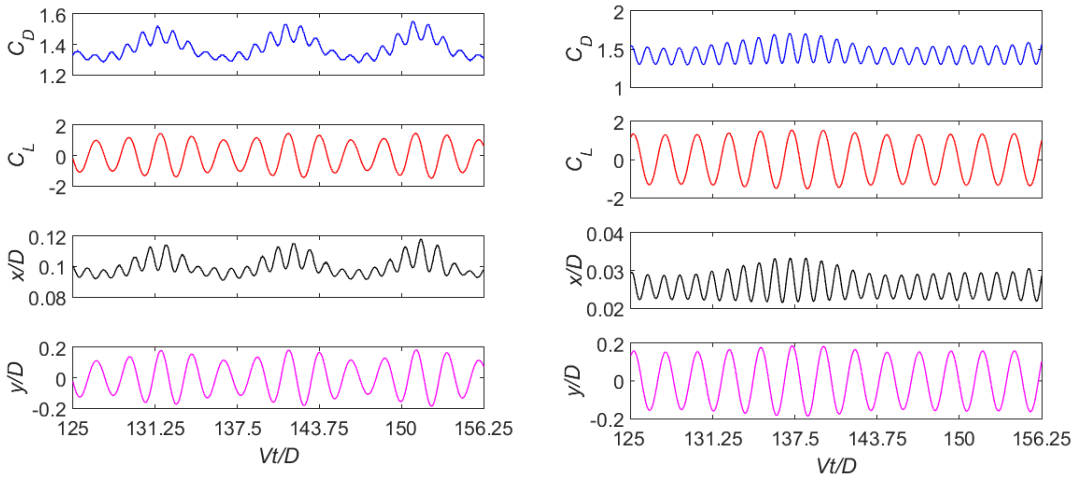

(a) (b)

Fig. 4.6 Time histories of the cylinder displacements and total lift and drag coefficients when $f^* = 1$: (a) $V_r = 3$ and (b) $V_r = 6$.

The time histories of the total drag coefficient $C_D = F_x/(0.5\rho V^2 DL)$, total lift coefficient $C_L = F_y/(0.5\rho V^2 DL)$, IL and CF displacements (x/D and y/D) at $V_r = 3$ and 6 when $f^* = 1$ are illustrated in Fig. 4.6, which reveal the vibrations are regular at $V_r = 6$ as compared to $V_r = 3$ where the beating phenomenon occurs. The beating phenomenon arises from off resonance vibrations of the system and the observed beating behaviour in the pre-lock-in range agrees with the observations of Al-Jamal and Dalton (2004) and Wu (2011) in their 2D CFD simulations as well as Navrose and Mittal (2013) and Zhao *et al.* (2014) in their 3D CFD simulations.

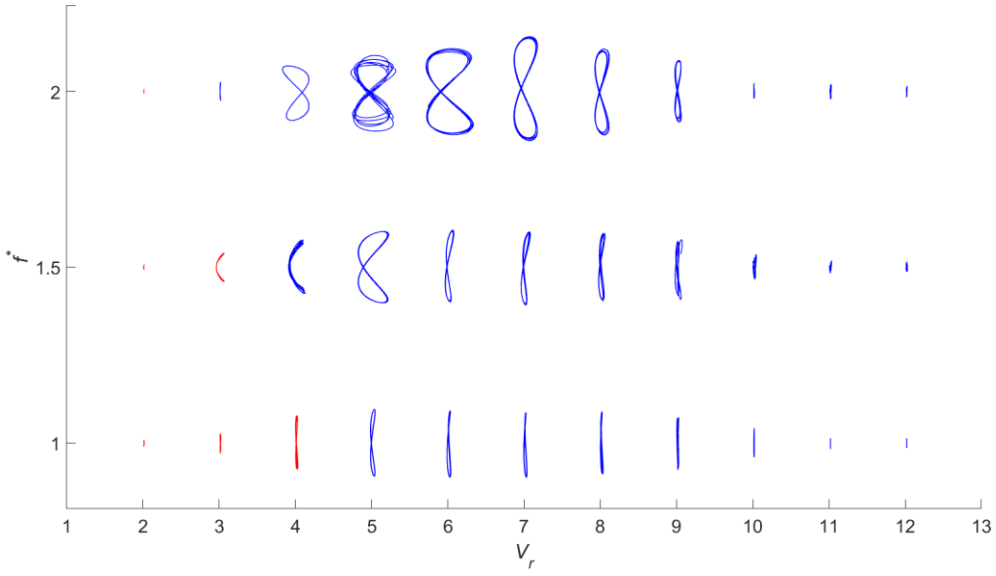

(a)

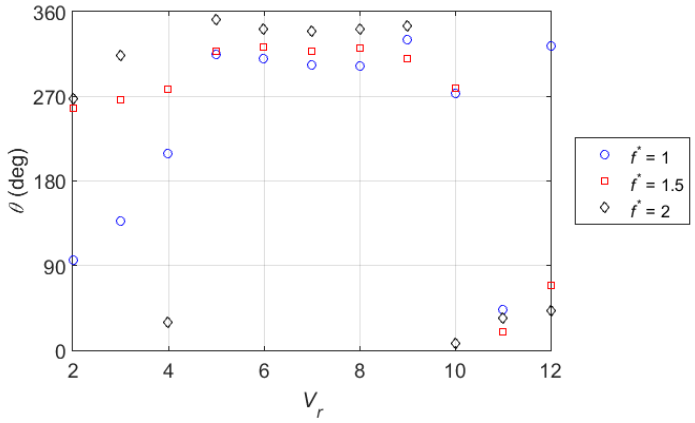

(b)

Fig. 4.7 (a) Variation of the orbital trajectories with the reduced velocity at different natural frequency ratios and (b) variation of the phase differences between in-line and cross-flow displacements with the reduced velocity at different natural frequency ratios.

4.2.3 Orbital Trajectories

Dahl *et al.* (2008) reported that the orbital shape of the cylinder is critical in defining the amplitude and frequency content of the hydrodynamic forces and according to Bourguet *et al.* (2013), the direction of the orbital motion is closely related to the energy transfer between the fluid and the structure. Therefore, it is of great significance to study the effect of the natural frequency ratio on the orbital trajectories of the cylinder. The variation of the orbital trajectories with the reduced velocity at different natural frequency ratios is displayed in Fig. 4.7(a). It can be observed that most of the orbital trajectories are of a figure-eight shape which is indicative of the 2:1 IL to CF oscillation frequency ratio. Therefore, the figure-eight trajectories are also the evidence of the occurrence of dual resonance (Dahl *et al.*, 2010).

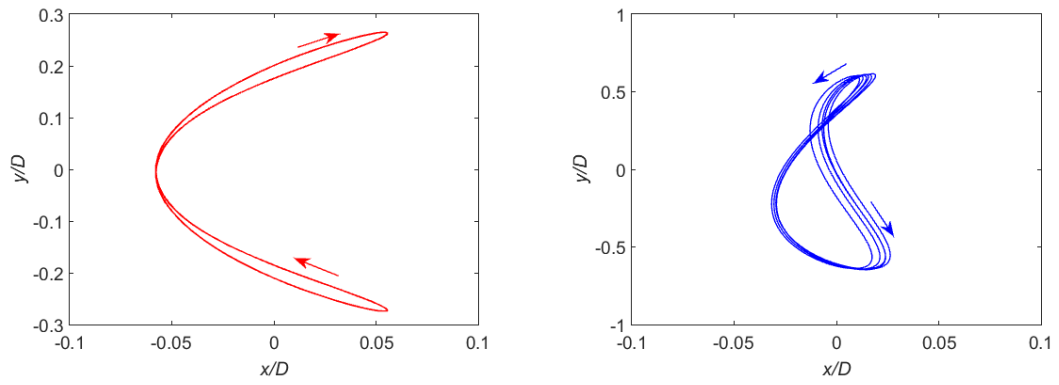

(a) (b)

Fig. 4.8 Zoom-in view of orbital trajectories: (a) clockwise figure-eight trajectory at V_r = 3 and f^* = 1.5 and (b) oblique counterclockwise figure-eight trajectory at V_r = 6 and f^* = 1.

The orbit orientation of a trajectory is related to the phase difference (θ) between the IL and CF displacements. As elucidated by Huera-Huarte and Bearman (2009) and Bourguet *et al.* (2013), the phase difference can be defined as $\theta = \theta_x - 2\theta_y$ where θ_x and θ_y are phase angles of the IL and CF responses, respectively. According to Jauvtis and Williamson (2004), an orbital trajectory is counterclockwise when $0^\circ \leq \theta < 90^\circ$ or $270^\circ < \theta \leq 360^\circ$ and clockwise when $90^\circ < \theta < 270^\circ$. Crescent shapes

correspond to θ = 90° or 270°. The phase differences demonstrated in Fig. 4.7(b) highlight that most of the orbital trajectories are counterclockwise, i.e., the cylinder motion is counterclockwise at the top of the figure-eight motion. The exceptional clockwise trajectories are highlighted in red in Fig. 4.7(a) and a close-up of the orbital trajectory at V_r = 3 and f^* = 1.5 is displayed in Fig. 4.8(a) revealing that the trajectory is of a clockwise figure-eight shape.

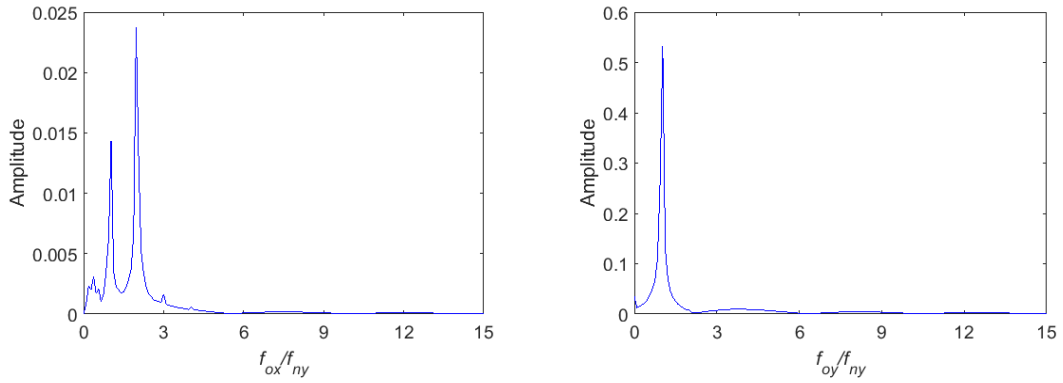

(a) (b)

Fig. 4.9 Amplitude spectra of displacements at V_r = 6 and f^* = 1: (a) in-line displacement and (b) cross-flow displacement.

It can be seen that clockwise orbital trajectories are mainly observed in the pre-lock-in range and the number of clockwise trajectories decreases as f^* increases from 1 to 2. The counterclockwise direction is the predominant orbit orientation in the lock-in range. This observation agrees with the conclusion of Bourguet *et al.* (2011) that the flow excites the cylinder under the lock-in condition with a preferential IL versus CF motion phase difference corresponding to counterclockwise, figure-eight orbits. Oblique figure-eight trajectories similar to those reported by Kang and Jia (2013) and Gedikli and Dahl (2014) are observed at V_r = 6, 7 and 8 when f^* = 1 in the present study. Fig. 4.8(b) illustrates the oblique figure-eight trajectory at V_r = 6 and f^* = 1. The amplitude spectra of the IL and CF displacements at V_r = 6 and f^* = 1 are plotted in Fig. 4.9. Similar to other cases under dual resonance, the ratio of the dominant IL to CF oscillation frequencies in an oblique figure-eight trajectory is also around 2. However, for the IL displacement, apart from the dominant frequency component at twice the CF oscillation frequency ($2f_{oy}$), there is also a frequency component equal

to $1f_{oy}$. The additional $1f_{oy}$ frequency component in the IL displacement leads to the asymmetry of the Lissajous figure.

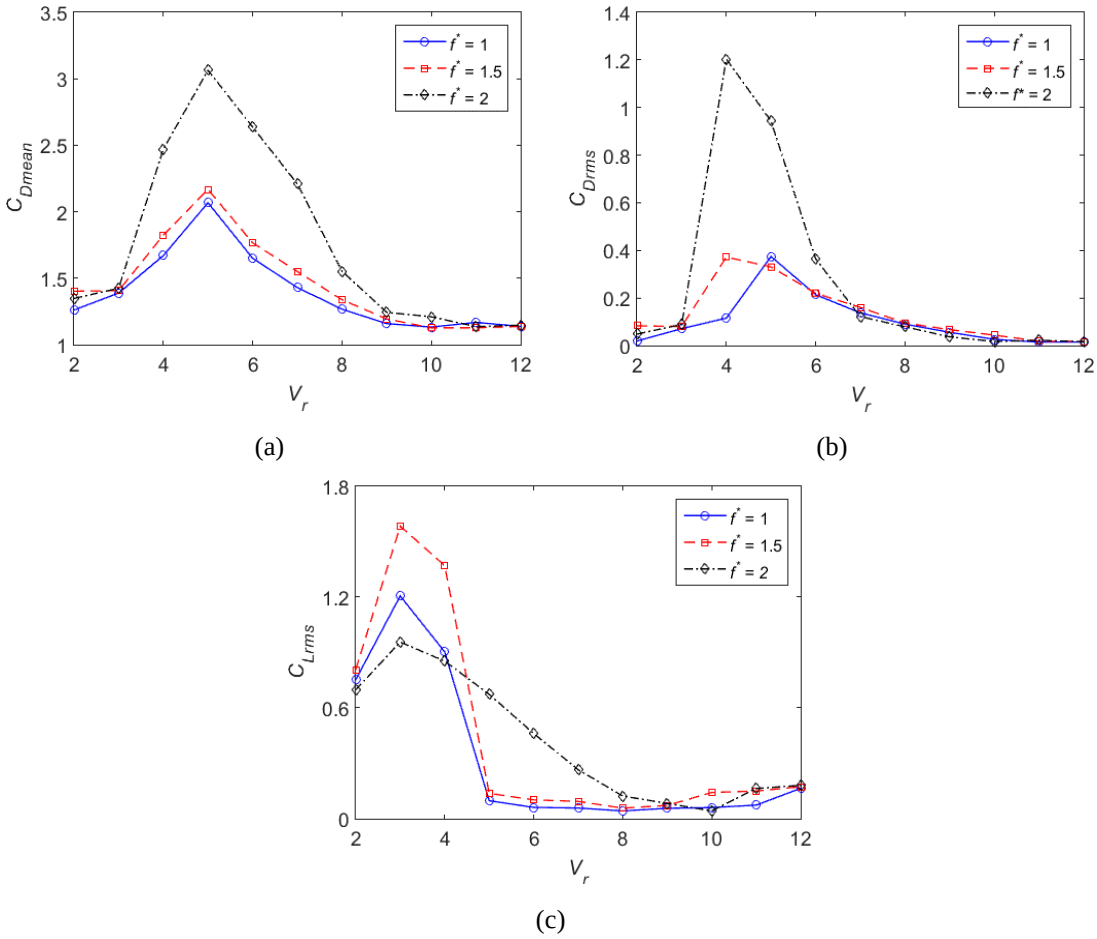

Fig. 4.10 Variation of the hydrodynamic force coefficients with the reduced velocity at different natural frequency ratios: (a) mean drag coefficients, (b) rms of total drag coefficients and (c) rms of total lift coefficients.

4.2.4 Hydrodynamic Forces

When the cylinder is vibrating in two degrees of freedom, the IL vibration has significant effects on the hydrodynamic forces. Fig. 4.10 shows the variation of the total lift and drag coefficients with the reduced velocity. As observed in Fig. 4.10(a), the mean drag coefficient (C_{Dmean}) curves of f^* = 1 and 1.5 nearly coincide, while an obvious increase in the mean drag coefficient is observed at f^* = 2. The rms values of the oscillating drag coefficient (C_{Drms}) show a remarkable jump at f^* = 2 and V_r = 4. The peak C_{Drms} reaches nearly three times as large as it is at f^* = 1 and 1.5. The large

drag fluctuation agrees with the observations by Dahl *et al.* (2010) and Bao *et al.* (2012). Compared to the oscillating drag, the fluctuation of the rms values of the oscillating lift coefficient (C_{Lrms}) is less sensitive to f^*.

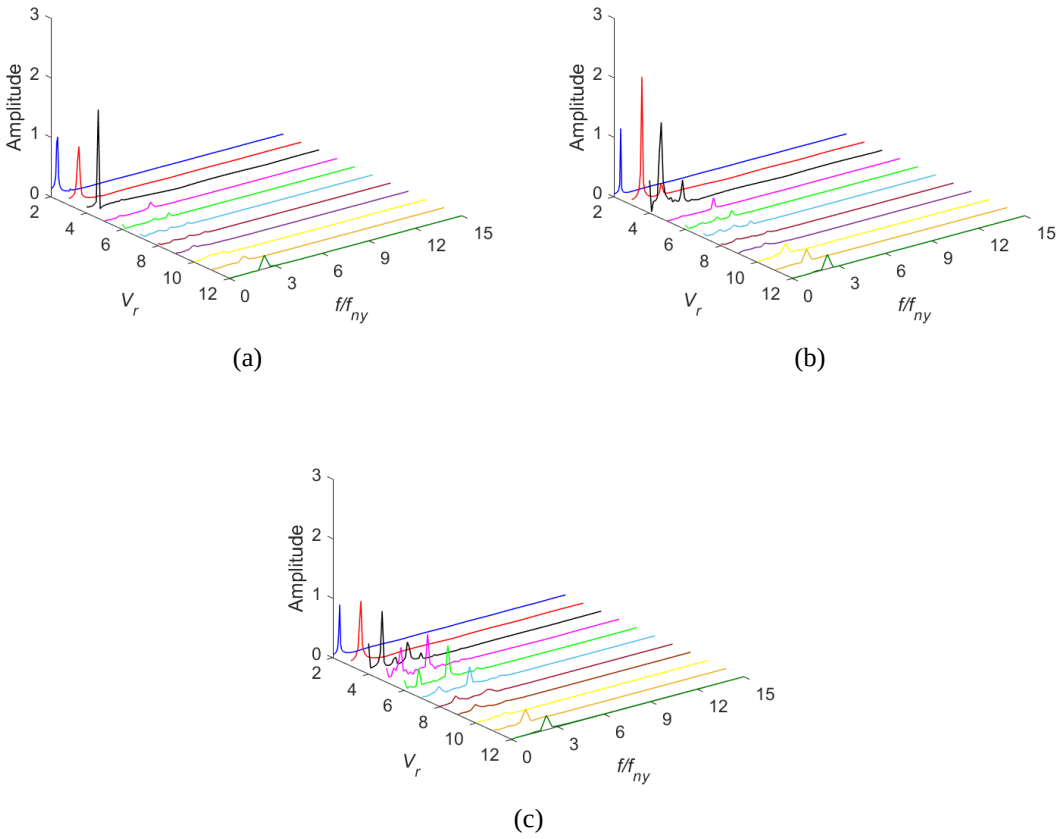

Fig. 4.11 Amplitude spectra of the total lift coefficients: (a) f^* = 1, (b) f^* = 1.5 and (c) f^* = 2.

The time histories of the total lift and drag coefficients at V_r = 3 and 6 when f^* = 1 are shown in Fig. 4.6. Similar to the VIV responses, the beating phenomenon is also discernible in the hydrodynamic force coefficients at V_r = 3. The total lift coefficient time history makes evident that there is a third harmonic component in the total lift coefficient at V_r = 6. Fig. 4.11 shows the amplitude spectra of the total lift coefficients at different f^*. It is apparent that for the three natural frequency ratios considered in the present study, there is a third harmonic component in the total lift coefficients in the lock-in range. The third harmonic forces were found to be associated with the counterclockwise motion of the cylinder by Dahl *et al.* (2010).

With the increase of the natural frequency ratio, the third harmonic component becomes larger.

4.2.5 Effective Added Mass Coefficients

It is observed in Fig. 4.5 that the IL to CF oscillation frequency ratio is always in the vicinity of 2 regardless of f^*. The 2:1 oscillation frequency ratio at different f^* is the consequence of the change in the effective added mass. According to Dahl *et al.* (2010), the oscillation frequency of the cylinder can be defined as follows.

$$f_o = \sqrt{\frac{K}{m + m_{ea}}} \tag{4.1}$$

where m_{ea} is the effective added mass. The effective fluid added mass force changes the effective added mass of the system leading to the 2:1 oscillation frequency ratio, although f^* may be distant from 2. Similar to the mass ratio m^*, the effective added mass can be nondimensionalised as $C_m = m_{ea}/(\rho\pi D^2 L/4)$. The coefficient C_m represents a force coefficient due to vortex dynamics that is in phase with the acceleration of the cylinder.

The effective added mass coefficients in the IL and CF directions (C_{mx} and C_{my}) are determined based on the second harmonic component of the fluctuating drag and the first harmonic component of the lift as in Jauvtis and Williamson (2004).

$$C_{mx} = \frac{2V^2 C_{D2}\cos(\phi_x)}{\pi(A_x/D)D^2(2\pi f_{ox})^2} \tag{4.2}$$

$$C_{my} = \frac{2V^2 C_{L1}\cos(\phi_y)}{\pi(A_y/D)D^2(2\pi f_{oy})^2} \tag{4.3}$$

where C_{D2} and ϕ_x are the magnitude of the second harmonic component of the fluctuating drag coefficient and its phase angle with respect to the IL displacement, respectively. C_{L1} and ϕ_y are the magnitude of the first harmonic component of total lift coefficient and its phase angle with respect to the CF displacement, respectively.

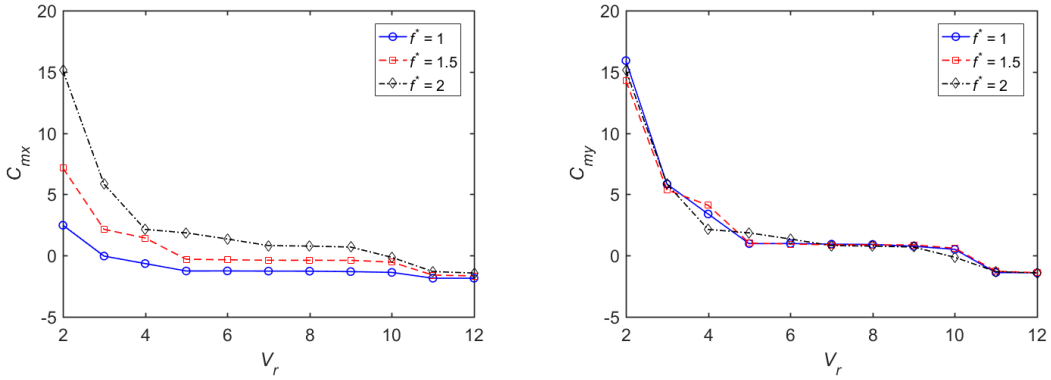

(a) (b)

Fig. 4.12 Variation of the effective added mass coefficients with the reduced velocity at different natural frequency ratios: (a) in-line effective added mass coefficients and (b) cross-flow effective added mass coefficients.

Fig. 4.12 demonstrates the variation of the effective added mass coefficients with the reduced velocity at different f^*. According to Fig. 4.12(a), C_{mx} decreases with the increase of the reduced velocity. The decreasing trend is observed for all the three natural frequency ratios considered and it is also reflected by the increase of the oscillation frequency with the increase of V_r as shown in Fig. 4.5. A large deviation is observed for the C_{mx} curves at different f^*. At $f^* = 1$, most of the effective added mass coefficients are negative. In contrast, they become positive throughout the V_r range considered when $f^* = 2$. Negative effective added mass coefficients in the IL direction with the lowest value being around -2 were also reported by Bao *et al.* (2012) in their 2D CFD study and in the reduced-order modelling by Zanganeh and Srinil (2014). In the CF direction, C_{my} also decreases with the increase of the reduced velocity. However, unlike the C_{mx} curves, the C_{my} curves at different f^* show obvious overlap in the range of V_r considered. This seems reasonable because a larger variation of the IL added mass is required in order to drive the oscillation frequency ratio to 2 when f^* is distant from 2.

4.2.6 Correlation Lengths

The three-dimensionality of the flow in the near wake of the cylinder which determines the fluctuations of the forces acting on the cylinder is measured by the

spanwise correlation length. Previous experimental and numerical studies indicated that there was a sharp drop in spanwise correlation at the end of the upper branch near the transition between the upper and the lower branches which does not diminish the response of the cylinder (Hover *et al.*, 2004; Hover *et al.*, 1998; Lucor *et al.*, 2003, 2005; Zhao *et al.*, 2014). In the present study, the autocorrelation function defined by Lucor *et al.* (2005) is used to quantify the correlation. The autocorrelation function is described as follows.

$$R(l,t)=\frac{1}{N_t}\sum_{j=1}^{N_t}\left[\frac{(1/N_z)\sum_{i=1}^{N_z}C_L(z_i,t_j)C_L(z_i-l_k,t_j)}{(1-N_z)\sum_{i=1}^{N_z}C_L^2(z_i,t_j)}\right] \tag{4.4}$$

where $C_L(z_i, t_j)$ is taken to be the fluctuation of the original signal $C^*_L(z_i, t_j)$ from which its mean quantity is subtracted. The signal $C_L(z_i, t_j)$ is given by

$$C_L(z_i,t_j)=C_L^*(z_i,t_j)-\frac{1}{N_t}\sum_{n=1}^{N_t}C_L(z_i,t_n) \tag{4.5}$$

The shift l_k in Eq. (4.4) is prescribed to be

$$l_k=k\times l=k\times dz \text{ with } dz=l/N_z \text{ and } k=\left[0,1,2,\ldots,\frac{N_z}{2}\right] \tag{4.6}$$

The correlation length L_C is then computed by

$$L_C(t)=2\int_0^{\frac{L/D}{2}}R(l,t)dl \tag{4.7}$$

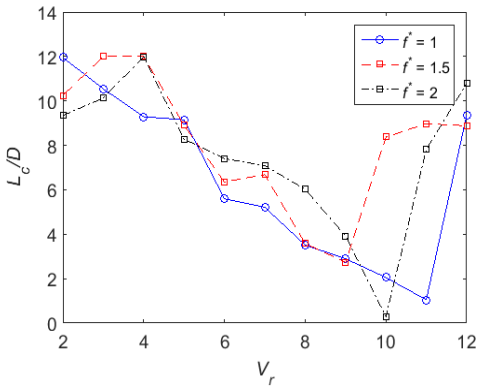

Fig. 4.13 Variation of the correlation lengths with the reduced velocity at different natural frequency ratios.

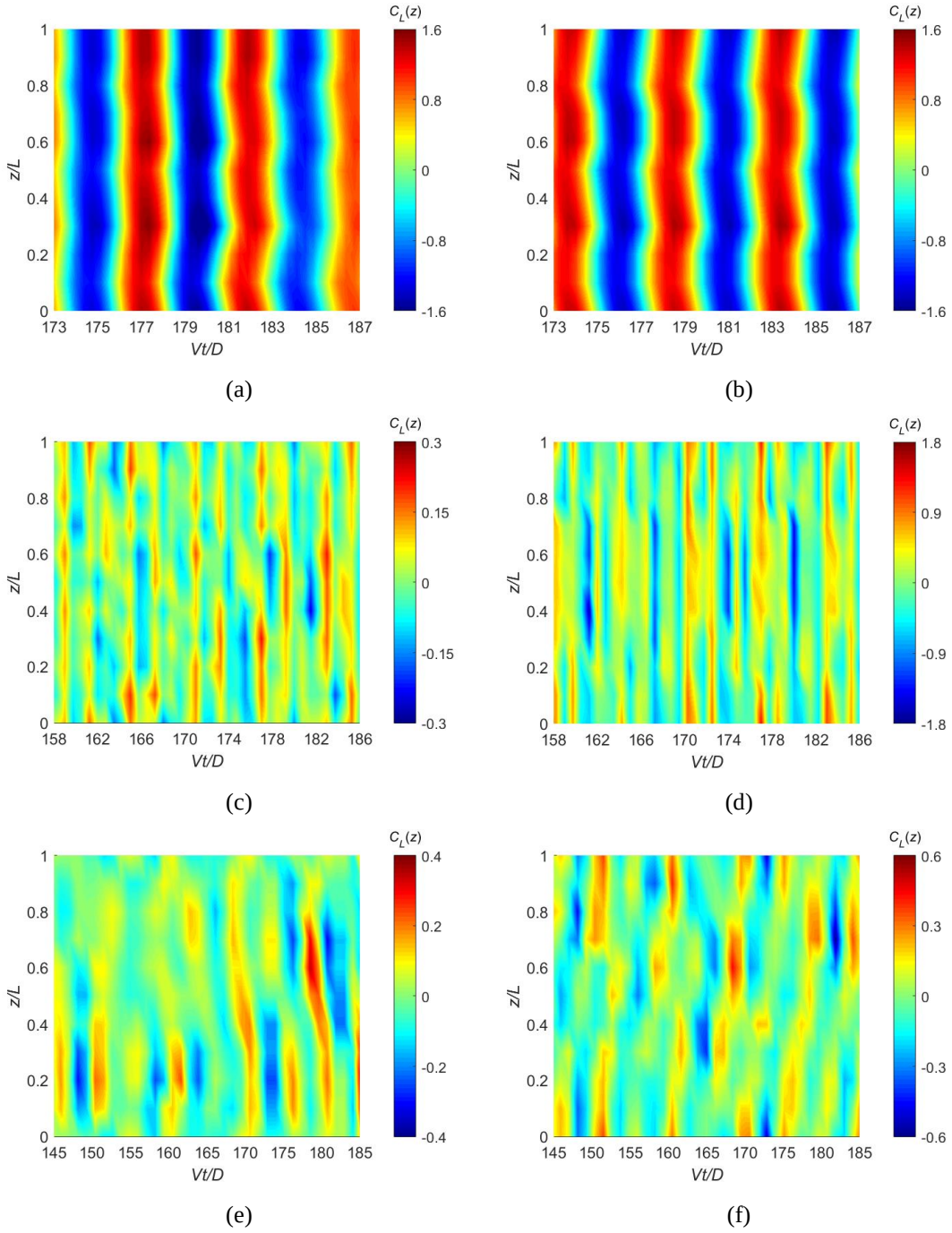

Fig. 4.14 Contours of the sectional lift coefficients: (a) V_r = 3 and f^* = 1, (b) V_r = 3 and f^* = 2, (c) V_r = 6 and f^* = 1, (d) V_r = 6 and f^* = 2, (e) V_r = 9 and f^* = 1 and (f) V_r = 9 and f^* = 2.

Fig. 4.13 shows the variation of the nondimensional correlation length (L_C/D) with V_r at different f^*. At f^* = 1, the maximum correlation length is witnessed at V_r = 2 while it shifts to V_r = 4 when f^* = 1.5 and 2. In general, the correlation lengths are very large for low reduced velocities in the pre-lock-in range which is an indication of the

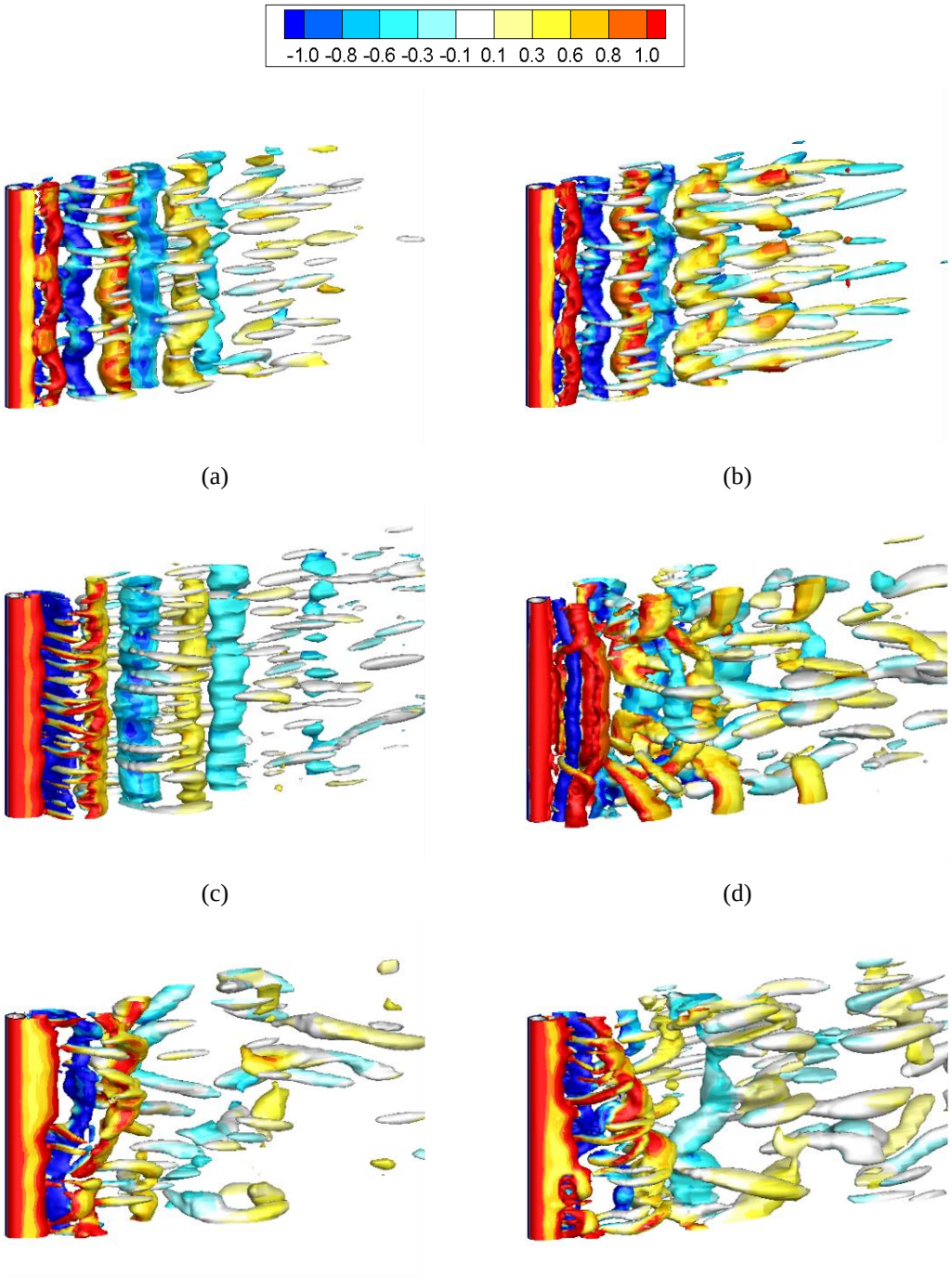

Fig. 4.15 Iso-surfaces of eigenvalue λ_2 = -0.1 with the contours of the spanwise vorticity ω_z on the iso-surfaces: (a) V_r = 3 and f^* = 1, (b) V_r = 3 and f^* = 2, (c) V_r = 6 and f^* = 1, (d) V_r = 6 and f^* = 2, (e) V_r = 9 and f^* = 1 and (f) V_r = 9 and f^* = 2.

strong two-dimensionality of the flow. There is a drop in the correlation as V_r increases and the correlation lengths reach their minimum values at reduced velocities close to the transition region between lock-in and post-lock-in ranges.

Finally, the correlation increases for higher reduced velocities in the post-lock-in range.

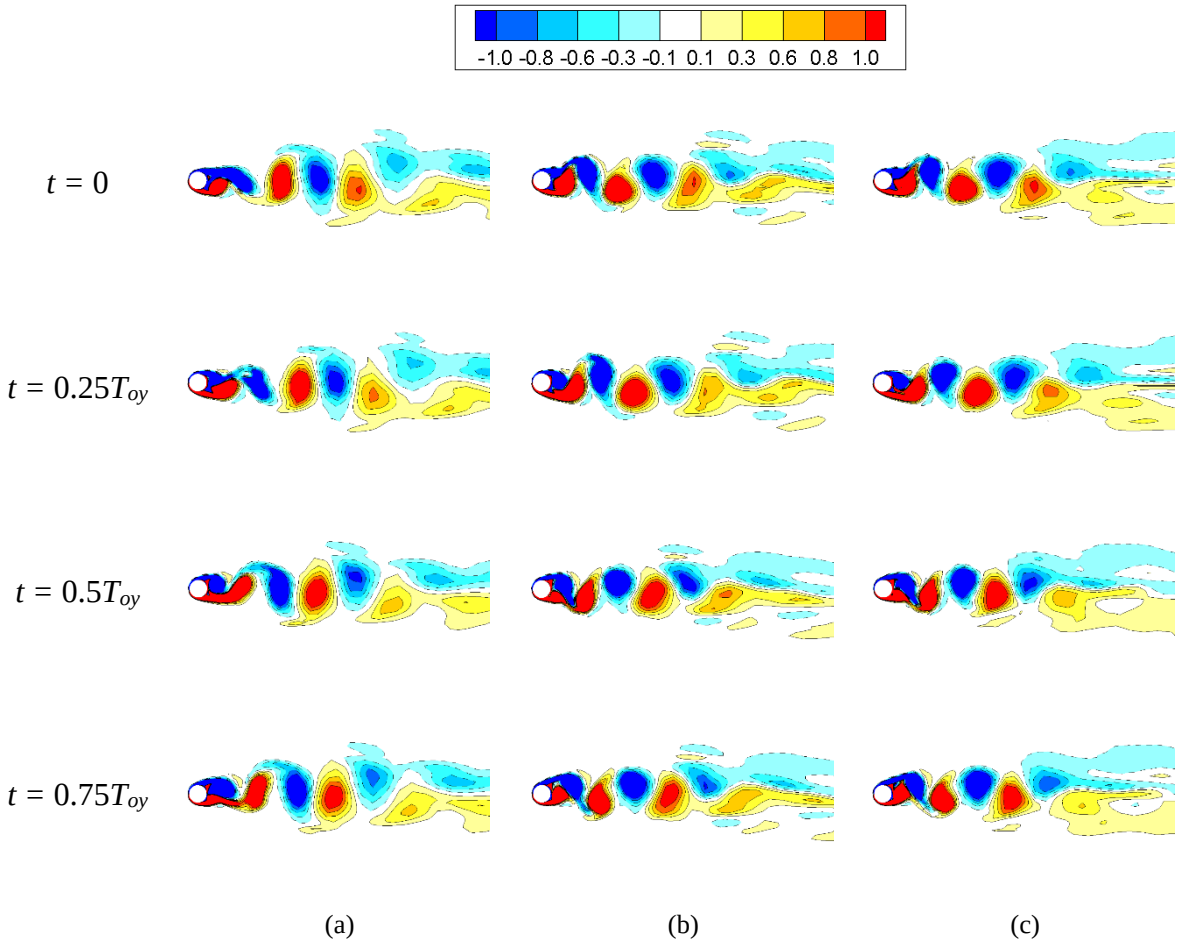

Fig. 4.16 Contours of spanwise vorticity ω_z at different instants of time in one cross-flow vibration cycle on three cross sections along the cylinder at V_r = 3 and f^* = 1: (a) z/L = 0.25, (b) z/L = 0.5 and (c) z/L = 0.75.

The variation of the lift coefficient along the span at V_r = 3, 6 and 9 for f^* = 1 and 2 is examined by plotting the contours of the sectional lift coefficient ($C_L(z) = F_y(z)/(0.5\rho V^2 D)$) on the $z - t$ plane. These three reduced velocities are selected in a way that V_r = 3 represents the cases with large correlation lengths. V_r = 6 is in proximity to the location where the maximum vibration amplitudes appear and V_r = 9 is near the region where the correlation lengths approach their minimum values. As for the two natural frequency ratios, f^* = 1 and 2 correspond to the most common case of 2DOF VIV and the scenario where perfect 2DOF resonance might occur,

respectively. Fig. 4.14 demonstrates that the lift distribution along the span is well organised at V_r = 3 for both f^* = 1 and 2 revealing the 2D feature of the flow at V_r = 3. When V_r increases to 6, the variation of the lift coefficient along the span grows stronger. The sectional lift coefficient signals at different spanwise locations suffer relative phase shifts with each other which consequently results in the variation of the phase differences between the sectional lift coefficients and the CF displacement along the cylinder. The decrease in the spanwise correlation can be attributed to the poor phasing between the forces and the displacement (Lucor *et al.*, 2003, 2005). With an increase in V_r to 9, the relative phase shifts among the sectional lift coefficient signals get more obvious leading to an even poorer correlation. The observation from the contours of $C_L(z)$ agrees with the conclusion drawn from the computed correlation lengths in Fig. 4.13.

4.2.7 Vortex Shedding

One of the objectives of this research is to study the effect of the natural frequency ratio on the vortex shedding of 2DOF VIV. The 3D vortex structures are defined using the λ_2 method proposed by Jeong and Hussain (1995) in which λ_2 is the second eigenvalue of the symmetric tensor $\mathbf{S}^2 + \mathbf{\Omega}^2$. Here, $\mathbf{S}$ and $\mathbf{\Omega}$ are the symmetric and antisymmetric parts of the velocity gradient tensor $\nabla\mathbf{u}$. Fig. 4.15 shows the iso-surfaces of λ_2 = -0.1 at V_r = 3, 6 and 9 for f^* = 1 and 2. The reasons for choosing the specific combinations of V_r and f^* are provided in Section 4.2.6. The spanwise vorticity defined as $\omega_z = \partial u_2/\partial x_1 - \partial u_1/\partial x_2$ is plotted on the iso-surfaces. It can be observed that the wake flow is entirely 3D. The wake in the lock-in range is wider than that in the non-lock-in range. Among the three reduced velocities considered for either frequency ratio, the widest wake is observed at V_r = 6 which is near the reduced velocity where the maximum vibration amplitude appears. The variation of the flow in the lock-in range is also stronger than that in the non-lock-in range. The vortices in the spanwise direction can be clearly identified at V_r = 3 for both frequency ratios. The clearly-identified spanwise vortices indicate the strong two-dimensionality of the flow at low reduced velocities. With the increases of V_r and f^*, the variation of the spanwise vortices becomes stronger but they can still be

identified at V_r = 6 and f^* = 1. However, it is hard to identify the spanwise vortices in the rest of the cases presented in Fig. 4.15. The changes in the spanwise vortices agree with the variation of the correlation lengths as shown in Fig. 4.13.

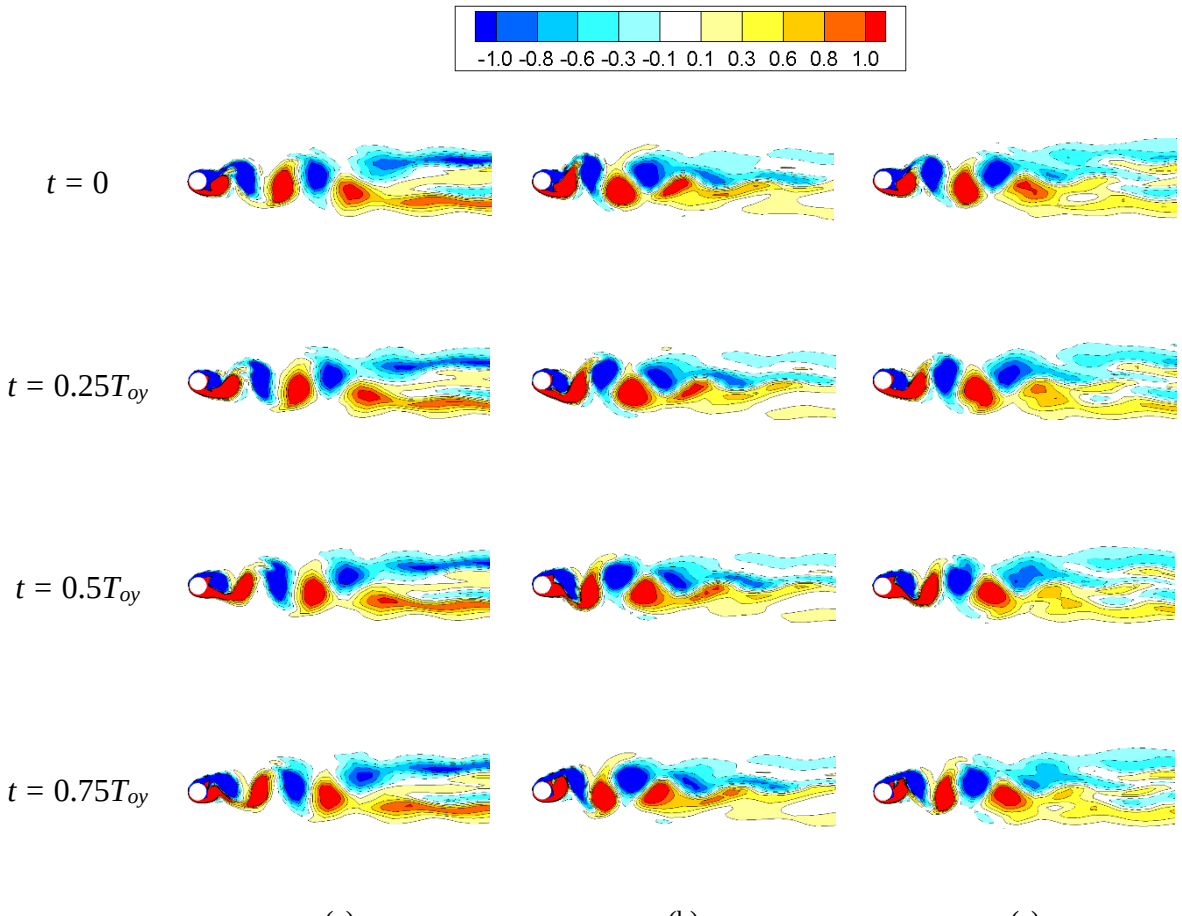

Fig. 4.17 Contours of spanwise vorticity ω_z at different instants of time in one cross-flow vibration cycle on three cross sections along the cylinder at V_r = 3 and f^* = 2: (a) z/L = 0.25, (b) z/L = 0.5 and (c) z/L = 0.75.

In order to further examine the variation of the flow in the spanwise direction of the cylinder, the contours of the spanwise vorticity at four instants of time in one cycle (t = 0, 0.25T_{oy}, 0.5T_{oy} and 0.75T_{oy} where T_{oy} is the period of the CF vibration) are plotted. The corresponding transverse displacements at different time instants are: y/D = 0, y/D = A_y/D, y/D = 0 and y/D = -A_y/D, respectively. At each time instant considered, spanwise vorticity contours on three cross sections (z/L = 0.25, 0.5 and 0.75) are presented to study the variation of the vortex shedding modes along the cylinder. The three cross sections are chosen in favour of those closer to the cylinder

ends to avoid the potential end effect of the periodic boundary condition employed on the two spanwise boundaries.

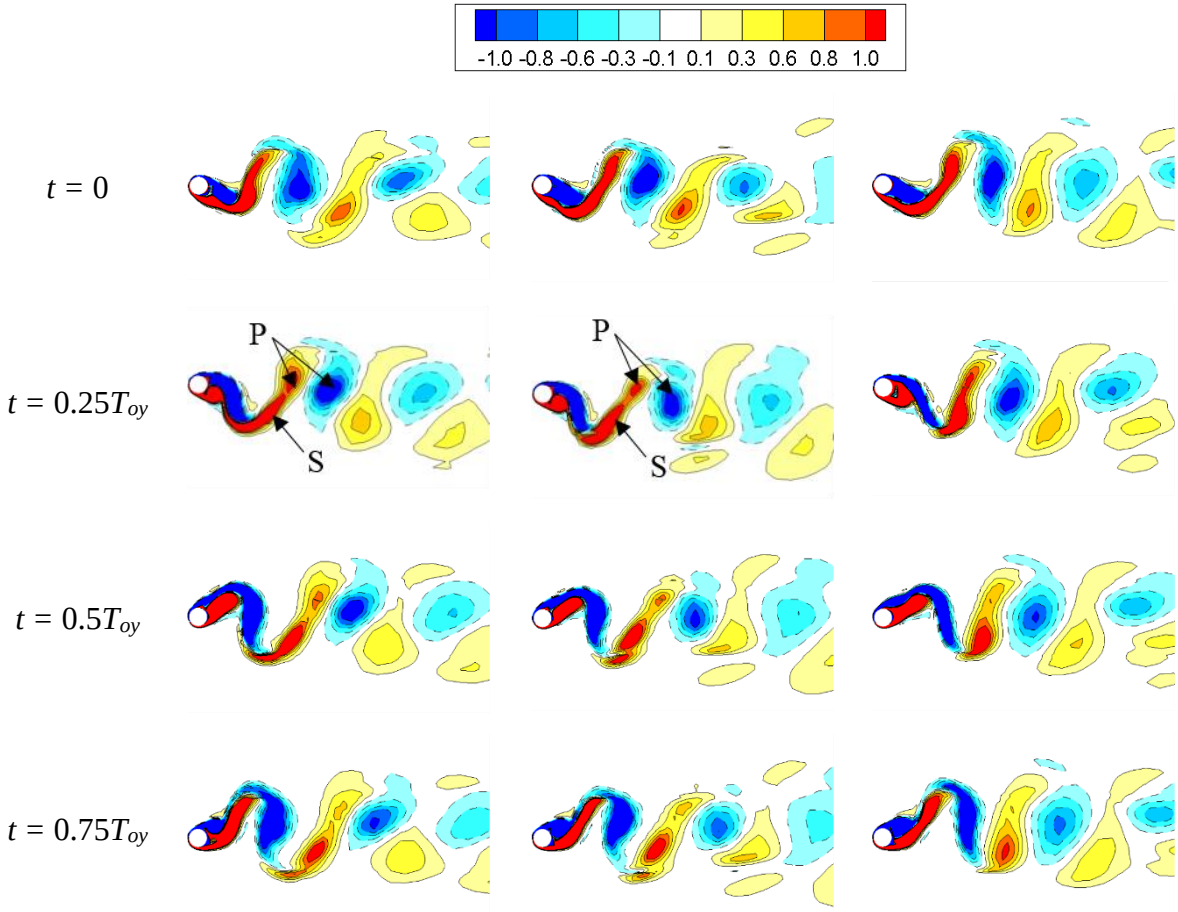

Fig. 4.18 Contours of spanwise vorticity ω_z at different instants of time in one cross-flow vibration cycle on three cross sections along the cylinder at V_r = 6 and f^* = 1: (a) z/L = 0.25, (b) z/L = 0.5 and (c) z/L = 0.75.

Fig. 4.16 and Fig. 4.17 are the spanwise vorticity contours in one cycle on the three cross sections when V_r = 3 for f^* = 1 and 2. By comparing the vorticity contours at different time instants on each cross section, it can be seen that the vortex shedding in both cases demonstrates a clear 2S pattern with two single vortices being formed in one cycle as described by Williamson and Roshko (1988). The vortex shedding flows on the different cross sections are nearly in phase with each other and the vortex shedding patterns are very similar indicating the strong two-dimensionality of the flow at low reduced velocities in the pre-lock-in range. Such vortex wake

structure leads to the well-organised distribution of the sectional lift force along the cylinder span at V_r = 3 as mentioned in Section 4.2.6.

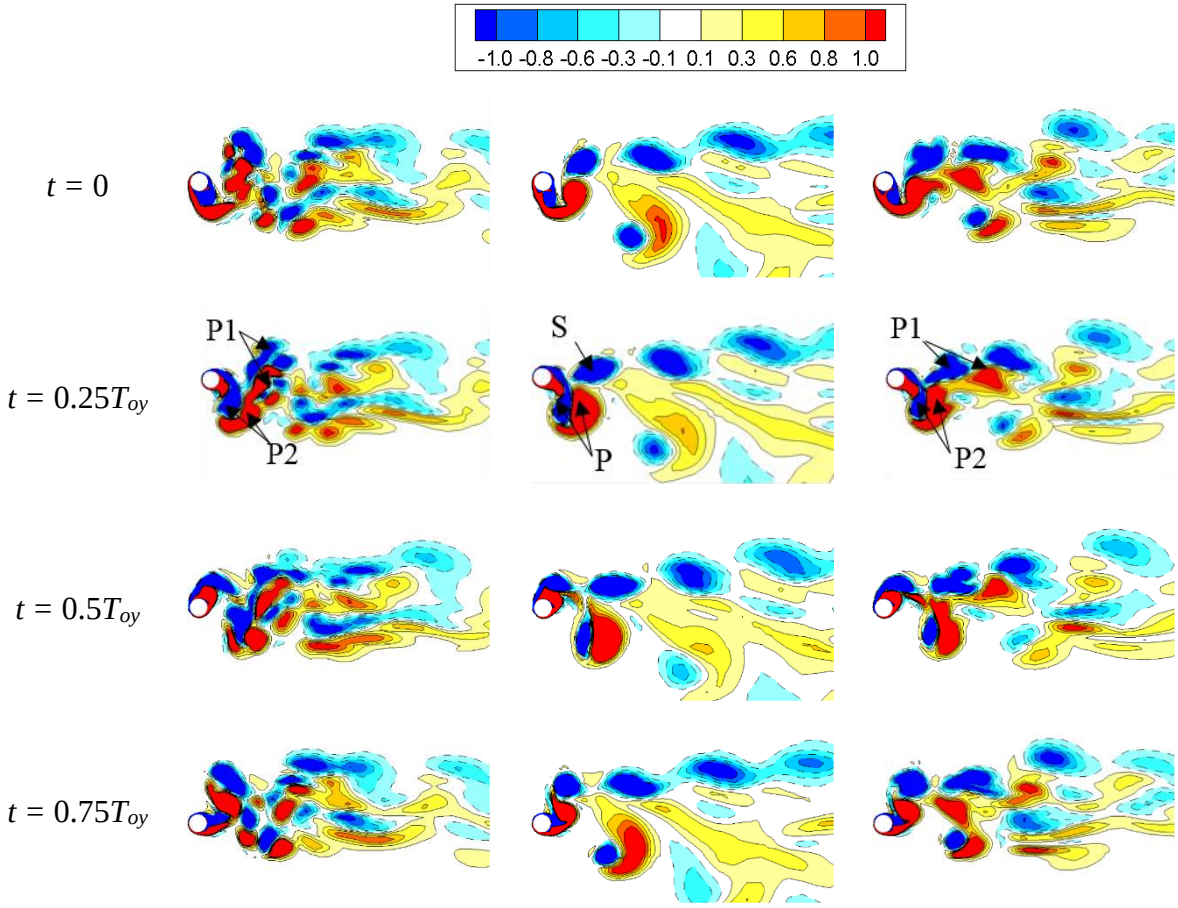

Fig. 4.19 Contours of spanwise vorticity ω_z at different instants of time in one cross-flow vibration cycle on three cross sections along the cylinder at V_r = 6 and f^* = 2: (a) z/L = 0.25, (b) z/L = 0.5 and (c) z/L = 0.75.

Fig. 4.18 shows the spanwise vorticity contours when V_r = 6 and f^* = 1. As discussed in Section 4.2.3, the orbital trajectory of the cylinder, in this case, is of an oblique figure-eight shape. Therefore, it is anticipated that the wake of the cylinder would display asymmetry. It can be seen from Fig. 4.18 that the vortex shedding at z/L = 0.25 and 0.5 exhibits a P + S mode where the cylinder sheds a single vortex and a vortex pair per cycle. The P + S mode was first identified in forced vibration experiments (Griffin and Ramberg, 1974; Zdero *et al.*, 1995) and recently has also been observed in the free vibration studies by Singh and Mittal (2005), Bao *et al.*

(2012) and Gedikli and Dahl (2014). In spite of the P + S mode at z/L = 0.25 and 0.5, a 2S mode appears at z/L = 0.75. The dominant asymmetric P + S vortex shedding at V_r = 6 and f^* = 1 is related to the additional $1f_{oy}$ frequency component in the IL motion and the oblique figure-eight trajectory.

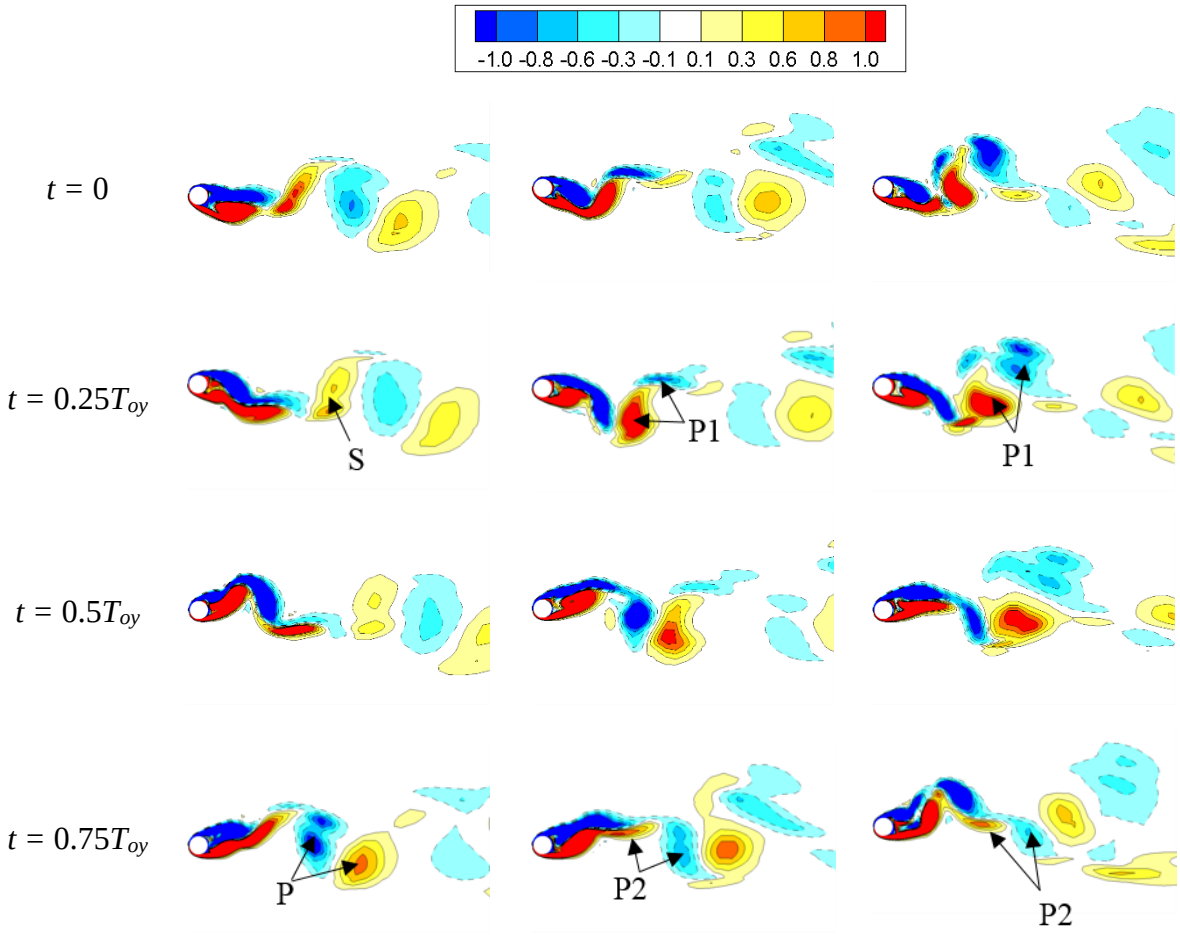

Fig. 4.20 Contours of spanwise vorticity ω_z at different instants of time in one cross-flow vibration cycle on three cross sections along the cylinder at V_r = 9 and f^* = 1: (a) z/L = 0.25, (b) z/L = 0.5 and (c) z/L = 0.75.

The vortex shedding along the cylinder at V_r = 6 and f^* = 2 is displayed in Fig. 4.19. The vortex shedding at z/L = 0.25 and 0.75 is in a 2P mode with two pairs of vortices being formed per cycle. Evidence of the 2P vortex shedding mode in free vibration was first exhibited by Brika and Laneville (1993, 1995). For the 2P mode at z/L = 0.25, the vortices are in pairs when they are shed from the cylinder. However, when

the vortex pairs progress downstream, they split into multiple small scale vortices. The present observation agrees qualitatively with the CFD results by Zhao *et al.* (2014). In contrast, the vortex pairs at z/L = 0.75 similar to the flow visualisation results in the experiment by Govardhan and Williamson (2000) are more stable. At z/L = 0.5, a P + S mode resembling that in Bao *et al.* (2012) is observed.

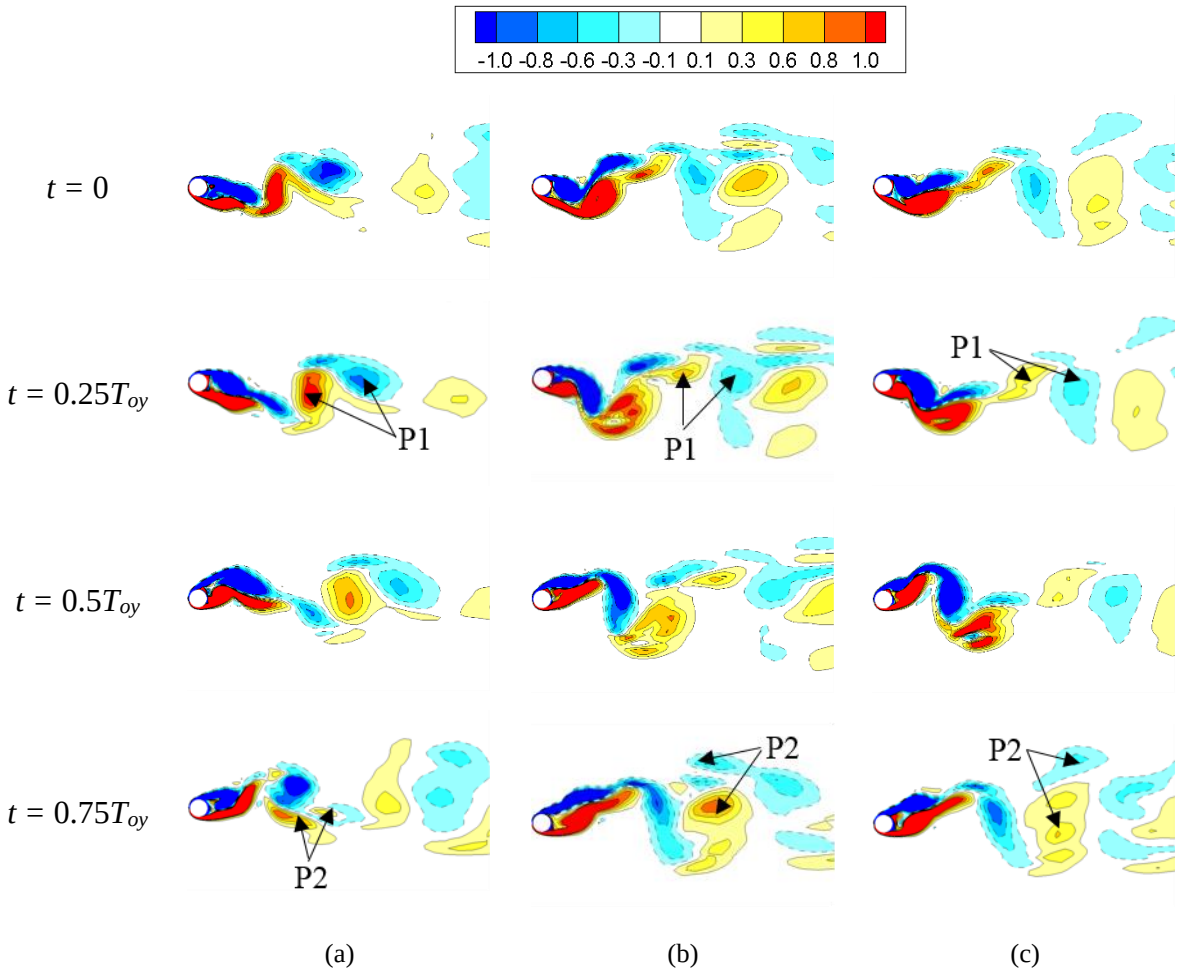

Fig. 4.21 Contours of spanwise vorticity ω_z at different instants of time in one cross-flow vibration cycle on three cross sections along the cylinder at V_r = 9 and f^* = 2: (a) z/L = 0.25, (b) z/L = 0.5 and (c) z/L = 0.75.

In the instance where V_r = 9 and f^* = 1 (Fig. 4.20), the vortex shedding at z/L = 0.25 exhibits a P + S mode and a 2P mode is observed at z/L = 0.5 and 0.75. As for V_r = 9 and f^* = 2 as shown in Fig. 4.21, although two pairs of vortices are shed in one cycle on the three cross sections, the vortex shedding patterns on the different cross sections are noticeably different.

The discussions above can be summarised as follows. When V_r = 3 at f^* = 1 and 2, the vortex shedding structures on the different cross sections are in phase and have similar 2S patterns, which leads to the well-organised distribution of the sectional lift force along the cylinder and relatively large correlation lengths. With the decrease of the spanwise correlation, variation of the vortex shedding patterns along the cylinder becomes obvious. This causes the relative phase shifts of the sectional lift coefficient signals at different spanwise locations as mentioned in Section 4.2.6 and consequently results in a poor phasing between the sectional lift forces and the CF displacement. According to Lucor *et al.* (2003, 2005), it is the poor phasing between the forces and the displacement that causes the decrease of the spanwise correlation. As for the dominant vortex shedding mode in the cases with poor spanwise correlation, it modifies from a P + S mode to a 2P mode when f^* increases from 1 to 2 at V_r = 6 and a 2P mode dominated vortex shedding is observed for both f^* = 1 and 2 at V_r = 9.

4.3 Concluding Remarks

The effect of the natural frequency ratio on two-degree-of-freedom vortex-induced vibration of an elastically mounted circular cylinder is numerically studied at Re = 500 using a three-dimensional computational fluid dynamics method. A low mass ratio m^* = 2 and zero structural damping are considered in the simulation. The reduced velocity ranges from 2 to 12 and the IL to CF natural frequency ratio varies from f^* = 1 – 2 with an increment of 0.5. Based on the qualitative and quantitative analyses of the numerical results, the findings of this study may be laid out as follows.

It is found that f^* has a significant impact on the response amplitudes of the cylinder. In the present study, the maximum vibration amplitude increases and shifts to a higher reduced velocity when f^* increases from 1 to 2. Where $m_x^* = m_y^*$, a single peak CF response is observed for f^* = 2. Dual resonance exists over a wide range of the natural frequency ratios with the oscillation frequency ratio being approximately

2 and most of the orbital trajectories having a figure-eight shape. The primary direction of the orbital trajectories in the lock-in range is counterclockwise. Clockwise orbits appear in the pre-lock-in range and the number of clockwise trajectories decreases as f^* increases.

C_{Dmean} and C_{Drms} experience evident increases as f^* approaches 2 while C_{Lrms} is not quite sensitive to f^*. A third harmonic component is observed in total lift coefficient in the lock-in range. It is also found that with the increase of f^*, the third harmonic component becomes larger. The large third harmonic forces are found to be related to the counterclockwise motion of the cylinder. At low V_r, the displacements and hydrodynamic forces exhibit beating features. In terms of the effective added mass coefficients, both C_{mx} and C_{my} decrease with the increase of V_r. As the variation of C_{mx} required to drive the oscillation frequency ratio to 2 is larger when f^* is distant from 2, the deviation in C_{mx} for different f^* is more obvious than that in C_{my}.

Large correlation lengths are observed for low V_r in the pre-lock-in range which indicates the 2D characteristics of the flow. The spanwise correlation experiences a decrease as V_r increases and reaches its minimum value at V_r near the transition region between the lock-in and post-lock-in ranges where the three-dimensionality of the flow is strongest. The decrease of the correlation length is due to the poor phasing between the forces and the displacement. After the trough, the spanwise correlation begins to increase with increases of V_r in the post-lock-in range.

The vortex shedding is also found to be related to f^*. It is revealed that the wake in the lock-in range is wider than that in the non-lock-in range. The variation of the spanwise vortices is weaker when the correlation length is large. With the decrease of the spanwise correlation, it becomes more difficult to identify the spanwise vortices. In the present study, three vortex shedding modes are observed, i.e., 2S, P + S and 2P modes. A 2S mode is observed at $V_r = 3$ for both $f^* = 1$ and 2. The vortex shedding structures on different spanwise cross sections are in phase with each other and the patterns are similar, which results in the strong correlation of the sectional lift coefficients at low V_r in the pre-lock-in range. At $V_r = 6$, variation of vortex shedding

modes along the cylinder is observed. When f^* = 1, the vortex shedding is dominated by a P + S mode with a 2S mode appearing in the upper part of the cylinder. The asymmetric nature of the P + S mode is associated with the additional $1f_{oy}$ frequency component in the in-line motion and the oblique figure-eight trajectory. The dominant vortex shedding mode switches to a 2P mode when f^* = 2 with a P + S mode being observed on the middle section of the cylinder. When V_r is further increased to 9, the dominant vortex shedding mode for both f^* = 1 and 2 is a 2P mode with a P + S mode being found in the lower part of the cylinder at f^* = 1. The variation of the sectional lift coefficients along the span is related to the variation of the vortex shedding flows.

The research in this chapter leads to the journal paper ‘Three-dimensional numerical simulation of two-degree-of-freedom VIV of a circular cylinder with varying natural frequency ratios at Re = 500’ published in the Journal of Fluids and Structures.

Chapter 5 Large Eddy Simulation of Vortex-Induced Vibration of a Vertical Riser in Uniform and Linearly Sheared Currents

"Turbulence is the most important unsolved problem of classical physics."

-Richard Feynman

Combined IL and CF VIV of a vertical riser in uniform and linearly sheared currents is studied using a fully 3D CFD approach. The model vertical riser tested at the MARINTEK by ExxonMobil is considered. The model riser has a length-to-diameter ratio L/D = 481.5 and a mass ratio m^* = 2.23. The structural damping is set to zero in the CFD simulation. A top tension T = 817 N is applied to the top end of the riser. The riser is pinned at both ends and free to move in both the IL (x) and CF (y) directions. A low flow velocity range is specially selected to cover the typical range where the IL fatigue damage is higher than the CF fatigue damage so that the importance of the IL fatigue damage can be addressed.

5.1 Problem Descriptions

5.1.1 Simulation Parameters

In the present study, two types of flow conditions are considered for VIV of a vertical riser, i.e., uniform flow and linearly sheared flow. The model vertical riser tested at the MARINTEK by ExxonMobil (Lehn, 2003) is considered. The main parameters of the model riser are summarised in Table 5.1. The model riser has a length-to-diameter ratio L/D = 481.5 and a mass ratio m^* = 2.23. The structural damping in this study is set to be zero. The physical configuration of a vertical riser subject to VIV is displayed in Fig. 5.1(a). The flow direction is parallel to the global x-axis. A top tension T = 817 N is applied to the top end of the riser. The riser is pinned at both ends and free to move in the IL and CF directions. Simulations are performed for four different test cases in the experiment, namely # 1103, # 1105, #

1201 and # 1205 with the same Reynolds numbers as in the experiments up to Re = 7381. The incoming flow velocity and other parameters of the four cases are summarised in Table 5.2 and the corresponding velocity profiles are displayed in Fig. 5.1(b). Detailed descriptions of the flow velocity profiles of the four cases are given as follows.

Table 5.1 Properties of the vertical riser model.

Properties	Values	SI units
L	9.63	m
D_o	20	mm
t_w	0.45	mm
E	1.025×10^{11}	N/m^2
T	817	N
m^*	2.23	-
L/D	481.5	-

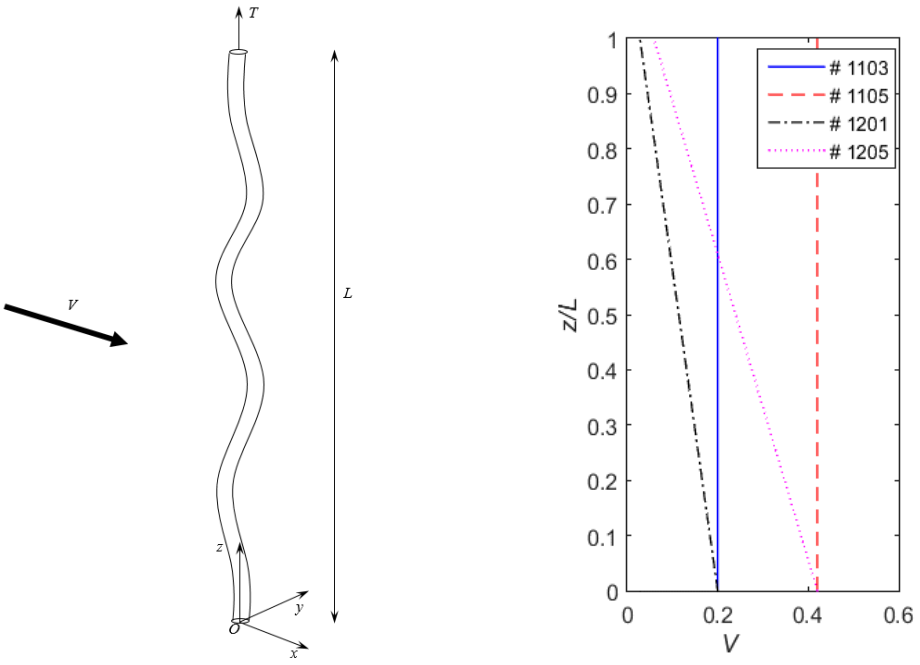

(a) (b)

Fig. 5.1 (a) Sketch of physical configurations and (b) Uniform and linearly sheared incoming flow velocity profiles.

The case # 1103 and the case # 1105 have uniform velocity profiles with V = 0.2 m/s and 0.42 m/s, respectively. Whereas the currents in the case # 1201 and the case # 1205 are linearly sheared with the maximum velocities at the bottom end of the riser (z = 0) being V_{max} = 0.2 m/s and V_{max} = 0.42 m/s, respectively. In both cases, the minimum velocity at the top end of the riser ($z = L$) $V_{min} = 0.14V_{max}$.

Table 5.2 Incoming flow velocity parameters of different cases.

Case #	Flow conditions	V_{max} (m/s)	V_{min}/V_{max}
1103	Uniform	0.2	1
1105	Uniform	0.42	1
1201	Linearly Sheared	0.2	0.14
1205	Linearly Sheared	0.42	0.14

Table 5.3 Eigenfrequencies for the vertical riser model.

Mode	$f_{n,\,string}$ (Hz)	$f_{n,\,beam}$ (Hz)	Theoretical Value (Hz)	FEA (Hz)	Error
1	1.77	0.24	1.79	1.7904	0.022%
2	3.55	0.94	3.67	3.6725	0.068%
3	5.32	2.12	5.73	5.7309	0.015%
4	7.1	3.77	8.04	8.0373	0.034%
5	8.87	5.89	10.65	10.649	0.0094%
6	10.64	8.48	13.62	13.61	0.073%
7	12.42	11.55	16.96	16.952	0.047%
8	14.2	15.08	20.71	20.698	0.058%

To estimate the eigenfrequencies for a vertical riser, it could be simplified as a tensioned beam with moment-free supports at both ends (Lie and Kaasen, 2006). The n^{th} eigenfrequency for the tensioned beam, $f_{n,\,t\text{-}beam}$ can be expressed in terms of the eigenfrequencies for a tensioned string and a nontensioned beam (Weaver *et al.*, 1974).

$$f_{n,t-beam} = \sqrt{f_{n,string}^2 + f_{n,beam}^2} \tag{5.1}$$

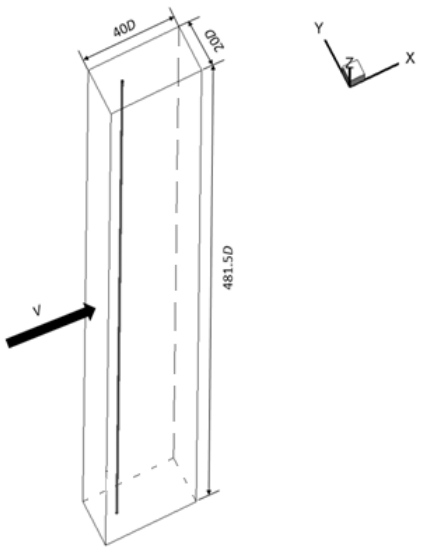

(a)

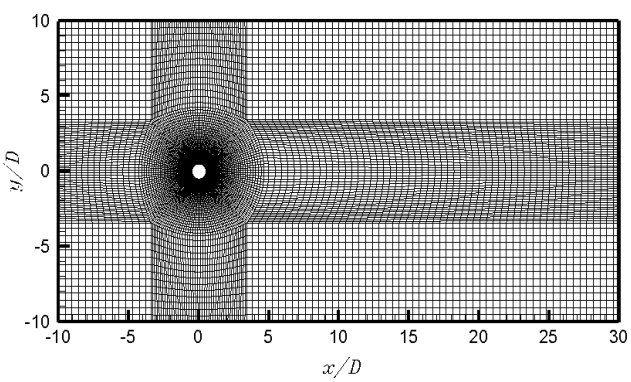

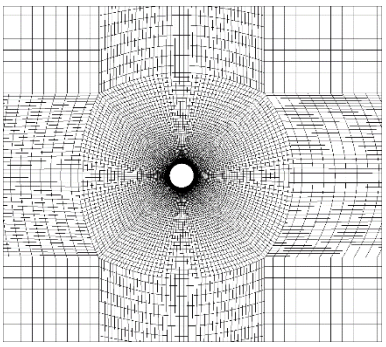

(b) (c)

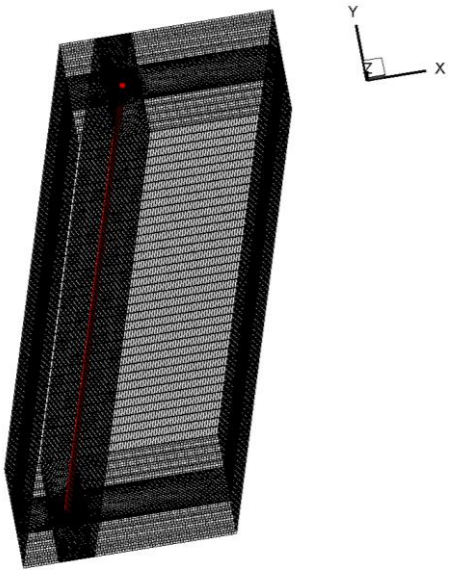

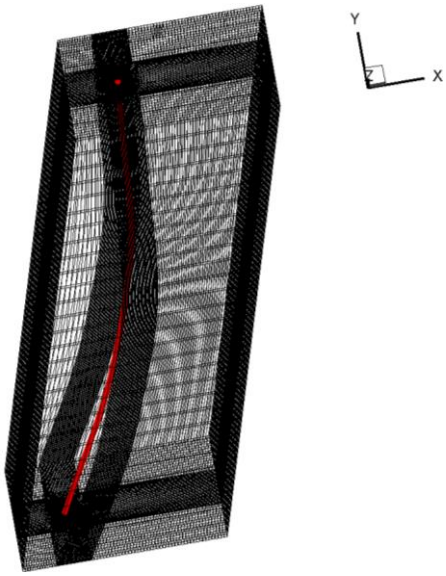

(d) (e)

Fig. 5.2 (a) Computational domain, (b) computational mesh in the *xy*-plane, (c) mesh around the cylinder, (d) initial mesh and (e) mesh with riser deflection.

where n is the mode number, $f_{n,string} = \frac{n}{2}\sqrt{\frac{T}{\rho_L L^2}}$ and $f_{n,beam} = \frac{n^2\pi}{2}\sqrt{\frac{EI}{\rho_L L^4}}$ are the eigenfrequencies for a tensioned string without bending stiffness and a nontensioned beam of equal length L and mass per unit length ρ_L.

Table 5.4 Eigenfrequencies of the vertical riser model: measured versus FEA results.

Mode	Measured (Hz)	FEA (Hz)	Error
1st Mode CF	1.9	1.79	6.10%
2nd Mode CF	3.9	3.67	6.30%
3rd Mode CF	6.1	5.73	6.50%
1st Mode IL	2.06	1.79	15.10%
2nd Mode IL	3.95	3.67	7.60%
3rd Mode IL	6.16	5.73	7.50%

The eigenfrequencies of the foremost eight modes are calculated with Eq. (5.1) along with a modal analysis carried out using ANSYS. The results are tabulated in Table 5.3. The eigenfrequencies from the modal analysis agree well with the corresponding theoretical values with all errors less than 0.1%. Table 5.4 shows the comparison of the eigenfrequencies of the first three modes in the IL and CF directions between the measured data in the experiment and the modal analysis results. It can be interpreted from the table that the measured IL and CF eigenfrequencies for each vibration mode are not identical. In contrast, due to inevitable simplifications of the FEA model, it is not able to replicate the unequal eigenfrequencies in the IL and CF directions and the discrepancies between the measured data and the modal analysis results are much larger than those between the theoretical values and modal analysis results as summarised in Table 5.3.

5.1.2 Fluid Domain and Boundary Conditions

Fig. 5.2(a) shows the computational domain for the CFD simulation of VIV of a vertical riser. The origin of the Cartesian coordinate system is located at the centre of the bottom end of the riser. The length of the domain is 40D with the riser being located at 10D downstream the inlet boundary. The width of the domain in the

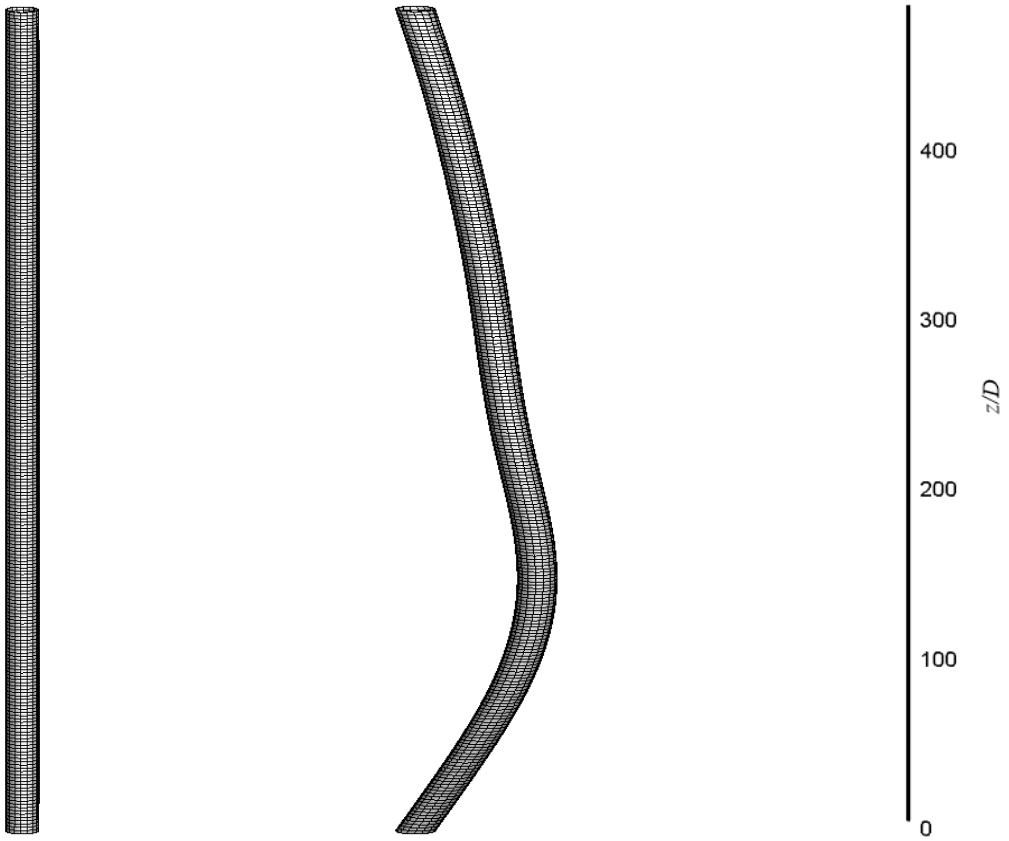

(a) (b)

Fig. 5.3 FEA mesh: (a) initial mesh and (b) mesh with riser deflection.

transverse direction (*y*-direction) is 20*D* and the length of the riser is 481.5*D*. The computational mesh in the *xy*-plane and a zoom-in view of the mesh around the cylinder are shown in Fig. 5.2(b) and (c), respectively. There are 180 nodes along the circumference of the riser and the minimum mesh size next to the riser surface in the radial direction is 0.001*D*. The nondimensional mesh size next to the riser surface is found to be $y^+ < 1$, where y^+ is defined as $y^+ = u_f y/v$ with u_f being the friction velocity and y being the distance to the nearest wall. The riser starts with a straight configuration (see Fig. 5.2(d)) and it deflects towards the current downstream after it is exposed to the different current profiles until its internal restoring force is sufficiently large to overcome the drag forces as shown in Fig. 5.2(e). The boundary conditions for the governing equations are as follows. The surface of the cylinder is assumed to be smooth, where no-slip boundary condition is employed. Apart from the no-slip boundary condition, the cylinder surface is also regarded as a fluid-solid

interface where the coupling data, i.e., forces and displacements are transferred. The inlet velocity boundary conditions are set to be the same as the freestream velocity. At the outflow boundary, the gradients of the fluid velocity in the streamwise direction are set to zero and the pressure at the outflow boundary is given a reference value of zero. On the two spanwise and the two transverse boundaries, the velocity in the direction normal to the boundary is zero.

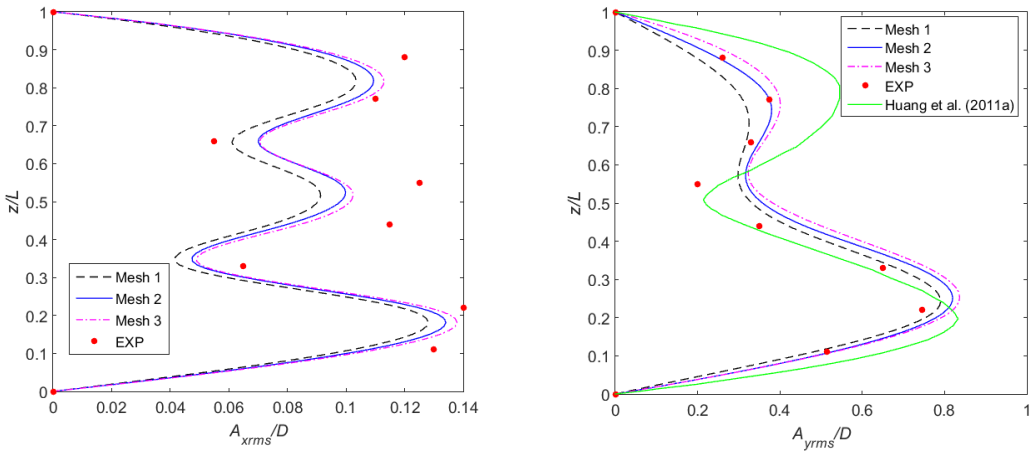

(a) (b)

Fig. 5.4 Comparison of the rms amplitudes between different mesh systems with published data: (a) IL rms amplitudes and (b) CF rms amplitudes.

5.1.3 Solid Domain and Boundary Conditions

Fig. 5.3 shows the computational mesh for the finite element analysis (FEA) of the present FSI simulation. The scale of the FEA model has been modified in order to clearly view the deflection of the model. Fig. 5.3(a) is the initial FEA mesh without riser deflection and Fig. 5.3(b) is the FEA mesh with riser deflection. A 3D 20-node solid element which exhibits quadratic displacement behaviour is used for the discretisation of the finite element model. The spanwise direction of the riser finite element model is discretised using 250 segments, which is a typical resolution for riser global dynamic analysis (Huang *et al.*, 2009). A top tension T = 817 N is applied to the top end of the riser. Both the top and bottom ends of the riser are pinned with zero rotational stiffness. The outer surface of the FEA model is also set to be a fluid-solid interface for data transfer.

Table 5.5 Mesh Dependency test results.

	N_{node} (M)	$\Delta r/D$	N_c	N_z	A_{xrm}/D	A_{yrm}/D
Mesh 1	0.626	0.001	180	30	0.118	0.781
Mesh 2	1.043	0.001	180	50	0.125	0.805
Mesh 3	2.087	0.001	180	100	0.128	0.823
EXP	-	-	-	-	0.14	0.745
Huang et al. (2011a)	1.480	??	182	50	??	0.833

5.1.4 Mesh Dependency Study

A multiblock structured mesh is used in the present CFD simulation. The meshing strategy is that a fine mesh is used in the *xy*-plane and a relatively coarse mesh is used in the spanwise direction. By using this strategy, it is possible to obtain reasonable results at the cost of sacrificing the resolution of small scale axial flow features. In order to ensure that the numerical results are independent of the grid size, a mesh dependency test is carried out. Three different meshes are used to simulate the case # 1105 and the results are compared with the experimental data by Lehn (2003) and the numerical results of Huang *et al.* (2011a). Table 5.5 shows the mesh characteristics, the maximum IL rms amplitude (A_{xrm}/D) and the maximum CF rms amplitude (A_{yrm}/D) computed using the three mesh systems. Comparing with the experimental data, A_{xrm}/D is slightly underpredicted while A_{yrm}/D is slightly overpredicted using the three meshes. The maximum difference of 5.93% occurs in the value of A_{xrm}/D between Mesh 1 and Mesh 2 whereas the difference between Mesh 2 and Mesh 3 reduces to only 2.4%. In the meanwhile, the differences in the value of A_{yrm}/D between Mesh 1 and Mesh 2 and between Mesh 2 and Mesh 3 are 3.07% and 2.24%, respectively. It can be concluded that the difference in the results predicted by Mesh 2 and Mesh 3 is within the acceptable range. The variation of rms amplitudes along the riser span in the IL and CF directions is displayed in Fig. 5.4. The IL and CF rms amplitudes and vibration modes predicted by the three meshes are quite similar and the maximum CF rms amplitudes predicted by Mesh 2 and Mesh 3 are in agreement with the numerical results of Huang *et al.* (2011a) with the

CF responses predicted by the two meshes showing better comparison with the experimental data in the upper part of the riser ($z/L > 0.6$) than the results of Huang *et al.* (2011a). Based on the discussions above and also taking into account the computational efforts, the simulations in this study are conducted with Mesh 2. As the present FEA mesh is able to predict the riser response with reasonable accuracy, the FEA mesh dependency study is not discussed in this study.

Table 5.6 Comparison of maximum rms amplitudes between different time-step sizes and experimental data.

	A_{xrm}/D	A_{yrm}/D
0.005	0.121	0.838
0.002	0.125	0.805
0.001	0.127	0.789
EXP	0.14	0.745

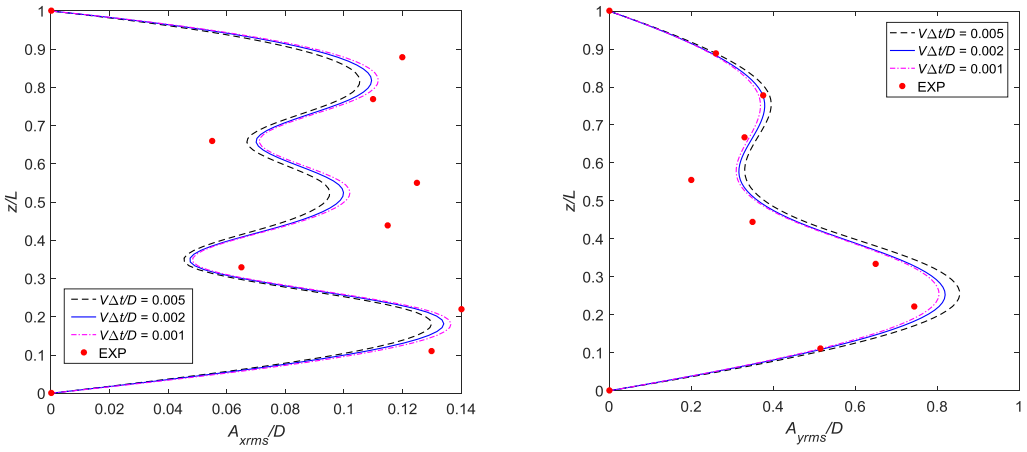

(a) (b)

Fig. 5.5 Comparison of rms amplitudes between different time-step sizes and experimental data: (a) IL rms amplitudes and (b) CF rms amplitudes.

5.1.5 Time-Step Size Dependency Test

In order to evaluate the dependency of the numerical results on the time-step size, a time-step size dependency test is performed with Mesh 2. The same case used in the mesh dependency test is considered. Three nondimensional time-step sizes are used

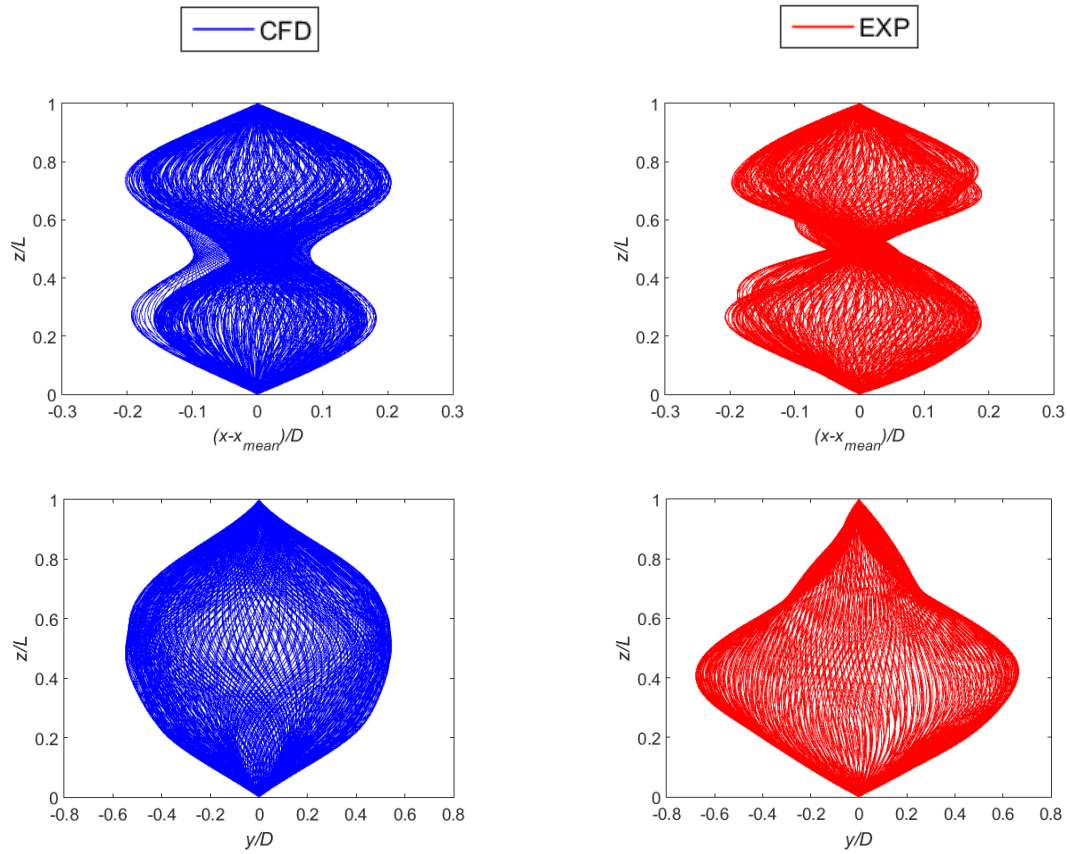

(a)

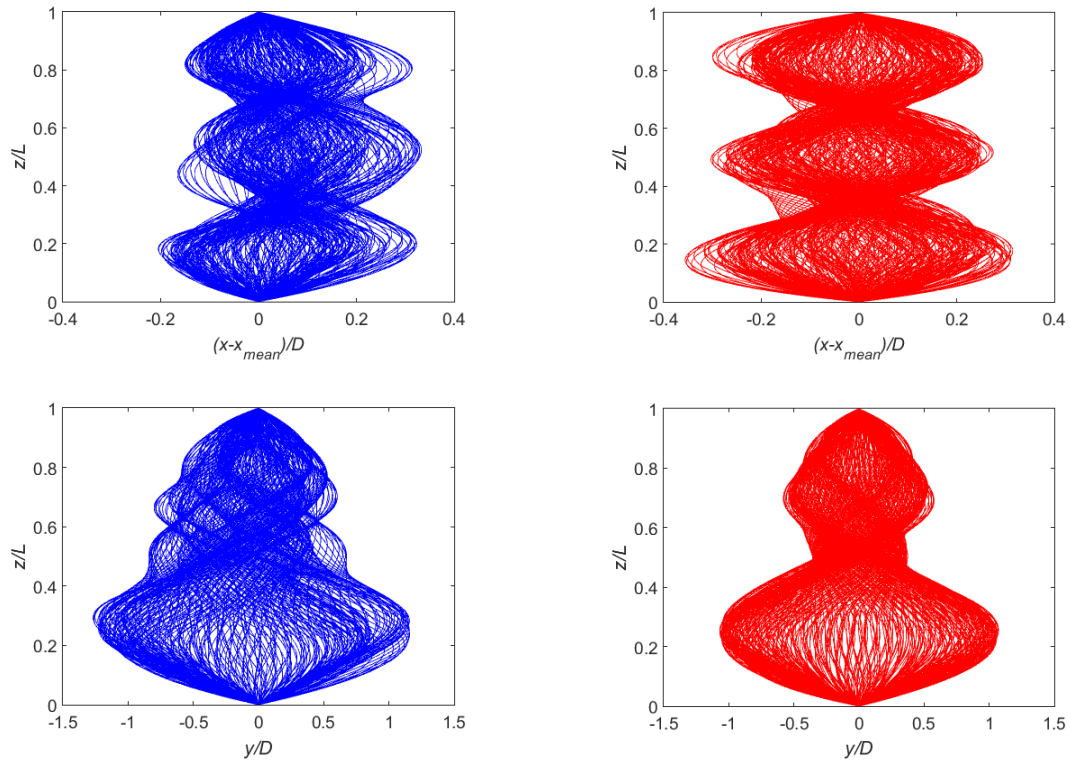

(b)

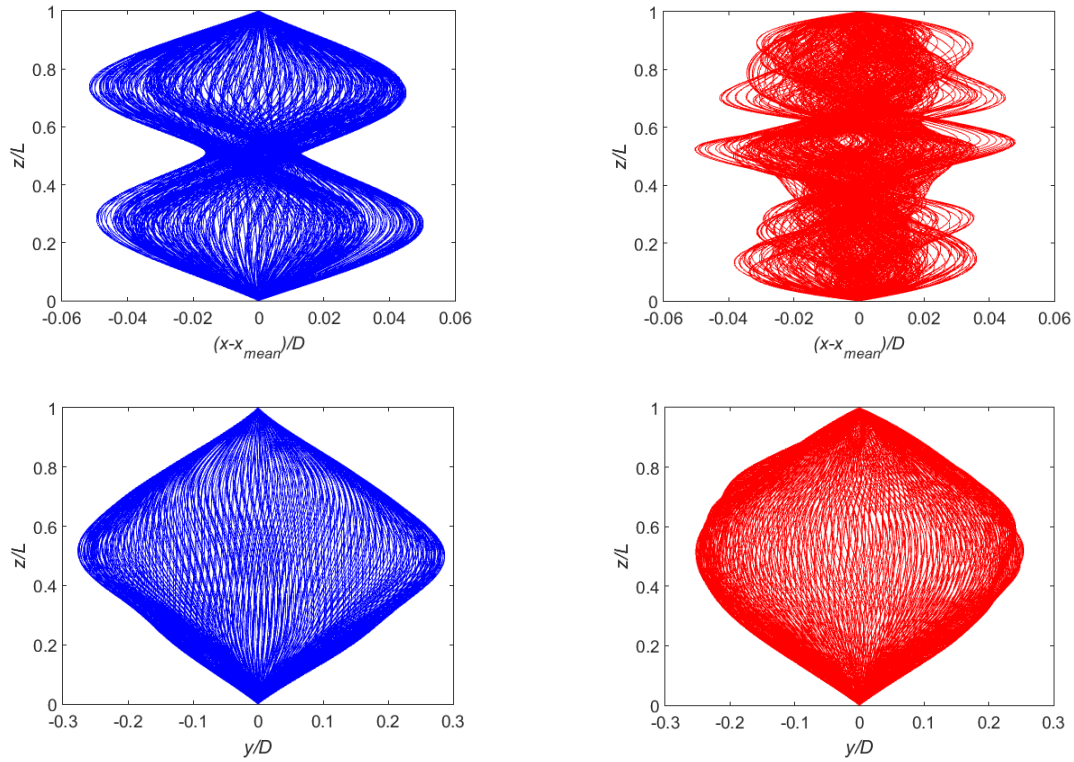

(c)

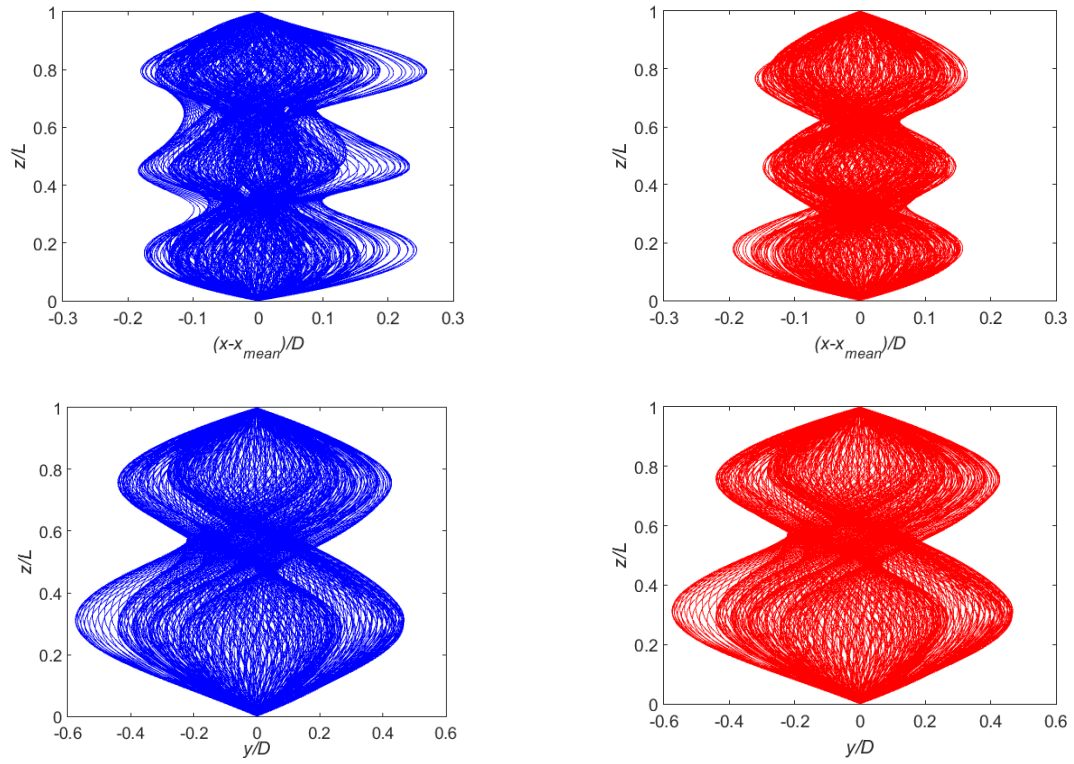

(d)

Fig. 5.6 Comparison of the riser response envelopes: (a) # 1103, (b) # 1105, (c) # 1201 and (d) # 1205.

herein, i.e., $V\Delta t/D$ = 0.005, 0.002 and 0.001. A_{xrm}/D and A_{yrm}/D predicted with the three nondimensional time-step sizes are provided in Table 5.6. According to the results, a maximum difference of 4.1% is observed between $V\Delta t/D$ = 0.005 and 0.002. The maximum difference between $V\Delta t/D$ = 0.002 and 0.001 reduces to approximately 2.03%. Fig. 5.5 illustrates the variation of rms amplitudes along the riser span in the IL and CF directions computed by different nondimensional time-step sizes. The three nondimensional time-step sizes predict similar IL and CF rms amplitudes and vibration modes with almost negligible difference in the results between $V\Delta t/D$ = 0.002 and 0.001. In the consideration of computational efforts, $V\Delta t/D$ = 0.002 is used in the present study.

5.2 Results and Discussions

Numerical simulations are performed for VIV of a vertical riser in uniform and linearly sheared currents. The velocity profiles considered are uniform velocities V = 0.2 m/s and 0.42 m/s and linearly sheared velocity profiles which can be described as $V_{profile} = (1 - 0.86z/L)V_{\max}$ where $V_{\max}$ = 0.2 m/s and 0.42 m/s. Both the IL and CF VIV results are compared with the experimental data by Lehn (2003).

5.2.1 Riser Dynamic Responses

Fig. 5.6 shows the comparison of the envelopes of the IL and CF displacements between the present simulation and the experiment. It is clear that the present results are in good agreement with the experimental data in terms of the dominant modes. In the case # 1103, the IL and CF vibrations are dominated by the second mode and the first mode, respectively. When the uniform flow velocity increases to V = 0.42 m/s, the dominant modes in the IL and CF directions change to the third mode and the second mode, respectively.

Similar to the uniform flow conditions, the dominant modes in the IL and CF directions in the two linearly sheared flow cases also change with the maximum flow velocity.

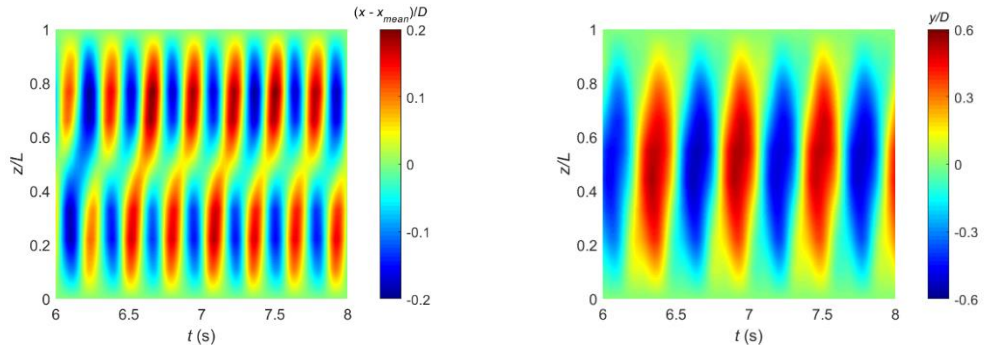

(a)

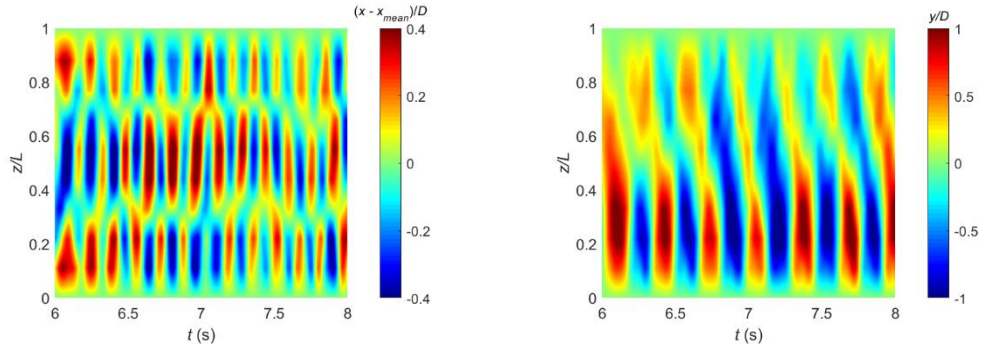

(b)

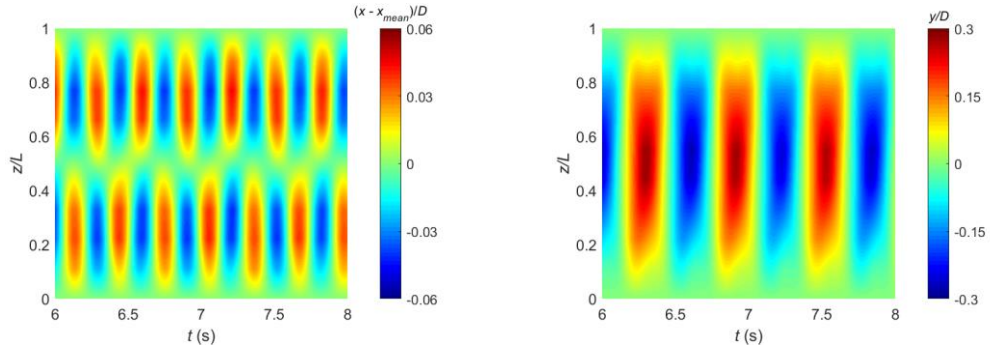

(c)

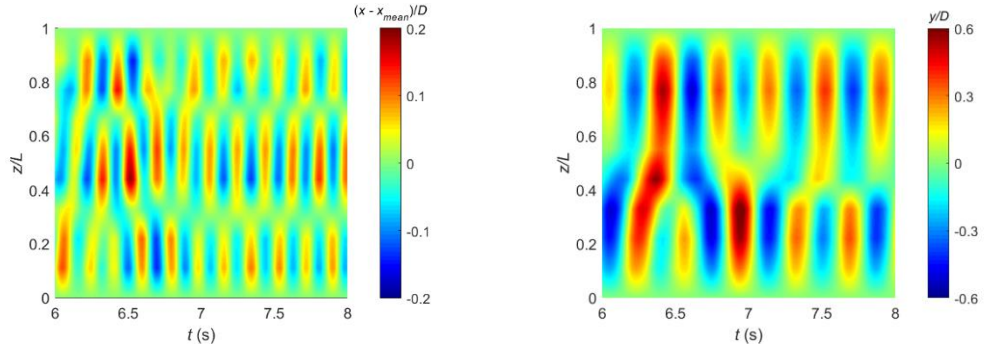

(d)

Fig. 5.7 The IL and CF motion evolution responses along the riser: (a) # 1103, (b) # 1105, (c) # 1201 and (d) # 1205.

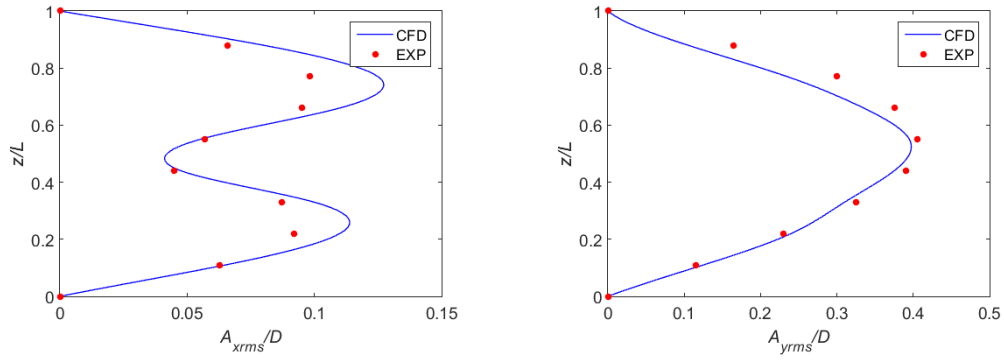

(a)

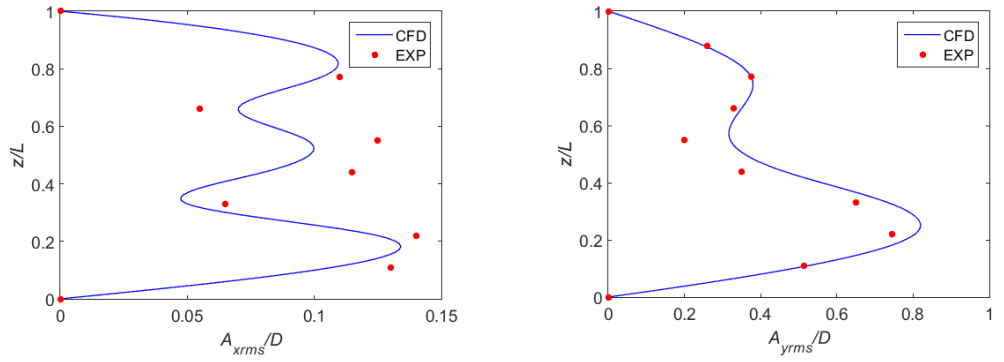

(b)

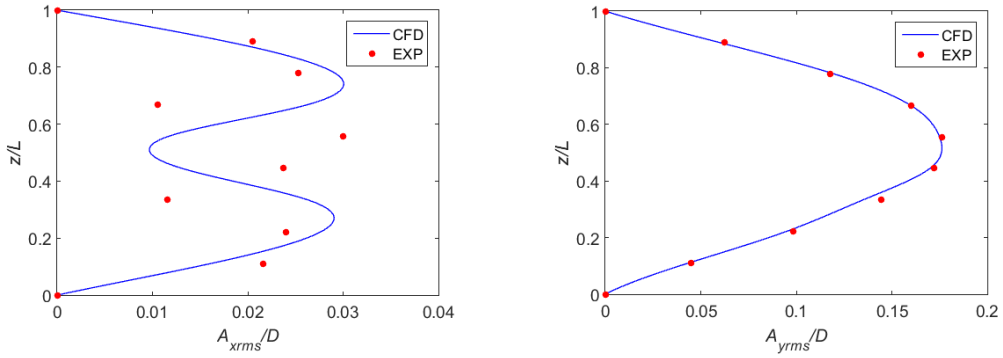

(c)

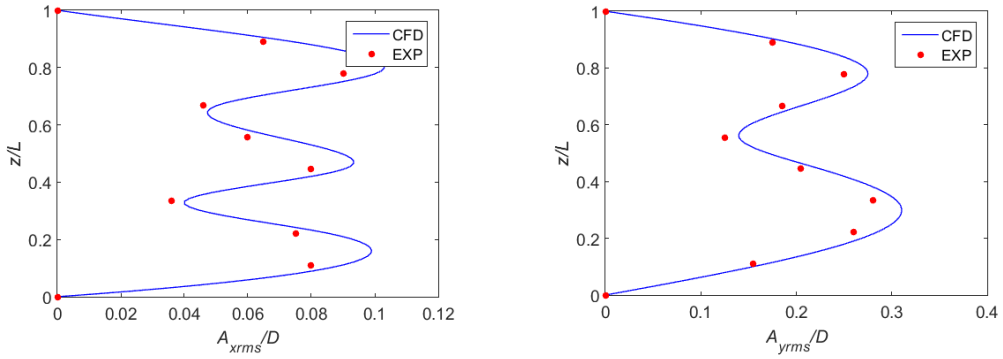

(d)

Fig. 5.8 Comparison of the rms amplitudes: (a) # 1103, (b) # 1105, (c) # 1201 and (d) # 1205.

In the present simulation, the variation of the dominant modes in the two linearly sheared flow cases is the same as that in the two uniform flow cases, i.e., the second mode and the first mode in the IL and CF directions for V_{max} = 0.2 m/s transfer into the third mode and the second mode when V_{max} increases to 0.42 m/s.

One discrepancy is observed in the IL dominant mode in the case # 1201. The present numerical simulation predicts a second mode, whereas the dominant mode is the third mode in the experiment. The reasons for this discrepancy are given as follows.

As an approximation, the IL response frequency may be estimated to be twice the CF response frequency. This implies that the IL mode number is twice the CF mode number for a tensioned string, whereas for a nontensioned beam it is lower, due to the quadratic relationship between n and frequency (Lie and Kaasen, 2006). According to Lehn (2003), the natural frequency of the riser is dominated by tension if $T \geq 4\pi^2 n^2 EI/L^2$. For the case # 1201 we discussed herein, the tension of the riser T = 817 N is larger than $4\pi^2 n^2 EI/L^2$ for n = 1, 2, and 3, therefore the natural frequencies of the first three modes are dominated by tension, which is also reflected in the modal analysis results in Table 5.3. Thus, in the FSI simulation, the behaviour of the riser would be similar to a tensioned string when it vibrates in low mode numbers ($n \leq 3$) with the IL dominant mode number being twice that in the CF direction. However, as shown in Table 5.4, there are some discrepancies between the measured eigenfrequencies and the modal analysis results. These discrepancies cause the difference in the IL oscillation frequency and hence the IL dominant mode between the present numerical results and the experimental data. Moreover, as shown in Fig. 5.8(c), the IL vibration amplitudes of the riser in the case # 1201 are so small that the computed and the measured data may not be reliable, which can also contribute to the discrepancy in the IL dominant mode between the numerical simulation and the experimental test.

The IL and CF motion evolution responses along the riser predicted by the present FSI simulation are analysed in an effort to understand the riser dynamics. As shown in Fig. 5.7, the variation of the dominant mode shapes with the flow conditions agrees with the observations from Fig. 5.6. Under the uniform flow condition, the IL dominant mode changes from the second to the third mode and the CF dominant mode shifts from the first mode to the second mode when V increases from 0.2 m/s to 0.42 m/s. The variation of the dominant modes in the two linearly sheared flow cases is the same as that in the two uniform flow cases when V_{max} increases from 0.2 m/s to 0.42 m/s. In most of the cases, the vibration of the riser exhibits a distinct standing wave response indicated by definite nodes and antinodes. An exception is observed for the case # 1105 where the CF vibration demonstrates a travelling wave response.

5.2.2 Root Mean Square Amplitudes

The rms amplitudes in the IL and CF directions (A_{xrms}/D and A_{yrms}/D) are compared with the experimental data as shown in Fig. 5.8. The experimental data are plotted in dots for easy identification. In the case # 1103, the maximum IL rms amplitude is found near the top end of the riser with its value $A_{xrm}/D \approx 0.13$ being overpredicted in the present simulation. The numerical results in the CF direction are in good agreement with the experimental data. The maximum CF rms amplitude is $A_{yrm}/D \approx 0.4$. When the uniform flow velocity increases to $V = 0.42$ m/s, the maximum IL rms amplitude increases slightly to $A_{xrm}/D \approx 0.14$ and appears near the bottom end of the riser at $z/L = 0.22$. In contrast, the maximum CF rms amplitude increases dramatically to $A_{yrm}/D \approx 0.81$ which is similar to the CF VIV amplitudes reported by Vandiver (1993) and Huera-Huarte and Bearman (2011).

Fig. 5.8(c) and (d) show the comparison of the rms amplitudes between the present numerical simulation and the experiment for linearly sheared flow. Similar to the uniform flow conditions, the maximum IL and CF rms amplitudes also increase with the maximum velocity V_{max} in the two linearly sheared flow cases. However, the maximum rms amplitudes in the two linearly sheared flow cases are much smaller

compared to those in the two uniform flow cases with $A_{xrm}/D \approx 0.03$ and $A_{yrm}/D \approx 0.18$ for $V_{max} = 0.2$ m/s and $A_{xrm}/D \approx 0.1$ and $A_{yrm}/D \approx 0.31$ for $V_{max} = 0.42$ m/s.

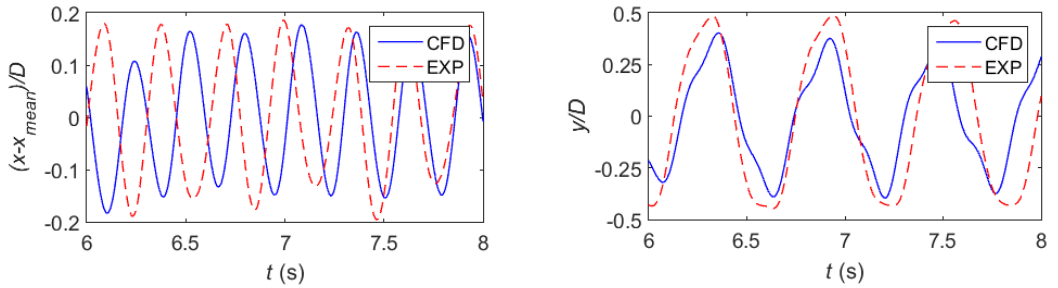

(a)

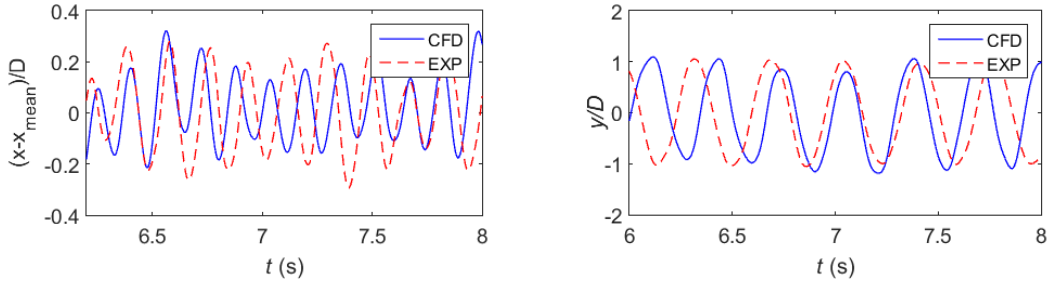

(b)

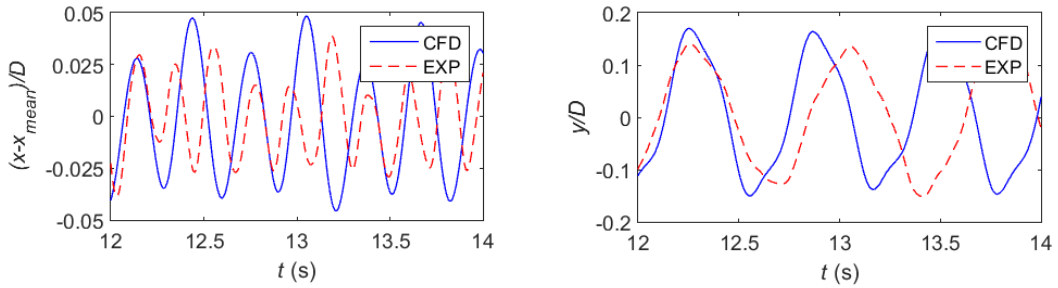

(c)

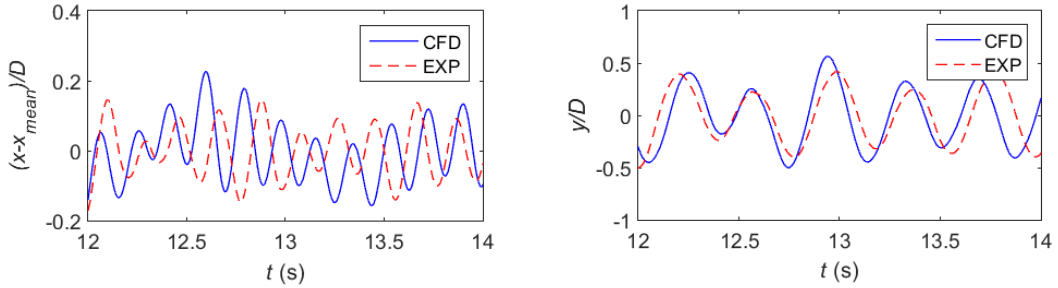

(d)

Fig. 5.9 Comparison of the displacement time histories at $z/L = 0.22$: (a) # 1103, (b) # 1105, (c) # 1201 and (d) # 1205.

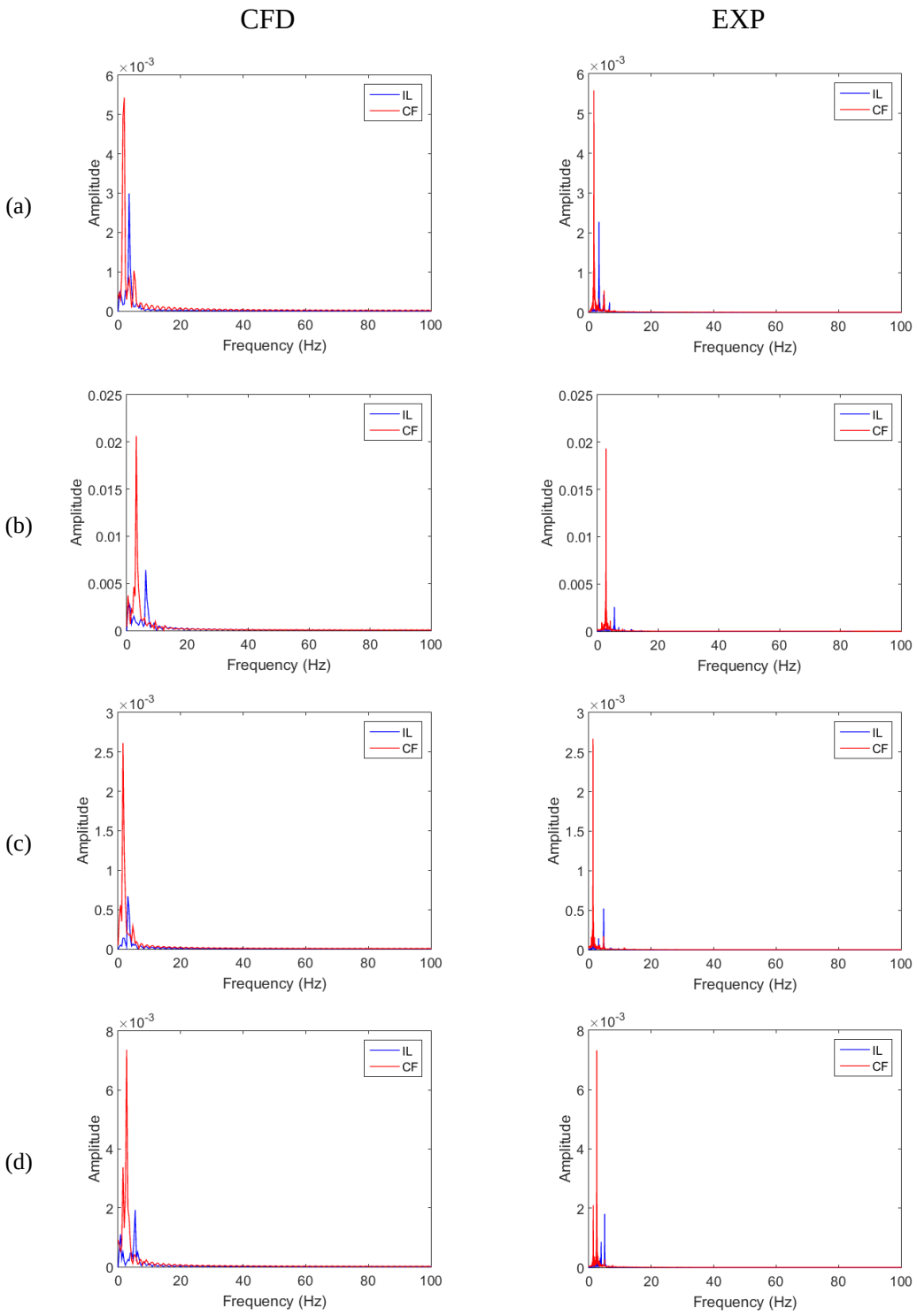

Fig. 5.10 Comparison of the oscillation frequencies at z/L = 0.22: (a) # 1103, (b) # 1105, (c) # 1201 and (d) # 1205.

5.2.3 Displacement Time Histories and Oscillation Frequencies

Fig. 5.9 shows the comparison of the displacement time histories at z/L = 0.22 between the present simulation and the experiment. In general, the numerical results are comparable with the experimental data. Because the onset of the vibration occurs randomly in the numerical simulation and the experiment, there are some phase differences between the numerical and experimental time histories. As there exist some discrepancies in the eigenfrequencies between the measured data and the modal analysis results, the comparison of the displacement time histories also shows some differences in the oscillation frequencies.

Fig. 5.10 shows the comparison of the IL and CF oscillation frequencies at z/L = 0.22. The predicted results show good agreement with the experimental data. In the present simulation, the ratio of the IL oscillation frequency to the CF oscillation frequency is around two, which conforms to the scenario of dual resonance. It is also found from the present results that the IL and CF oscillation frequencies increase with the flow velocity. In the two uniform flow cases, the IL and CF oscillation frequencies increase from f_{ox} = 3.516 Hz and f_{oy} = 1.953 Hz to f_{ox} = 6.25 Hz and f_{oy} = 3.125 Hz when V increases from 0.2 m/s to 0.42 m/s. Similarly, in the two linearly sheared flow cases, the IL and CF oscillation frequencies increase from f_{ox} = 3.125 Hz and f_{oy} = 1.563 Hz to f_{ox} = 5.469 Hz and f_{oy} = 2.734 Hz when $V_{\max}$ increases from 0.2 m/s to 0.42 m/s. The predicted IL and CF oscillation frequencies in the two linearly sheared flow cases are slightly lower than those in the two uniform flow cases. A quantitative difference in the IL oscillation frequency between the present results and the experimental data is observed in the case # 1201 (Fig. 5.10(c)). The IL oscillation frequency in the present simulation is f_{ox} = 3.125 Hz while it is f_{ox} = 4.73 Hz in the experiment. The difference in the IL oscillation frequency leads to the discrepancy in the IL dominant mode as mentioned in Section 5.2.1. The possible reasons for the difference in the IL oscillation frequency might be due to the discrepancies in the eigenfrequencies between the experimental measurements and modal analysis computations and the small-amplitude vibrations in the IL direction.

The predicted displacements and oscillation frequencies along the riser are further examined for all the cases. It is found that the motion at a single frequency and in a

single mode shape is typical for the CF response of the riser, and a third harmonic frequency component at three times the first harmonic frequency is observed in the CF response at some locations along the riser.

Fig. 5.11(a) and (b) show the predicted displacements and oscillation frequencies along the riser in the case # 1103. The IL and CF responses have consistent dominant frequencies around 3.516 Hz and 1.953 Hz along the riser which correspond to the structure's second mode and first mode, respectively. The 2:1 IL to CF oscillation frequency ratio indicates the occurrence of dual resonance. In addition, a third harmonic frequency component is observed in the CF response at some locations along the riser.

Fig. 5.11(c) and (d) are the predicted displacements and oscillation frequencies along the riser in the case # 1201. The CF response is also consistent along the entire riser at a frequency of f_{oy} = 1.563 Hz and again a third harmonic frequency component is found in the CF response at some locations along the riser. It is notable that in this case, the IL response at some locations has appreciable contributions at both twice the CF response frequency and the CF response frequency itself. Similar IL response has also been reported by Tognarelli *et al.* (2004).

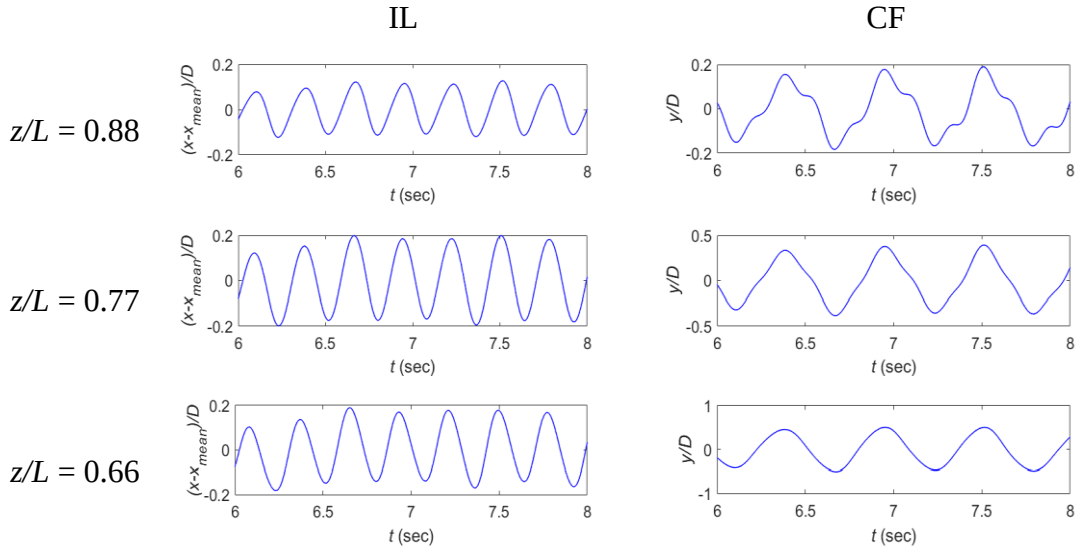

z/L = 0.55

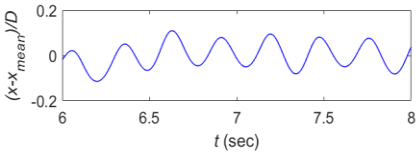

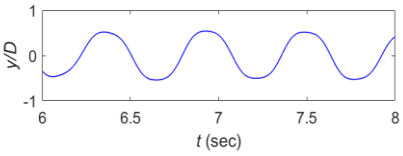

z/L = 0.44

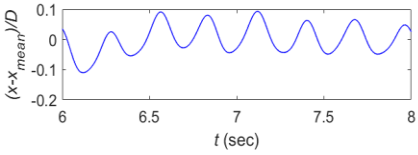

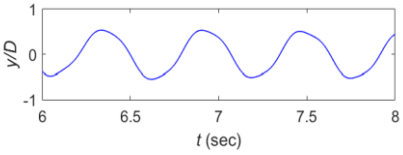

z/L = 0.33

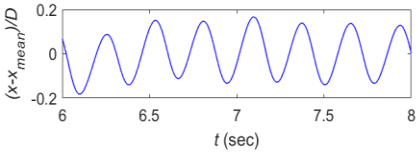

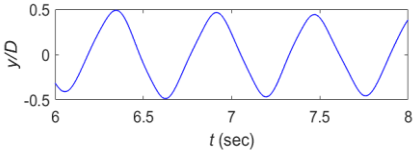

z/L = 0.22

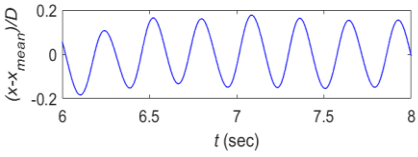

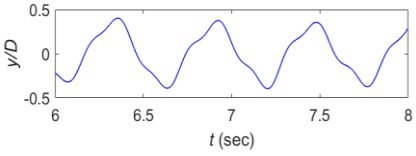

z/L = 0.11

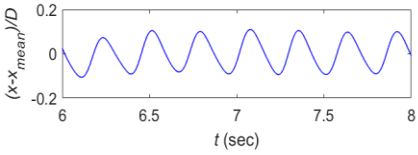

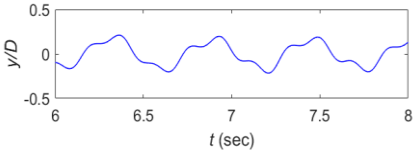

(a)

IL

CF

z/L = 0.88

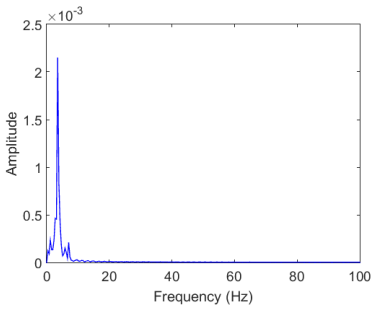

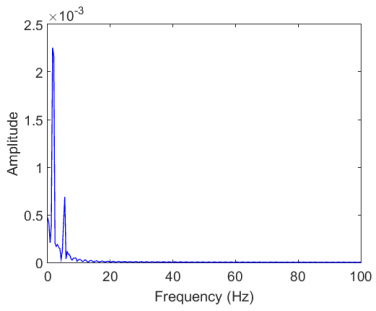

z/L = 0.77

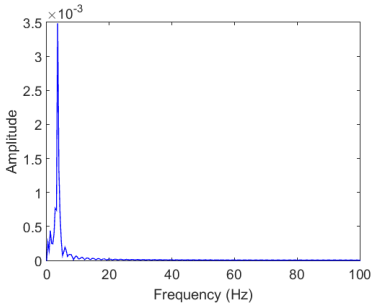

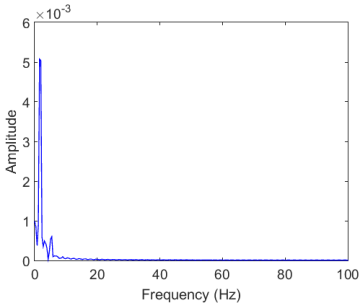

z/L = 0.66

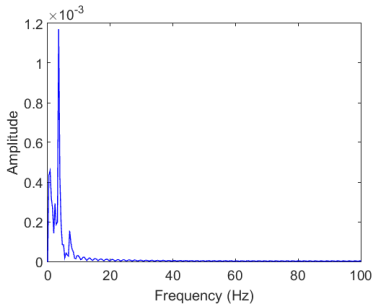

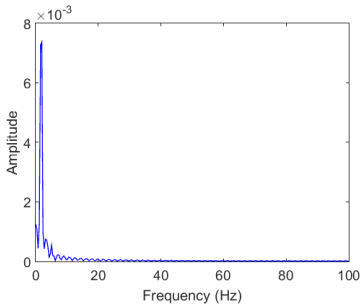

z/L = 0.55

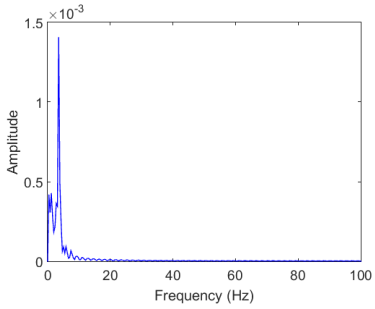

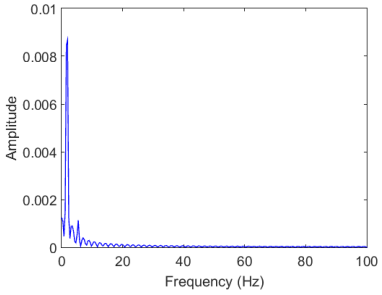

z/L = 0.44

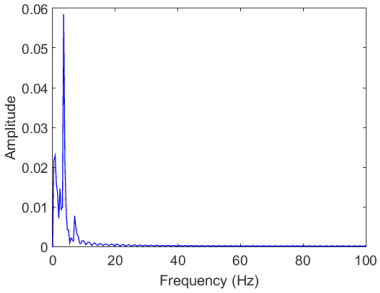

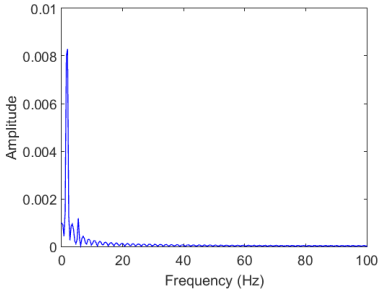

z/L = 0.33

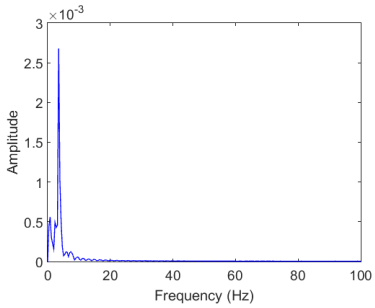

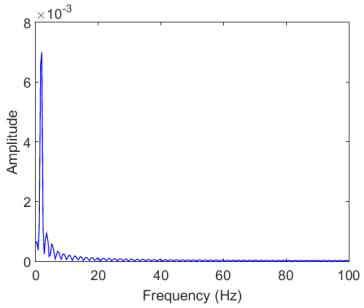

z/L = 0.22

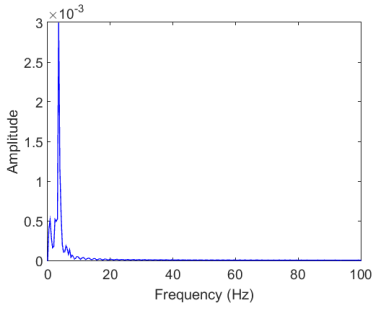

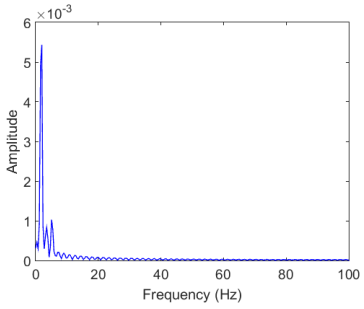

z/L = 0.11

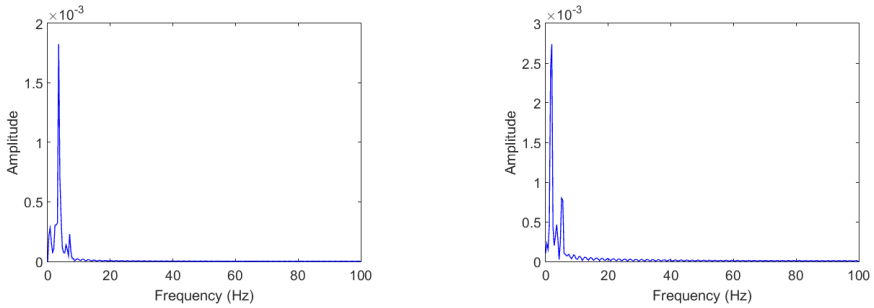

(b)

IL CF

z/L = 0.88

z/L = 0.77

z/L = 0.66

z/L = 0.55

z/L = 0.44

z/L = 0.33

z/L = 0.22

z/L = 0.11

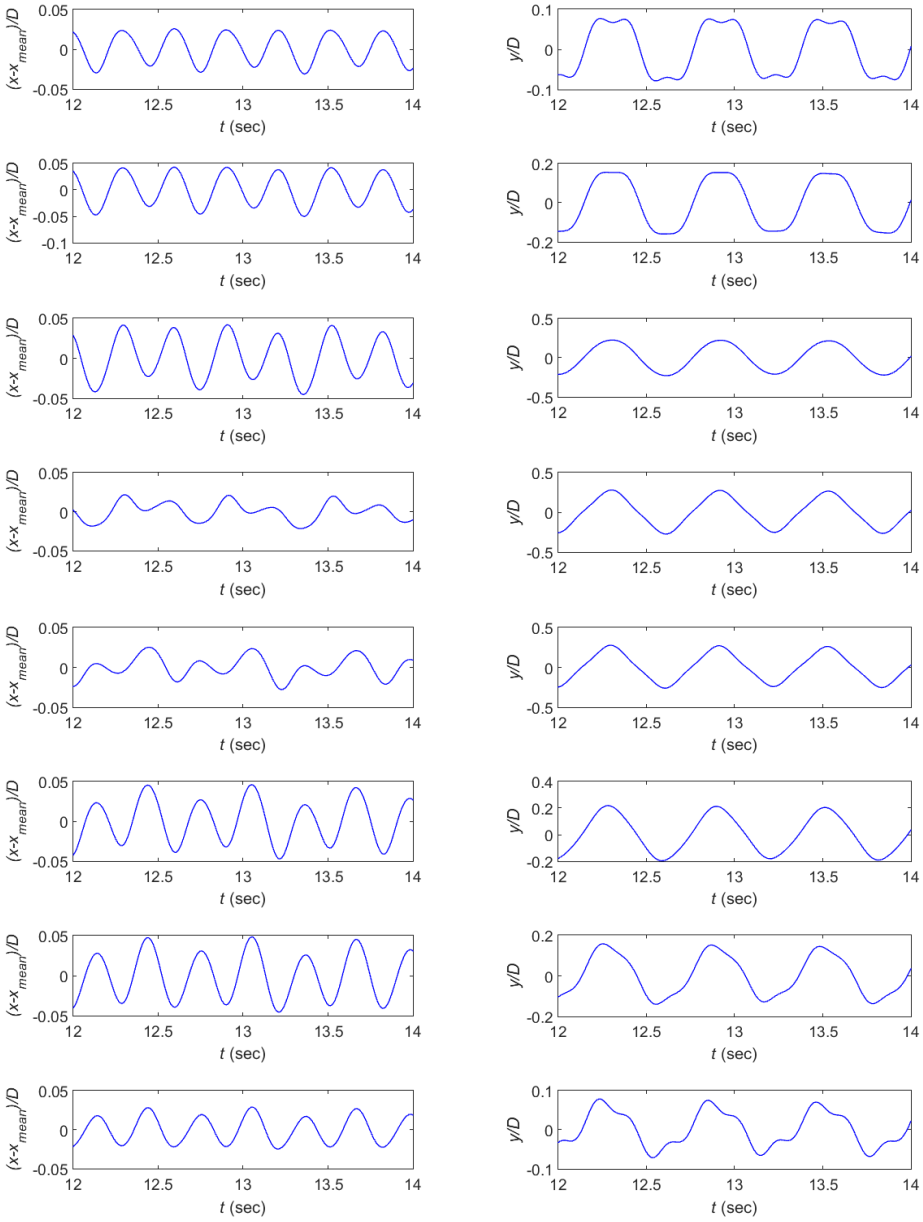

(c)

	IL	CF
z/L = 0.88	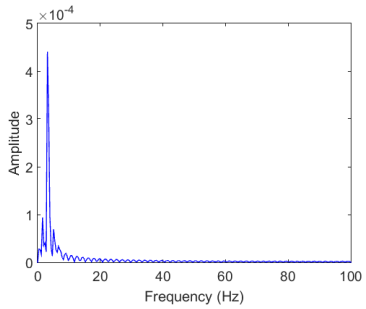	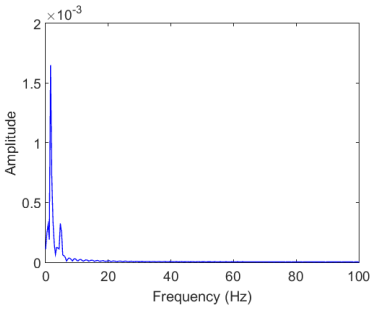
z/L = 0.77	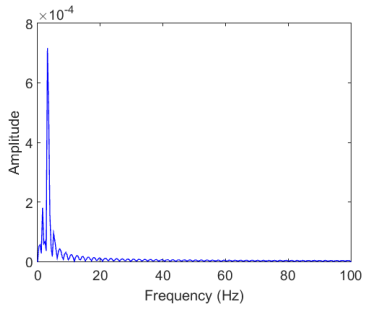	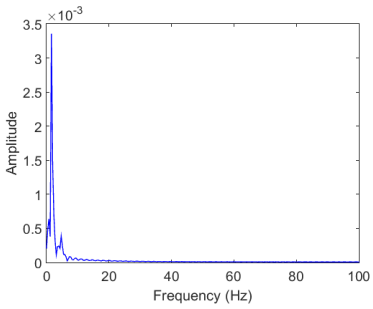
z/L = 0.66	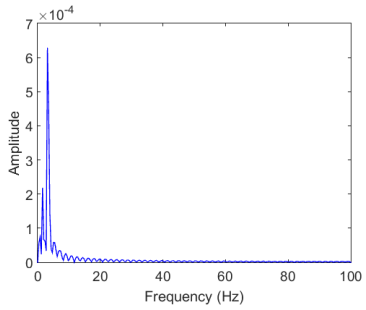	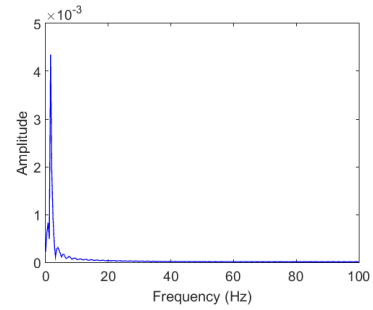
z/L = 0.55	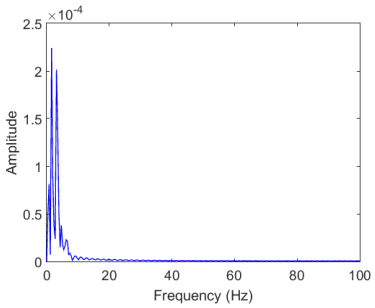	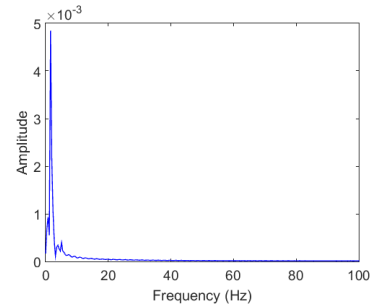
z/L = 0.44	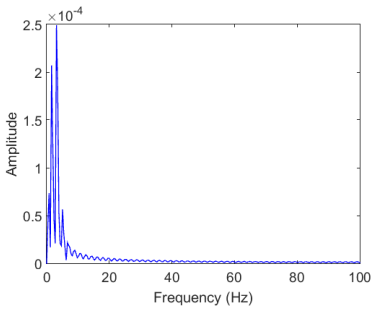	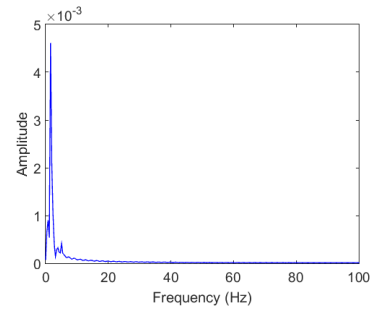

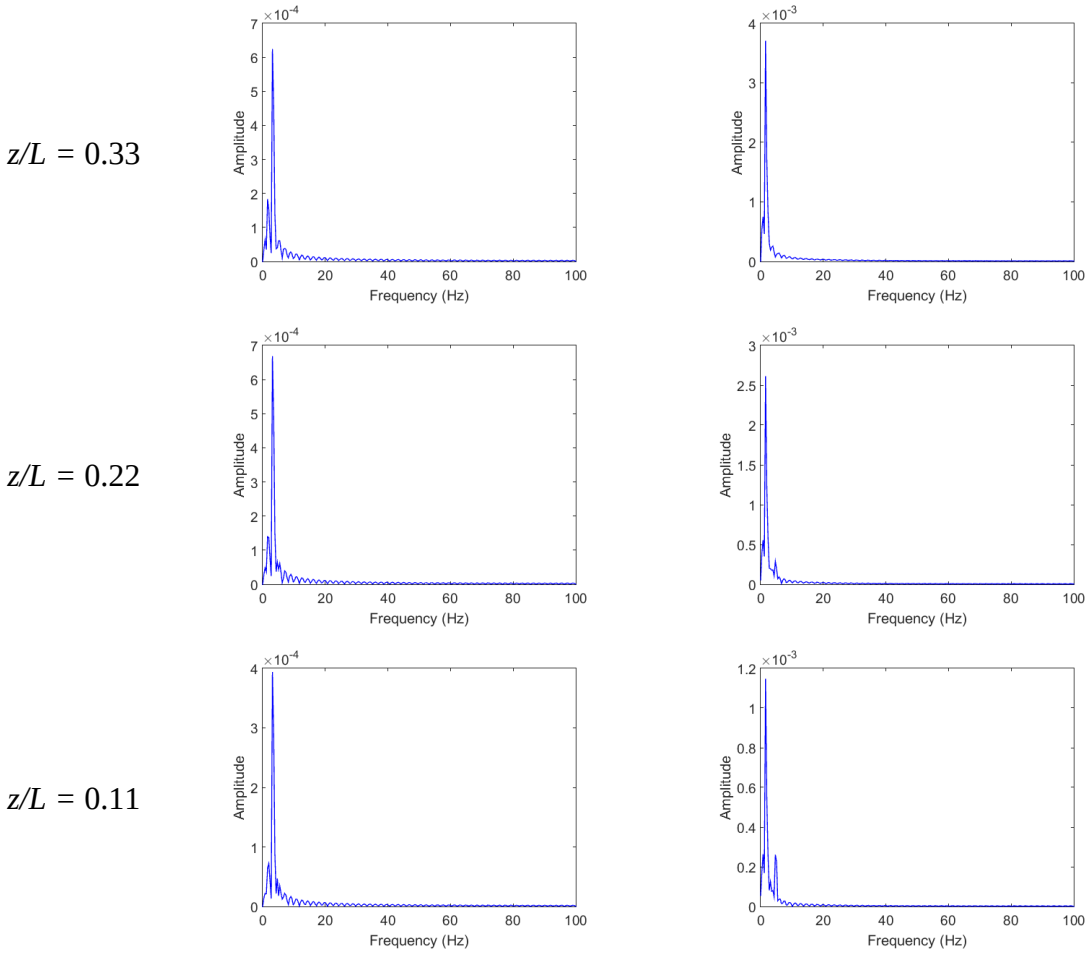

(d)

Fig. 5.11 Displacements and oscillation frequencies along the riser: (a) displacement time histories (# 1103), (b) oscillation frequencies (# 1103), (c) displacement time histories (# 1201) and (d) oscillation frequencies (#1201).

5.2.4 Orbital Trajectories

The predicted orbital trajectories at eight different positions along the riser span (z/L = 0.11, 0.22, 0.33, 0.44, 0.55, 0.66, 0.77 and 0.88) are compared with the experimental data in Fig. 5.12. The selected positions coincide with the locations of the accelerometers in the experiment. As can be seen from Fig. 5.12, most of the orbital trajectories are of a figure-eight shape indicating the occurrence of dual resonance where the IL and CF vibration frequencies have a ratio of two (Dahl *et al.*, 2010). Another interesting phenomenon is that most of the orbital trajectories are counterclockwise (CC), i.e., the cylinder motion is counterclockwise at the top of the

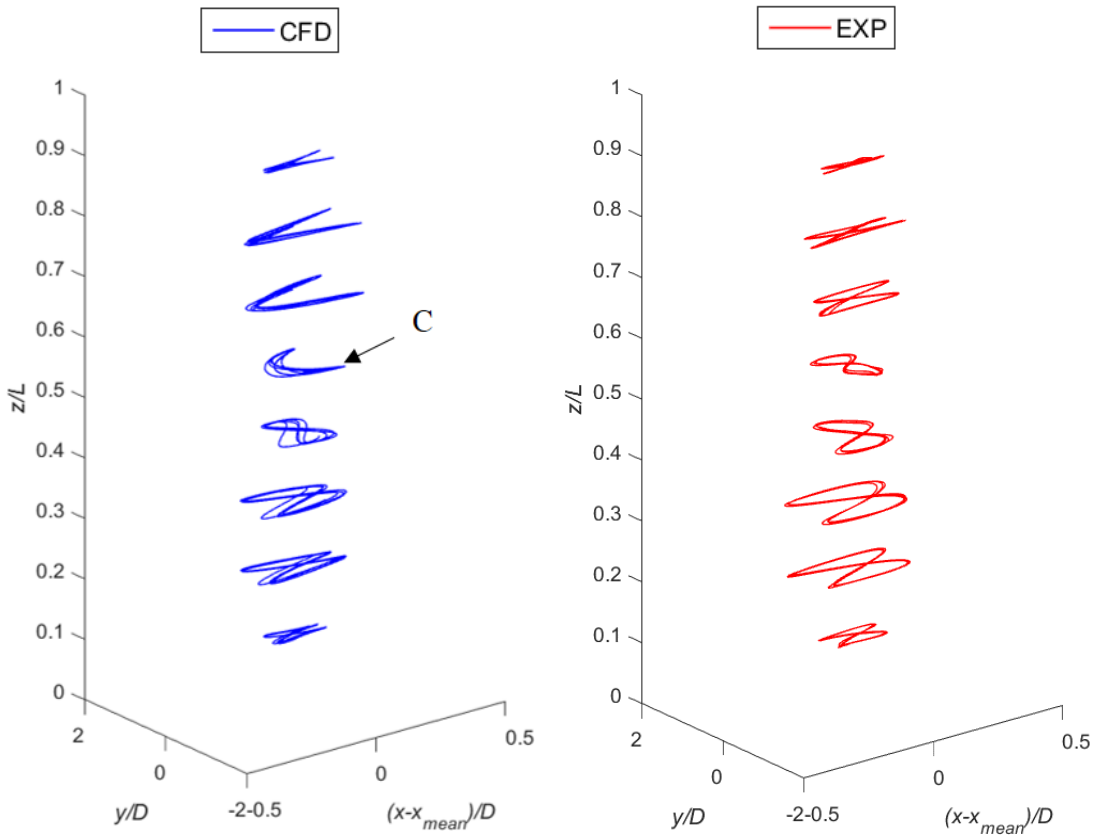

(a)

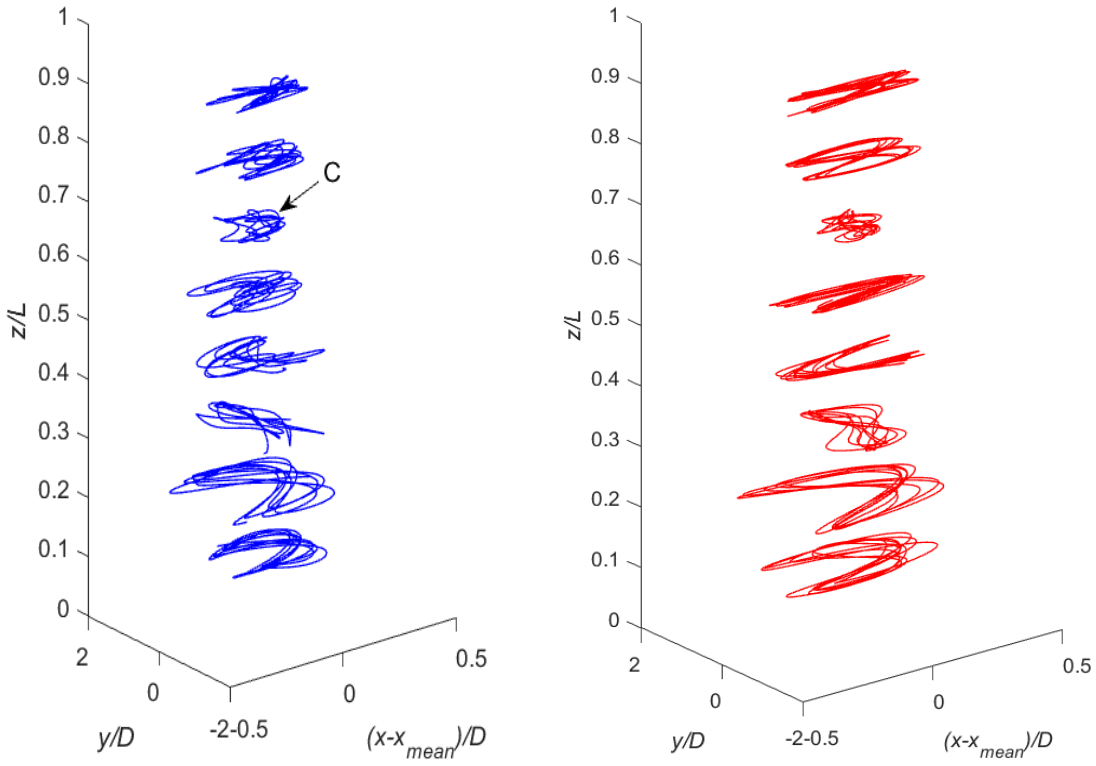

(b)

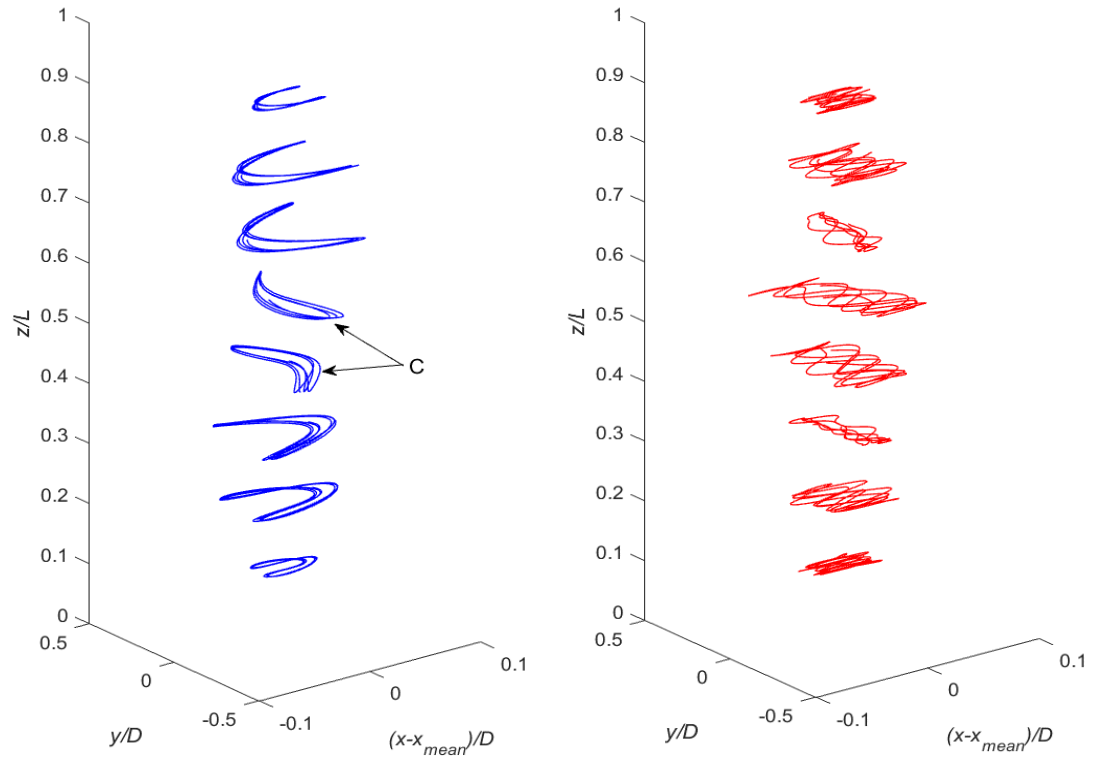

(c)

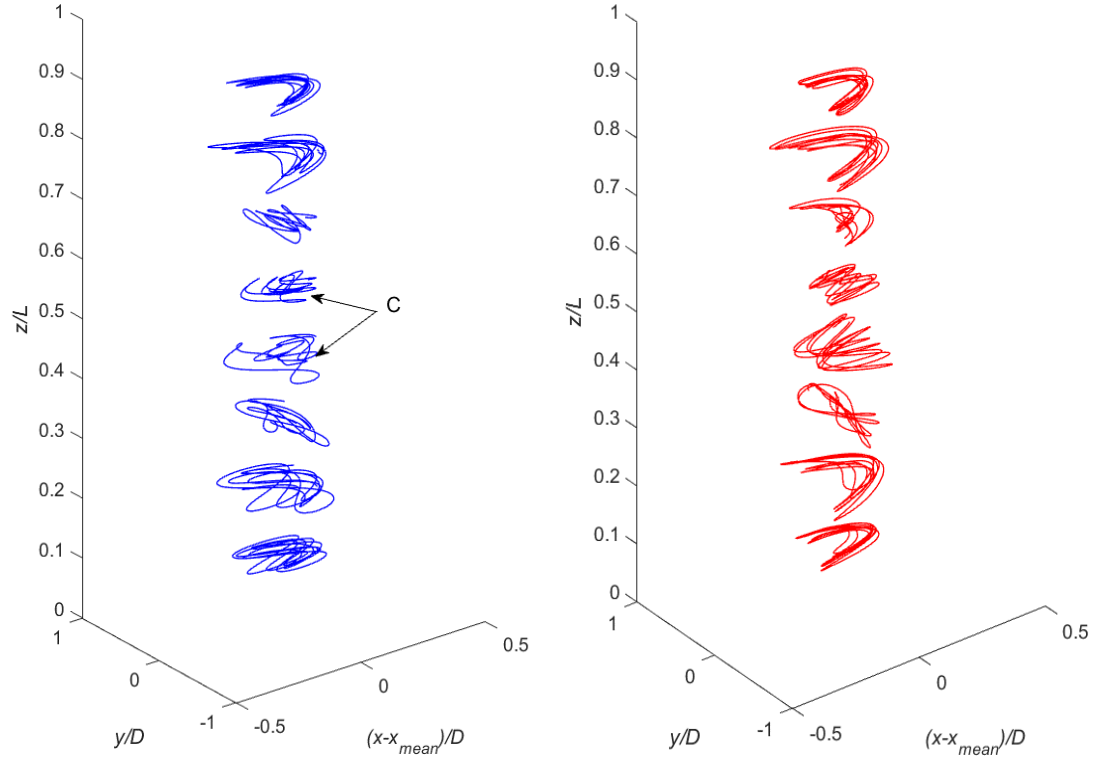

(d)

Fig. 5.12 Comparison of the orbital trajectories at various positions: (a) # 1103, (b) # 1105, (c) # 1201 and (d) # 1205.

figure-eight motion. The exceptional clockwise (C) trajectories are marked with letter "C" in Fig. 5.12. The upstream motion of the cylinder in the CC trajectory leads to a closer proximity of the cylinder and the recently shed vortices (Dahl *et al.*, 2007). According to Bourguet *et al.* (2011), the CC direction is the predominant orbit orientation in the lock-in region.

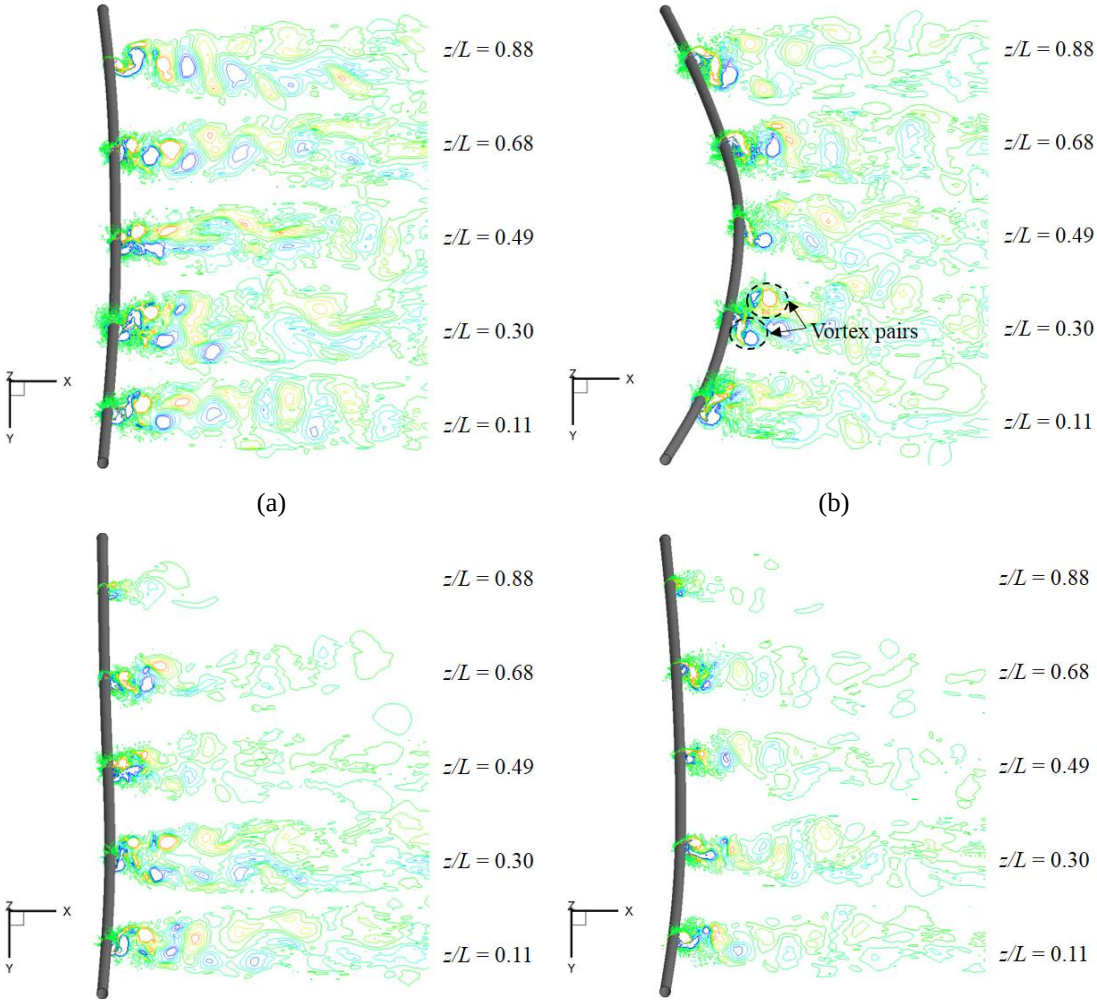

Fig. 5.13 Vortex shedding under different current profiles: (a) # 1103, (b) # 1105, (c) # 1201 and (d) # 1205.

5.2.5 Vortex Shedding Modes

Fig. 5.13 shows the vortex shedding at five different planes along the riser, i.e., z/L = 0.11, 0.3, 0.49, 0.68 and 0.88 under different current profiles. It can be seen from the

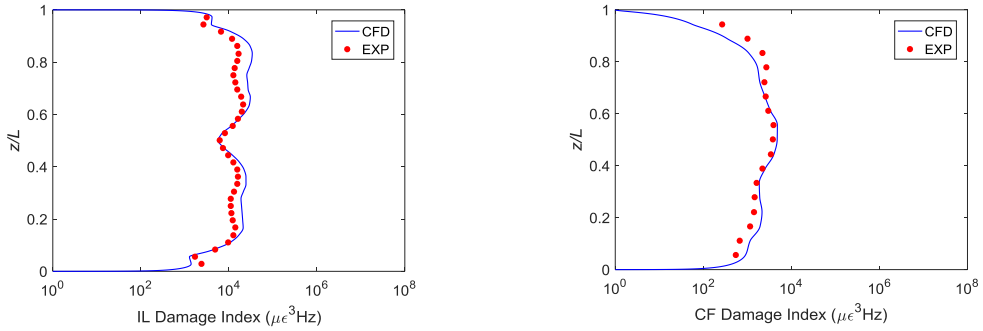

(a)

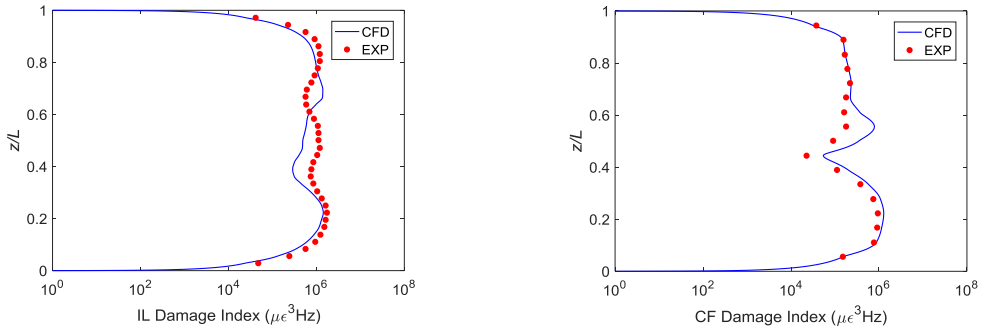

(b)

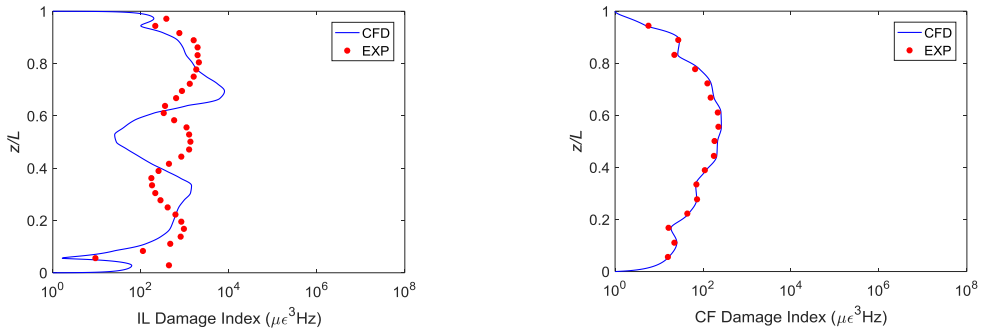

(c)

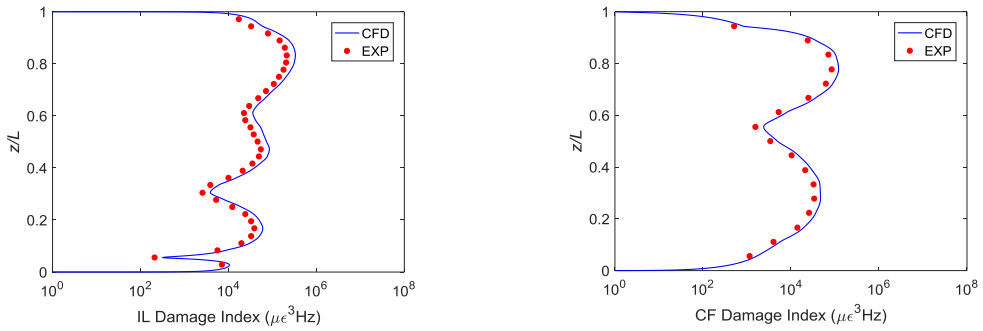

(d)

Fig. 5.14 Comparison of the fatigue damage indices: (a) # 1103, (b) # 1105, (c) # 1201 and (d) # 1205.

vorticity contour plots that the majority of the vortex shedding shows a clear 2S pattern (two single vortices per cycle), whereas a 2P mode (two vortex pairs formed in each cycle of the body motion) is observed in the case # 1105 at z/L = 0.3 near the position z/L = 0.22 where the maximum vibration amplitude appears. The present observation agrees with the conclusions of Meneghini *et al.* (2004), Yamamoto *et al.* (2004) and Sun *et al.* (2012) for VIV of flexible risers that a 2S mode is found in regions of small amplitudes and a 2P mode is observed in regions of larger amplitudes.

5.2.6 Fatigue Damage Indices

One of the objectives to study flexible riser VIV is to assess the fatigue damage caused by the vibration, thus the fatigue damage index as defined by Tognarelli *et al.* (2004) is evaluated in this section. The damage index is defined as $DI = f_{z,\varepsilon}\varepsilon^3$ where $f_{z,\varepsilon}$ is the zero-crossing frequency of the bending strain and ε is the rms strain. In the present simulation, the strain data in the IL and CF directions are obtained from ANSYS. The calculated fatigue damage indices are compared to the experimental data in Fig. 5.14. The comparison shows that the present numerical results are generally in good agreement with the experimental data. As shown in Fig. 5.14, the IL and CF fatigue damage indices increase with the flow velocity in all the cases considered. According to Section 5.2.3, the response frequencies in the case # 1105 are slightly higher than those in the case # 1205, however, the fatigue damage indices in the case # 1105 are considerably higher than those in the case # 1205 in the lower part of the riser. That is because the large-amplitude vibration associated by the 2P vortex shedding mode produces significantly larger strains in the IL and CF directions. According to Tognarelli *et al.* (2004), the fatigue damage index is determined by the mode number, the response frequency and the response amplitude. As there are discrepancies in the IL dominant mode number and response frequency in the case # 1201 between the present numerical results and the experimental data, a discrepancy is also observed in the IL fatigue damage index. It is noteworthy that in all the four cases considered in the present simulation the IL fatigue damage is, in fact, higher than CF fatigue damage in the two low flow velocity cases, i.e., # 1103

and # 1201. It is only when the flow velocity or maximum flow velocity increases to 0.42 m/s that the CF fatigue damage reaches the same order of magnitude as the IL fatigue damage. This finding agrees with the conclusion of Tognarelli *et al.* (2004). Although the present numerical simulation does not cover as many velocities as the experiment did, the available results have already suggested that, from a design point of view, the IL fatigue damage is not negligible especially for low flow velocity or low mode number applications such as pipeline spans or some drilling and production risers.

5.3 Concluding Remarks

VIV of a vertical riser in the uniform and linearly sheared currents is numerically studied using a fully 3D FSI simulation methodology. The results of a total of four cases are presented for two uniform flow profiles with V = 0.2 m/s and 0.42 m/s and two linearly sheared flow profiles with V_{max} = 0.2 m/s and 0.42 m/s at the bottom end and V_{min}/V_{max} = 0.14. The predicted numerical results are in good agreement with the ExxonMobil vertical riser model test results. The overall comparison indicates that the present numerical method is reliable and capable of predicting reasonably accurate VIV responses of long risers subject to uniform currents and linearly sheared currents. In addition, with our numerical modelling, flow visualisation results which are hard to obtain in the experimental tests are provided. The main findings of the present study can be summarised as follows.

The dynamic response of the riser is studied by examining the dominant modes, rms amplitudes, displacement time histories, dominant frequencies and orbital trajectories. It is found that the dominant mode numbers in the IL and CF directions increase with the flow velocity. The variation of the dominant modes in the two linearly sheared flow cases is the same as that in the two uniform flow cases. In terms of the rms amplitudes, the maximum IL and CF rms amplitudes are found to increase with the flow velocity under both flow conditions. However, the maximum rms amplitudes in the two linearly sheared flow cases are much smaller than those in the two uniform flow cases. In general, the IL response has a dominant frequency twice the CF

response frequency. Both the IL and CF oscillation frequencies increase with the flow velocity. In the meanwhile, the IL and CF oscillation frequencies in the two linearly sheared flow cases are slightly lower than those in the two uniform flow cases. The motion at a single frequency and in a single mode shape is typical for the CF response of the riser. A third harmonic CF frequency component is found at some locations along the riser. In certain cases, the IL response at some locations has appreciable contributions at both twice the CF response frequency and the CF response frequency itself. As for the orbital trajectories, most of the orbital trajectories are of a figure-eight shape indicating the occurrence of dual resonance and the majority of them are characterised by counterclockwise orbits.

As vortex shedding is an important aspect of flexible riser VIV analysis, the vortex shedding modes at different slices along the riser span are studied. Two different vortex shedding modes are observed in the present simulation, i.e., 2S and 2P modes. A 2S mode is widely observed in most of the cases considered, whereas a 2P mode is found to be associated with the maximum amplitude.

The fatigue damage due to VIV is analysed in the consideration of its significance in practical applications. It is found that the IL and CF fatigue damage indices increase with the flow velocity as a result of the increased mode number, the increased response frequency and the increased response amplitude. The larger-amplitude vibration associated by the 2P vortex shedding mode in the lower part of the riser in the case # 1105 produces significantly larger strains in the IL and CF directions leading to considerably higher fatigue damage indices. The IL fatigue damage is higher than the CF fatigue damage at low flow velocities in the cases # 1103 and # 1201. The CF fatigue damage reaches the same order of magnitude as the IL fatigue damage in the cases # 1105 and # 1205. The results emphasise the importance of the IL fatigue damage especially for low flow velocity or low mode number applications.

As this study mainly focusses on a low flow velocity range and only the uniform flow and linearly sheared flow cases are considered. Future research on riser VIV in a higher flow velocity range under more complex flow conditions is worthwhile.

Overall, the present numerical method is able to reasonably predict VIV response of a vertical riser under uniform and linearly sheared flow conditions and can be used as an alternative to the existing prediction models for deepwater riser VIV prediction.

The output publication from this chapter is ‘Numerical simulation of vortex-induced vibration of a vertical riser in uniform and linearly sheared currents’ published in Ocean Engineering.

Chapter 6 The Effect of Spacing on the Vortex-Induced Vibrations of Two Tandem Flexible Cylinders

"Two are better than one."

-Ecclesiastes

VIV of two tandem flexible cylinders at three centre-to-centre spacing ratios (i.e., S_x/D = 2.5, 3.5 and 5) is studied at a fixed Reynolds number Re = 500 using a two-way explicit FSI method. In the present study, two identical flexible cylinders fixed at both ends and free to vibrate in the CF direction are considered. The mass ratio and length-to-diameter ratio of the cylinders are m^* = 10 and L/D = 12, respectively. In order to maximise the vortex-induced responses, the structural damping is set to zero. The main objective of the present work is to numerically study the effect of spacing on the hydrodynamic interactions and VIV responses of the two tandem flexible cylinders. Particular attention is paid to the aspects which have not been fully addressed by previous studies such as the correlation lengths and the time-dependent 3D wake structures.

6.1 Problem Descriptions

6.1.1 Simulation Parameters

VIV of two tandem flexible cylinders is investigated numerically. Two identical flexible cylinders with diameter D and length L are aligned in the direction of the flow in their rest positions. To simplify the problem, the vibrations of the cylinders are confined to the cross-flow direction. Similar simplifications have been adopted by previous researchers such as Evangelinos and Karniadakis (1999), Evangelinos *et al.* (2000) and Xie *et al.* (2012) to study VIV of a flexible cylinder. The length-to-diameter ratio is L/D = 12, which allows the discretisation of the cylinder span with fine mesh to resolve the characteristics of the flow with acceptable computational efforts. Moreover, L/D = 12 is also comparable to the L/D values used by Evangelinos *et al.* (2000) and Xie *et al.* (2012) in their numerical studies. A moderate

mass ratio $m^* = 4m/\rho\pi D^2 L = 10$ is considered. The influence of the structural damping is mainly reflected in the maximum vibration amplitude and in order to maximise the vortex-induced responses of the flexible cylinders, the structural damping is set to zero. A fixed Reynolds number Re = 500 is adopted in the present simulation. The reduced velocity $V_r = V/f_1 D$ ranges from 4 to 10. Here, f_1 is the fundamental natural frequency (i.e., the first eigenfrequency) of the flexible cylinder and for a beam with two fixed ends, $f_1 = \frac{p}{2}\left(1+\frac{1}{2}\right)^2 \sqrt{\frac{EI}{r_L L^4}}$. Since V is fixed in the present study, the bending stiffness EI is varied in each simulation to obtain the corresponding f_1 of the desired V_r.

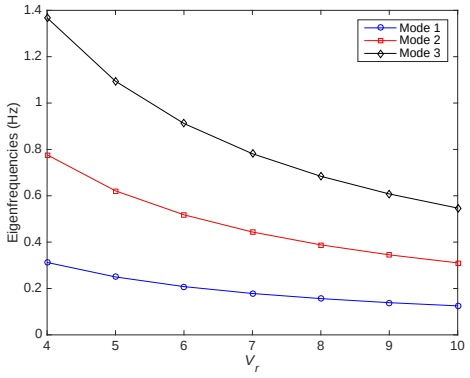

Fig. 6.1 Variation of eigenfrequencies of the first three modes with V_r.

Fig. 6.1 shows the variation of the eigenfrequencies of the first three vibration modes with V_r. It can be seen that, due to the quadratic relationship between the eigenfrequency of the n^{th} mode f_n and $(n + 1/2)$, the gaps between the eigenfrequencies of two neighbouring vibration modes become narrower as V_r increases. In order to study the effect of spacing on the VIV of two tandem flexible cylinders, three different centre-to-centre spacing ratios are selected, i.e., S_x/D = 2.5, 3.5, and 5 as in Papaioannou *et al.* (2008). These three spacing ratios are based on different regimes in the stationary system. S_x/D = 2.5 belongs to the reattachment regime where the shear layers from the upstream cylinder reattach onto the surface of the downstream cylinder; S_x/D = 5 represents the binary-vortex regime where the separated shear layers of the upstream cylinder roll up in the gap region and a binary vortex street is formed behind the downstream cylinder consisting of the interacting

wakes of the two cylinders and the spacing S_x/D = 3.5 is very close to the critical spacing of transition from the reattachment regime to the binary-vortex regime.

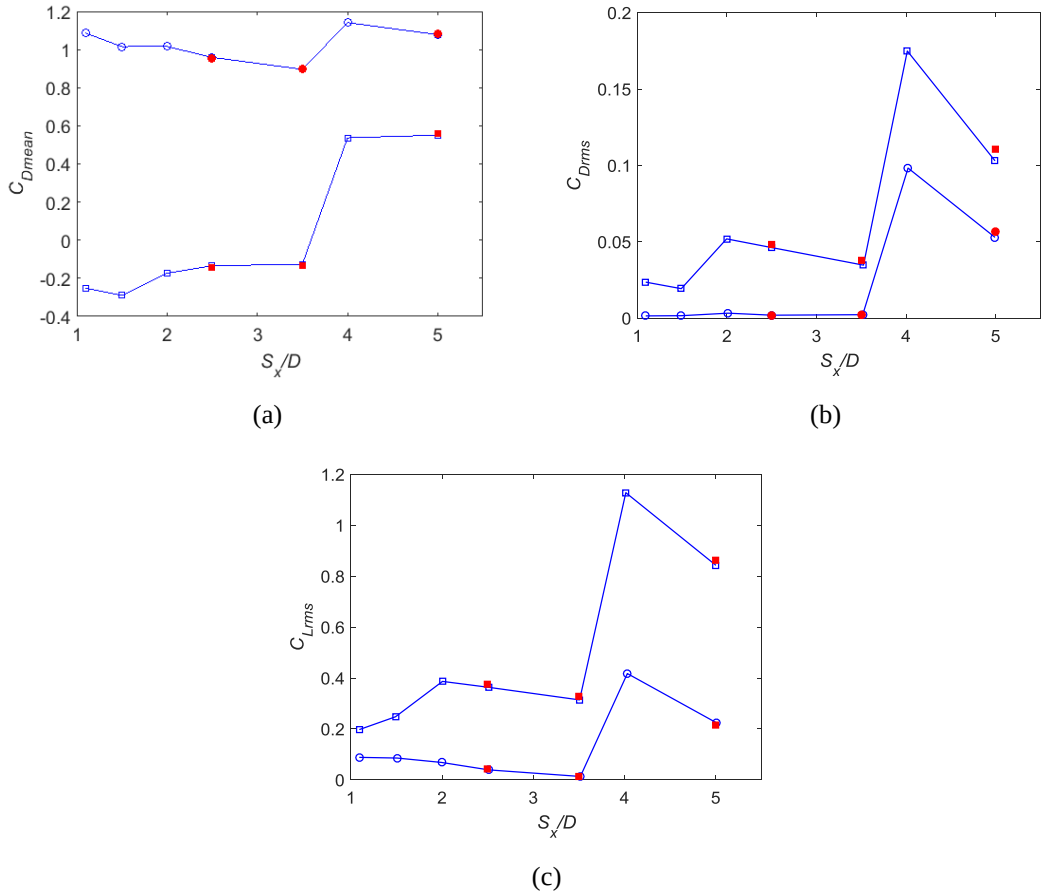

Fig. 6.2 Comparison of spanwise force coefficients: (a) mean drag coefficients, (b) rms drag coefficients and (c) rms lift coefficients; —○—, upstream cylinder (Papaioannou *et al.*, 2006); —□—, downstream cylinder (Papaioannou *et al.*, 2006); ●, upstream cylinder (present simulation); ■, downstream cylinder (present simulation).

To confirm the flow regimes for the three spacing ratios predicted by the present methods, flow past two tandem stationary cylinders at Re = 500 was simulated and the hydrodynamic force coefficients (mean drag coefficient C_{Dmean}, rms drag coefficient C_{Drms} and rms lift coefficient C_{Lrms}) were compared with the numerical results of Papaioannou *et al.* (2006) in Fig. 6.2. It can be seen that the present results are in good agreement with those of Papaioannou *et al.* (2006). The hydrodynamic force coefficients experience a jump at the critical spacing when the flow regime changes from reattachment to binary-vortex. This jump is more pronounced on the

hydrodynamic force coefficients of the downstream cylinder. Fig. 6.3 and Fig. 6.4 show the 3D flow structures and the vortex shedding at z/L = 0.5 around two stationary cylinders in tandem arrangement. The present results agree with the descriptions of the different flow patterns for two tandem stationary cylinders by Igarashi (1981, 1984), Zdravkovich (1987), Papaioannou (2004), Xu and Zhou (2004), Zhou and Yiu (2006), Carmo *et al.* (2010a, 2010b) and Sumner (2010).

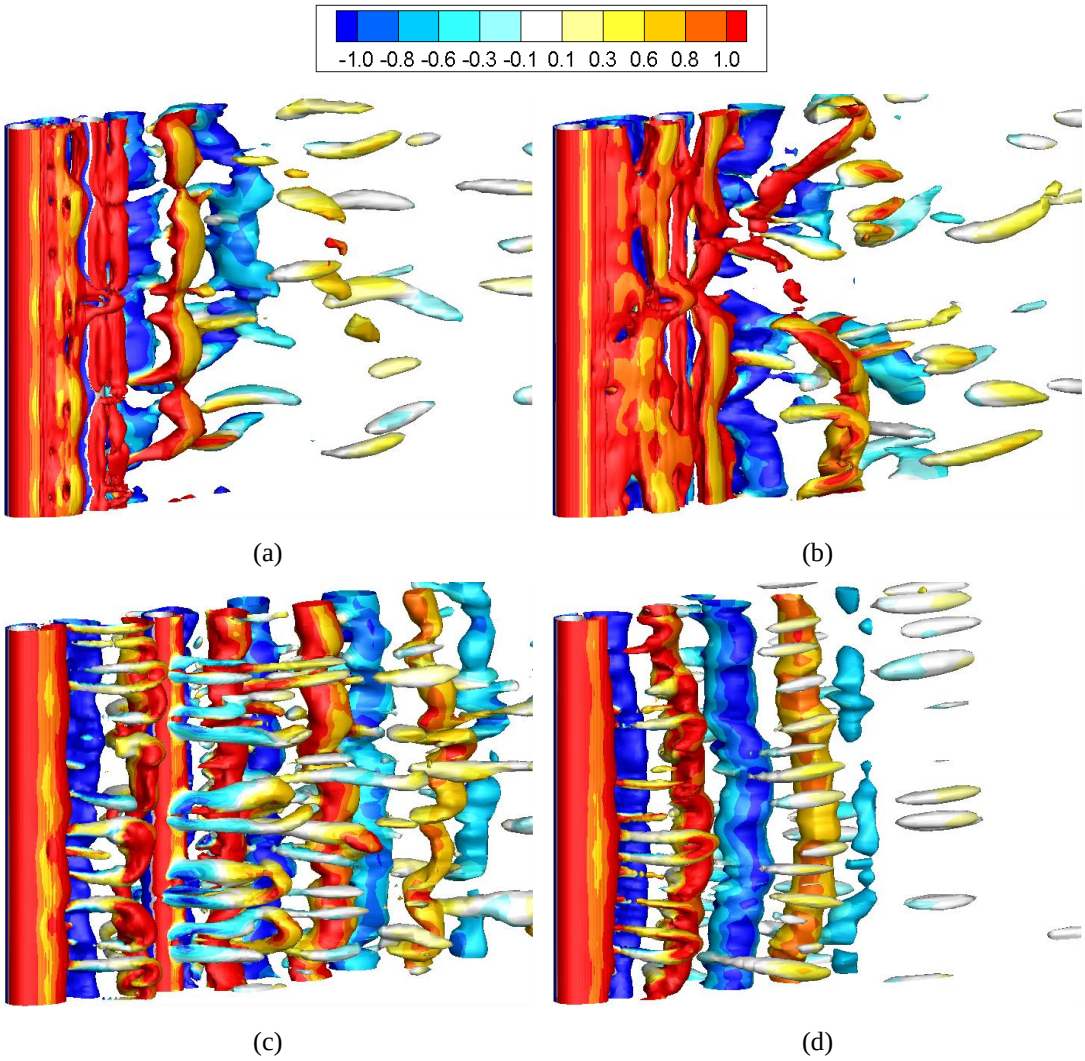

Fig. 6.3 Iso-surfaces of the eigenvalue λ_2 = -0.1 with the contours of the spanwise vorticity ω_z on the iso-surfaces for stationary cylinders: (a) S_x/D = 2.5, (b) S_x/D = 3.5, (c) S_x/D = 5 and (d) single cylinder.

6.1.2 Fluid Domain and Boundary Conditions

Fig. 6.5(a) shows the computational domain used in the CFD simulation. The origin of the Cartesian coordinate system is located at the centre of the bottom end of the upstream cylinder as shown in Fig. 6.5(a). The length of the computational domain is 40*D* in the streamwise direction (*x*-direction) with the upstream cylinder located at 10*D* downstream the inlet boundary. The width of the domain in the cross-flow direction (*y*-direction) is 20D and the computational domain size in the spanwise direction (*z*-direction) is set to the cylinder length which is 12*D*. The computational mesh for S_x/D = 5 used in the CFD simulation is shown in Fig. 6.5(b). The boundary conditions for the governing equations are as follows. The surfaces of the cylinders are assumed to be smooth, where no-slip boundary conditions are employed. Apart from the no-slip boundary conditions, the cylinder surfaces are also set to be fluid-solid interfaces where force and displacement data are transferred. The inlet velocity boundary condition is set to be the same as the freestream velocity. At the outflow boundary, the gradients of the fluid velocity in the streamwise direction are set to zero and the pressure at the outflow boundary is given a reference value of zero. On the two transverse boundaries, the velocity in the direction normal to the boundary is zero and a periodic boundary condition is imposed on the top and bottom boundaries.

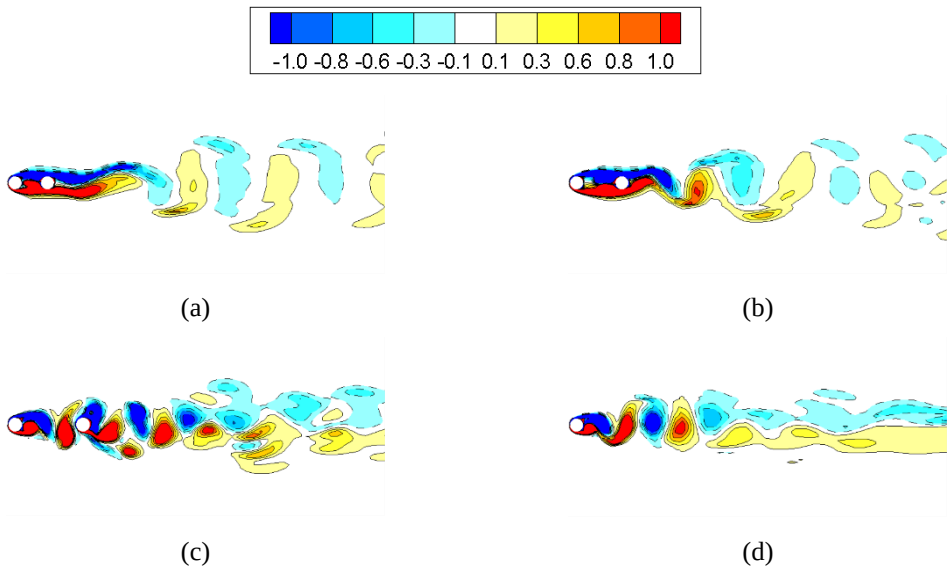

Fig. 6.4 Spanwise vorticity contours ω_z for stationary cylinders at z/L = 0.5: (a) S_x/D = 2.5, (b) S_x/D = 3.5, (c) S_x/D = 5 and (d) single cylinder.

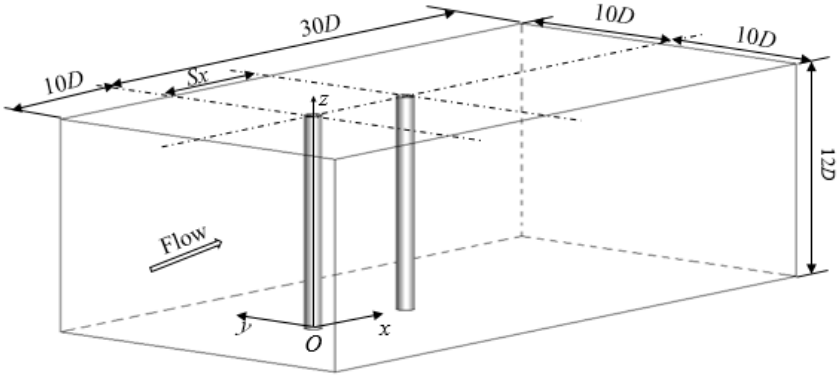

(a)

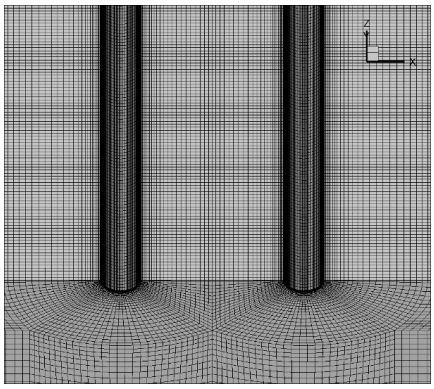

(b)

Fig. 6.5 (a) Computational domain and (b) computational mesh in the CFD simulation.

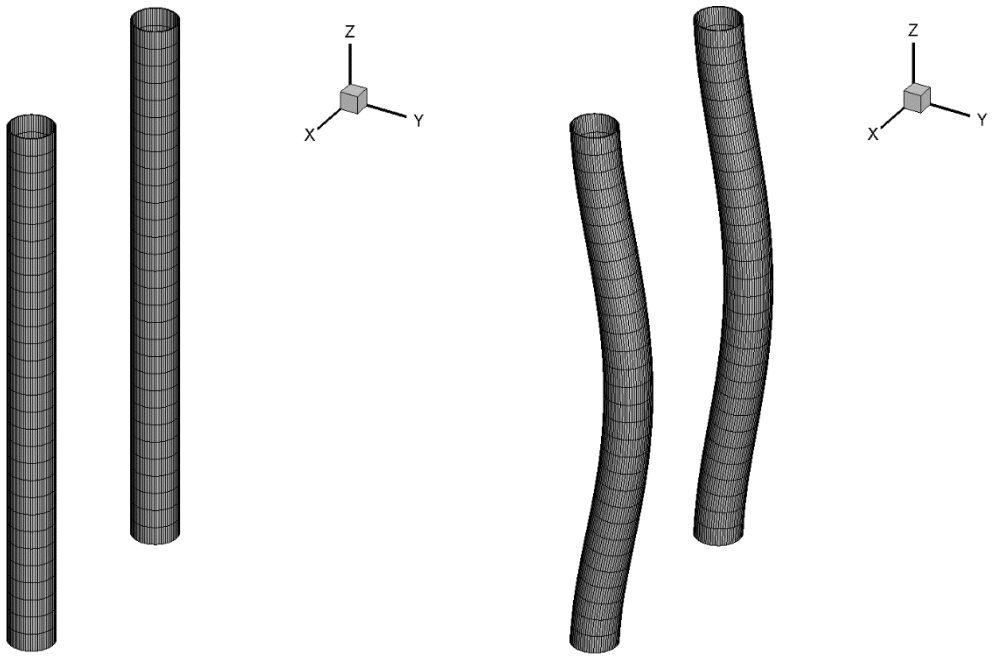

(a) (b)

Fig. 6.6 Computational mesh in the FEA simulation at S_x/D = 5: (a) initial configuration and (b) mesh after deflections.

6.1.3 Solid Domain and Boundary Conditions

A 3D 20-node solid element which exhibits quadratic displacement behaviour is used for the discretisation of the FEA models of the flexible cylinders. The element is defined by 20 nodes having three degrees of freedom per node: translations in the nodal *x*-, *y*- and *z*-directions (ANSYS Inc., 2013b). Fig. 6.6(a) and (b) show the finite elements of the two tandem flexible cylinders for S_x/D = 5 in the initial configuration and after deflections, respectively. In the solid domain, the surfaces of the cylinders are also set to be fluid-solid interfaces for data transfer.

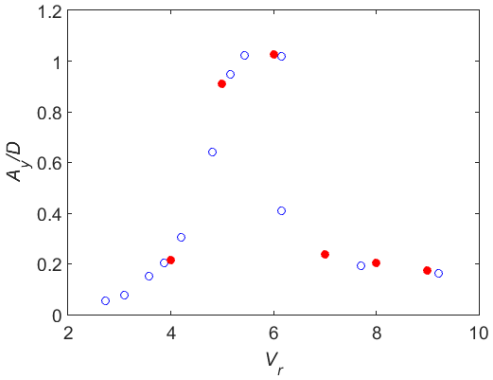

Fig. 6.7 Comparison of vibration amplitudes of a single flexible cylinder with m^* = 10, L/D = 12 at Re = 1000: ○, Xie *et al.* (2012); ●, present simulation.

6.1.4 Validation Test

The FSI solver has been used in our previous study (Wang and Xiao, 2016) to investigate VIV of a vertical riser with L/D = 481.5 in uniform and linearly sheared currents and the numerical results were compared with the ExxonMobil vertical riser model test results obtained at the MARINTEK by Lehn (2003). The numerical results were in good agreement with the experimental data. In the present study, further investigations on cross-flow VIV of a single flexible cylinder with m^* = 10, L/D = 12 and two fixed ends at Re = 1000 were conducted using the present numerical methods and the results are compared with the numerical results by Xie *et al.* (2012) in Fig. 6.7. It demonstrates that the present numerical methods are capable

of accurately predicting VIV responses of flexible cylinders at early subcritical Reynolds numbers.

Table 6.1 CFD mesh dependency test results.

CFDM	N_c	$\Delta r/D$	$\Delta z/D$	A_y/D	C_{Dmean}	C_{Drms}	C_{Lrms}
1	80	0.002	0.2	0.7443	1.5975	0.2501	0.1717
2	120	0.001	0.1	0.7480	1.6127	0.2449	0.1661
3	160	0.0005	0.05	0.7524	1.6039	0.2482	0.1638

Table 6.2 FEA mesh dependency test results.

FEAM	N_z	A_y/D	C_{Dmean}	C_{Drms}	C_{Lrms}
1	15	0.7515	1.5964	0.2421	0.1673
2	30	0.7480	1.6127	0.2449	0.1661
3	60	0.7480	1.6076	0.2453	0.1652

6.1.5 Mesh Dependency Test

According to a series of publications on 3D numerical simulations of VIV of an elastically mounted circular cylinder (Zhao and Cheng, 2011, 2014; Zhao *et al.*, 2014), the important mesh parameters in the CFD simulation are the number of nodes along the circumference of the cylinder N_c, the minimum mesh size next to the cylinder surface in the radial direction Δr and the mesh size in the spanwise direction of the cylinder Δz. Similarly, the important mesh parameter in the FEA of the present FSI simulations is the number of segments along the cylinder span N_z. In order to evaluate the dependency of the numerical results on the CFD mesh parameters, simulations were carried out for VIV of a single flexible cylinder with $m^* = 10$ and $L/D = 12$ at $V_r = 6$ and Re = 500 with three different CFD mesh systems while using the same FEA mesh with $N_z = 30$. The results computed using the different CFD meshes are tabulated in Table 6.1. As shown in the table, the maximum difference of 3.36% occurs in the value of the spanwise rms lift coefficient C_{Lrms} between CFDM1 and CFDM2, whereas the maximum difference between CFDM2 and CFDM3 reduces to 1.4%. It can be concluded that the combination of $N_c = 120$, $\Delta r = 0.001D$ and $\Delta z = 0.1D$ is sufficient for the CFD simulation of VIV of flexible cylinders in the present study. Then, CFDM2 was used to study the dependency of the numerical

results on the FEA mesh parameter. Three FEA meshes are generated with N_z = 15, 30 and 60. The comparison of the results computed with different FEA mesh parameters is shown in Table 6.2. The maximum difference between FEAM1 and FEAM2 is observed in the spanwise rms drag coefficient C_{Drms} and takes the value of 1.14%. In contrast, the maximum difference between FEAM2 and FEAM3 is 0.55% which appears in C_{Lrms}. Based on the FEA mesh dependency test results, N_z = 30 is used in the present study.

6.1.6 Time-Step Size Dependency Test

Based on the mesh dependency test results in Section 6.1.5, the mesh parameters of CFDM2 and FEAM2 are used in the time-step size dependency test to simulate the same case as the mesh dependency test with the purpose of eliminating the effect of the time-step size on the numerical results. The three nondimensional time-step sizes considered in the time-step size dependency test are $V\Delta t/D$ = 0.005, 0.002 and 0.001, respectively and the detailed results are summarised in Table 6.3. By analysing the results, the maximum difference between $V\Delta t/D$ = 0.005 and 0.002 is nearly 4.3% which is observed in C_{Lrms}. The comparison of the results using $V\Delta t/D$ = 0.002 and 0.001 shows a maximum difference of 1.2% in C_{Drms}. Therefore, $V\Delta t/D$ = 0.002 is used for the FSI simulation in the present study.

Table 6.3 Comparison of the results using different time-step sizes.

$V\Delta t/D$	A_y/D	C_{Dmean}	C_{Drms}	C_{Lrms}
0.005	0.732	1.634	0.2365	0.159
0.002	0.748	1.6127	0.2449	0.1661
0.001	0.7468	1.6093	0.2421	0.1667

6.2 Results and Discussions

Numerical simulation was performed for VIV of two tandem flexible cylinders with three different spacing ratios (S_x/D = 2.5, 3.5 and 5) at an early subcritical Reynolds number Re = 500 in a reduced velocity range V_r = 4 – 10. The results are compared with those of a single flexible cylinder to investigate the effect of spacing on the

hydrodynamic interactions and the VIV responses of the two tandem flexible cylinders.

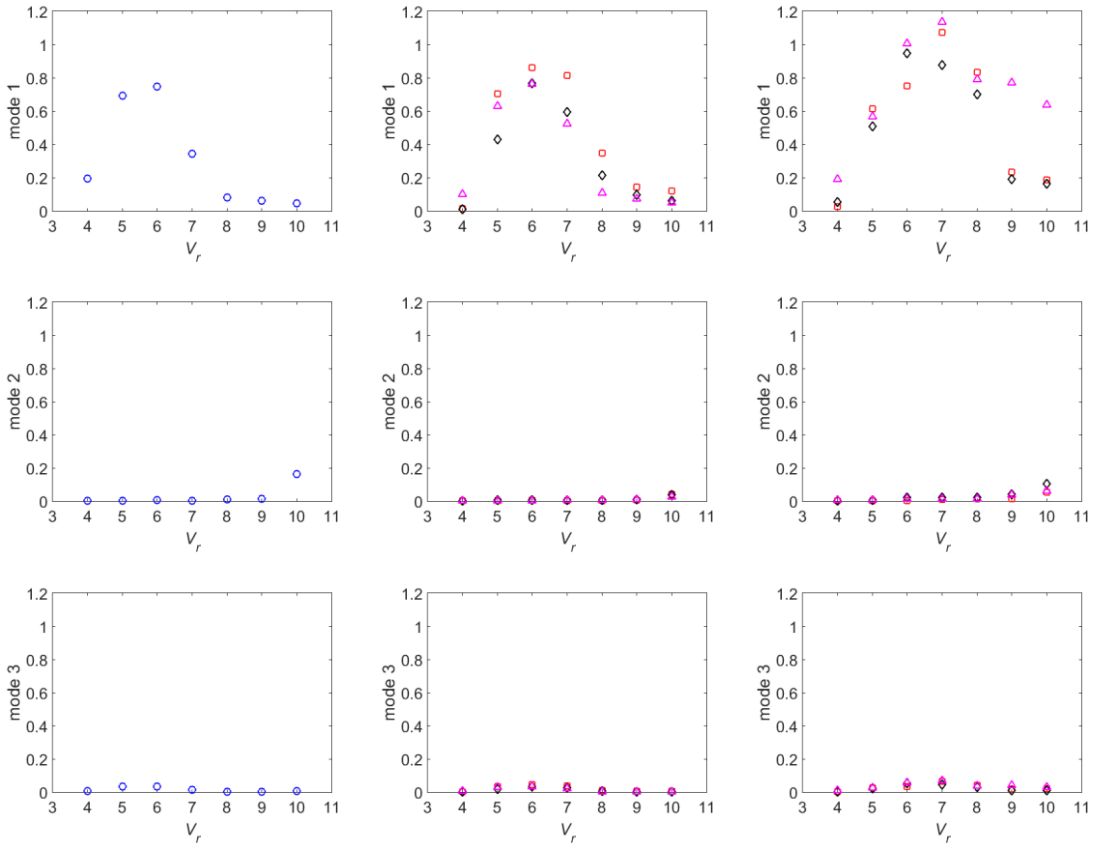

Fig. 6.8 Variation of modal amplitudes with V_r: (a) single flexible cylinder, (b) upstream cylinder and (c) downstream cylinder. ○, single flexible cylinder; □, tandem, S_x/D = 2.5; ◊, tandem, S_x/D = 3.5; Δ, tandem, S_x/D = 5.

6.2.1 Dominant Modes

In order to investigate the dominant modes of the flexible cylinders and the contributions of each vibration mode to the overall dynamic responses, the modal amplitudes are computed using the same modal decomposition method as in Huera-Huarte and Bearman (2009, 2011). The modal analysis is based on the fact that the cylinder response can be expressed in matrix form as a linear combination of its modes.

$$\mathbf{y}(z,t) = \mathbf{\Phi}(z)\mathbf{y}_M(t) \tag{6.1}$$

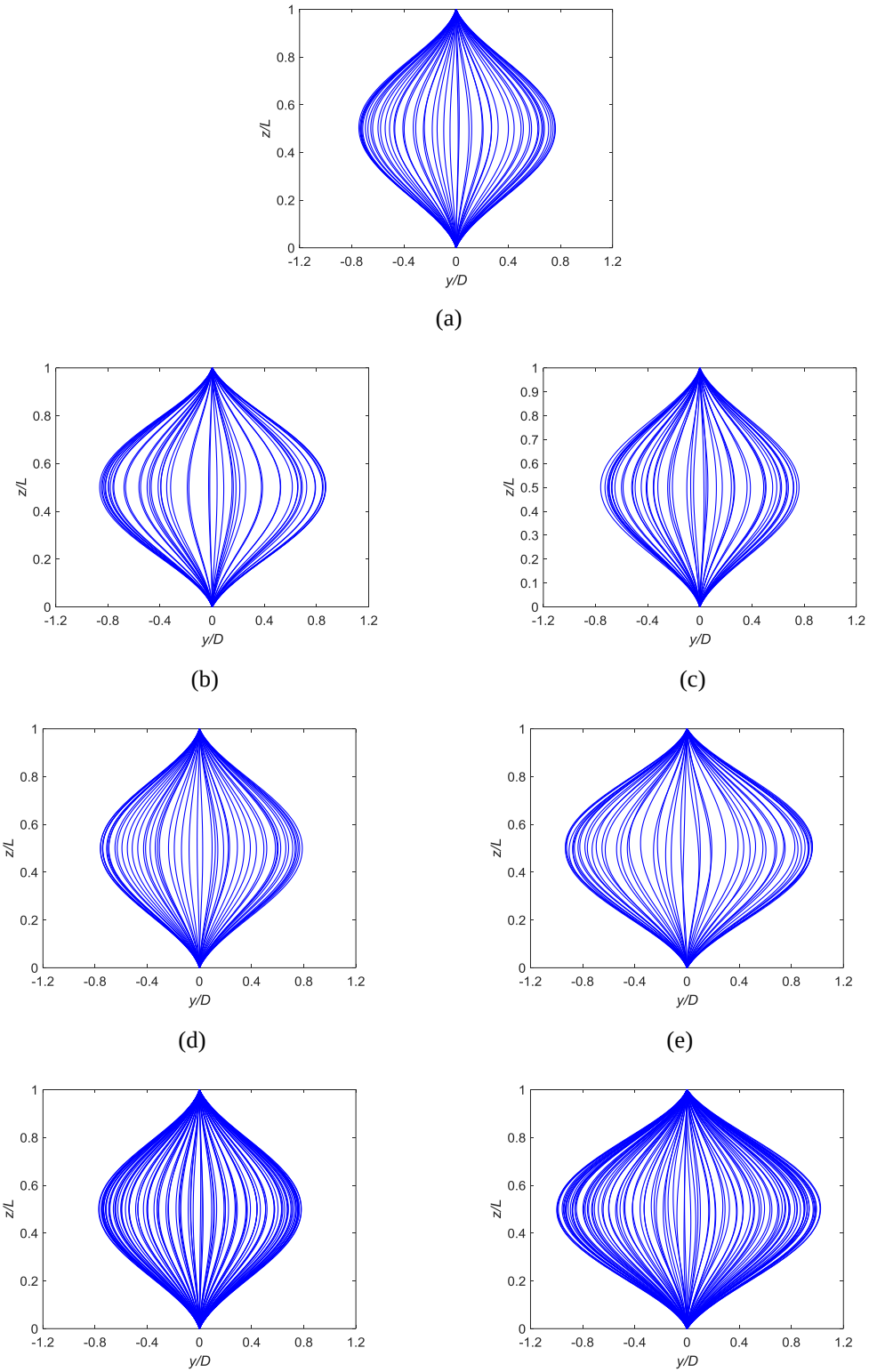

Fig. 6.9 Instantaneous nondimensional deflections of the flexible cylinders at V_r = 6: (a) single flexible cylinder, (b) upstream cylinder, S_x/D = 2.5, (c) downstream cylinder, S_x/D = 2.5, (d) upstream cylinder, S_x/D = 3.5, (e) downstream cylinder, S_x/D = 3.5, (f) upstream cylinder, S_x/D = 5 and (g) downstream cylinder, S_x/D = 5.

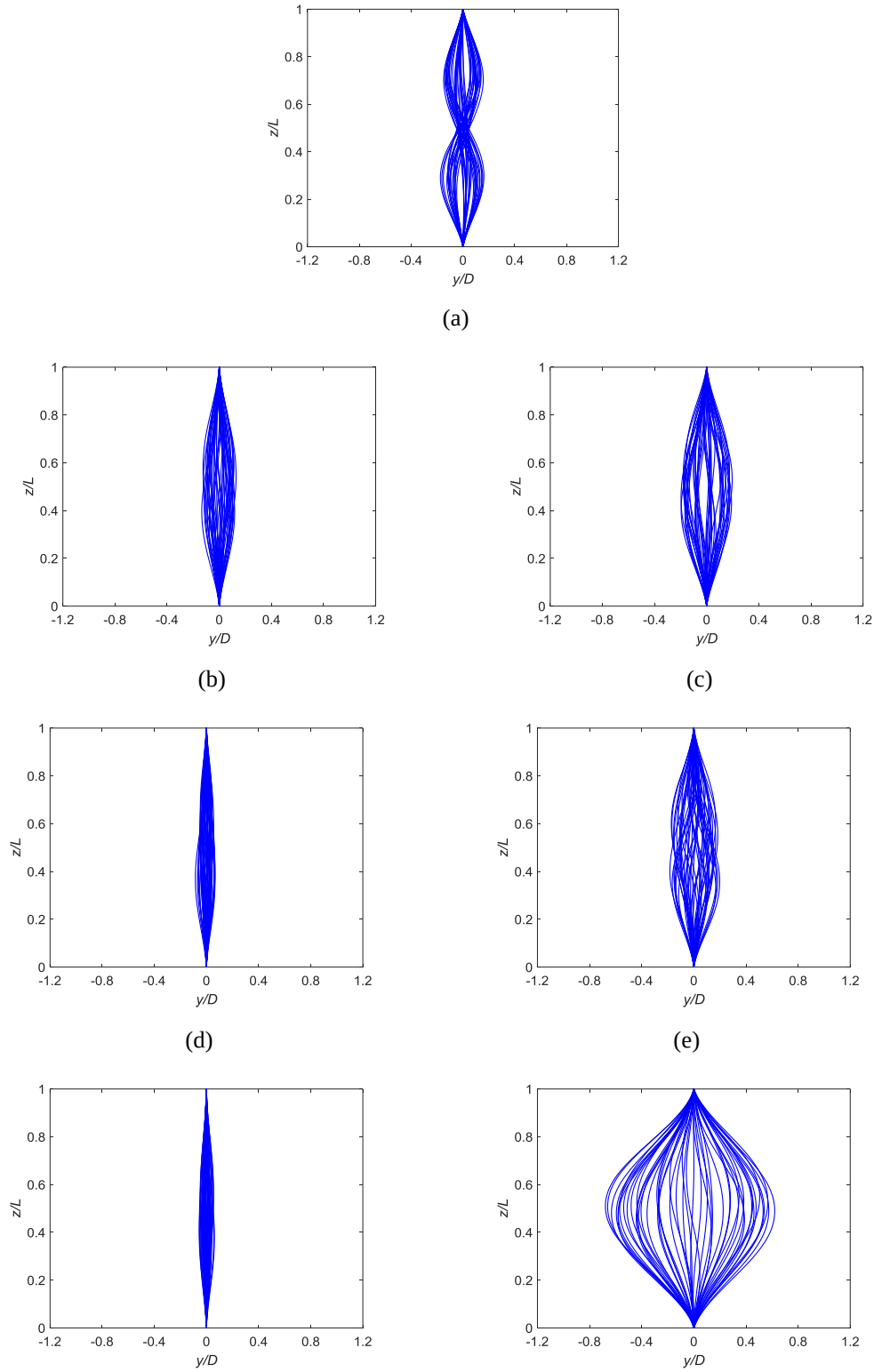

Fig. 6.10 Instantaneous nondimensional deflections of the flexible cylinders at V_r = 10: (a) single flexible cylinder, (b) upstream cylinder, S_x/D = 2.5, (c) downstream cylinder, S_x/D = 2.5, (d) upstream cylinder, S_x/D = 3.5, (e) downstream cylinder, S_x/D = 3.5, (f) upstream cylinder, S_x/D = 5 and (g) downstream cylinder, S_x/D = 5.

where $\mathbf{\Phi} = [\phi_1, \phi_2, \ldots, \phi_n]$ is the displacement modal-shape matrix which is built by stacking the nondimensional mode shapes normalised to be 1 at its maximum as columns. $\mathbf{y}(z, t) = [y_1(z_1, t), y_2(z_2, t), \ldots, y_n(z_n, t)]$ is the computed displacement matrix whose row vectors are the time series of the computed displacements along the cylinder. $\mathbf{y}_M(t)$ is the modal contribution matrix containing the time series of each mode's contribution to the overall response as the row vectors $\mathbf{y}_M(t) = [y_{M1}(t), y_{M2}(t), \ldots, y_{Mn}(t)]$. We have

$$\mathbf{y}_M(t) = \mathbf{\Phi}^{-1}(z)\mathbf{y}(z,t) \tag{6.2}$$

Fig. 6.8 shows the variation of the modal amplitudes of the first three modes with V_r. It can be seen from the figure that the dominant mode in most of the cases is the first mode. The contribution of the second mode is relatively small compared to that of the first mode at low V_r but it increases gradually with the increase of V_r. At $V_r = 10$, the modal amplitude of the second mode overtakes that of the first mode for a single flexible cylinder and for the two tandem flexible cylinders, the contribution of the second mode becomes comparable with that of the first mode except for the downstream cylinder at $S_x/D = 5$. This is because the difference in the eigenfrequencies of the first and second modes is small at $V_r = 10$ and the oscillation frequencies of the cylinders are in between the bandwidths of the two vibration modes. As for the contribution of the third mode, it remains small throughout the V_r range considered. Fig. 6.9 shows the instantaneous nondimensional deflections of the flexible cylinders at $V_r = 6$. As shown in Fig. 6.9, all the vibrations at $V_r = 6$ demonstrate clear first mode characteristics. The instantaneous nondimensional deflections of the flexible cylinders at $V_r = 10$ are presented in Fig. 6.10. It can be seen that the vibration of a single flexible cylinder is dominated by the second mode. Meanwhile, the vibrations of the two tandem flexible cylinders at $V_r = 10$ are not as regular as those at $V_r = 6$. The irregularity in the vibrations of the two tandem flexible cylinders is due to the fact that contributions of the first and the second modes are comparable at $V_r = 10$.

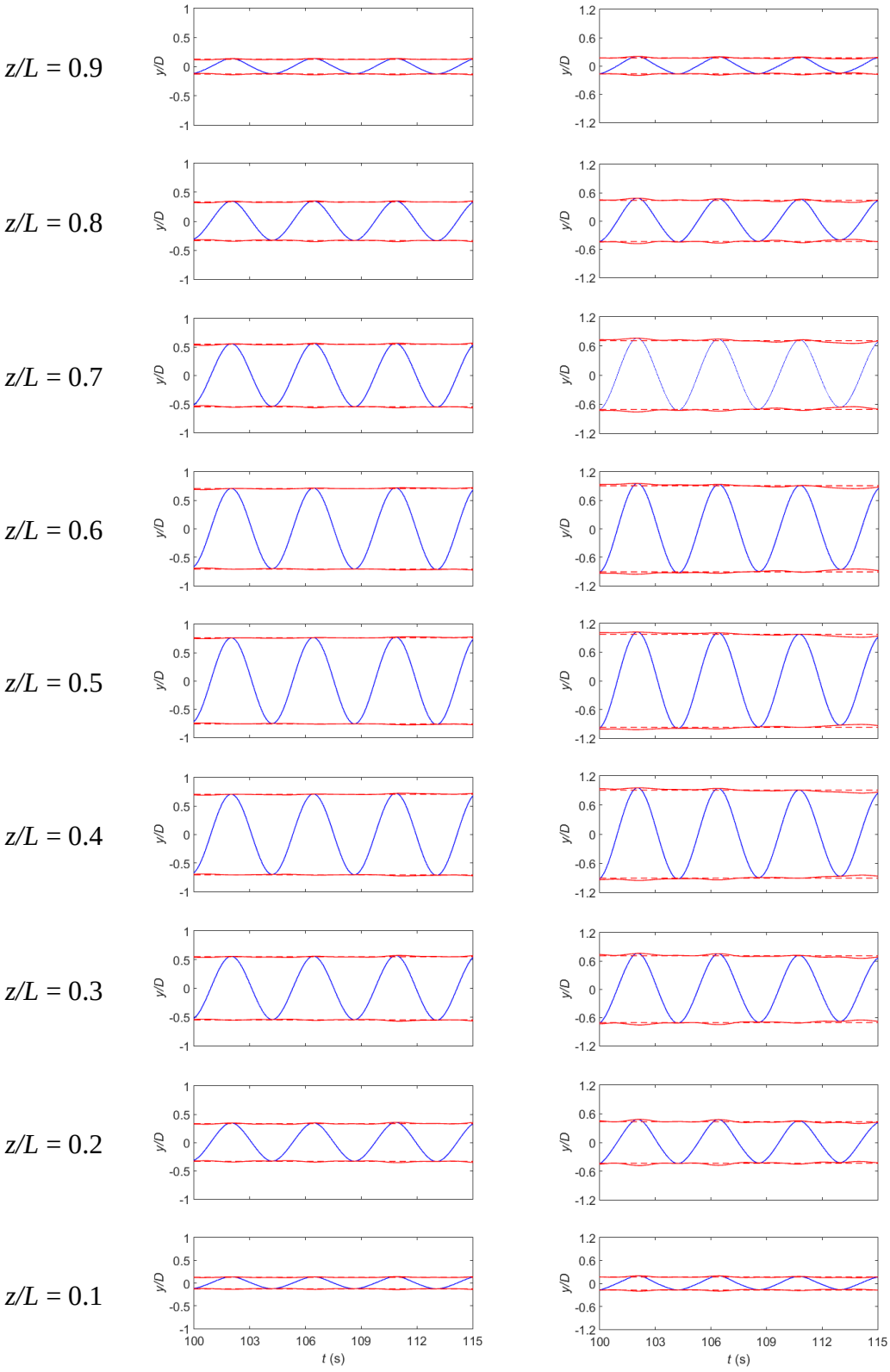

Fig. 6.11 Displacement time histories on different cross sections along two tandem flexible cylinders at S_x/D = 5: (a) upstream cylinder and (b) downstream cylinder. —, displacement signals; —, envelopes of the signals; ---, mean values of the envelopes.

6.2.2 Response Amplitudes

In Huera-Huarte and Bearman (2011), the authors calculated the envelopes of the displacements using the analytical signals described by Pikovsky *et al.* (2001), based on the use of Hilbert transforms and used the mean values of the envelopes to represent the vibration amplitudes (A_y/D). The same technique is used in the present study to determine A_y/D of the flexible cylinders. Fig. 6.11 shows the time histories of the nondimensional displacements (y/D) on the different cross sections along the two tandem flexible cylinders when $S_x/D = 5$ and $V_r = 6$. The solid red lines are the envelopes of the signals and the dashed red lines represent the mean values of the envelopes inside the selected time window by which the sectional vibration amplitudes ($A_y(z)/D$) are denoted. A_y/D is determined by the maximum value of $A_y(z)/D$ along each cylinder. Fig. 6.12 shows the variation of A_y/D with V_r for the two tandem flexible cylinders at different S_x/D. The results for a single flexible cylinder are also included for comparison. As the dominant mode in most of the cases considered in the present study is the first mode, the majority of A_y/D is observed at $z/L = 0.5$. The exceptions appear at $V_r = 10$ when the contribution of the second mode is of similar order of magnitude to that of the first mode. As shown in Fig. 6.10, for two tandem flexible cylinders, A_y/D appears around $z/L = 0.4$ and it shifts to $z/L \approx 0.3$ in the single flexible cylinder case where the second mode vibration dominates. In general, the A_y/D response curves in Fig. 6.12 are similar to the modal amplitude response curves of the first mode in Fig. 6.8 due to the fact that the first mode is the dominant mode in most of cases.

The maximum vibration amplitudes (A_{ym}/D) of the upstream cylinder for $S_x/D = 3.5$ and 5 are observed at an identical reduced velocity $V_r = 6$ with a magnitude of $A_{ym}/D \approx 0.76$ which is similar to A_{ym}/D of a single flexible cylinder. As the spacing decreases to $S_x/D = 2.5$, A_{ym}/D of the upstream cylinder increases to 0.87. The increase in A_{ym}/D of the upstream cylinder with the decrease of S_x/D was also observed by Huera-Huarte and Bearman (2011) in their experimental study with Re up to 12000 and by Papaioannou *et al.* (2008) in their 2D numerical simulation at Re

= 160. Compared to the upstream cylinder, the effect of the hydrodynamic interactions between the two tandem flexible cylinders on the vibration amplitude responses of the downstream cylinder is more obvious. The maximum vibration amplitudes of the downstream cylinder for S_x/D = 3.5 and 5 are found to be similar ($A_{ym}/D \approx 1$). This is different from the results of Papaioannou *et al.* (2008) in which the maximum vibration amplitude of the downstream cylinder in the case S_x/D = 3.5 is similar to that at S_x/D = 2.5. It is anticipated that this difference can be attributed to the difference in Re. Papaioannou *et al.* (2008) considered a relatively low Reynolds number Re = 160. In contrast, the Reynolds number in the present simulation is Re = 500. According to Sumner (2010), the critical spacing $(S_x/D)_{cr}$ is particularly sensitive to the Reynolds number. Ljungkrona and Sundén (1993) reported that $(S_x/D)_{cr}$ at Re = 160 is around 4.54 and it decreases to $(S_x/D)_{cr} \approx 3.7$ when Re increases to 500. Therefore, S_x/D = 3.5 is further below $(S_x/D)_{cr}$ in the study of Papaioannou *et al.* (2008) than in the present study resulting in A_{ym}/D at S_x/D = 3.5 being similar to that at S_x/D = 2.5 in their study.

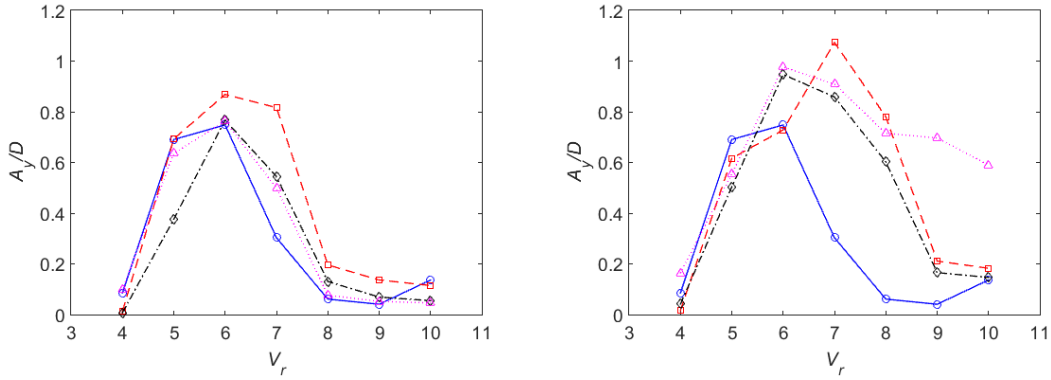

Fig. 6.12 Variation of the vibration amplitudes with V_r for flexible cylinders: (a) upstream cylinder and (b) downstream cylinder. —○—, single flexible cylinder; ---□---, tandem S_x/D = 2.5; -·-·◊·-·-, tandem, S_x/D = 3.5; ····Δ····, tandem, S_x/D = 5.

In the present study, when S_x/D reduces to 2.5, A_{ym}/D of the downstream cylinder increases to 1.1 and it shifts to a higher reduced velocity V_r = 7 due to the shielding effect of the upstream cylinder. When V_r = 8 – 10, for the three spacing ratios considered, the upstream cylinder shows a typical VIV response with very small

vibration amplitudes at high V_r. In terms of the downstream cylinder, a lower-branch VIV response is observed for S_x/D = 2.5 and 3.5 due to the fact that the vortices impinging on the downstream cylinder are connected to the shear layers of the upstream cylinder as illustrated by the spanwise vorticity ($\omega_z = \partial u_2/\partial x_1 - \partial u_1/\partial x_2$) contours in Fig. 6.24(a) and (b). In contrast, at S_x/D = 5, the completely detached vortices from the upstream cylinder in Fig. 6.24(c) cause the WIV of the downstream cylinder with large-amplitude vibration being maintained till the maximum V_r considered in the present study. Assi *et al.* (2013) classified the response of an elastically mounted downstream cylinder into three regimes: (i) before the vortex shedding frequency f_v = the natural frequency of the cylinder f_n, when the Strouhal number St = 0.2 is approaching f_n, the A_y/D response resembles the typical VIV response; (ii) the second regime, between $f_v = f_n$ and the equivalent natural frequency of the wake stiffness $f_w = f_n$, is marked by a steep slope in the A_y/D response curve and (iii) the third regime, beyond $f_w = f_n$ is characterised by a change of the slope in the A_y/D response curve. According to their descriptions, the A_y/D response of the flexible downstream cylinder at S_x/D = 5 in Fig. 6.12 is similar to the first two regimes and the third regime is not observed in the present study. The possible reasons will be provided in Section 6.2.3. We also notice that the present A_y/D in the second regime shows a plateau instead of increasing monotonically with V_r as shown in the experimental results of Hover and Triantafyllou (2001), Assi *et al.* (2010) and Assi *et al.* (2013). This discrepancy can be attributed to the different treatments of Re between the present study and the experiments. In the present study, V and Re are fixed and EI is varied to obtain the desired V_r. In contrast, V, as well as Re, is usually increased in the experiment in order to increase V_r. Assi *et al.* (2013) concluded that the increasing trend of the vibration amplitude in WIV is a direct effect of Re rather than V_r. Therefore, it is not surprising that the aforementioned difference in the A_y/D responses in the second regime exists between the present results and the experimental data.

6.2.3 Response Frequencies

Spectral analysis is conducted for the time histories of the displacements after the eliminations of the transient responses. The oscillation frequencies (f_{oy}) are determined by the frequencies associated with the prominent peaks of the y/D amplitude spectra and then normalised using f_1. Fig. 6.13 shows the comparison of the nondimensional oscillation frequencies (f_{oy}/f_1) between two tandem flexible cylinders and a single flexible cylinder. Based on the synchronisation between f_{oy} and f_1, the lock-in range of the single flexible cylinder in terms of V_r is from 4 to 7. In the lock-in range, f_{oy} locks into f_1 of the flexible cylinder. As V_r increases beyond the lock-in range, f_{oy} follows the Strouhal line. It can be seen that frequency response of a single flexible cylinder is similar to that of an elastically mounted circular cylinder reported by Zhao *et al.* (2014) and Govardhan and Williamson (2000). For two tandem flexible cylinders, the lock-in ranges for S_x/D = 2.5 and 3.5 are identical (i.e., V_r = 4 – 8). When S_x/D increases to 5, the lock-in range of the upstream cylinder changes to V_r = 5 – 8. The synchronisation of the downstream cylinder also starts at V_r = 5. However, it extends to the maximum V_r considered in the present simulation. The f_{oy}/f_1 response of the flexible downstream cylinder at S_x/D = 5 in Fig. 6.13 is similar to the first two regimes described by Assi *et al.* (2013), i.e., in the first regime, f_{oy} follows the Strouhal line; and in the second regime, f_{oy} remains rather close to f_1. As mentioned in the previous section, the third regime characterised by $f_{oy} = f_w$ is not observed for the flexible downstream cylinder with two fixed ends in the present simulation. The reasons are as follows: unlike an elastically mounted rigid cylinder, a flexible cylinder has an infinite number of natural frequencies. In order for the third regime to occur, f_w needs to dominate over all the natural frequencies of a flexible cylinder, which is unrealistic. In addition, for a flexible downstream cylinder with two fixed ends, the natural frequencies of two neighbouring vibration modes are so close that when f_w surpasses the natural frequency of one mode, it is already within the bandwidth of the next mode. Therefore, it is expected that, with the increase of V_r, the response of the present flexible downstream cylinder will repeat the first two regimes for the different vibration modes.

Unlike the single flexible cylinder, f_{oy} of the two tandem flexible cylinders in the post-lock-in range deviates from the Strouhal line, which reveals the effect of

hydrodynamic interactions on f_{oy} of the two tandem flexible cylinders. It should also be noted that f_{oy} of the downstream cylinder in the post-lock-in range is the same as the corresponding f_{oy} of the upstream cylinder for S_x/D = 2.5 and 3.5. This is related to the aforementioned fact that the vortices rolling up in the gap region between the two cylinders are still connected to the upstream cylinder through the shear layers when they impinge on the downstream cylinder. Consequently, for configurations with S_x/D = 2.5 and 3.5, the oscillation frequencies of the two cylinders in the post-lock-in range are identical.

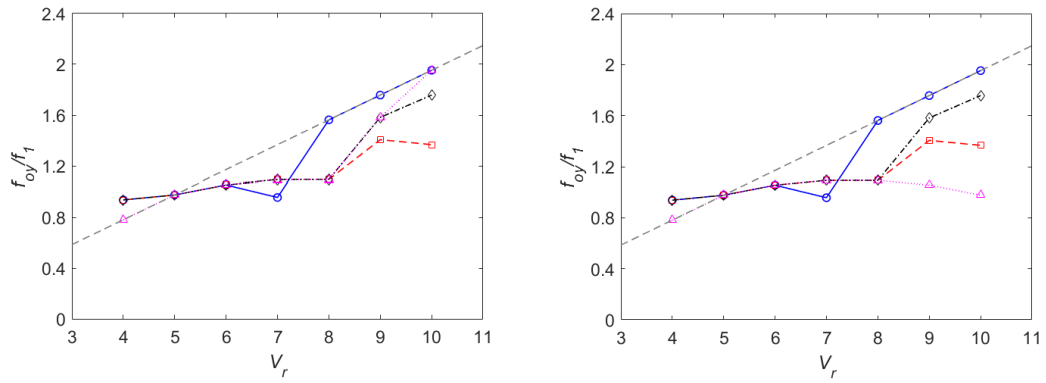

(a) (b)

Fig. 6.13 Variation of oscillation frequencies with V_r for flexible cylinders: (a) upstream cylinder and (b) downstream cylinder. ------, St = 0.2; —○—, single flexible cylinder; ---□---, tandem S_x/D = 2.5; -·-·◊·-·-, tandem, S_x/D = 3.5; ····Δ····, tandem, S_x/D = 5.

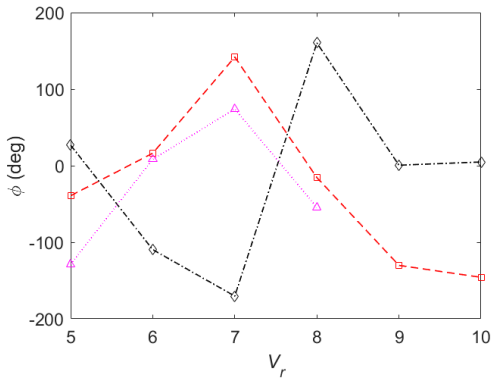

Fig. 6.14 Variation of phase differences ϕ between the cross-flow displacements at z/L = 0.5 of the two tandem flexible cylinders in the time range of t = 100 – 115 s with V_r: ---□---, tandem S_x/D = 2.5; -·-·◊·-·-, tandem, S_x/D = 3.5; ····Δ····, tandem, S_x/D = 5.

6.2.4 Phase Differences between Displacements of Two Tandem Flexible Cylinders

In this section, the phase differences (ϕ) between the cross-flow displacements at z/L = 0.5 of the two tandem flexible cylinders are analysed. The instantaneous phase difference $\phi(t)$ can be determined by using the concept of the analytical signal (Pikovsky *et al.*, 2001), based on Hilbert transforms. In the present study, $\phi(t)$ is calculated for the cases with two cylinders vibrating at an identical frequency in the time range of t = 100 – 115 s when the responses of the two cylinders are in their steady states. In addition, $\phi(t)$ at V_r = 4 is excluded as the motions of the cylinders are so small that the computed $\phi(t)$ is not reliable. In all the cases considered, $\phi(t)$ fluctuates around a constant value within the selected time range. Therefore, ϕ is represented by the mean value of $\phi(t)$. Fig. 6.14 illustrates the variations of ϕ with V_r for the three spacing ratios considered in the present study. In Fig. 6.14, positive ϕ means that y/D of the upstream cylinder leads that of the downstream cylinder and negative ϕ indicates that y/D of the upstream cylinder lags that of the downstream cylinder. Based on the changes in the sign of ϕ, it can be concluded that, for each of the three spacing ratios, the phase relation between the displacements of the two tandem flexible cylinders changes twice over the V_r range considered. At V_r = 5, ϕ is negative (i.e., y/D of the upstream cylinder lags that of the downstream cylinder) for S_x/D = 2.5 and 5 and it becomes positive (i.e., y/D of the upstream cylinder leads that of the downstream cylinder) when V_r increases to 6. With the increase of V_r, the sign of ϕ experiences a second change, taking place in the range of V_r = 7 – 8. As for S_x/D = 3.5, the V_r ranges associated with the two changes of the phase relation are the same as those of the other two spacing ratios, whereas the variations in phase relation are opposite. According to the discussion above, the two phase relation changes occur at reduced velocities corresponding to the left of the upper branch and the transition region between the upper and lower branches, respectively. Therefore, it can be speculated that the transitions from one mode of response to another (i.e., from the initial branch to the upper branch and from the upper branch to the lower branch) might have some bearing on the variations of the phase relation between the cross-flow displacements of the two flexible cylinders. Nevertheless, qualitative and

quantitative differences in the variations of ϕ with V_r are observed for different spacing ratios reflecting that the phase difference between the cross-flow displacements of the two tandem flexible cylinders depends on V_r and S_x/D. This conclusion agrees with that of Laneville and Brika (1999) drawn from their wind tunnel test on VIV of two tandem flexible cylinders.

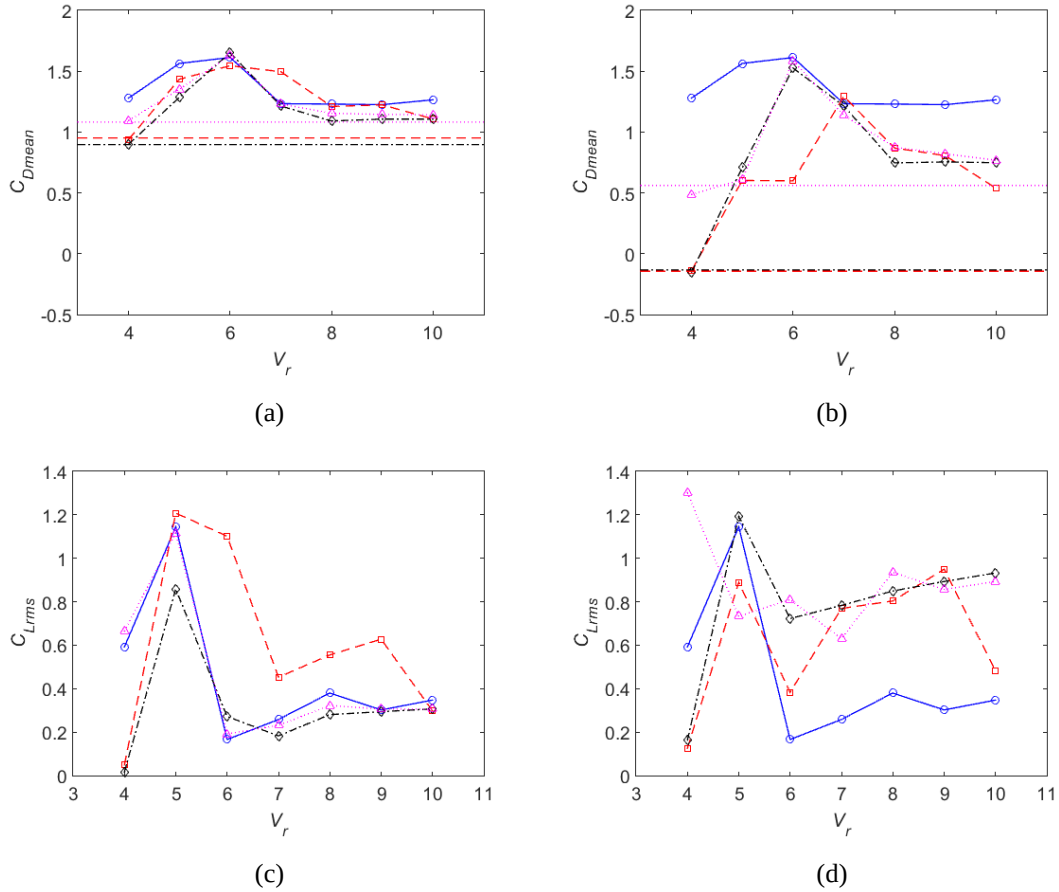

Fig. 6.15 Variation of total force coefficients with V_r for flexible cylinders: (a) C_{Dmean} of the upstream cylinder, (b) C_{Dmean} of the downstream cylinder, (c) C_{Lrms} of the upstream cylinder and (d) C_{Lrms} of the downstream cylinder. —○—, single flexible cylinder; ---□---, tandem S_x/D = 2.5; -·-·◊·-·-, tandem, S_x/D = 3.5; ····Δ····, tandem, S_x/D = 5.

6.2.5 Hydrodynamic Forces

The total drag and lift coefficients are defined as $C_D = F_x/(0.5\rho V^2 DL)$ and $C_L = F_y/(0.5\rho V^2 DL)$, respectively. Here, F_x and F_y represent the total in-line and cross-flow hydrodynamic forces computed by summing the dot product of the pressure and

viscous forces with the specified force vector over the cylinder surface. Fig. 6.15(a) and (b) show the variation of the mean drag coefficients (C_{Dmean}) with V_r. The constant horizontal lines indicate the values of each cylinder in the stationary system for each S_x/D. At V_r = 4, the vibration amplitudes of both cylinders for the three spacing ratios considered are very small. The flow around the two tandem flexible cylinders in Fig. 6.21 at each S_x/D are essentially similar to that around two tandem stationary cylinders in Fig. 6.6. Therefore, the mean drag coefficients of both cylinders are close to the values corresponding to the stationary system. Similar to the single flexible cylinder case, the mean drag coefficients of both cylinders reach their maximum values at reduced velocities where the maximum vibration amplitudes appear. For V_r in the post-lock-in range, the values of C_{Dmean} of the upstream cylinder at the three spacing ratios nearly coincide with each other. Overlaps in the C_{Dmean} response curves of the downstream cylinder are observed for S_x/D = 3.5 and 5 when $V_r \geq 5$.

Fig. 6.15(c) and (d) present the variation of the rms values of the oscillating lift coefficients (C_{Lrms}) with V_r. It shows that the C_{Lrms} response curve of the upstream cylinder at S_x/D = 5 resembles that of a single flexible cylinder indicating the negligible effect of the downstream cylinder on the upstream cylinder when S_x/D = 5. The maximum C_{Lrms} values of the upstream cylinder for the three spacing ratios considered appear at an identical reduced velocity V_r = 5. The C_{Lrms} of the upstream cylinder attains a common value when V_r is large enough that the response of the upstream cylinder is very small for S_x/D = 3.5 and 5. This is observed because the oscillations corresponding to those reduced velocities are still large enough to allow vortices to form in the gap region. Similar C_{Lrms} values of the two cylinders are observed at V_r = 4 for S_x/D = 2.5 and 3.5. The flow patterns in these two cases are essentially similar, namely the shear layers from the upstream cylinder reattach onto the surface of the downstream cylinder forming a single Kármán vortex street behind the downstream cylinder (Fig. 6.21(a) and (b)). However, large discrepancies take place in the C_{Lrms} response of the upstream cylinder between S_x/D = 2.5 and the other two spacing ratios for V_r = 6 – 9, which reflects that for S_x/D = 2.5 the oscillations at those reduced velocities are not large enough for the vortex shedding flow in the gap

region to get fully developed. As shown in Fig. 6.15(d), the C_{Lrms} responses of the downstream cylinder for all the three spacing ratios are quite different from each other and from that of the single flexible cylinder, which highlights the fact that the wake behind the downstream cylinder is a combination of the interacting wakes of the two cylinders.

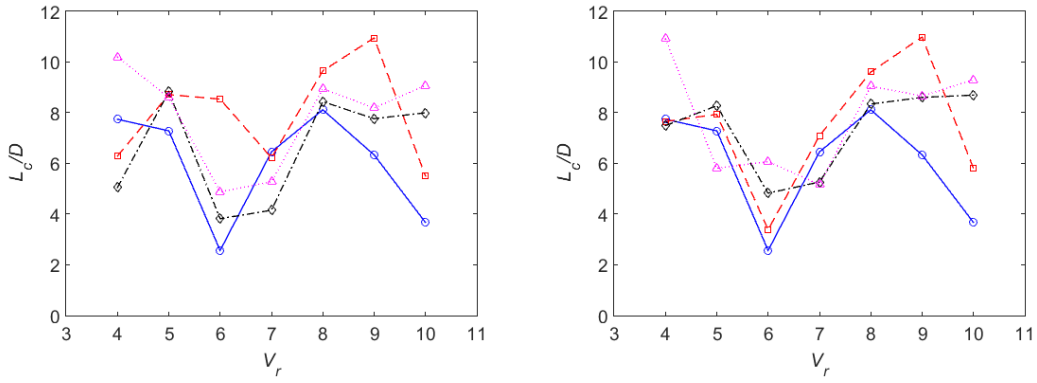

(a) (b)

Fig. 6.16 Variation of correlation lengths with V_r for flexible cylinders: (a) upstream cylinder and (b) downstream cylinder. —○—, single flexible cylinder; ---□---, tandem S_x/D = 2.5; -·-·◊·-·-, tandem, S_x/D = 3.5; ····△····, tandem, S_x/D = 5.

6.2.6 Correlation Lengths

The three-dimensionality of the flow in the near wake of the cylinder which determines the fluctuations of the forces acting on the cylinder is measured by the spanwise correlation length. Previous experimental and numerical studies on VIV of an elastically mounted circular cylinder indicated that there was a sharp drop in the spanwise correlation at the end of the upper branch near the transition between the upper and the lower branches, which does not diminish the response of the cylinder (Hover *et al.*, 2004; Hover *et al.*, 1998; Lucor *et al.*, 2003, 2005; Zhao *et al.*, 2014). In the present study, the autocorrelation function as defined in Lucor *et al.* (2005) is used to quantify the correlation. The autocorrelation function is described as follows.

$$R(l,t)=\frac{1}{N_t}\sum_{j=1}^{N_t}\left[\frac{(1/N_z)\sum_{i=1}^{N_z}C_L(z_i,t_j)C_L(z_i-l_k,t_j)}{(1-N_z)\sum_{i=1}^{N_z}C_L^2(z_i,t_j)}\right] \tag{6.3}$$

where $C_L(z_i, t_j)$ is taken to be the fluctuation of the original signal $C_L^*(z_i, t_j)$ from which its mean quantity is subtracted. The signal $C_L(z_i, t_j)$ is given by

$$C_L\left(z_i,t_j\right)=C_L^*\left(z_i,t_j\right)-\frac{1}{N_t}\sum_{n=1}^{N_t}C_L\left(z_i,t_n\right) \tag{6.4}$$

The shift l_k in Eq. (6.3) is prescribed to be

$$l_k=k\times l=k\times dz \text{ with } dz=l/N_z \text{ and } k=\left[0,1,2,\ldots\frac{N_z}{2}\right] \tag{6.5}$$

The correlation length L_C is then computed by

$$L_C\left(t\right)=2\int_0^{\frac{L/D}{2}}R\left(l,t\right)dl \tag{6.6}$$

Fig. 6.16 shows the variation of the nondimensional correlation lengths (L_C/D) with V_r for flexible cylinders. In general, L_C/D is quite large for low V_r around 4 or 5, representing the initial branch or the left of the upper branch. The large L_C/D is indicative of the strong two-dimensionality of the flow at low V_r. As V_r increases, there is a drop in L_C/D and it reaches its minimum value between V_r = 6 and 7, close to the transition region between the upper and lower branches. Finally, L_C/D increases for higher V_r corresponding to the lower branch of response. Lucor *et al.* (2005) conducted a 3D numerical study on 1DOF VIV of an elastically mounted circular cylinder and observed similar variation trends of L_C/D with V_r. For two tandem stationary cylinders, Wu *et al.* (1994) noticed that when the two cylinders were close together (S_x/D < 3), the downstream cylinder suppressed the shedding of the upstream vortices resulting in the large correlation lengths of the upstream cylinder. As the turbulence intensity and three-dimensionality of the impinging flow on the downstream cylinder were weak, high spanwise correlation was also observed for the downstream cylinder. For two tandem flexible cylinders undergoing VIV, in most of the cases, the correlation lengths of the two flexible cylinders at S_x/D = 2.5 are larger than those for S_x/D = 3.5 and 5, which agrees with the conclusion of Wu *et al.* (1994) drawn from two tandem stationary cylinders. With the increase of S_x/D, the suppression effect of the downstream cylinder on the upstream vortex shedding

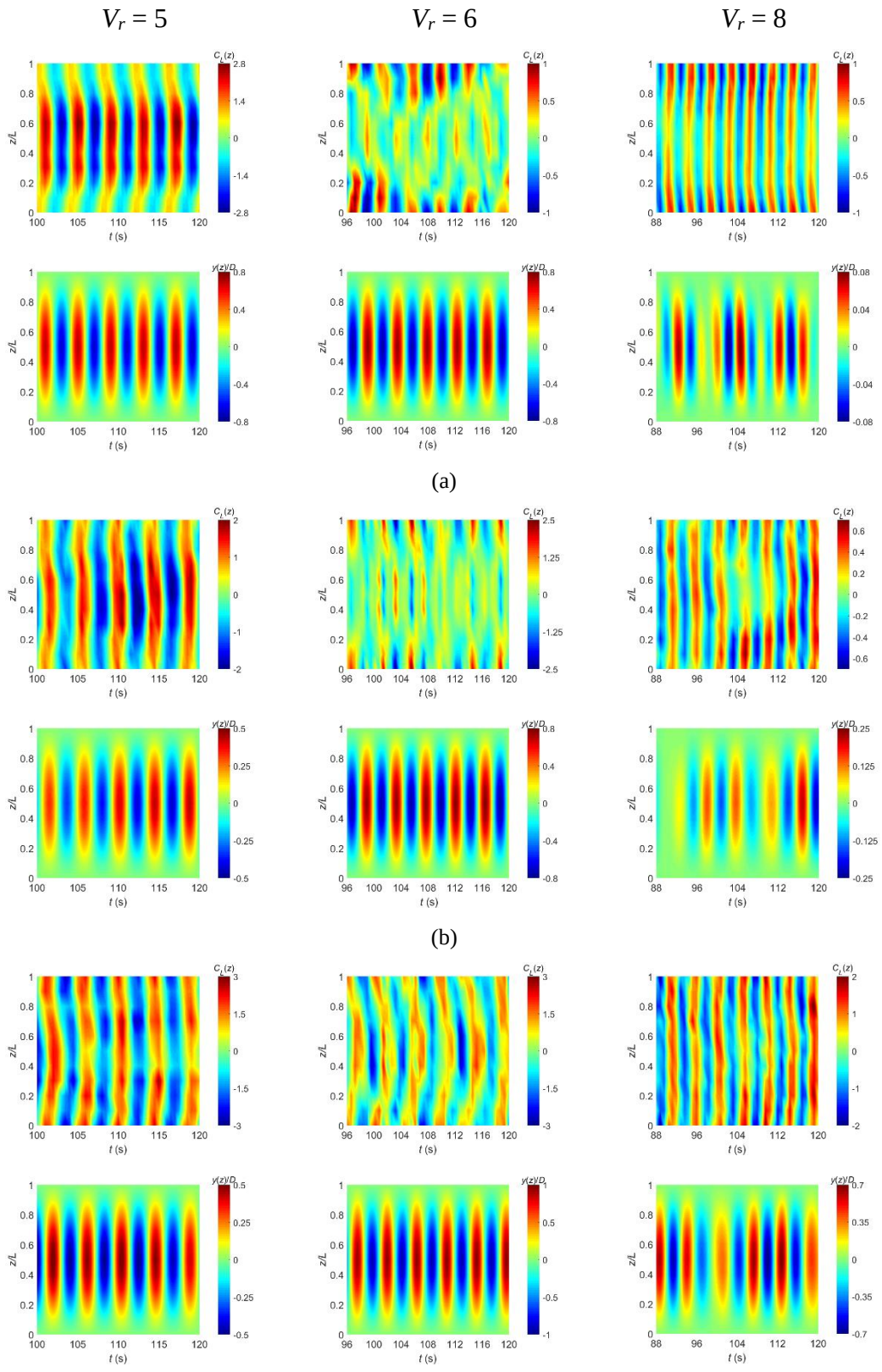

Fig. 6.17 Contours of sectional lift coefficients and sectional displacements of flexible cylinders: (a) single flexible cylinder, (b) upstream cylinder at S_x/D = 3.5 and (c) downstream cylinder at S_x/D = 3.5.

diminishes gradually, which leads to similar variations of the upstream cylinder correlation lengths for S_x/D = 3.5 and 5 when $V_r \geq 5$. However, as the level and form of the velocity perturbation introduced by the presence of the upstream cylinder depend on the distance between the two cylinders (Wu *et al.*, 1994), discrepancies in the correlation lengths of the downstream cylinder are observed for S_x/D = 3.5 and 5.

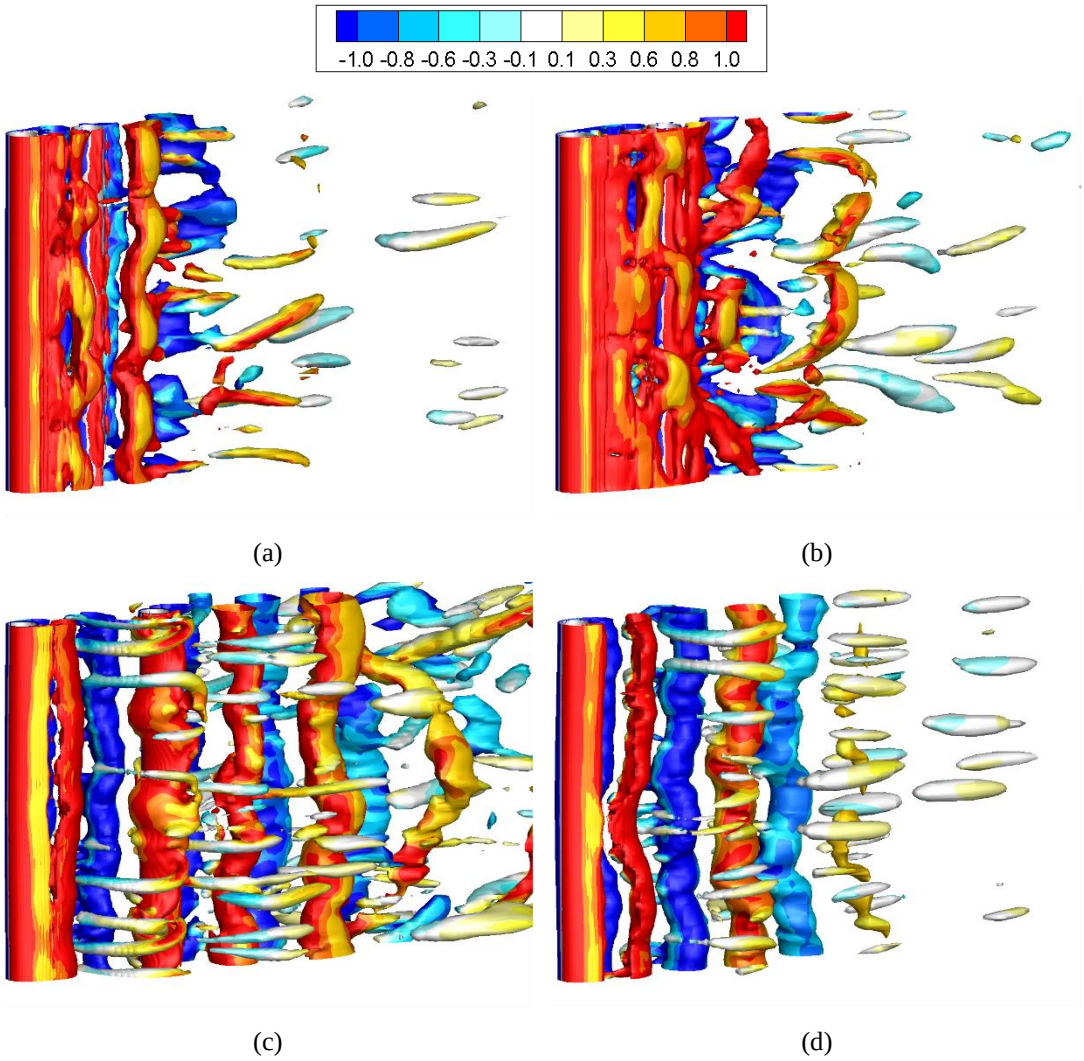

Fig. 6.18 Iso-surfaces of the eigenvalue λ_2 = -0.1 with the contours of the spanwise vorticity ω_z on the iso-surfaces for flexible cylinders at V_r = 4: (a) S_x/D = 2.5, (b) S_x/D = 3.5, (c) S_x/D = 5 and (d) single flexible cylinder.

The variations of the lift coefficients and the displacements along the span at V_r = 5, 6 and 8 are examined by plotting the contours of the sectional lift coefficients ($C_L(z)$

= $F_y(z)/(0.5\rho V^2 D)$, in which the sectional force in the cross-flow direction $F_y(z)$ is obtained by summing up the dot product of the pressure and viscous forces with the specified force vector over a circular cross section) and the sectional displacements ($y(z)/D$) on the $z - t$ plane. The choice of the three reduced velocities stems from the

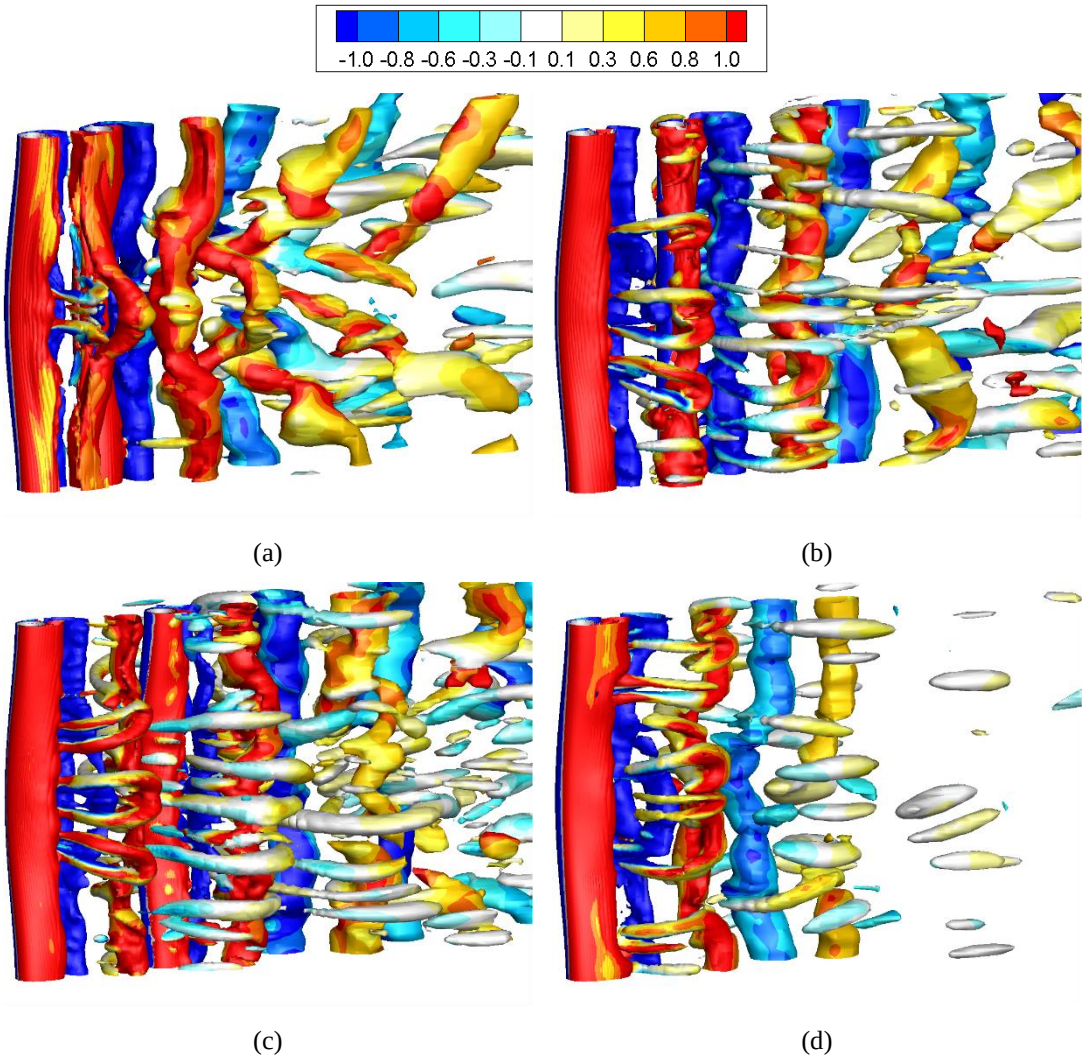

Fig. 6.19 Iso-surfaces of the eigenvalue λ_2 = -0.1 with the contours of the spanwise vorticity ω_z on the iso-surfaces for flexible cylinders at V_r = 6: (a) S_x/D = 2.5, (b) S_x/D = 3.5, (c) S_x/D = 5 and (d) single flexible cylinder.

following considerations. V_r = 5 represents the large correlation lengths on the left of the upper branch. V_r = 6 is near the region where the correlation lengths approach their minimum values and V_r = 8 stands for the large correlation lengths in the lower branch. The results for a single flexible cylinder and two tandem flexible cylinders

when S_x/D = 3.5 are given in Fig. 6.17. It can be seen that, for the single flexible cylinder and the two tandem flexible cylinders, when L_C/D is large, the distributions of $C_L(z)$ and $y(z)/D$ are well organised. The phase differences between $C_L(z)$ and $y(z)/D$ along the cylinder in each high correlation case are very regular. In contrast, when the correlation is low, $C_L(z)$ signals at different spanwise locations suffer from relative phase shifts despite the fact that $y(z)/D$ signals along the cylinder are nearly in phase. This is caused by the variation of the phase differences between $C_L(z)$ and $y(z)/D$ along the cylinder. The poor phasing between $C_L(z)$ and $y(z)/D$ leads to the decrease of the spanwise correlation (Lucor *et al.*, 2005).

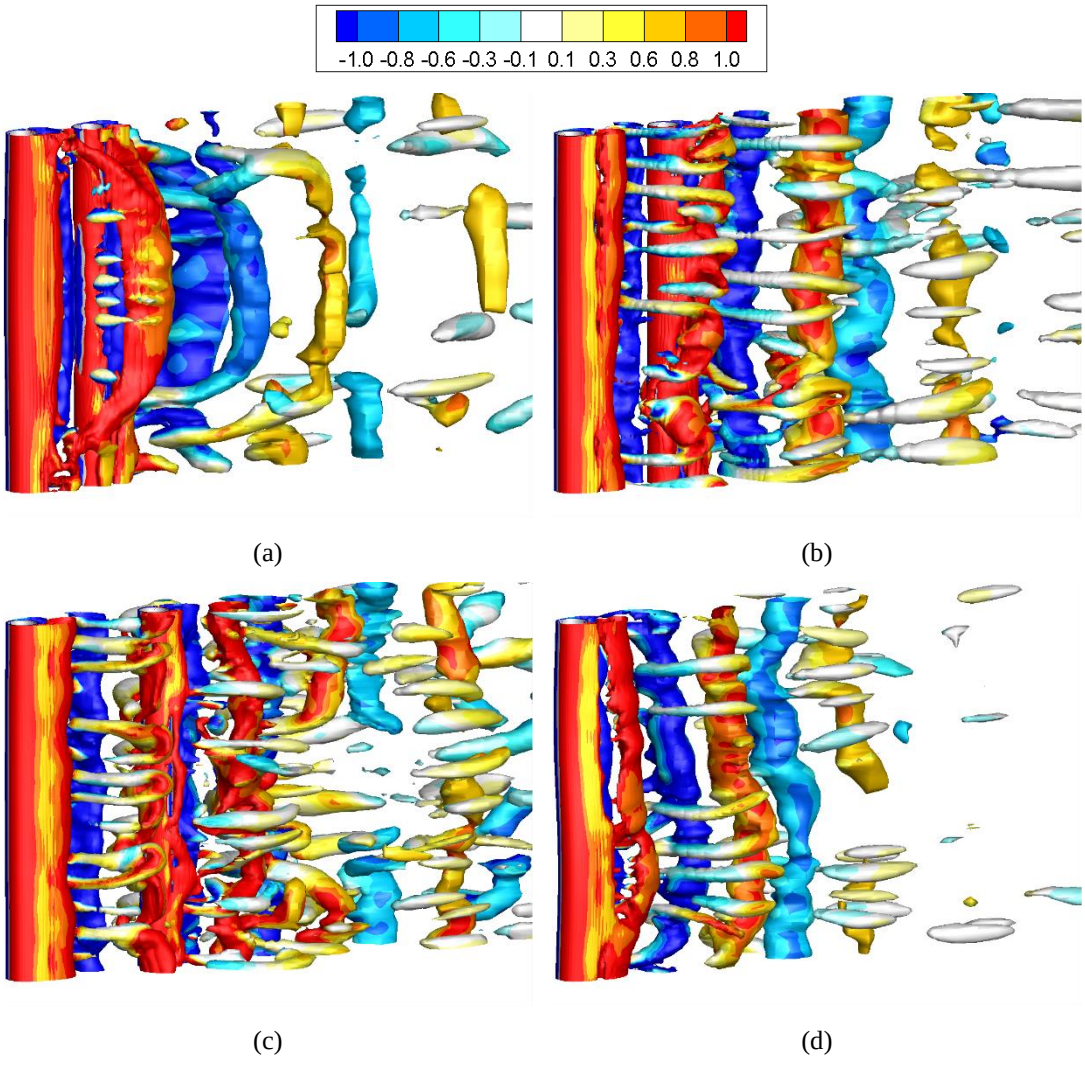

Fig. 6.20 Iso-surfaces of the eigenvalue λ_2 = -0.1 with the contours of the spanwise vorticity ω_z on the iso-surfaces for flexible cylinders at V_r = 10: (a) S_x/D = 2.5, (b) S_x/D = 3.5, (c) S_x/D = 5 and (d) single flexible cylinder.

6.2.7 Vortex Shedding

One of the objectives of the present study is to investigate the vortex shedding of two tandem flexible cylinders undergoing VIV. The λ_2 method by Jeong and Hussain (1995) is used to describe the 3D vortex structures in which λ_2 is the second eigenvalue of the symmetric tensor $\mathbf{S}^2 + \mathbf{\Omega}^2$. Here $\mathbf{S}$ and $\mathbf{\Omega}$ are the symmetric and antisymmetric parts of the velocity gradient tensor $\nabla\mathbf{u}$. Fig. 6.18- Fig. 6.20 present the iso-surfaces of λ_2 = -0.1 at V_r = 4, 6 and 10. The iso-surfaces are coloured by ω_z. It can be observed that the wake flow is totally 3D. The variation of the flow in the spanwise direction is stronger in the cases with smaller correlation lengths. Our previous discussions reveal that the hydrodynamic coefficients of the two tandem flexible cylinders at V_r = 4 are close to those of two tandem stationary cylinders. Therefore, it is expected that the 3D vortex structures of the two tandem flexible cylinders at this V_r should be similar to those of two tandem stationary cylinders. It can be seen from Fig. 6.18 that the 3D vortex structures of the flexible cylinders at V_r = 4 does share similar features to that of the corresponding stationary system for each S_x/D in Fig. 6.5. As shown in Fig. 6.18, when S_x/D = 2.5 and 3.5, the shear layers from the upstream cylinder reattach onto the surface of the downstream cylinder. When S_x/D increases to 5, vortex shedding occurs in the gap region between the two cylinders and the wake behind the downstream cylinder is a combination of the wakes of the two cylinders. Fig. 6.19 presents the 3D vortex structures of the flexible cylinders at V_r = 6. Compared to the results in Fig. 6.18, the variation of the flow in the spanwise direction becomes stronger in most of the cases apart from the upstream cylinder at S_x/D = 2.5. In the cases of S_x/D = 2.5 and 3.5 as shown in Fig. 6.19(a) and (b), the oscillations of the two tandem flexible cylinders provide extra time and space for the separated shear layers from the upstream cylinder to roll up into vortices. When V_r increases to 10, the correlation of the spanwise vortices of the flexible cylinders in most of the cases becomes higher than that at V_r = 6 except for the upstream cylinder at S_x/D = 2.5. It is worth noting that although the vibration amplitudes of the two tandem flexible cylinders for S_x/D = 2.5 and 3.5 are quite small at V_r = 10, the shear layers from the upstream cylinder still roll up.

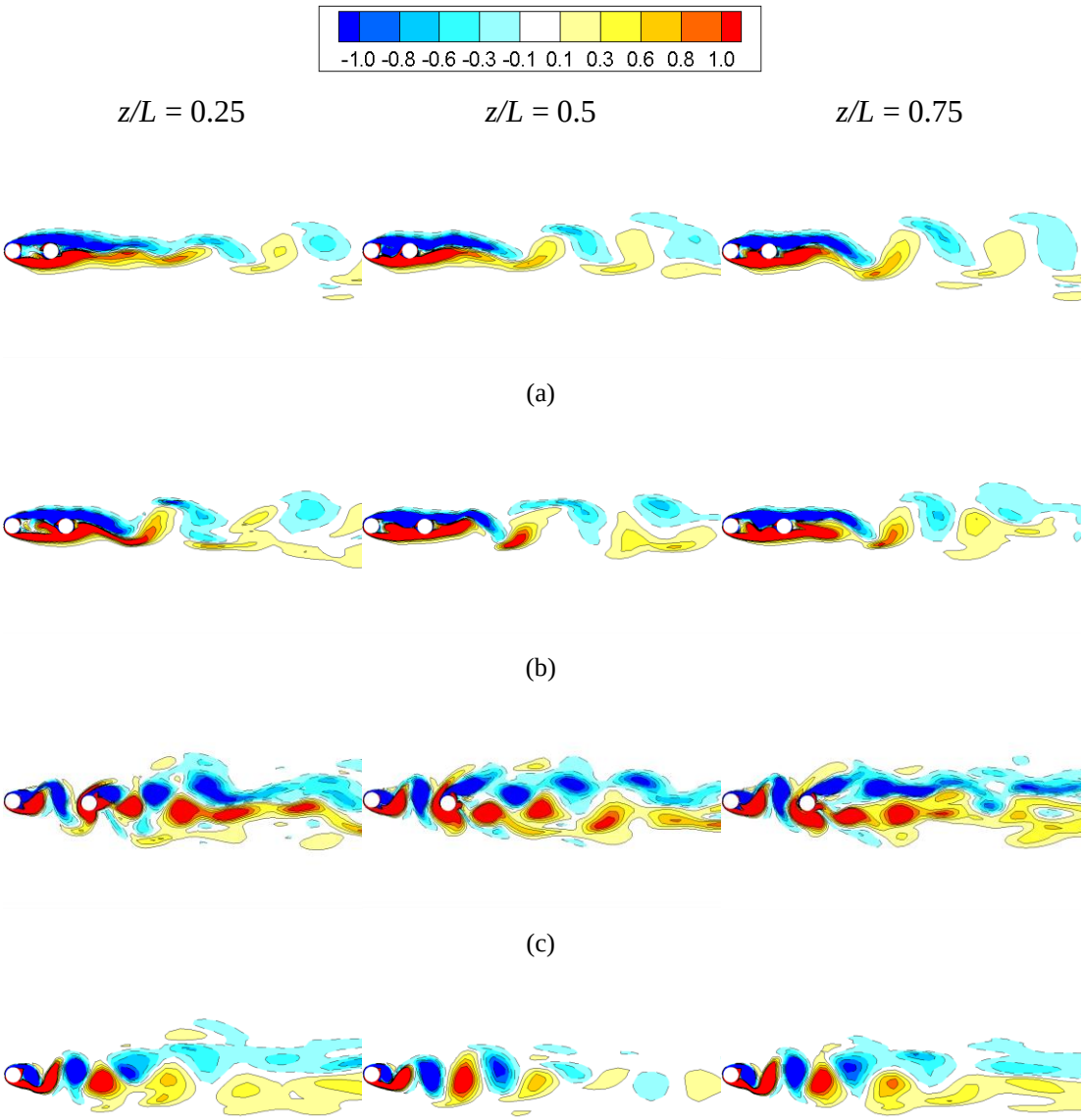

Fig. 6.21 Contours of spanwise vorticity ω_z on three different cross sections along the flexible cylinders at V_r = 4: (a) S_x/D = 2.5, (b) S_x/D = 3.5, (c) S_x/D = 5 and (d) single flexible cylinder.

The contours of ω_z on three different cross sections, i.e., z/L = 0.25, 0.5 and 0.75 are plotted in order to examine the variation of the flow in the spanwise direction of the flexible cylinders. The three cross sections are chosen in favour of those closer to the cylinder ends to avoid the potential end effect of the periodic boundary condition employed on the two spanwise boundaries. Fig. 6.21 shows ω_z contours of the flexible cylinders on the three cross sections when V_r = 4. The vortex shedding

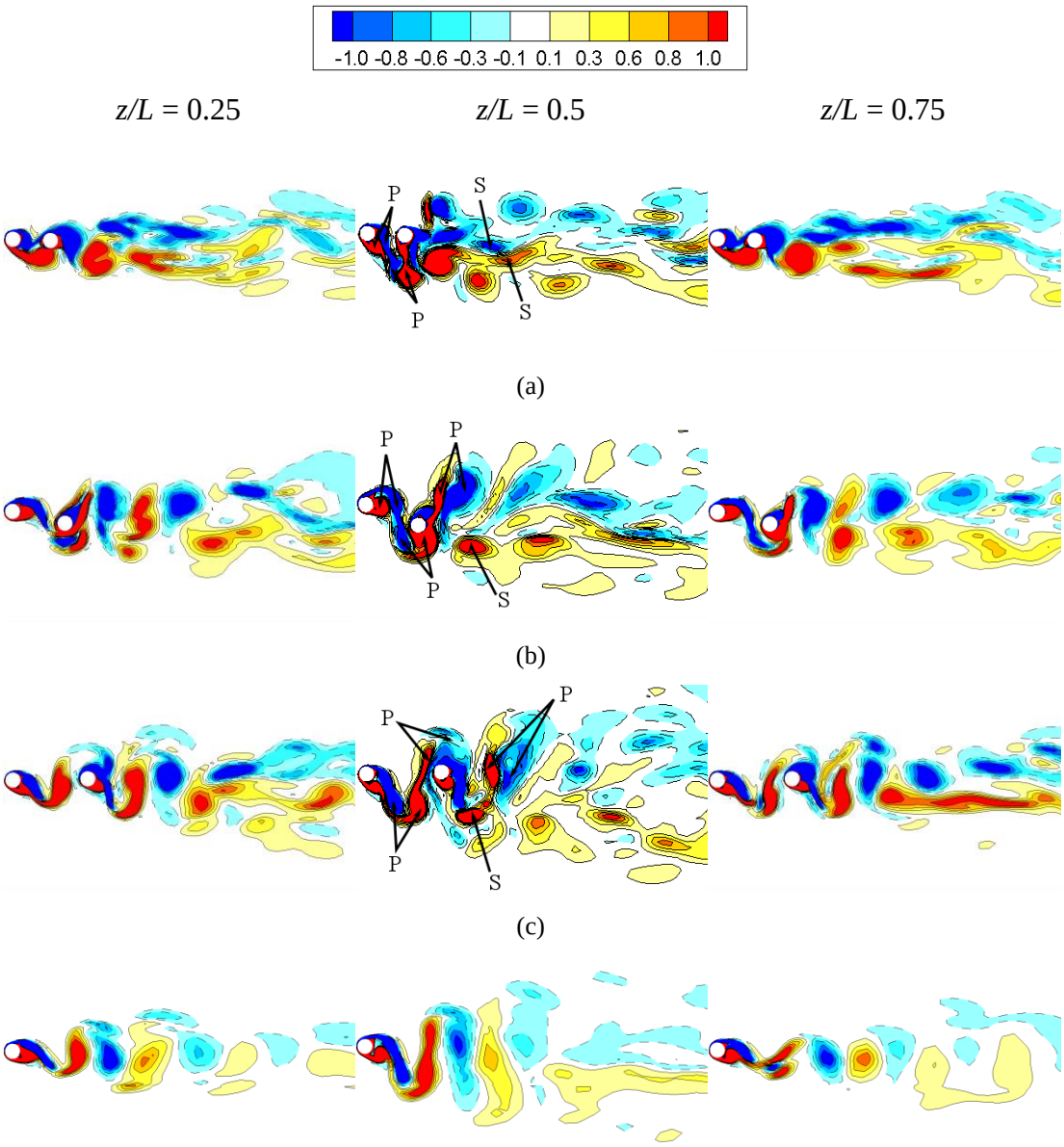

Fig. 6.22 Contours of spanwise vorticity ω_z on three different cross sections along the flexible cylinders at V_r = 6: (a) S_x/D = 2.5, (b) S_x/D = 3.5, (c) S_x/D = 5 and (d) single flexible cylinder.

patterns are qualitatively similar to those in Fig. 6.6 for stationary cylinders. When S_x/D = 2.5 and 3.5, the shear layers from the upstream cylinder reattach onto the surface of the downstream cylinder. At S_x/D = 5, vortex shedding occurs in the gap region between the two cylinders and a binary vortex street forms behind the downstream cylinder. The vortex shedding demonstrates a clear 2S pattern with two single vortices being formed in one cycle as described by Williamson and Roshko

(1988). As V_r increases to 6 (Fig. 6.22), the wake flow behind the flexible cylinders becomes wider. Vortices are formed behind the upstream cylinder in the gap region and these upstream vortices interact with the shear layers of the downstream cylinder when they impinge on the surface of the downstream cylinder. Variation of the vortex shedding modes along the cylinders is observed. The vortex shedding exhibits a 2S mode at z/L = 0.25 and 0.75 where the vibration amplitudes are small. With the increase of the vibration amplitudes towards the middle sections of the cylinders (z/L = 0.5), a 2P vortex shedding mode with two pairs of vortices being formed per cycle is observed behind the upstream cylinder. Brika and Laneville (1993, 1995) were the first to show evidence of the 2P vortex shedding mode in free vibration. The 2P mode at V_r = 6 in the present study is qualitatively similar to the 2P mode in the upper branch found by Govardhan and Williamson (2000) and Jauvtis and Williamson (2004), in which one vortex of each vortex pair is weaker than the other. This upper-branch 2P mode is associated with the large-amplitude vibration of the upstream cylinder. For the downstream cylinder, a 2S mode is observed at S_x/D = 2.5, whereas the vortex shedding for S_x/D = 3.5 and 5 shows a P + S mode where the cylinder sheds a single vortex and a vortex pair per cycle. Fig. 6.23 shows the vortex shedding on the middle sections of the two tandem flexible cylinders at different time instants in one vibration cycle when V_r = 6 for S_x/D = 3.5 and 5. It can be seen that a single vortex and a vortex pair are shed from the downstream cylinder when it moves to its positive and negative peaks, respectively, which confirms the P + S vortex shedding. Although the P + S mode is usually observed in forced vibration experiments (Griffin and Ramberg, 1974; Zdero *et al.*, 1995), it has also been identified in free vibration studies at reduced velocities around the maximum vibration amplitude for an elastically mounted cylinder at low Re (Bao *et al.*, 2012; Singh and Mittal, 2005) as well as a flexible cylinder undergoing low mode number vibrations (Gedikli and Dahl, 2014). Therefore, the large-amplitude vibration of the downstream cylinder when S_x/D = 3.5 and 5 is related to the P + S vortex shedding mode. The variation of the vortex shedding patterns along the cylinders causes the relative phase shifts of $C_L(z)$ which subsequently leads to the decrease of the spanwise correlation. The ω_z contours on three different sections along the flexible cylinders at V_r = 10 are displayed in Fig. 6.24. The shear layers from the upstream

cylinder are observed to roll up for S_x/D = 2.5 and 3.5 despite the vibration amplitudes of the two tandem flexible cylinders are quite small at V_r = 10. This confirms the observation from the 3D vortex structures as shown in Fig. 6.20. When S_x/D = 2.5, the vortex shedding patterns of the downstream cylinder vary from a 2S mode at z/L = 0.25 and 0.75 to a lower-branch 2P mode at z/L = 0.5. Unlike the upper-branch 2P mode observed at V_r = 6, the two vortices in each vortex pair of the lower-branch 2P mode at V_r = 10 have almost equal strength, thus the small-amplitude vibration of the downstream cylinder at S_x/D = 2.5 is related to the lower-branch 2P mode. A 2S vortex shedding mode is observed for the rest of the cases in Fig. 6.24.

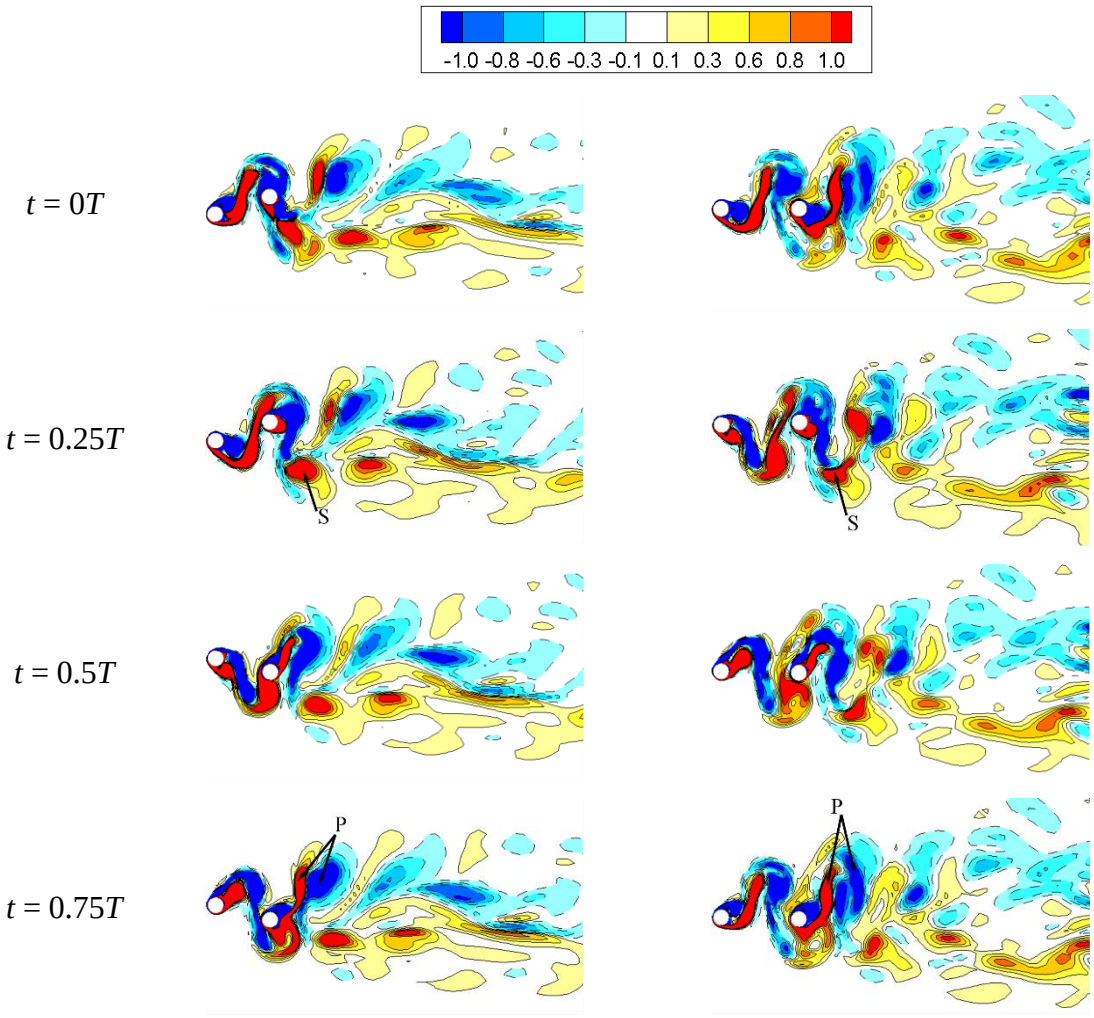

Fig. 6.23 Contours of spanwise vorticity ω_z on the middle sections of the two tandem flexible cylinders at different time instants in one vibration cycle when V_r = 6: (a) S_x/D = 3.5 and (b) S_x/D = 5.

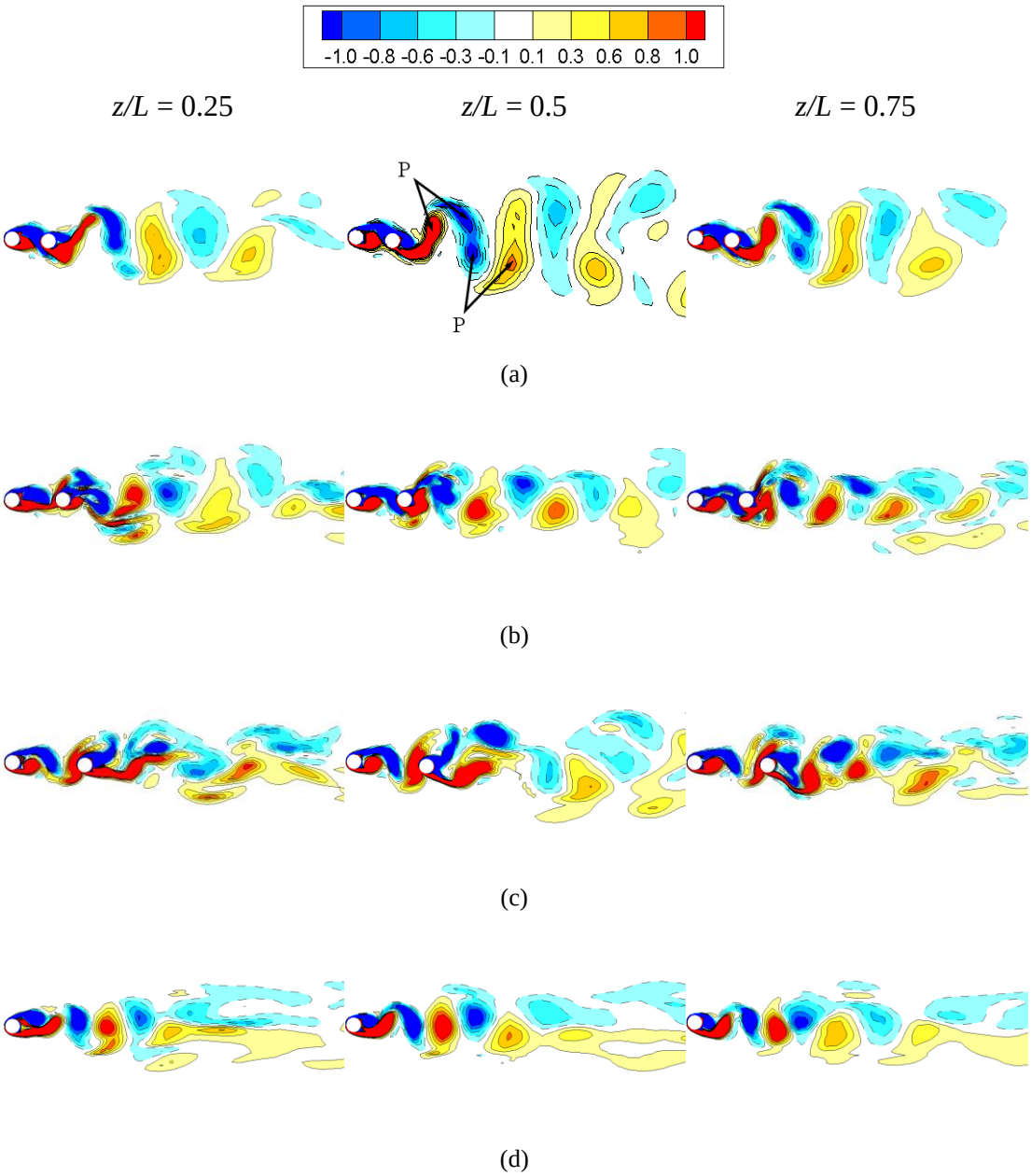

Fig. 6.24 Contours of spanwise vorticity ω_z on three different cross sections along the flexible cylinders at V_r = 10: (a) S_x/D = 2.5, (b) S_x/D = 3.5, (c) S_x/D = 5 and (d) single flexible cylinder.

6.3 Concluding Remarks

The effect of spacing on the cross-flow vortex-induced vibrations of two tandem flexible cylinders is numerically studied at Re = 500 using a two-way fluid-structure interaction method. A moderate mass ratio m^* = 10, a length-to-diameter ratio L/D = 12 and zero structural damping are considered in the simulation. The reduced

velocity ranges from 4 to 10 in which the flexible cylinders mainly vibrate in the first mode. Three spacing ratios (S_x/D = 2.5, 3.5 and 5) are examined. Based on the numerical results, the effect of spacing on the hydrodynamic interactions and the VIV responses of the two tandem flexible cylinders is investigated. In particular, the aspects which are rarely reported in previous studies such as the correlation lengths and the three-dimensional flow structures of two tandem flexible cylinders are provided. The conclusions are summarised as follows.

The upstream cylinder shows a classical VIV response for the three spacing ratios considered. As the vortices impinging on the downstream cylinder are still connected to the shear layers of the upstream cylinder in the cases of small spacing ratios, the response of the downstream cylinder is also similar to a typical VIV response. When the spacing between the two tandem flexible cylinders is large enough for the vortices to be shed from the upstream cylinder, the downstream cylinder undergoes WIV with large amplitudes at high reduced velocities and an extended lock-in range. However, in contrast to an elastically mounted downstream cylinder whose response can be divided into three regimes, only the first two regimes appear in the present study. The third response regime is not observed due to the fact that the flexible downstream cylinder with two fixed ends has an infinite number of natural frequencies and the natural frequencies of two neighbouring vibration modes are very close. As a constant Re is used in the present study, a flattened amplitude response is observed in the second response regime of the downstream cylinder.

It is found that there exist two changes of the phase relation between the cross-flow displacements of the two tandem flexible cylinders. The reduced velocity ranges associated with the phase relation changes correspond to the left of the upper branch and the transition between the upper and lower branches, respectively. Thus, the variations of phase relation between the cross-flow displacements of the two tandem flexible cylinders are presumed to be related to the transitions from the initial branch to the upper branch and from the upper branch to the lower branch. It is also found that the phase differences between the cross-flow displacements of the two tandem flexible cylinders are different for different reduced velocities and spacing ratios.

At very low reduced velocities when the vibration amplitudes of the two tandem flexible cylinders are small, the flow around the two tandem flexible cylinders is essentially similar to that around two tandem stationary cylinders. Consequently, the hydrodynamic force coefficients are close to the values corresponding to the stationary system. The effect of the downstream cylinder on the upstream cylinder is nearly negligible for large spacing ratios and for small spacing ratios, the oscillations in the classical VIV resonance range are not large enough for the vortex shedding to get fully developed in the gap region. For two vibrating flexible cylinders in tandem arrangement, the wake behind the downstream cylinder consists of the interacting wakes of the two cylinders.

The variation of the correlation lengths of the two tandem flexible cylinders with the reduced velocity roughly follows that of an elastically mounted circular cylinder. In particular, the correlation lengths experience a sharp drop at reduced velocities around the mode transition between the upper and lower branches. For small spacing ratios, the presence of the downstream cylinder suppresses the three-dimensionality of the upstream flow resulting in the large correlation lengths of the upstream cylinder and the resulting weak turbulence intensity and three-dimensionality of the upstream flow consequently lead to high spanwise correlation of the downstream cylinder. Large correlation lengths are found to be associated with regular phase differences between the sectional lift forces and sectional displacements along the cylinder, whereas the decrease of the spanwise correlation is attributed to the poor phasing between the forces and the displacements.

The flow around two tandem flexible cylinders subject to VIV is totally three-dimensional. The flow in the spanwise direction suffers stronger variations when the correlation is poor. In the case with spacing ratios corresponding to the reattachment regime of two tandem stationary cylinders, the large-amplitude vibrations of the two tandem flexible cylinders in the resonance range provide the time and space for the vortices to roll up in the gap. The wake in the lock-in range is found to be wider than that in the non-lock-in range. 2S, 2P and P + S vortex shedding modes are identified

in the present study. The upper-branch 2P mode with one vortex being stronger than the other in each vortex pair is found to be associated with the large-amplitude vibration of the upstream cylinder in the lock-in range and the P + S mode is related to the large-amplitude vibration of the downstream cylinder for S_x/D = 3.5 and 5. In contrast, the lower-branch 2P mode with two equal-strength vortices in each vortex pair leads to the lower-branch response of the downstream cylinder at high reduced velocity at S_x/D = 2.5. Variation of the vortex shedding modes in the spanwise direction is observed in the cases with poor spanwise correlation.

Overall, the present results confirmed various important conclusions obtained from previous experimental studies. Meanwhile, they also highlighted some new aspects such as the disappearance of the third response regime for a flexible downstream cylinder with two fixed ends at large spacing ratios, and also the transitions between different response branches (i.e., between the initial branch and the upper branch and between the upper branch and the lower branch) may explain the changes in the phase relation between the cross-flow displacements of the two flexible cylinders in tandem arrangement. Furthermore, the correlation lengths and the 3D flow structures which are difficult to obtain in the experimental studies are provided.

As the present study is one of the first few numerical investigations on VIV of two tandem flexible cylinders, there are also some limitations. The Reynolds number used in the numerical simulations is fixed which leads to the consequence that the monotonically increasing amplitude in the second response regime of the flexible downstream cylinder at large spacing ratios was not observed. Another limitation in terms of the Reynolds number is that the present study is focussed on a low Reynolds number regime. The maximum vibration amplitudes will be larger if a higher Reynolds number range is considered. The Reynolds number also influences the critical spacing of the two tandem flexible cylinders. The responses of the two tandem flexible cylinders, especially when S_x/D = 3.5 might change if the Reynolds number is different. Moreover, the vibrations of the two tandem flexible cylinders in the present study are confined in the cross-flow direction. As we considered a moderate mass ratio, the effect of the in-line degree of freedom on the maximum

vibration amplitudes may not be very pronounced. However, the in-line motion may have an impact on other aspects of the VIV responses of the two tandem flexible cylinders as it will change the gap between the two cylinders when they vibrate. Given the limitations of the present study, future research on coupled in-line and cross-flow VIV of two tandem flexible cylinders in a higher Re range is worthwhile.

A journal paper based on the investigations in this chapter titled ‘The effect of spacing on the vortex-induced vibrations of two tandem flexible cylinders’ has been published in Physics of Fluids.

Chapter 7 Conclusions and Future Work

"A conclusion is simply the place where you got tired of thinking."

-Dan Chaon

Vortex-induced vibration (VIV) of rigid and flexible circular cylinders is investigated using three-dimensional (3D) fluid-structure interaction (FSI) simulations. The numerical results in this thesis are compared with published numerical as well as experimental data. Different aspects of the VIV phenomenon are examined with particular attention being paid to the aspects which have not been fully addressed by previous studies such as the correlation lengths and the time-dependent 3D wake structures.

7.1 Conclusions

The main outcomes of the thesis are summarised as follows.

7.1.1 Three-Dimensional Numerical Simulation of Two-Degree-of-Freedom Vortex-Induced Vibration of a Circular Cylinder with Varying Natural Frequency Ratios

Two-degree-of-freedom (2DOF) VIV of an elastically mounted cicular cylinder with varying natural frequency ratios (f^*) is studied numerically. The fluid flow around the cylinder is modelled by solving the 3D unsteady incompressible Navier-Stokes equations and the structural vibrations of the cylinder are computed by 2DOF oscillators. The aim of this study is to investigate the effect of f^* on the 2DOF VIV responses and the 3D characteristics of the flow. The numerical results show that the vibration amplitude of the cylinder increases significantly and the peak amplitude shifts to a higher reduced velocity when f^* increases from 1 to 2. As identical in-line (IL) and cross-flow (CF) mass ratios are considered, the CF response at $f^* = 2$ shows a single peak. Dual resonance is observed for the range of f^* examined in this study. It is found that the cylinder prefers to move in counterclockwise figure-eight patterns

in the lock-in range while oblique figure-eight trajectories are observed in the lock-in range of $f^* = 1$. The third harmonic component in the lift coefficient increases with the increase of f^*. A decrease in the spanwise correlation occurs in the lock-in range and the minimum correlation length appears near the transition region between the lock-in and post-lock-in ranges. The 2S, P + S and 2P vortex shedding modes are observed in the present study. The oblique figure-eight trajectories are associated with a dominant P + S mode. The poor correlation of the sectional lift forces can be attributed to the variation of vortex shedding flow along the cylinder.

7.1.2 Large Eddy Simulation of Vortex-Induced Vibration of a Vertical Riser in Uniform and Linearly Sheared Currents

Numerical simulation is performed for VIV of a vertical riser subject to uniform and linearly sheared currents. The flow model is 3D unsteady incompressible Navier-Stokes equations in conjunction with the large eddy simulation (LES) wall-adapted local eddy-viscosity (WALE) model. A finite element model is built to simulate the ExxonMobil model vertical riser tested at the MARINTEK. Good agreement between the numerical results and the experimental data is achieved. The results show that the dominant mode numbers, the maximum root mean square amplitudes, the dominant frequencies and the fatigue damage indices increase with the flow velocity. It is found that dual resonance occurs at most of the locations along the riser. There is a third harmonic frequency component in the CF response at some locations along the riser. A frequency component at the CF response frequency appears in the IL response in certain cases together with the frequency component at twice the CF response frequency normally observed in the IL response. The vortex shedding mainly shows a 2S pattern and a 2P mode is found to be associated with the maximum vibration amplitude. One of the important findings of the present research is that it proves that it is incorrect to assume because the IL VIV response amplitude is small, the fatigue damage due to IL motion is small relative to the cross-flow damage. The present results show that the IL fatigue damage can be higher than that in the CF direction at low flow velocity as the accumulation of the fatigue damage is a function of the mode number and frequency of response. In the cases considered,

the mode number and frequency of the IL direction can be on the order of twice the mode number and frequency of the CF direction. The higher IL fatigue damage in these scenarios can be important for low flow velocity or low mode number applications.

7.1.3 The Effect of Spacing on the Vortex-Induced Vibrations of Two Tandem Flexible Cylinders

In this research, the effect of spacing on the VIV of two tandem flexible cylinders is investigated using 3D FSI simulations. A finite element solver for the structural dynamics of the two tandem flexible cylinders is coupled to the unsteady incompressible flow solver. Classical VIV responses are observed for the two tandem flexible cylinders when the spacing ratio (S_x/D) is small. When S_x/D is large enough for completely detached vortices from the upstream cylinder, the response of the upstream cylinder resembles the typical VIV response while the downstream cylinder exhibits wake-induced vibration (WIV) response. For flexible downstream cylinders with two fixed ends in the present study, the response of the flexible downstream cylinder is similar to the first two response regimes of the rigid downstream cylinder classified by Assi *et al.* (2013). It is found that the changes in the phase relation between the cross-flow displacements of the two tandem flexible cylinders are related to the transitions from one mode of response to another. There exist sharp drops in the correlation lengths of the two tandem flexible cylinders in the transition range between the upper and lower branches. Three vortex shedding modes are identified in the present research, i.e., 2S, P + S and 2P modes. The upper-branch 2P vortex shedding mode contributes to the large-amplitude vibration of the upstream cylinder and the P + S mode is associated with the large-amplitude vibration of the downstream cylinder for S_x/D = 3.5 and 5. In contrast, the small-amplitude vibration of the downstream cylinder in the post-lock-in range at S_x/D = 2.5 is the result of the lower-branch 2P mode. The variation of the vortex shedding flow along the flexible cylinders leads to the relative phase shifts of the sectional lift coefficients on different spanwise cross sections. The relative phase shifts of the sectional lift coefficients on different spanwise cross sections are the cause of poor

phasing between the forces and displacements related to the decrease of the correlation lengths.

7.2 Recommendations for Future Research

Fully 3D FSI simulation of VIV of rigid and flexible cylindrical structures is a relatively new research area. Due to the complexity of the problem and the limited time and computing resources available, the studies in this thesis inevitably have some limitations and there are other interesting areas which can be further investigated. Therefore, the following research topics are suggested for future research.

1. The Reynolds numbers (Re) in the present studies are relatively low which results in the maximum attainable amplitude and the vibration mode number being lower than the experimental results in higher Re regimes. Thus, numerical simulations of VIV of cylindrical structures at higher Re can be studied. Such a study can be beneficial for VIV prediction in high Re and high mode number applications.

2. The structural damping is neglected in this thesis. The prediction of the VIV response of cylindrical structures can be improved by taking into account the effect of damping. A reasonable mathematical model for the nonlinear damping is very important in deepwater riser VIV prediction.

3. The IL degree of freedom of the two tandem flexible cylinders can be considered in the future study. As a moderate mass ratio is used in the present research, the effect of the IL degree of freedom on the maximum vibration amplitudes may not be very pronounced. However, the IL motion may have an impact on other aspects of the VIV responses of the two tandem flexible cylinders as it will change the gap between the two cylinders. More importantly, for cylindrical structures in offshore engineering with low mass ratios, the IL degree of freedom can cause a dramatic change in the FSI.

4. The numerical simulations on VIV of flexible cylinders presented in this thesis are all performed for vertical configurations. The numerical methods can be developed and applied to steel catenary risers (SCRs). Apart from the analyses conducted for vertical layouts, the influence of changing flow direction and its effect on the in-plane and out-of-plane oscillations of SCRs can be investigated.

5. The present FSI model can provide reliable and accurate predictions of VIV of rigid and flexible circular cylinder subject to uniform and linearly sheared flow. The offshore structures are usually exposed to ocean waves as well. Hence, the effect of ocean waves can be taken into account as this will result in more realistic replication of environmental conditions.

6. VIV of cylindrical structures caused by external flow is investigated in this thesis. In offshore engineering, another cause of the fatigue damage of the flowlines, risers and subsea jumpers is the internal slug flow-induced vibration (FIV). The combined external flow VIV and the internal slug FIV is of great practical importance and is suggested for further study.

7. Recent research has confirmed a new type of VIV in risers, purely caused by vessel motion. Vessel motion-induced VIV occurs because the riser is exposed to the equivalent oscillating current due to its own motions relative to the still water. Preliminary results indicate that vessel motion-induced VIV is quite different from ocean current-induced VIV and is characterised by distinct time-varying features. Therefore, another proposed future study can be numerical simulation of vessel motion-induced VIV of marine risers.

References

Al-Jamal, H., Dalton, C., 2004. Vortex induced vibrations using Large Eddy Simulation at a moderate Reynolds number. Journal of Fluids and Structures 19, 73 - 92.

Alam, M.M., Moriya, M., Takai, K., Sakamoto, H., 2003. Fluctuating fluid forces acting on two circular cylinders in a tandem arrangment at a subcritical Reynolds number. Journal of Wind Engineering and Industrial Aerodynamics 91, 139 - 154.

ANSYS Inc., 2013a. ANSYS CFX-Solver Theory Guide, Canonsburg, USA.

ANSYS Inc., 2013b. ANSYS Mechanical APDL Element Reference, Canonsburg, USA.

Assi, G.R.S., Bearman, P.W., Carmo, B.S., Meneghini, J.R., Sherwin, S.J., Willden, R.H.J., 2013. The role of wake stiffness on the wake-induced vibration of the downstream cylinder of a tandem pair. Journal of Fluid Mechanics 718, 201 - 245.

Assi, G.R.S., Bearman, P.W., Kitney, N., 2009. Low drag solutions for suppressing vortex-induced vibration of circular cylinders. Journal of Fluids and Structures 25, 666 - 675.

Assi, G.R.S., Bearman, P.W., Meneghini, J.R., 2010. On the wake-induced vibration of tandem circular cylinders: the vortex interaction excitation mechanism. Journal of Fluid Mechanics 661, 365 - 401.

Bai, X., Qin, W., 2014. Using vortex strength wake oscillator in modelling vortex-induced vibration in two degrees of freedom. European Journal of Mechanics-B/Fluids 48, 165 - 173.

Bao, Y., Huang, C., Zhou, D., Tu, J., Han, Z., 2012. Two-degree-of-freedom flow-induced vibrations on isolated and tandem cylinders with varying natural frequency ratios. Journal of Fluids and Structures 35, 50 - 75.

Barth, T.J., Jespersen, D.C., 1989. The design and application of upwind schemes on unstructured meshes, 27th Aerospace Sciences Meeting. AIAA, Reno, USA.

Barton, C., Hambling, H., Albaugh, E.K., Mahlstedt, B., Davis, D., 2015. 2015 Deepwater Solutions and Records for Concept Selection, Houston, USA.

Batcho, P., Karniadakis, G.E., 1991. Chaotic transport of two- and three-dimensional flow past a cylinder. Physics of Fluids A 3, 1051 - 1062.

Bearman, P.W., 2011. Circular cylinder wakes and vortex-induced vibrations. Journal of Fluids and Structures 27, 648 - 658.

Biermann, D., Herrnstein, W.H., 1934. The interference between struts in various combinations. NACA.

Blackburn, H., Henderson, R., 1996. Lock-in behaviour in simulated vortex-induced vibration. Experimental Thermal and Fluid Science 12, 184 - 189.

Blevins, R.D., 1977. Flow-Induced Vibration. Van Nostrand Reinhold Company, New York, USA.

Blevins, R.D., Coughran, C.S., 2009. Experimental investigation of vortex-induced vibration in one and two dimensions with variable mass, damping and Reynolds number. Journal of Fluids Engineering 131 (101202), 1 - 7.

Bourguet, R., Karniadakis, G.E., Triantafyllou, M.S., 2013. Phasing mechanisms between the in-line and cross-flow vortex-induced vibrations of a long tensioned beam in shear flow. Computers and Structures 122, 155 - 163.

Bourguet, R., Modarres-Sadeghi, Y., Karniadakis, G.E., Triantafyllou, M.S., 2011. Wake-body resonance of long flexible structures is dominated by counterclockwise orbits. Physical Review Letters 107 (134502), 1 - 4.

Brany, M., Chakkarapani, V., Coombes, J., Harte, G., Lega, J.C., Melillo, J., Oke, O., Whooley, A., 2015. 2015 Deepwater Production Riser Systems and Components, Houston, USA.

Brika, D., Laneville, A., 1993. Vortex-induced vibrations of a long flexible circular cylinder. Journal of Fluid Mechanics 250, 481 - 508.

Brika, D., Laneville, A., 1995. An experimental study of the aeolian vibrations of a flexible circular cylinder at different incidences. Journal of Fluids and Structures 9, 371 - 391.

Brika, D., Laneville, A., 1997. Wake interference between two circular cylinders. J. Wind Eng. Ind. Aerodyn. 72, 61-70.

Brika, D., Laneville, A., 1999. The flow interaction between a stationary cylinder and a downstream flexible cylinder. J. Fluids Struct. 13, 579-606.

Carmo, B.S., Assi, G.R.S., Meneghini, J.R., 2013. Computational simulation of flow-induced vibration of a circular cylinder subjected to wake interference. Journal of Fluids and Structures 41, 99 - 108.

Carmo, B.S., Meneghini, J.R., Sherwin, S.J., 2010a. Possible states in the flow around two circular cylinders in tandem with separations in the vicinity of the drag inversion spacing. Physics of Fluids 22 (054101), 1 - 7.

Carmo, B.S., Meneghini, J.R., Sherwin, S.J., 2010b. Secondary instabilities in the flow around two circular cylinders in tandem Journal of Fluid Mechanics 644, 395 - 431.

Carmo, B.S., Sherwin, S.J., Bearman, P.W., Willden, R.H.J., 2011. Flow-induced vibration of a circular cylinder subjected to wake interference at low Reynolds number. Journal of Fluids and Structures 27, 503 - 522.

Catalano, P., Wang, M., Iaccarino, G., Moin, P., 2003. Numerical simulation of the flow around a circular cylinder at high Reynolds numbers. International Journal of Heat and Fluid Flow 24, 463 - 469.

Chaplin, J.R., Bearman, P.W., Huera Huarte, F.J., Pattenden, R.J., 2005. Laboratory measurement of vortex-induced vibrations of a vertical tension riser in a stepped current. Journal of Fluids and Structures 21, 3 - 24.

Chen, H.C., Chen, C.R., Huang, K., 2013. CFD simulation of vortex-induced and wake-induced vibrations of dual vertical risers, In: Proceedings of the 23rd (2013) International Offshore and Polar Engineering, Anchorage, Alaska, USA.

Constantinides, Y., Oakley, O.H., 2008. Numerical prediction of VIV and comparison with field experiments, OMAE2008-57215, In: Proceedings of the ASME 27th International Conference on Ocean, Offshore and Arctic Engineering, Estoril, Portugal.

Dahl, J.M., 2008. Vortex-induced vibration of a circular cylinder with combined in-line and cross-flow motion, Department of Mechanical Engineering Massachusetts Institute of Technology, Cambridge, Massachusetts, USA.

Dahl, J.M., Hover, F.S., Triantafyllou, M.S., 2006. Two-degree-of-freedom vortex-induced vibrations using a force assisted apparatus. Journal of Fluids and Structures 22, 807 - 818.

Dahl, J.M., Hover, F.S., Triantafyllou, M.S., 2007. Resonant vibrations of bluff bodies cause multivortex shedding and high frequency forces. Physical Review Letters 99 (144503), 1 - 4.

Dahl, J.M., Hover, F.S., Triantafyllou, M.S., 2008. Third harmonic lift forces from phase variation in forced crossflow and in-line cylinder motions, In: Proceedings of the Ninth International Conference on Flow-Induced Vibrations, Prague, Czech Republic.

Dahl, J.M., Hover, F.S., Triantafyllou, M.S., Oakley, O.H., 2010. Dual resonance in vortex-induced vibrations at subcritical and supercritical Reynolds numbers. Journal of Fluid Mechanics 643, 395 - 424.

Ding, L., Zhang, L., Wu, C., Kim, E.S., Bernitsas, M.M., 2017. Numerical study on the effect of tandem spacing on flow-induced motions of two cylinders with passive turbulence control. Journal of Offshore Mechanics and Arctic Engineering 139, 0218011 - 0218018.

Evangelinos, C., Karniadakis, G.E., 1999. Dynamics and flow structures in the turbulent of rigid and flexible cylinders subject to vortex-induced vibrations. Journal of Fluid Mechanics 400, 91 - 124.

Evangelinos, C., Lucor, D., Karniadakis, G.E., 2000. DNS-derived force distribution on flexible cylinders subject to vortex-induced vibration. Journal of Fluids and Structures 14, 429 - 440.

Facchinetti, M.L., de Langre, E., Biolley, F., 2004. Coupling structure and wake oscillators in vortex-induced vibrations. Journal of Fluids and Structures 19, 123 - 140.

Farshidianfar, A., Zanganeh, H., 2010. A modified wake oscillator model for vortex-induced vibration of circular cylinders for a wide range of mass-damping ratio. Journal of Fluids and Structures 26, 430 - 441.

Feng, C.C., 1968. The measurements of vortex-induced effects in flow past a stationary and oscillating circular and D-section cylinders. University of British Columbia, Vancouver, Canada.

Gabbai, R.D., Benaroya, H., 2005. An overview of modelling and experiments of vortex-induced vibrations of circular cylinders. Journal of Sound and Vibration 282, 575 - 646.

Gao, Y., Fu, S., Ren, T., Xiong, Y., Song, L., 2015. VIV response of a long flexible riser fitted with strakes in uniform and linearly sheared currents. Applied Ocean Research 52, 102 - 114.

Gedikli, E.D., Dahl, J.M., 2014. Mode shape vibration for a low-mode number flexible cylinder subject to vortex-induced vibrations, In: Proceedings of the ASME 33rd International Conference on Ocean, Offshore and Arctic Engineering, San Francisco, USA.

Gharib, M.R., Leonard, A., Gharib, M., Roshko, A., 1998. The absence of lock-in and the role of mass ratio, In: Proceedings of Conference on Bluff Body Wakes and Vortex-Induced Vibrations, Washington, D.C. USA.

González, L.M., Rodriguez, A., Garrido, C.A., Suarez, J.C., Huera Huarte, F.J., 2015. CFD simulation on the vortex-induced vibrations of a flexible cylinder with wake interference, OMAE2015-41128, In: Proceedings of the ASME 34th International Conference on Offshore Mechanics and Arctic Engineering, St. Johns, Canada.

Govardhan, R., Williamson, C.H.K., 2000. Modes of vortex formation and frequency response for a freely-vibrating cylinder. Journal of Fluid Mechanics 420, 85 - 130.

Govardhan, R., Williamson, C.H.K., 2002. Resonance forever: existence of a critical mass and an infinite regime of resonance in vortex-induced vibration. Journal of Fluid Mechanics 473, 147 - 166.

Govardhan, R., Williamson, C.H.K., 2004. Critical mass in vortex-induced vibration of a cylinder. European Journal of Mechanics-B/Fluids 23, 17 - 27.

Griffin, O.M., Ramberg, S.E., 1974. The vortex street wakes of vibrating cylinders. Journal of Fluid Mechanics 66, 553 - 576.

Gsell, S., Bourguet, R., Braza, M., 2016. Two-degree-of-freedom vortex-induced vibrations of a circular cylinder at Re = 3900. Journal of Fluids and Structures 67, 156 - 172.

Gu, J., Vitola, M., Coelho, J., W., P., Duan, M., Levi, C., 2013. An experimental investigation by towing tank on VIV of a long flexible cylinder for deep water riser application. Journal of Marine Science and Technology 18, 358 - 369.

Guilmineau, E., Queutey, 2004. Numerical simulation of vortex-induced vibration of a circular cylinder with low mass-damping in a turbulent flow. Journal of Fluids and Structures 19, 449 - 466.

Hilber, H.M., Hughes, T.J.R., Taylor, R.L., 1977. Improved numerical dissipation for time integration algorithm in structural dynamics. Earthquake Engineering and Structural Dynamics 5, 283-292.

Holmes, S., Oakley, O.H., Constantinides, Y., 2006. Simulation of riser VIV using fully three dimensional CFD simulations, OMAE2006-92124, In: Proceedings of the ASME 25th International Conference on Ocean, Offshore and Arctic Engineering, Hamburg, Germany.

House, K.Z., Schrag, D.P., Harvey, C.F., Lackner, K.S., 2006. Permanent carbon dioxide storage in deep-sea sediments. Proceedings of the National Academy of Sciences of the United States of America 103, 12291 - 12295.

Hover, F.S., Davis, J.T., Triantafyllou, M.S., 2004. Three-dimensional mode transition in vortex-induced vibrations of a circular cylinder. European Journal of Mechanics-B/Fluids 23, 29 - 40.

Hover, F.S., Techet, A.H., Triantafyllou, M.S., 1998. Forces on oscillating uniform and tapered cylinders in crossflow. Journal of Fluid Mechanics 363, 97 - 114.

Hover, F.S., Triantafyllou, M.S., 2001. Galloping response of a cylinder with upstream wake interference. Journal of Fluids and Structures 15, 503 - 512.

Huang, K., Chen, H.C., Chen, C.R., 2009. Vertical riser VIV simulation in uniform currents. Journal of Offshore Mechanics and Arctic Engineering 132, 1 - 10.

Huang, K., Chen, H.C., Chen, C.R., 2011a. Numerical scheme for riser motion calculation during 3D VIV simulation. Journal of Fluids and Structures 27, 947 - 961.

Huang, S., Khorasanchi, M., Herfjord, K., 2011b. Drag amplification of long flexible riser models undergoing multi-mode VIV in uniform currents. Journal of Fluids and Structures 27, 342 - 353.

Huera-Huarte, F.J., Bangash, Z.A., González, L.M., 2014. Towing tank experiments on the vortex-induced vibrations of a flexible cylinder with wake interference, OMAE2014-23873, In: Proceedings of the ASME 32nd International Conference on Ocean, Offshore and Arctic Engineering, San Francisco, California, USA.

Huera-Huarte, F.J., Bearman, P.W., 2009. Wake structures and vortex-induced vibrations of a long flexible cylinder - Part I: Dynamic response. Journal of Fluids and Structures 25, 969 - 990.

Huera-Huarte, F.J., Bearman, P.W., 2011. Vortex and wake-induced vibrations of a tandem arrangement of two flexible circular cylinders with near wake interference. Journal of Fluids and Structures 27, 193 - 211.

Huera-Huarte, F.J., Gharib, M., 2011. Vortex- and wake-induced vibrations of a tandem arrangment of two flexible circular cylinders with far wake interference. Journal of Fluids and Structures 27, 824 - 828.

Hughes, T.J.R., 1987. The Finite Element Method: Linear Static and Dynamic Finite Element Analysis. Prentice-Hall, Inc., New Jersey, USA.

Igarashi, T., 1981. Characteristics of the flow around two circular cylinders arranged in tandem (1st report). Bulletin of the JSME 24, 323 - 331.

Igarashi, T., 1984. Characteristics of the flow around two circular cylinders arranged in tandem (second report, unique flow phenomenon at small spacing). Bulletin of the JSME 27, 2380 - 2387.

Jasak, H., Weller, H.G., Gosman, A.D., 1999. High resolution NVD differencing scheme for arbitrary unstructured meshes. International Journal for Numerical Methods in Fluids 31, 431 - 449.

Jauvtis, N., Williamson, C.H.K., 2004. The effect of two degrees of freedom on vortex-induced vibration at low mass and damping. Journal of Fluid Mechanics 509, 23 - 62.

Jeong, J., Hussain, F., 1995. On the identification of a vortex. Journal of Fluid Mechanics 285, 69 - 94.

Jhingran, V., Vandiver, J.K., 2007. Incorporating the higher harmonics in VIV fatigue predictions, OMAE2007-29352, In: Proceedings of the ASME 26th International Conference on Offshore Mechanics and Arctic Engineering, San Diego, USA.

Kang, Z., Jia, L., 2013. An experimental study of cylinder's two degree of freedom VIV trajectories. Ocean Engineering 70, 129 - 140.

Khalak, A., Williamson, C.H.K., 1997a. Fluid forces and dynamics of a hydroelastic structure with very low mass and damping. Journal of Fluids and Structures 11, 973 - 982.

Khalak, A., Williamson, C.H.K., 1997b. Investigation of the relative effects of mass and damping in vortex-induced vibration of a circular cylinder. Journal of Wind Engineering and Industrial Aerodynamics 69 - 71, 341 - 350.

Khalak, A., Williamson, C.H.K., 1999. Motions, forces and mode transitions in vortex-induced vibration at low mass-damping. Journal of Fluids and Structures 13, 813 - 851.

Klamo, J.T., Leomard, A., Roshko, A., 2006. The effects of damping on the amplitude and frequency response of a freely vibrating cylinder in cross-flow. Journal of Fluids and Structures 22, 845 - 856.

Kondo, N., 2012. Three-dimensional computation for flow-induced vibrations in in-line and cross-flow directions of a circular cylinder. International Journal for Numerical Methods in Fluids 70, 158 - 185.

Lackner, K.S., 2002. Carbonate chemistry for sequestering fossil carbon. Annual Review of Energy and the Environment 27, 193 - 232.

Laneville, A., Brika, D., 1999. The fluid and mechanical coupling between two circular cylinders in tandem arrangement. J. Fluids Struct. 13 (967-986).

Lehn, E., 2003. VIV Suppression Tests on High L/D Flexible Cylinders. Norwegian Marine Technology Research Institute, Trondheim, Norway.

Leonard, B.P., 1991. The ULTIMATE conservative difference scheme applied to unsteady one-dimensional advection. Computer Methods in Applied Mechanics and Engineering 88, 17 - 74.

Leontini, J.S., Thompson, M.C., Hourigan, K., 2006. The beginning of branching behaviour of vortex-induced vibration during two-dimensional flow. Journal of Fluids and Structures 22, 857 - 864.

Lie, H., Kaasen, K.E., 2006. Modal analysis of measurements from a large-scale VIV model test of a riser in linearly sheared flow. Journal of Fluids and Structures 22, 557 - 575.

Lin, J., Yang, Y., Rockwell, D., 2002. Flow past two cylinders in tandem: instantaneous and averaged flow structure. J. Fluids Struct. 16, 1059-1071.

Ljungkrona, L., Norberg, C., Sundén, B., 1991. Free-stream turbulence and tube spacing effects on surface pressure fluctuations for two tubes in an in-line arrangment. Journal of Fluids and Structures 5, 701 - 727.

Ljungkrona, L., Sundén, B., 1993. Flow visualisation and surface pressure measurement on two tubes in an inline arrangement. Experimental Thermal and Fluid Science 6, 15 - 27.

Lucor, D., Foo, J., Karniadakis, G.E., 2003. Correlation length and force phasing of a rigid cylinder subject to VIV, in: Benaroya, H., Wei, T. (Eds.), In: IUTAM Symposium on Integrated Modelling of Fully Coupled Fluid Structure Interactions Using Analysis, Computations and Experiments. Springer Dordrecht, pp. 187 - 199.

Lucor, D., Foo, J., Karniadakis, G.E., 2005. Vortex mode selection of a rigid cylinder subject to VIV at low mass-damping. Journal of Fluids and Structures 20, 483 - 503.

Lucor, D., Triantafyllou, M.S., 2008. Parametric study of a two degree-of-freedom cylinder subject to vortex-induced vibrations. Journal of Fluids and Structures 24, 1284 - 1293.

Meneghini, J.R., Bearman, P.W., 1995. Numerical simulation of high amplitude oscillatory flow around a circular cylinder. Journal of Fluids and Structures 9, 435 - 455.

Meneghini, J.R., Saltara, F., R.A., F., Yamamoto, C.T., Casaprima, E., Ferrari, J.A., 2004. Numerical simulation of VIV on long flexible cylinders immersed in complex flow fields. European Journal of Mechanics-B/Fluids 23, 51 - 63.

Menter, F., Sharkey, P., Yakubov, S., Kuntz, M., 2006. Overview of fluid-structure coupling in ANSYS-CFX, OMAE2006-92145, In: Proceedings of the ASME 25th International Conference on Ocean, Offshore and Arctic Engineering, Hamburg, Germany.

Moe, G., Wu, Z.J., 1990. The lift force on a cylinder vibrating in a current. Journal of Offshore Mechanics and Arctic Engineering 112, 297 - 303.

Navrose, Mittal, S., 2013. Free vibrations of a cylinder: 3-D computations at Re = 1000. Journal of Fluids and Structures 41, 109 - 118.

Newman, D.J., Karniadakis, G.E., 1997. A direct numerical simulation study of flow past a freely vibrating cable. Journal of Fluid Mechanics 344, 95 - 136.

Nicoud, F., Ducros, F., 1999. Subgrid-scale stress modelling based on the square of the velocity gradient tensor. Flow, Turbulence and Combustion 62, 183 - 200.

Ozaki, M., Ohsumi, T., Kajiyama, R., 2013. Ship-based offshore CCS featuring CO_2 shuttle ships equipped with injection facilities. Energy Procedia 37, 3184 - 3190.

Païdoussis, M.P., Price, S.J., de Langre, E., 2014. Fluid-Structure Interactions: Cross-Flow-Induced Instabilities. Cambridge University Press, New York, USA.

Papaioannou, G.V., 2004. A Numerical Study of Flow-Structure Interactions with Application to Flow Past a Pair of Cylinders. Massachusetts Institute of Technology, Massachusetts, USA.

Papaioannou, G.V., Yue, D.K.P., Triantafyllou, M.S., Karniadakis, G.E., 2006. Three-dimensionality effect in flow around two tandem cylinders. Journal of Fluid Mechanics 558, 387 - 413.

Papaioannou, G.V., Yue, D.K.P., Triantafyllou, M.S., Karniadakis, G.E., 2008. On the effect of spacing on the vortex-induced vibrations of two tandem cylinders. Journal of Fluids and Structures 24, 833 - 854.

Pershad, H., Slater, S., 2007. Development of a CO_2 transport and storage network in the North Sea: report to the North Sea Basin Task Force, Aberdeen, UK.

Pikovsky, A., Rosenblum, M., Kurths, J., 2001. Synchronisation: A Universal Concept in Nonlinear Sciences. Cambridge University Press, New York, USA.

Placzek, A., Sigrist, J., Hamdouni, A., 2009. Numerical simulation of an oscillating cylinder in a cross-flow at low Reynolds number: Forced and free oscillations. Computers and Fluids 38, 80 - 100.

Pontaza, J.P., Chen, H.C., 2006. Three-dimensional numerical simulations of circular cylinders undergoing two degree-of-freedom vortex-induced vibrations. Journal of Offshore Mechanics and Arctic Engineering 129, 158 - 164.

Prasanth, T.K., Mittal, S., 2009. Flow-induced oscillation of two circular cylinders in tandem arrangement at low Re. Journal of Fluids and Structures 25, 1029 - 1048.

Rhie, C., Chow, W., 1982. A numerical study of the turbulent flow past an isolated airfoil with trailing edge separation, 3rd Joint Thermophysics, Fluids, Plasma and Heat Transfer Conference. AIAA, St. Louis, USA.

Rodi, W., 1997. Comparison of LES and RANS calculations of the flow around bluff bodies. Journal of Wind Engineering and Industrial Aerodynamics 71, 55 - 75.

Roshko, A., 1961. Experiments on the flow past a circular cylinder at very high Reynolds number. Journal of Fluid Mechanics 10, 345 - 356.

Saltara, F., Neto, A.D., Lopez, J.I.H., 2011. 3D CFD simulation of vortex-induced vibration of cylinder. International Journal of Offshore and Polar Engineering 21, 192 - 197.

Sanchis, A., Sælevik, G., Grue, J., 2008. Two-degree-of-freedom vortex-induced vibrations of a spring-mounted rigid cylinder with low mass ratio. Journal of Fluids and Structures 24, 907 - 919.

Sarpkaya, T., 1995. Hydrodynamics damping, flow-induced oscillations and biharmonic response. Journal of Offshore Mechanics and Arctic Engineering 117, 232 - 238.

Schewe, G., 1983. On the force fluctuations acting on a circular cylinder in cross-flow from subcritical up to transcritical Reynolds numbers. Journal of Fluid Mechanics 113, 265 - 285.

Singh, S.P., Mittal, S., 2005. Vortex-induced oscillations at low Reynolds numbers: Hysteresis and vortex shedding modes. Journal of Fluids and Structures 20, 1085 - 1104.

Spence, B., Horan, D., Turcker, O., 2014. The Peterhead-Goldeneye gas post-combustion CCS project. Energy Procedia 63, 6258 - 6266.

Srinil, N., Rega, G., Chucheepsakul, S., 2007. Two-to-one resonant multi-modal dynamics of horizontal/inclined cables. Part I: Theoretical formulation and model validation. Nonlinear Dynamics 48, 231 - 252.

Srinil, N., Zanganeh, H., 2012. Modelling of coupled cross-flow/in-line vortex-induced vibrations using double Duffing and van der Pol oscillators. Ocean Engineering 53, 83 - 97.

Srinil, N., Zanganeh, H., Day, A., 2013. Two-degree-of-freedom VIV of a circular cylinder with variable natural frequency ratio: Experimental and numerical investigations. Ocean Engineering 73, 179 - 194.

Srinil, S., Rega, G., 2007. Two-to-one resonant multi-modal dynamics of horizontal/inclined cables: Part II: Internal resonance activation, reduced-order models and nonlinear normal modes. Nonlinear Dynamics 48, 253 - 274.

Stappenbelt, B., Lalji, F., Tan, G., 2007. Low mass ratio vortex-induced motion, In: Proceedings of the 16th Australasian Fluid Mechanics Conference, Gold Coast, Australia.

Sumer, B.M., Fredsøe, J., 2006. Hydrodynamics around Cylindrical Structures. World Scientific Publishing Co. Pte. Ltd., London, UK.

Sumner, D., 2010. Two circular cylinders in cross-flow: A review. Journal of Fluids and Structures 26, 849 - 899.

Sun, L., Zong, Z., Dong, J., Dong, G.H., Liu, C.F., 2012. Stripwise discrete vortex method for VIV analysis of flexible risers. Journal of Fluids and Structures 35, 21 - 49.

Swithenbank, B.S., Vandiver, J.K., Larsen, C.M., Lie, H., 2008. Reynolds number dependence of flexible cylinder VIV response data, OMAE2008-57045, In: Proceedings of the ASME 27th International Conference on Offshore Mechanics and Arctic Engineering, Estoril, Portugal.

Tognarelli, M.A., Slocum, S.T., Frank, W.R., Campbell, R.B., 2004. VIV response of a long flexible cylinder in uniform and linearly sheared currents, OTC 16338, In: Proceedings of the 2004 Offshore Technology Conference, Houston, USA.

Tognarelli, M.A., Taggart, S., Campbell, M., 2008. Actual VIV fatigue response of full scale drilling risers: with and without suppression devices, OMAE2008-57046,

In: Proceedings of the ASME 27th International Conference on Ocean, Offshore and Arctic Engineering, Estoril, Portugal.

Triantafyllou, M.S., Bourguet, R., Dahl, J.M., Modarres-Sadeghi, Y., 2016. Vortex-Induced Vibrations, in: Dhanak, M.R., Xiros, N.I. (Eds.), Springer Handbook of Ocean Engineering. Springer International Publishing, London, UK.

Trim, A.D., Braaten, H., Lie, H., Tognarelli, M.A., 2005. Experimental investigation of vortex-induced vibration of long marine risers. Journal of Fluids and Structures 21 335 - 361.

Vandiver, J.K., 1993. Dimensionless parameters important to the prediction of vortex-induced vibration of long, flexible cylinders in ocean currents. Journal of Fluids and Structures 7, 423 - 455.

Vandiver, J.K., Jaiswal, V., Jhingran, V., 2009. Insights on vortex-induced, travelling waves on long risers. Journal of Fluids and Structures 25, 641 - 653.

Vandiver, J.K., Jong, J.Y., 1987. The relationship between in-line and cross-flow vortex-induced vibration of cylinders. Journal of Fluids and Structures 1, 381 - 399.

Vandiver, J.K., Swithenbank, S., Jaiswal, V., Marcollo, H., 2006. The effectiveness of helical strakes in the suppression of high-mode-number VIV, OTC 18276, In: Proceedings of the 2006 Offshore Technology Conference, Houston, USA.

Wang, E., Xiao, Q., 2016. Numerical simulation of vortex-induced vibration of a vertical riser in uniform and linearly sheared currents. Ocean Engineering 121, 492 - 515.

Weaver, W., Timoshenko, S.P., Young, D.H., 1974. Vibration Problems in Engineering. John Wiley and Sons, New York, USA.

Willden, R.H.J., Graham, J.M.R., 2001. Numerical prediction of VIV on long flexible circular cylinders. Journal of Fluids and Structures 15, 659 - 669.

Williamson, C.H.K., 1988. The existence of two stages in the transition to three-dimensionality of a cylinder wake. Physics of Fluids 31, 3165 - 3168.

Williamson, C.H.K., 1989. Oblique and parallel modes of vortex shedding in the wake of a circular cylinder at low Reynolds number. Journal of Fluid Mechanics 206, 579 - 627.

Williamson, C.H.K., 1992. The natural and forced formation of spot-like 'vortex dislocations' in the transition of a wake. Journal of Fluid Mechanics 243, 393 - 441.

Williamson, C.H.K., Govardhan, R., 2004. Vortex-induced vibrations. Annual Review of Fluid Mechanics 36, 413 - 455.

Williamson, C.H.K., Roshko, A., 1988. Vortex formation in the wake of an oscillating cylinder. Journal of Fluids and Structures 2, 355 - 381.

Wu, J., Lie, H., Larsen, C.M., Liapis, S., Baarholm, R., 2016. Vortex-induced vibration of a flexible cylinder: Interaction of the in-line and cross-flow responses. Journal of Fluids and Structures 63, 238 - 258.

Wu, J., Welch, L.W., Welsh, M.C., Sheridan, J., G.J., W., 1994. Spanwise wake structures of a circular cylinder and two circular cylinders in tandem. Experimental Thermal and Fluid Science 9, 299 - 308.

Wu, W., 2011. Two-Dimensional RANS Simulation of Flow Induced Motion of Circular Cylinder with Passive Turbulence Control, Naval Architecture and Marine Engineering. University of Michigan, Ann Arbor, Michigan, USA.

Wu, X., Ge, F., Hong, Y., 2012. A review of recent studies on vortex-induced vibrations of long slender cylinders. Journal of Fluids and Structures 28, 292 - 308.

Xie, F., Deng, J., Xiao, Q., Zheng, Y., 2012. A numerical simulation of VIV on a flexible circular cylinder. Fluid Dynamics Research 44 (045508), 1 - 21.

Xu, G., Zhou, Y., 2004. Strouhal numbers in the wake of two inline cylinders. Experiments in Fluids 37, 248 - 256.

Yamamoto, C.T., Meneghini, J.R., Saltara, F., Fregonesi, R.A., Ferrari, J.A., 2004. Numerical simulations of vortex-induced vibration on flexible cylinders. Journal of Fluids and Structures 19, 467 - 489.

Young, M.E., Ooi, A., 2004. Turbulence models and boundary conditions for bluff body flow, In: Proceedings of the 15th Australasian Fluid Mechanics Conference, Sydney, Australia.

Zanganeh, H., Srinil, N., 2014. Characterisation of variable hydrodynamic coefficients and maximum responses in two-dimensional vortex-induced vibrations with dual resonance. Journal of Vibrations and Acoustics 136 (0510101), 1 - 15.

Zdero, R., Turan, Ö.F., Havard, D.G., 1995. Towards understanding galloping: Near-wake study of oscillating smooth and stranded circular cylinders in forced motion. Experimental Thermal and Fluid Science 10, 28 - 43.

Zdravkovich, M.M., 1977. Review of flow interference between circular cylinders in cross flow. Journal of Fluids and Structures 1, 239 - 261.

Zdravkovich, M.M., 1985. Flow induced oscillations of two interfering circular cylinders. Journal of Sound and Vibration 101, 511-521.

Zdravkovich, M.M., 1987. The effects of interference between circular cylinders in cross flow. Journal of Fluids and Structures 1, 239 - 261.

Zdravkovich, M.M., Pridden, D.L., 1977. Interference between two circular cylinders; series of unexpected discontinuities. Journal of Industrial Aerodynamics 4, 305 - 319.

Zhao, M., 2013. Flow induced vibration of two rigidly coupled circular cylinders in tandem and side-by-side arrangements at a low Reynolds number of 150. Physics of Fluids 25, 1236011 - 12360131.

Zhao, M., Cheng, L., 2011. Numerical simulation of two-degree-of-freedom vortex-induced vibration of a circular cylinder close to a plane boundary. Journal of Fluids and Structures 27 1097 - 1110.

Zhao, M., Cheng, L., 2014. Vortex-induced vibration of a circular cylinder of finite length. Physics of Fluids 26, 0151111 - 01511126.

Zhao, M., Cheng, L., An, H., Lu, L., 2014. Three-dimensional numerical simulation of vortex-induced vibration of an elastically mounted rigid circular cylinder in steady current. Journal of Fluids and Structures 50, 292 - 311.

Zhou, Y., Yiu, M.W., 2006. Flow structure, momentum and heat transport in a two-tandem-cylinder wake. Journal of Fluid Mechanics 548, 17 - 48.

Publications

The following papers have been published during my PhD.

Journal Articles

Wang, E., Xiao, Q., Zhu, Q., Incecik, A., 2017. The effect of spacing on the vortex-induced vibrations of two tandem flexible cylinders. Physics of Fluids 29, 077103.

Wang, E., Xiao, Q., Incecik, A., 2017. Three-dimensional numerical simulation of two-degree-of-freedom VIV of a circular cylinder with varying natural frequency ratios at Re = 500. Journal of Fluids and Structures 73, 162 – 182.

Wang, E., Xiao, Q., 2016. Numerical simulation of vortex-induced vibration of a vertical riser in uniform and linearly sheared currents. Ocean Engineering 121, 492 – 515.

Conference Papers

Wang, E., Xiao, Q., Incecik, A., 2015. CFD simulation of vortex-induced vibration of a vertical riser, In: Proceedings of the 9th International Workshop on Ship and Marine Hydrodynamics, Glasgow, UK.

Wang, E., Xiao, Q., Liu, W., 2014. Numerical simulation of multi-modal vortex-induced vibration of a 3D flexible circular cylinder, In: Proceedings of the 2nd International Conference on Maritime Technology, Glasgow, UK.

Wang, E., Xiao, Q., Liu, W., 2013. System damping effect on VIV energy extraction device, In: Proceedings of the 8th International Workshop on Ship Hydrodynamics, Seoul, Korea.

Wang, E., Xiao, Q., Srinil, N., Zanganeh, H., 2013. Vortex-induced vibration of a circular cylinder with two degrees of freedom: computational fluid dynamics vs. reduced-order models, OMAE2013-10456, In: Proceedings of the ASME 32nd International Conference on Ocean Offshore and Arctic Engineering, Nantes, France.

"Diligence is the path up the mountain of knowledge. Hard work is the boat across the endless sea of learning."

- Han Yu